# Antje Thiele

# 3D Building Reconstruction
# From High Resolution Multi-Aspect
# Interferometric Synthetic Aperture RADAR Data

**München 2013**

# 3D Building Reconstruction
# From High Resolution Multi-Aspect
# Interferometric Synthetic Aperture RADAR Data

Von der Fakultät für Bauingenieurwesen und Geodäsie
der Gottfried Wilhelm Leibniz Universität Hannover
zur Erlangung des Grades
Doktor-Ingenieur (Dr.-Ing.)
genehmigte Dissertation

von

## Dipl.-Ing. Antje Thiele

geboren
am 13.12.1979 in Freiberg

München 2013

Prüfungskommission

Vorsitzender:     Prof. Dr. Ing. habil. Jürgen Müller
Referent:          Prof. Dr.-Ing. Uwe Sörgel
Korreferenten:  Prof. Dr.-Ing. Uwe Stilla
                       Prof. Dr.-Ing. habil. Stefan Hinz
                       Prof. Dr.-Ing. Claus Brenner

Tag der Einreichung der Arbeit:  20.11.2012
Tag der mündlichen Prüfung:      18.01.2013

# Content

# Abstract

The main advantages of the Synthetic Aperture Radar (SAR) technique, cloud coverage and daytime independency, offer the opportunity to apply such technique for tasks that require rapid data acquisition (e.g. monitoring of disasters like floodings, landslides, or earthquakes).

The new generation of airborne SAR-Sensors (e.g. PAMIR, MetaSensing, and STAR-Series) and spaceborne SAR sensors (e.g. TerraSAR-X) allows mapping of wide areas providing geometric resolution in the range from metre up to decimetre scale. This spatial resolution enables a detailed analysis of urban areas from industrial to residential buildings. Beyond the acquisition of single SAR datasets used for mapping, the across-track configuration of SAR sensors provides single-pass or repeat-pass Interferometric SAR (InSAR) data. InSAR phases allow the computation of a Digital Surface Model (DSM) of the imaged area. Based on this three-dimensional (3D) information not only object detection, but also object reconstruction is possible.

Within this thesis, we focus initially on a detailed analysis of building signatures in InSAR data to select reliable features for building reconstruction. The appearance of buildings in magnitude and interferometric phase data is characterised by typical signal distributions due to areas of direct reflection (e.g. *layover*), of multi-bounce reflection (e.g. *building corner*), and of no-response (e.g. *shadow*). The analysis will consider InSAR data of different sensor types, sensor configurations, illumination geometries, and building types to extract the most suitable building features.

Then, a new approach of building reconstruction exploiting different building parts is presented. Given that, especially in dense built-up areas, occlusion effects between neighbouring buildings and trees hamper the reconstruction, also multi-aspect data are considered to fill gaps of the reconstruction. First, primitive building objects are extracted from magnitude and interferometric phase signature by utilising each aspect separately. Afterwards, the fusion of these primitives is accomplished in a common coordinate system. Based on these multi-aspect features, building hypotheses are generated during a grouping step. This intermediate result is used to simulate InSAR phases of the hypothesis. Furthermore, a filtering is carried out on the measured phases to improve the comparison of measured and simulated phase signatures. Based on the correlation level of both, it is decided whether or not the building hypotheses are post-processed. Eventually, assembled building hypotheses are updated and the final building roof geometry is determined.

The capability of the developed algorithm is demonstrated by airborne InSAR data taken over urban environment. The achieved reconstruction results are evaluated by considering cadastral and airborne Light Detection and Ranging (LIDAR) data as reference.

**Keywords:**     Remote Sensing, Synthetic Aperture Radar Interferometry, Building Reconstruction

# Kurzfassung

Die Hauptvorteile der Synthetic Aperture Radar-Technik (SAR) sind die Wetter- und Tageszeit-unabhängigkeit, die den Einsatz dieser Technik insbesondere für Anwendungen mit zeitkritischer Datenerhebung (z. B. Erfassung von Katastrophen wie Überschwemmungen, Erdrutsche oder Erdbeben) anbieten.

Die neue Generation luftgetragener SAR-Sensoren (z. B. PAMIR, MetaSensing und STAR-Serie) und satellitengestützter SAR-Sensoren (z. B. TerraSAR-X) ermöglicht die großflächige Aufnahme von Gebieten in einer geometrischen Auflösung von einigen Metern bis Dezimetern. Diese räumliche Auflösung ermöglicht eine detaillierte Analyse städtischer Gebiete, beginnend bei industriellen Anlagen bis hin zu Wohnhäusern. Neben der Aufnahme von einzelnen SAR-Streifen, die für Kartierungen genutzt werden, können in einer *across-track* Konfiguration der Sensoren *single-pass* oder *repeat-pass* interferometrische SAR- (InSAR) Daten aufgezeichnet werden. Die InSAR-Phasen ermöglichen die Berechnung eines Digitalen Oberflächenmodells für das aufgenommene Gebiet. Basierend auf diesen drei-dimensionalen (3D) Informationen ist nicht nur eine Objekterkennung, sondern auch eine Objektrekonstruktion möglich.

In dieser Dissertation wird detailliert die Gebäudesignatur in InSAR-Daten analysiert, um die Auswahl geeigneter Objektmerkmale für die Gebäuderekonstruktion zu gewährleisten. Das Erscheinungsbild von Gebäuden in SAR-Magnituden-Bildern und InSAR-Phasen ist gekennzeichnet durch typische Signalverteilungen, die von Bereichen direkter Reflexion (z. B. *layover*), Mehrfachreflexion (z. B. am Gebäudecorner) und ohne Rückstreuung (z. B. Radarschatten) herrühren. Die Analyse berücksichtigt InSAR-Daten verschiedener Sensortypen, Sensorkonfigurationen, Aufnahmegeometrien und Gebäudetypen, um die geeignetsten Gebäudemerkmale zu extrahieren.

Anschließend erfolgt die Vorstellung eines neuen Verfahrens zur Gebäuderekonstruktion anhand unterschiedlicher Merkmale. Da speziell in dicht besiedelten Gebieten Abschattungen zwischen benachbarten Gebäuden und Bäumen die Rekonstruktion erschweren, werden Daten aus verschiedenen Richtungen (*multi-aspekt* Daten) berücksichtigt, um Lücken zu schließen. Zuerst werden aus der Magnituden- und InSAR-Phasensignatur die Gebäudemerkmale unabhängig für jede Aufnahmerichtung extrahiert. Anschließend werden die Merkmale in ein gemeinsames Koordinatensystem überführt und fusioniert. Die Generierung der Gebäudehypothesen erfolgt in einem Gruppierungsschritt, der auf den *multi-aspekt* Merkmalen fußt. Anhand der generierten Gebäudehypothesen erfolgt eine Simulation der InSAR-Phasen. Des Weiteren wird eine Filterung der InSAR-Phasen durchgeführt, die den Abgleich zwischen realen und simulierten Daten verbessert. Anhand ihrer Ähnlichkeit wird über die Notwendigkeit einer Nachprozessierung entschieden. Abschließend werden generierte Gebäudehypothesen aktualisiert und deren Gebäudedachgeometrie ermittelt.

Der entwickelte Algorithmus wird anhand von erflogenen InSAR-Daten eines städtischen Gebietes getestet. Die Bewertung der erzielten Rekonstruktionsergebnisse erfolgt durch Berücksichtigung von Kataster- und LIDAR-Daten als Referenz.

**Stichwörter:**    Fernerkundung, Synthetic Aperture Radar Interferometrie, Gebäuderekonstruktion

# Abbreviations

| | |
|---|---|
| 1D, 2D, 3D | One-, two-, three-dimensional |
| CFAR | Constant False Alarm Rate |
| CoV | Coefficient of Variation |
| CoVAmCoh | Coefficient of Variation Amplitude Coherence |
| CRF, MRF, GMRF | Conditional, Markov, Gaussian Markov Random Field |
| D1, D2 | CFAR line detectors of Tupin [135] |
| DEM | Digital Elevation Model |
| DSM | Digital Surface Model |
| DTM | Digital Terrain Model |
| ENL | Equivalent Number of Looks |
| GCP | Ground Control Point |
| GIS | Geographic Information System |
| GO | Geometrical Optics |
| HF-, VHF-, UHF-band | High, Very High, Ultra High Frequency band |
| InSAR | Interferometric Synthetic Aperture Radar |
| IRF | Impulse Response Function |
| LIDAR | Light Detection and Ranging |
| MF | Membership Function |
| NESZ | Noise Equivalent Sigma Zero |
| PO | Physical Optics |
| pdf | Probability Density Function |
| PSI | Persistent Scatterer (PS) Interferometry |
| RADAR | Radiofrequency Detection and Ranging |
| RAR | Real Aperture Radar |
| RCS | Radar Cross Section |
| RGB | Red Green Blue |
| RMS | Root Mean Square |
| SAR | Synthetic Aperture Radar |

SLC                     Single Look Complex

SNR                     Signal to Noise Ratio

SRTM                    Shuttle Radar Topography Mission

SVA                     Spatially Variant Apodization

# Symbols

| | |
|---|---|
| $A, A_1, A_2$ | Amplitude of SAR signal, amplitudes of InSAR image pair $(A_1, A_2)$ |
| $A_{1,A}, A_{1,B}, A_{1,C}, A_{2,A}, A_{2,B}, A_{2,C}$ | Amplitude of object point $P_i$ with $i \in \{A, B, C\}$ measured at Antenna $T_j$ with $j \in \{1, 2\}$ |
| $A_{T,1}, A_{T,2}$ | General amplitude with regard to the antenna |
| $\overline{A}, \overline{A}_{dB}$ | Arithmetic average of $A_1, A_2$, dB scaled mean amplitude $\overline{A}$ |
| $a$ | Distance between parallel lines |
| $a_0, a_1$ | Parameter of translation |
| $area_{pg_{CC}}$ | Span-area of parallelogram $pg_{cc}$ |
| $area_{struct}$ | Span-area of structure ($struct = L, T, X$) |
| $BW$ | Bandwidth of the signal |
| $B, B_\perp, B_H, B_V$ | Interferometric baseline; perpendicular, horizontal, vertical part of the spatial baseline |
| $B_c, B_{c\perp}$ | Critical baseline; perpendicular part of the critical baseline |
| $b$ | Width of layover line / stretching-affected signature part |
| $b_0, b_1$ | Parameter of scaling |
| $b_o$ | Binary map of orientation $o$ |
| $C$ | Complex cross-correlation coefficient |
| $C_{veg}, C_{urb}$ | Superclass of vegetated area, urban area |
| $C_{veg\_fus}$ | Fused superclass of vegetated area form all multi-aspect data |
| $CoV, CoV_A, CoV_I, CoV_{\sigma^\circ}$ | Coefficient of Variation; $CoV$ of amplitudes, intensities, normalised RCS |
| $\overline{CoV}, \overline{CoV_A}, \overline{CoV_I}, \overline{CoV_{\sigma^\circ}}$ | Averaged Coefficient of Variation; $\overline{CoV}$ of amplitudes, intensities, normalised RCS |
| $c \approx 3 \cdot 10^8 \, m/s$ | Speed of light |
| $c$ | Width of building in slant range direction |
| $f$ | Foreshortening-affected signature part |
| $f_n$ | Fragments of the DSM profile with $n = 1, 2, ...$ |
| $fp$ | All footprints of building hypotheses |
| $fp_{cc}, fp_{cl}, fp_{ll}$ | Footprints of building hypotheses resulting from the parallelograms |
| $fp_{cc\_f}, fp_{cl\_f}, fp_{ll\_f}$ | Filtered footprints of building hypotheses |
| $G$ | Antenna gain |

| | |
|---|---|
| $g$ | Weibull distribution |
| $\Delta h$ | Unambiguous range |
| $\bar{h}$ | Global mean terrain height |
| $h_i$ | Interferometric height at pixel position $i$ |
| $h, h_e, h_f, h_r$ | Height of object, $h$ of eave ($e$), flat roof ($f$), ridge ($r$) |
| $h_{e\_g}, h_{e\_h}, h_{e\_m}$ | Eave height of gable-, hipped-, monopitch roof |
| $h_{f\_g}, h_{f\_h}, h_{f\_m}$ | Ridge height of gable-, hipped-, monopitch roof |
| $h_l$ | Local height along building feature |
| $h_n$ | Normalised interferometric height |
| $H$ | Height of sensor over ground |
| $I$ | Intensity of SAR signal |
| $i_0, i_1$ | Step width to adapt translation parameter |
| $j$ | Imaginary unit ($j = \sqrt{-1}$) |
| $j_0, j_1$ | Step width to adapt scaling parameter |
| $k, k_a, k_r, k_{rect}, k_{Hamm}$ | 3 dB bandwidth of the signal main lobe, in azimuth, range direction, after applying rectangular, Hamming weighting function |
| $k_s$ | Calibration and processor scaling factor |
| $L$ | Sensor losses |
| $L_{ra}, L_{sa}$ | Length of real aperture and of synthetic aperture |
| $l$ | Length of building / layover-affected signature part |
| $l_{all}$ | Extracted lines of all $l_{fo}$ |
| $l_c, l_{cl}, l_{cl\_s}, l_{cl\_d}$ | Corner lines, long corner lines, "single" $l_{cl}$, "double" $l_{cl}$ |
| $l_l, l_{ll}$ | Layover lines, long layover lines |
| $l_o$ | Overlap of parallel lines |
| $l_o, l_{fo}$ | Group of lines extracted from $b_o$ with $o = 1,...,8$, filtered $l_o$ |
| $l_s$ | Symmetry of parallel lines |
| $l_t$ | Length of detector template |
| $m$ | Multi-bounce affected signature part |
| $mask_i$ | Binary mask of height calculation at pixel position $i$ |
| $\vec{n}$ | Normal vector |
| $n_s, n_z, n_e$ | Illumination of target by radar beams $n$ at start time $t_s$, at crossing of Doppler null plane $t_z$, and at end time $t_e$ |
| $o$ | Index of template orientation |
| $P_A, P_B, P_C$ | Object points contributing to the same pixel cell |

| | |
|---|---|
| $P_i$ | Sampled ground range cell with $i = 1, 2, ...$ |
| $P_{n,S}, P_{n,E}$ | Start and end point of fragment $f_n$ |
| $P$ | Crossing point of two orthogonal lines |
| $P_R$ | Received power |
| $P_T$ | Transmitted power |
| $p$ | Parameter describing InSAR acquisition mode (1 or 2) |
| $p_o$ | Probability image of orientation $o$ |
| $patch_n$ | Image patch of $l_{cl,n}$ with $n = 1, ..., \#l_{cl}$ |
| $peak_{n,m}$ | Peaks of parameter calculation with $n = 1, ..., \#l_{cl}$ and $m = 1, 2, ...$ |
| $pg_{all}$ | Set of parallelograms resulting from all corner and layover lines |
| $pg_{cc}, pg_{cl}, pg_{ll}$ | Set of parallelograms resulting from two corner, one corner and one layover, and two layover lines |
| $R_q$ | Root mean square height of object surface |
| $\Delta r$ | Difference of runtime distances between two antennas |
| $r$ | Slant range distance between SAR sensor and ground object |
| $r_{1,A}, r_{1,B}, r_{1,C}, r_{2,A}, r_{2,B}, r_{2,C}$ | Slant range distance between Antenna $T_j$ with $j \in \{1, 2\}$ and object point $P_i$ with $i \in \{A, B, C\}$ |
| $r_{area}$ | Ratio between $area_{pg_{CC}}$ and $area_{struct}$ |
| $r_l$ | Maximum probability value of line |
| $r_{line}, r_{m,n}$ | Probability value of line, probability value of indices $(m,n) \in \{(1,2),(2,3)\}$ |
| $r_1, r_2$ | Range direction of aspect 1, aspect 2 |
| $S, S_1, S_2$ | SAR image / SAR interferogram, SAR signals of interferometric image pair |
| $S_y, S_{zero}$ | Averaged interferogram in y-direction, zero-centred interferogram |
| $[S]$ | Scatter matrix of SAR signal |
| $S_{HH}, S_{HV}, S_{VH}, S_{VV}$ | Components of scatter matrix with horizontal and vertical polarisation of transmitter and receiver signals |
| $s$ | Parameter of Rayleigh distribution / shadow-affected signature part |
| $s, s_{slant}, s_{ground}$ | Shadow affected signature part in slant and ground geometry |
| $s_i, s_q$ | Real and imaginary parts of SAR signal $S$ |
| $struct$ | Structure of two crossing lines ($struct = L, T, X$) |
| $T_1, T_2$ | Antennas of an InSAR sensor configuration |

| | |
|---|---|
| $t_s, t_z, t_e$ | Illumination of target at start time $t_s$, at crossing of Doppler null plane $t_z$, and at end time $t_e$ |
| $\Delta t$ | Difference of signal runtime between two antennas |
| $u_0, u_1$ | Interval border to adapt translation parameter |
| $v_0, v_1$ | Interval border to adapt scaling parameter |
| $w$ | Weighting function during SAR data processing / width of building |
| $w_{t,c}, w_{t,n}$ | Width of detector template at centre (c) and at neighbour (n) part |
| $\Delta x, \Delta y$ | Location constraints of corner-layover pairs |
| $x_{n,S}, y_{n,S}, z_{n,S}, x_{n,E}, y_{n,E}, z_{n,E}$ | Coordinates of the start and end point of the DSM fragment |
| | |
| $\alpha, \alpha_g, \alpha_h, \alpha_m$ | Pitch angle of building, $\alpha$ of gable-, hipped-, monopitch roof |
| $\alpha_{slant}, \alpha_{ground}$ | Pitch angle in slant range profile, in ground range geometry |
| $\beta$ | Hip pitch angle of building |
| $\beta^0$ | Beta Naught coefficients (local incidence angle corrected $\sigma^0$) |
| $\gamma, \gamma_{min}, \overline{\gamma}$ | Coherence, minimum level of coherence, average of coherence |
| $\gamma_i$ | Coherence value at pixel position $i$ |
| $\gamma_{noisy}, \gamma_{ground}, \gamma_{building}, \gamma_{shadow}, \gamma_{\Delta\varphi}$ | Correlation terms of noisy phase simulation, i.e., ground part, building part, shadow part, relation to simulated phases |
| $\gamma_{DC}, \gamma_{geom}, \gamma_{proc}$ | Decorrelation due to differences in the Doppler centroids, look angle, processing |
| $\gamma_{thermal}, \gamma_{temp}, \gamma_{vol}$ | Decorrelation due to thermal noise, temporal changes, volume scattering |
| $\gamma_{total}$ | Total correlation of interferometric image pair |
| $\Delta, \Delta_a, \Delta_r$ | Image pixel spacing azimuth and range direction |
| $\delta$ | Parameter of azimuth filtering |
| $\delta_a, \delta_r$ | SAR geometric resolution in azimuth and range direction related to used weighting function |
| $\delta_{ra}, \delta_{raf}, \delta_{ran}$ | RAR spatial resolution in azimuth direction, especially at far (f) and near (n) range positions |
| $\delta_{rg}, \delta_{rgf}, \delta_{rgn}$ | RAR ground resolution in range direction, especially at far (f) and near (n) range positions |
| $\delta_{rs}$ | RAR spatial resolution in slant range direction |
| $\delta_{sa}$ | SAR spatial resolution in azimuth direction |
| $\varepsilon_r$ | Relative permittivity of object material |

| | |
|---|---|
| $\zeta$ | Local incidence angle |
| $\zeta_{1,A}, \zeta_{1,B}, \zeta_{1,C}, \zeta_{2,A}, \zeta_{2,B}, \zeta_{2,C}$ | Local incidence angle at object point $P_i$ with $i \in \{A,B,C\}$ in relation to Antenna $T_j$ with $j \in \{1,2\}$ |
| $\eta$ | Shape parameter of Weibull distribution |
| $\theta, \theta_f, \theta_n$ | Span angle between nadir and illumination direction, especially at far and near range positions (off-nadir look angle) |
| $\kappa$ | Span angle between building ridge and sensor azimuth direction |
| $\lambda$ | Wavelength |
| $\mu, \mu_A, \mu_I, \mu_{\sigma^\circ}$ | Mean value, mean of amplitudes, intensities, and Sigma Naught coefficients |
| $\mu_{\text{diff}}$ | Mean value of differences between simulated and measured phases |
| $\mu_m, \mu_n$ | Mean values of line detector |
| $\nu$ | Hamming coefficient |
| $\xi$ | Span angle between baseline and horizontal part of baseline |
| $\rho$ | Cross correlation between simulated and measured phases |
| $\sigma$ | Radar Cross Section (RCS) of an object / standard deviation |
| $\sigma^0, \sigma_1^0, \sigma_2^0$ | Sigma Naught coefficient (normalised RCS), coefficients of interferometric image pair ($\sigma_1^0, \sigma_2^0$) |
| $\overline{\sigma^0}, \overline{\sigma_{\text{dB}}^0}$ | Arithmetic average of $\sigma_1^0, \sigma_2^0$, dB scaled mean $\overline{\sigma^0}$ |
| $\sigma_{\text{diff}}$ | Standard deviation of differences of simulated and measured phases |
| $\sigma_h, \sigma_{\overline{h}}$ | Standard deviation of object height, of global mean terrain height |
| $\sigma_A, \sigma_I, \sigma_{\sigma^\circ}$ | Standard deviation of amplitudes, intensities, and Sigma Naught coefficients |
| $\sigma_\varphi$ | Standard deviation of SAR signal phase |
| $\tau$ | Radar pulse duration |
| $\varphi, \varphi_1, \varphi_2$ | Phase of SAR signal, phases of interferometric image pair |
| $\varphi_{1,A}, \varphi_{1,B}, \varphi_{1,C}, \varphi_{2,A}, \varphi_{2,B}, \varphi_{2,C}$ | Phase of object point $P_i$ with $i \in \{A,B,C\}$ measured at Antenna $T_j$ with $j \in \{1,2\}$ |
| $\Delta\varphi$ | Phase difference between interferometric image pair |
| $\Delta\varphi_{\text{sim}}, \Delta\varphi_{\text{noisy}}$ | Simulated phases, noisy simulated phase |
| $\Delta\varphi_{\text{thermal}}, \Delta\varphi_{\text{geom}}, \Delta\varphi_{\text{shadow}}$ | Phase terms for simulation, i.e., thermal part, geometrical part, shadow part |
| $\varphi_{\text{ra}}, \varphi_{\text{sa}}$ | Angular aperture of RAR and SAR |
| $\varphi_{\text{flat}}$ | Phase contribution based on flat earth effect |

| | |
|---|---|
| $\varphi_{topo}$ | Phase contribution based on topography |
| $\varphi_{dist}$ | Phase contribution referring to distortions |
| $\varphi_{scat}$ | Phase contribution referring to backscatter properties of object |
| $\varphi_{noise}$ | Phase contribution referring to noise effects |
| $\psi$ | Scale parameter of Weibull distribution |

# 1 Introduction

## 1.1 Motivation

Synthetic Aperture Radar (SAR) is a technique, which images the earth surface by active illumination with microwave pulses. Hence, disturbances due to signal loss in the atmosphere as experienced by passive optical or active laser systems are almost negligible. This is an advantage if rapid acquisition of area-wide information is in demand for regions that were hit by natural disasters such as floodings, landslides, or earthquakes. Furthermore, the special InSAR mode provides the possibility to measure heights and height differences for the imaged regions. In addition to data acquisition, a major issue after such events is the rapid data interpretation, which is especially important in urban areas to support the authorities for decision-making. Here, the analysis of man-made structures and in particular of buildings is in demand, supported by pattern recognition methods to automatically derive detailed two-dimensional (2D) and three-dimensional (3D) information.

Besides a mandatory coherence of developed techniques and given application, the requirements and technical capabilities must match. Considering airborne sensors, since the beginning of the 21st century the commercial InSAR systems (e.g. Star-Series [85]) deliver spatial resolution up to half metre and the new generation of experimental systems (e.g. PAMIR [20] and SETHI [15]) even up to one decimetre. A similar major step forward was made by the new generation of spaceborne SAR sensors launched since 2006 (e.g. TerraSAR-X [25] and COSMO-SkyMed [32]), which provide data with a spatial resolution of up to one metre and even better for military purpose. Since such high resolution SAR data are available, the analysis of urban structures from multi-family down to one-family houses is possible. Furthermore, these new airborne and spaceborne sensors enable the acquisition of InSAR data, which additionally allows 3D building reconstruction besides the 2D approaches.

In previous studies concerning building reconstruction, the analysis was limited to certain areas due to lower spatial resolution. These included rural, industrial, or urban areas characterised by large buildings and in very rare cases also multi-family houses. Furthermore, these approaches were mainly driven by a detailed analysis of the SAR magnitude signature, while occlusion effects were compensated by fusing multi-aspect magnitude data. This step of information fusion was implemented by comparing and updating building hypotheses only, where a successful assembly of hypotheses in one single aspect is possible. Such approaches are limited by the stability of the chosen building features that are highly depending on the building extension. Hence, existing features have to be evaluated and probably new features have to be defined to handle the challenge of analysing single-family houses. Beyond the magnitude data, InSAR systems deliver also interferometric phase data, which can be seen as surface heights when taken in across-track configuration. In recent work, the exploitation of these interferometric heights was restricted to height calculation averaged over the assembled building footprint. With regard to the new sensor generation, the potential of

such data in the context of building reconstruction has to be analysed and exploited in much more detail, especially with respect to the high spatial resolution.

## 1.2     State of the Art

In the following sections, an overview on building recognition and reconstruction is given, thereby mainly focusing on SAR and InSAR data. The overview contains the progress on analysing building signatures in magnitude and phase image layers driven by the improvement of the spatial data resolution. Furthermore, early as well as matured state-of-the-art approaches of building reconstruction are introduced, subdividing them according to the underlying data and technique (SAR, InSAR, single-, and multi-aspect data).

### 1.2.1     Analysis of Building Signature

The analysis of man-made objects in SAR data started in the 1980s and was pushed by military organisations. The automatic delineation of urban areas from other land coverage, for example, forest and water, was investigated first. Here, the focus was set on the interpretation of the intensity [63], urban textures [73], and the modelling of urban clutter statistics [29]. In parallel, first detailed Radar Cross Section (RCS, Subsection 2.2.1) simulations of scatter effects at building locations supported the interpretation of urban areas [36]. Subsequent advances from low to higher spatial resolution data enabled signature studies on single building level. In the following subsections, research focussing on the analysis of magnitude and interferometric phase signature of buildings is discussed.

#### Magnitude Signature of Buildings

The detailed analysis of buildings in SAR data started with the interpretation of the magnitude signature, which is dominated by effects stemming from the inherent oblique scene illumination. These lead to foreshortening, layover, and radar shadow and depend on building shape and illumination geometry characterising the appearance of elevated objects in SAR images ([108], Subsection 2.2.2). In [116], a study on these effects is presented with the goal of estimating the visibility in dense urban areas to optimise flight planning. First approaches on building detection also focused on such phenomena (Subsection 1.2.2). Another research line deals with the development of SAR simulation tools to deepen the understanding of SAR imaging and to enhance the interpretation abilities of human interpreters. The tools (e.g. [91] and [4]) complied with the main requirements such as nearly real time capability and the simulation of large areas, often at the expense of precise physical modelling. The technical progress and the concomitant improvement of the spatial resolution led to new observable effects at building locations (e.g. windows and façade structures [2]).

In addition to the mentioned well-understood effects, multi-bounce scattering of different orders became more and more visible. The resulting bright point and line patterns are caused by the smoothness and rectangular set-up of dense building structures among themselves and relatively to their surrounding (e.g. streets). For the first time, very detailed building structures like pillars and railings at roofs, and rows of metal folds at eaves were observed in airborne data of military experimental SAR systems with spatial resolutions of decimetre [117] up to centimetre range [21].

These fine structured signatures represent further challenges of SAR image interpretation, whereby the new generation of recent SAR simulation tools are expected to provide valuable assistance. For more realistic SAR simulations, the consideration of two different optical descriptions to model the characteristics of the electromagnetic waves is necessary. On one side, the SAR imaging modelling based on waves is called physical optics (PO), which includes diffraction and interference effects. On the other side, modelling based on rays, referred to as geometrical optics (GO), considers passing or reflecting properties at objects. A detailed analytical description of scattering effects at buildings is given in [47] by regarding different combinations of GO and PO effects. In [58], [24], and [144] single buildings are simulated to support SAR image interpretation and to bring forward building detection and reconstruction. The latter lead to questions referring to the stability of signature parts under different conditions. The focus is set in particular on the double-bounce scattering from wall-ground structures as a function of the aspect angle [36], building orientations and sizes [59], wall-ground material [48], [45], sensor wavelength and wave polarisation [66], [96]. From this development, also the interpretation of the new high resolution spaceborne SAR data could benefit. First work on this is presented in [110] and [2] by focusing on the simulation and interpretation of different multi-bounce scatterers at building façades in TerraSAR-X data. Due to the large coverage and the high spatial resolution of the new sensors, the requirements on SAR simulation tools are growing fast. In particular, the simulation of large scenes [60] of high level of detail [1] in nearly real time is in demand.

**Interferometric SAR Signature of Buildings**

Similar to the SAR magnitude signature, the image geometry dominates also InSAR phase data in particular by layover and shadow. However, coherence – "temporal stability" – of the two SAR acquisitions is even more important for analysing interferometric phases. Hence, utilising InSAR phases focused first on removing noise and artefacts during the task of tree and building extraction [26], and height map generation. The mapping of known building structures into InSAR heights and coherence data as well as studies to identify and remove the layover mixture areas were presented first in [9]. In this context, the significant appearance of the layover in interferometric phase data at buildings was referred to as "front porch". Then, similar to the history of magnitude analysis, investigations on the statistics of InSAR images and the simulation of interferometric phases came up by concentrating especially on layover areas [142]. These studies focused mainly on the reproduction and analysis of coherence phenomena, for example coherence loss at steep gradient relief [97]. A comparison with real InSAR data became possible with the new high resolution airborne SAR sensors. These InSAR data enabled a detailed analysis of individual buildings [126] and building substructures [21] and led to further developments in the area of InSAR simulation. In particular, the understanding of the contribution of different scattering objects was a prerequisite for the exploitation of the layover signal. Also, the influence of varying sensor parameters, building sizes, roof types [125], and contribution power [42] on the InSAR phase signature was analysed based on simulations.

With the new generation of spaceborne SAR sensors (e.g. TerraSAR-X, COSMO-SkyMed), the recording of very high resolution repeat-pass InSAR image stacks of large coverage has been realised, which lead to a boost in the field of Persistent Scatterer Interferometry (PSI). The PSI technique

enables a very precise extraction of height coordinates and height changes over a long time interval for selected points, which are characterised by a long-term stable phase, so-called Persistent Scatterers (PS). The arising new possibilities of urban area interpretation and additional long-term monitoring are presented for example in [55] and [41]. Furthermore, another technique called SAR tomography was applied for urban analysis from space. First experiments based on airborne data focussed on a general classification of vegetation, forest, and man-made objects [102]. Studies on spaceborne data started with low spatial resolution shown in [46], but the very high benefit of InSAR tomography for urban analysis became obvious with the new very high resolution data [150]. In the future, urban signature interpretation will profit from a combined PSI and tomography analysis. Furthermore, the interpretation and the reconstruction of urban areas and single buildings in particular will speed up due to the availability of the first single-pass spaceborne InSAR configuration of TerraSAR-X and TanDEM-X.

### 1.2.2    Detection and Reconstruction of Buildings

The great variety of methods for urban object recognition based on different remote sensing data sources have lately been presented in [146]. In the following paragraphs, particular focus is put on developments in the area of building reconstruction from SAR and InSAR data. First studies aimed at the classification of urban areas by exploiting SAR magnitude and InSAR coherence signatures [16]. Then, the individual signal distributions of urban structures in SAR magnitude data were investigated to achieve an improved classification [130]. The fusion of SAR magnitude based classifications with InSAR height data delivered urban height maps [132], an important contribution for building reconstruction. Recent approaches of urban structure analysis [136], [107] show the benefit of the availability of multi-aspect data to reduce occlusion effects behind elevated buildings in dense areas. A similar trend is also evident for the detection and reconstruction of individual buildings, which will be described in the following paragraphs.

#### Single-Aspect Data

In this paragraph, approaches considering a single SAR image or a single InSAR image pair are summarised. The group of magnitude-based approaches can be subdivided into those preferring iterative simulation and comparison between synthetic and real building signatures, and those extracting parameters or primitive objects directly from the SAR magnitude signature by analysing range lines, image patches, or the RCS of objects. The InSAR approaches focus on the segmentation of roof areas to extract mean building heights or on the analysis of layover areas to enable or to improve 3D building reconstruction, whereby the latter is mostly presented on simulated InSAR data.

#### *Single-Aspect SAR Magnitude Data*

First, we introduce algorithms making use of SAR intensity simulations. A semiautomatic method on building reconstruction was presented in [5]. By exploiting simple building models of different roof types, backscattering intensities are simulated by considering Lambertian scattering. A human operator conducts the subsequent comparison between real SAR magnitude data and simulation results as well as the choice of an appropriate building model semiautomatically. The realtime ca-

pability of the used simulation tool [4] is the most important benefit, especially for visualisation and training applications. The usage of SAR intensity simulations for building height estimation and temporal change detection was presented in [24]. By utilising 2D GIS information, the intensity signature of buildings considering single and double-bounce scattering is simulated. The estimation of the building height is realised by searching for the correlation maximum between simulated and real building signatures, with testing an iteratively increasing building height during the simulation step. The presented task on change detection requires 3D GIS information (e.g. from pre-event stereo optical data) to detect and evaluate differences between simulated pre-event and real measured post-event SAR signatures. The drawbacks of such approaches are the required isolatedness and plainness of buildings to achieve high correlation between simulated and real SAR signatures.

The second group of algorithms analyses the building signature by measuring in SAR intensity data or by applying computer vision techniques to extract object parameters. First investigations (e.g. [71]) focused on the evaluation of correlations between layover-shadow-length and object height in range direction. The subsequent extraction of object heights (e.g. vegetation and buildings) was combined with low pass filtering and averaging over roof areas. In later work, the extraction of characteristic building borders is addressed to estimate building heights and building footprints. The extraction of building height by investigating RCS of layover, shadow and double-bounce scattering is given in simulated data in [59] and in very high resolution airborne SAR data in [49]. The detection of building borders is realised by searching for bright lines or by analysing edges between bright and dark areas. In [135], the detection of parallel edges is aimed at extracting enclosing layover areas. The space in range direction between parallel edges allows estimating an initial building height. Considering several pairs of edges, the final building height is determined by a weighted mean of all heights. An approach of radar footprint detection is presented in [44] by extracting bright lines, bright areas, and dark areas. The classification and combination of these primitives by investigating membership functions and a subsequent post-processing delivers rectangular radar footprints. These correspond with building layover areas and give a hint to building positions. Another approach published in [100] is based on the Bayesian information extraction method by using a hierarchical model. The scene is a cluster of buildings, which is described by mutual interacting marked points. Furthermore, the buildings are hierarchically decomposable into facets, characterised by radiometric and geometric features, connected to a set of pixels in image space. Finally, maximum a posteriori probability estimation is carried out. In this way, parallelepipedal buildings with flat or gabled roof and round towers can be modelled. An approach of building reconstruction allowing footprints that are more complex is described in [30]. First primitives corresponding to single, double, triple or multiple echoes are extracted. For the generation of the building shape a production system is set up by using a rule set resulting from theoretical visibility studies. Distinctive range profiles crossing the detected primitives are the input for the system. Utilising production rules, type and position of primitives and additional information of textured and shadowed areas are used to assemble iteratively different building cuboids and combinations of different hypotheses to receive the final building shape. In comparison to the first group based on SAR simulations, these approaches are more flexible since single features (e.g. layover and double-bounce) or combinations of features are used for building detection and reconstruction. In this way, missing signature parts due to occlusion effects, for example, can probably be compensated. The introduction of further model knowledge can support the building detection in a similar manner, but al-

though these approaches provide fast availability the main drawback remains the mono-aspect leading to lower information content.

### *Single-Aspect Interferometric SAR Data*

Besides the analysis of the SAR magnitude signature of buildings, the acquisition of InSAR data provides the possibility to directly extract approximate surface heights. Most of the approaches described in the following combine magnitude and interferometric phase signature. Yet they differ in the level of detail with which the interferometric phases at building locations are analysed. In most cases, single-pass airborne InSAR data are investigated due to their high coherency and availability.

Initial works [52] focused on the extraction of building footprint, height and position by use of a machine vision approach of best-fitting planes to range images. The prerequisite step of data segmentation is carried out by a region growing approach based on the InSAR height data. The segmented areas correspond with planes from roof, wall or ground. The approach is demonstrated on data of a relatively dense urban area and compared with results on LIDAR data [53]. Several drawbacks are mentioned, for example, layover, shadow, and occlusion effects as well as an underestimation of the building footprint. The approaches presented in [131] and [121] combine intensity and interferometric height data during region growing processes. The first considers range line based segmentation of building shadows in order to support building height and especially shape extraction from InSAR data. An energy function containing height and amplitude constraints is computed, whereby its minimisation delivers potential building height and extension in each range line. A subsequent regularisation step removes possible streaking in azimuth direction to achieve more linear building edges. In [121] interferometric coherence is used for the initial segmentation of intensity values and for the weighted height calculation. The resulting depth map is post-processed by considering segment relations to reduce under- or over-segmentation. Both approaches are suitable to reconstruct large (e.g. industrial halls) and complex buildings of arbitrary shape since no specific building model is assumed. Concerning small buildings, the region growing will fail due to the lack of homogeneous segments in magnitude and interferometric height data.

The second group of approaches focused on a detailed analysis of layover areas to improve the generation of digital elevation models [26] or to support the phase unwrapping at building locations [98]. The first one extracts and removes layover areas - also called front-porch anomalies – by analysing intensity values, elevation values, and binning numbers. The binning number corresponds to the quantity of contributions projected to the same image cell by the transformation from ground to slant geometry. The layover areas are distinguished by high intensities and binning numbers. The second algorithm detects interferogram areas related to layover by exploiting the given spectral shift between the InSAR image pair. Decomposition into sub-interferograms and their summing up to achieve two slope interferograms are demonstrated on simulated data of 2SIR [97]. Finally, the successful unwrapping of simulated layover phases based on the slope interferograms is shown to support reconstruction of 3D building shape. Recent work focuses on the analysis of building phase signatures to enable the detection of building edges. In [43] a stochastic approach by investigating local Gaussian Markov Random Fields (GMRF) is chosen. Results on simulated and real InSAR data and an improvement by combining multi-channel InSAR simulations (e.g. different baselines and frequencies) are shown.

The results derived from single InSAR datasets are less complex than the ones based on magnitude data, which is probably due to the lack of freely available high resolution single-pass InSAR data. With the new InSAR configuration of TerraSAR-X and TanDEM-X, new findings are expected.

## Multi-Aspect Data

Investigations on multi-aspect data are a result of the high interest of detecting and reconstructing dense urban areas with a high level of completeness. Occlusion and overlapping effects between elevated objects (e.g. building and trees) prevent obtaining such high detection rates based on single-aspect data. Focusing on the analysis of SAR data, much research is directed towards fusing multi-sensor or multi-aspect data. Due to the fact that an imaged object shows different radiometric and geometric properties in multi-aspect and in multi-sensor data, the fusion of object information is mostly realised on a higher semantic level than on pixel level. Recent work on combining optical and SAR/InSAR building features by investigating Markov Random Field classifiers (MRF) [138] and Conditional Random Field classifiers (CRF) [140] are mainly motivated by time-critical applications (e.g. earthquakes and flooding). Considering the rising number of airborne and spaceborne SAR sensors in the last years and the well-known advantages of SAR data (e.g. weather independency), the exploitation of multi-aspect SAR/InSAR data on its own is also promising. In the next paragraph, recently presented algorithms on this topic are described and their main differences about data configuration, model assumption, and level of building reconstruction are discussed.

### Multi-Aspect SAR Magnitude Data

Similar to the single-aspect approaches, research work on building reconstruction based on multi-aspect data focused first on the analysis of layover and shadow areas. In [7], [69], and [64] building reconstruction by multiple active contours evolving simultaneously on all available SAR images of the scene is proposed. Parameterised wire-frame building models of flat and gabled roofs are used to simulate the appearance of building in all images of the scene. During the rattling rectangular delineation, which is in principle an optimisation step, building parameters are continuously adjusted until a best-fit segmentation of the building layover and shadow in all images is achieved. The consideration of multi-aspect data might reduce occlusion effects and resolve ambiguities in the building modelling. However, the limitation to rural and suburban areas and to a very simplified simulation of building appearance remains a severe constraint.

The second group of algorithms deals with interpretation and feature extraction by means of different dual-aspect configurations, for example small changes in look angle [114], orthogonal views [118], and opposite views [147]. The extraction of low-level primitives (e.g. bright scattering from façade and double-bounce scattering from building wall and ground) is realised by using computer vision methods or SAR specific Constant False Alarm Rate detectors (CFAR, Section 4.6). The complexity of post-processing these primitives (e.g. hotspots and lines) reaches from assembling of L- and T-structures [114] up to investigating so-called Gestalt Algebra. With the latter, a production system can be set up to receive high-level objects (e.g. symmetry clusters) [92]. Similar differences are given in the implementation of the additional stereo processing. A matching approach of bright crosses representing L- and T-primitives of different aspects by using discrete dynamic processing is discussed in [114]. The 3D building shape is reconstructed from the disparity between

matched crosses and by assuming rectangular building shape. The complex production system ("stereo gestalt system") of [118] contains clustering, recursive grouping and a level of stereo production to obtain 3D rows, angles, and clusters from 2D high-level objects. The resulting 3D objects and their averaged height characterise the final building geometry. The two approaches take advantage of the high density of building structures in very high resolution airborne SAR images and show their main advantage in their less restricted model assumptions. The prime example for this strategy, also called radargrammetry, is the extracted elevation image presented in [95]. Here, conventional image matching is accomplished on very high resolution SAR images recorded by a circular flight. Then height maps are calculated by maximising the correlation of small patches that are extracted from neighboured images. Each of these height maps covers an arc interval of 15 degrees, and their fusion over a flight track of 300 degrees leads to a LIDAR like elevation map with only a few gaps. Nevertheless, the main prerequisite for this kind of radargrammetry is the detection and matching of corresponding objects, which becomes more and more difficult with decreasing number of images and increasing difference of look angles. As an example, in [147] detected L-structures in ascending and descending spaceborne SAR images are only combined to receive possible building footprints.

In [34] and [145] polarimetric airborne SAR data acquired from four orthogonal and antiparallel viewing directions are used to reconstruct 3D buildings. For both approaches, buildings are modelled as cuboids or groups of cuboids. Image coregistration by manual control point measurements and manual detection of building signatures in image pairs from opposite viewing direction are required in [34]. The building signature is analysed in a coherency matrix, which allows good detection of the building location. The calculation of the building height is realised by disparity estimation between cumulated azimuth profiles in the opposite images. In [145] an automatic approach is presented, starting with the extraction of edges followed by a local Hough transformation to receive parallel line segments fitted to parallelograms. A classification takes place in order to discriminate parallelograms caused by direct reflection of façades from others that are due to double-bounce signal propagation and shadow. A maximum likelihood method is adopted to match all multi-aspect façade images and to three-dimensionally reconstruct buildings. Prerequisites of both approaches are homogeneous layover regions or similar layover signatures from different aspects to enable satisfying primitive extraction and successful disparity estimation between azimuth profiles. Furthermore, detached buildings are required, because interfering façade images from multiple high buildings will lead to imprecise reconstruction results.

In general, utilising multi-aspect data in comparison to single-aspect data may help to reduce occlusion effects, to detect more building details, and to resolve ambiguities in building modelling in order to come up with more robust reconstruction results. The level of improvement depends on the number of images available and on the complexity of the urban scene to be reconstructed. An additional benefit on building reconstruction can be achieved by considering multi-aspect InSAR data due to direct measurement of runtime differences convertible into elevation data.

### *Multi-Aspect Interferometric SAR Data*

Two research groups presented recent work on building reconstruction using multi-aspect InSAR data. In the following, both approaches are discussed and open questions are pointed out.

In [14], work on building detection and reconstruction based on InSAR height and coherence images was shown. A maximum decision strategy is deployed to combine four different views of a village consisting of small buildings. First, the maximum height value of all four acquisitions is chosen and the resulting height map is smoothed by a median filter. Thereafter, a binary mask with potential building regions is generated by subtracting bare earth from the original height map. Minimum bounding rectangles are fit to regions of interest after some morphological filter operations have been applied. Differentiation between buildings and other elevated objects like vegetation is done by exploiting mean and standard deviation of the coherence of the region and of the height map. Furthermore, simple building models with either flat roof or symmetric gabled roof are fit to the segmented building regions. This approach is further extended in [13] including information from corresponding SAR magnitude data. Optimal results are achieved if measurements from building shadow analysis are combined with hints from the InSAR height map to reduce the influence of layover, also called front porch areas. With the shadows, building positions and outlines can be estimated while height information is deduced from InSAR heights. Moreover, a simulation step is proposed to refine reconstruction results. A SAR image is simulated using the previously reconstructed 3D hypothesis as input. Subsequently, by comparing real and simulated signatures, the 3D hypothesis is adjusted and refined to minimise differences. Problems arise if buildings stand closely together, if they are higher than the ambiguity height of the InSAR acquisition, and if they are too small to show homogeneous height information inside the building footprint since this approach very much relies on the InSAR height map.

The iterative approach on building reconstruction presented in [115] is carried out in two separate steps: building detection and building reconstruction. For building detection, the SAR data are preprocessed in order to reduce speckle. Additionally, primitive objects are extracted by applying a segmentation of the slant range data. Edge and line structures are detected in intensity data while connected components with a significant elevation above ground are segmented in height data. Building hypotheses are set up by creating complex objects from primitive objects. Thereafter, such hypotheses are projected from slant range geometry to ground range geometry in order to prepare for building structure extraction. Model knowledge is introduced in this step, as buildings are reconstructed as elevated objects with three different kinds of parametric roof models (flat, gabled, and pent roofs) as well as right-angled footprints. More complex building structures are addressed introducing right-angled polygons as footprints and allowing different heights of adjacent building parts (prismatic model). Building heights and roof types are estimated by analysing shadow areas and by fitting planes to the height data. In order to fill occluded areas and to compensate for layover effects, building candidates from multiple aspects of the same scene are fused. They are used as input for a simulation to detect layover and shadow regions. In the next step, the simulated SAR data are re-projected to slant range geometry and compared to the original SAR data. If differences are detected, false detections are eliminated and new building hypotheses are created. The entire procedure is repeated iteratively and is expected to converge towards a description of the real 3D scene. Criteria for stopping the process are either a maximum number of iterations or a threshold of the root mean square error between simulated and real world DEM.

The main requirement of this approach is setting up a building hypothesis in at least one of the different views. This will fail often for small buildings since their magnitude signature contains only

layover, double-bounce, and shadow area (Section 3.3). Furthermore, building signature analysis of dense urban area in new airborne and spaceborne InSAR data (e.g. [117], [22], and [40]) showed that investigations on building shadow could become difficult. Hence, also new strategies of extracting roof shape have to be found. At this point, a more detailed interpretation of the InSAR phases appears to be reasonable, especially by focusing on the aforementioned front porch area.

Summarising these points, the characteristics of new InSAR sensors enables the recognition of smaller objects, especially smaller buildings, which requires further developments and enhancements of existing work to achieve good detection and reconstruction results.

## 1.3     Contribution of this Thesis

In this thesis, an automatic scheme based on multi-aspect InSAR data especially for 3D reconstruction of small buildings is presented. This is possible since the new generation of SAR sensors delivers data, where in addition to large extended buildings also small buildings up to one family houses become visible.

As new sensors are able to take images of very large scenes, a classification of vegetated areas is introduced to support the task of building detection and lower the number of false detections. To this end, fuzzy logic is used to formulate a new robust classification concept, which contains expert knowledge about InSAR relevant image content. Simple rule sets are defined to enable their applicability on different InSAR data. Additionally, classification results of multi-aspect data are fused to reduce misclassification due to occlusion effects [123].

Based on a detailed analysis of the magnitude and interferometric phase data, radiometrically stable and geometrically correct building features, appropriate for large and small buildings, are extracted. Moreover, these features are independent from SAR sensor type, illumination geometry, and building geometry to a large extent [124].

In contrast to previous algorithms (e.g. [115]), the fusion of multi-aspect information is realised on a lower level to handle building constellations of weak feature support. This contains a transformation from individual slant range geometries into common ground range geometry (e.g. WGS84) at feature level. The subsequent assembly of building hypotheses benefits from the multi-aspect information [124].

Furthermore, the interpretation of the interferometric phase information is enhanced to utilise the high geometric information density in the layover/front porch region [125]. For this, an InSAR simulation tool is developed to explore superposition effects and to support especially the reconstruction of small buildings [126].

As the interferometric phases suffer from considerable noise, phase filtering is mandatory to assist the exploitation of the InSAR phases, for example, to extract building heights. Conventional rectangular filter masks can destroy significant layover areas if building orientations and sensor flight direction are not aligned. Hence, a new InSAR phase filter is introduced that preserves especially the front porch region [128]. The parameterisation of the new filter masks relies on the assembled building hypotheses and the simulated InSAR phases.

In addition, new post-processing strategies are developed that benefit from the new InSAR phase simulation as well as from the new InSAR phase filtering. Especially the selection of the appropriate roof geometry benefits from those [127].

Beyond the improvements on building interpretation and reconstruction, the adaptation on high resolution airborne InSAR data shows the potentials of this topic for the future.

## 1.4    Structure of this Thesis

The structure of the thesis is driven by the goal to understand the appearance of buildings in In-SAR data and to transfer these findings into a 3D reconstruction algorithm. Hence, in **Chapter 2** the principles of SAR data acquisition are described by considering relevant characteristics of the SAR principle, the radiometric and geometric properties, and the available SAR sensors. In **Chapter 3**, the appearance of buildings in InSAR data is analysed by focusing on magnitude and interferometric phase signature. At this point, changes in the building signature due to different sensors, processing modes, illumination properties or building geometries are studied and visualised in detail.

**Chapter 4** develops the reconstruction scheme, starting with a description of the underlying building model and an overview of the whole workflow. Subsequently, the individual processing steps are introduced and their implementation and parameterisation is described. Additionally, intermediate results are shown to emphasise the necessity of subsequent processing steps.

In **Chapter 5** the investigated test area and InSAR data set are characterised, reconstruction results are shown, and the potential of the algorithm is discussed. The evaluation of the reconstruction results is assisted by considering cadastral data as 2D reference and LIDAR data as height reference. The summary of this thesis and an outlook are given in **Chapter 6**.

# 2    Basics of Imaging Radar

In the following sections, the basics of imaging radar are discussed. First, the principles of the two imaging methods Real Aperture Radar (RAR) and SAR are summarised followed by an introduction to SAR image formation and the most frequently applied SAR imaging modes. Second, imaging properties of SAR sensors are described by considering radiometric and geometric aspects. Also spaceborne and airborne SAR sensors currently in use are characterised.

## 2.1    Principle

Imaging from air to ground by radar (Radiofrequency Detection and Ranging) became operational first in the military domain during World War II. Due to the engineering progress at this time, smaller antennas could be developed and installed on aircraft allowing the detection of enemy objects during night and bad weather conditions. The usage of imaging radar for geoscience applications started after the war. Driven by the desire to enhance the angular resolution of diffraction-limited RAR, the new imaging technique SAR was developed in the 1950s. In the following subsections, the RAR and SAR principles are described, the SAR image formation is explained, and the most common SAR imaging modes are presented.

### 2.1.1    Real Aperture Radar

In comparison to passive optical imaging systems, radar sensors emit radar pulses to illuminate actively the scene from the side. In nadir view, the angular resolution would be very low due to signal diffraction (see equation (2-3) below). Moreover, on either side of the nadir axis same distances are given, consequently the echoes of these points cannot be separated. The resulting acquisition geometry of a RAR and SAR system is shown in Fig. 2.1. Focusing first on the general image geometry, the coordinate system of a radar image is defined by the slant range direction (across track) and the azimuth direction (along track). The slant range coordinate in the image is specified by the smallest distance between sensor and covered object. Sensor movement and imaging starting time define the azimuth coordinate.

Using this side-looking geometry, runtime measurements enable the determination of resolution in range depending on the pulse length. In Fig. 2.1a the footprint of the radar beam on ground is shown with marked near range and far range position (indices $n$ and $f$). The spatial resolution in slant range $\delta_{rs}$ is a function of $c$, the speed of light, and $\tau$, the radar pulse duration, or $BW$, the bandwidth of the signal [72]:

$$\delta_{rs} = \frac{c \cdot \tau}{2} = \frac{c}{2 \cdot BW}, \quad \text{with} \quad \tau \cdot BW \approx 1 \tag{2-1}$$

Considering also ground range projection, a geometric relation between object position represented by the off-nadir look angle $\theta$ and ground range resolution $\delta_{rg}$ is given by:

**a**



**b**
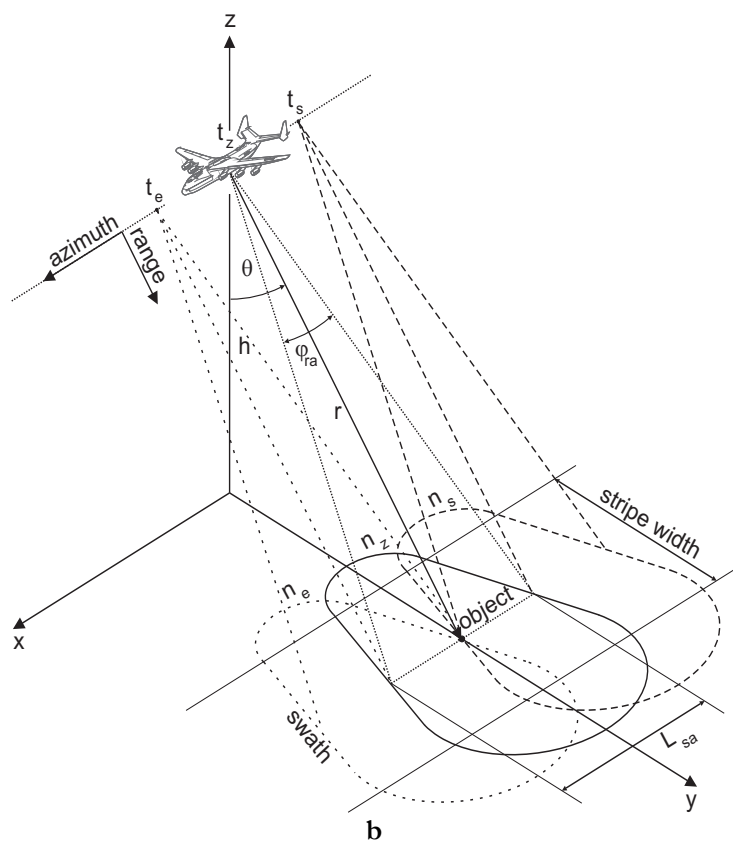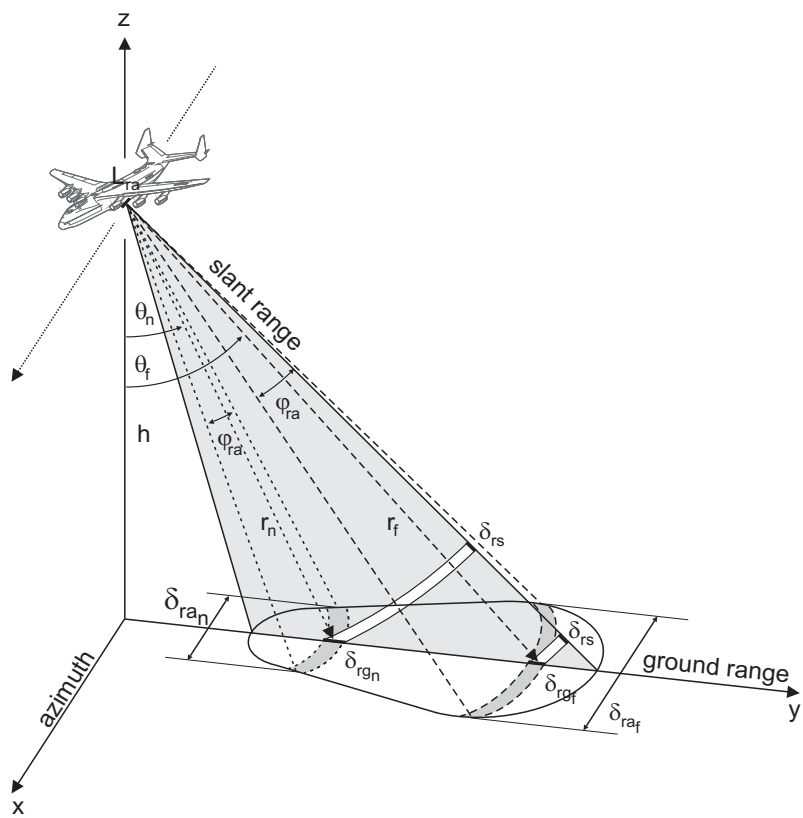
**Figure 2.1:** Scheme of RAR principle (a) and SAR principle (b)

$$\delta_{rg} = \frac{c \cdot \tau}{2 \cdot \sin\theta} = \frac{c}{2 \cdot BW \cdot \sin\theta} \tag{2-2}$$

Hence, with increasing off-nadir look angle (e.g. from $\theta_n$ to $\theta_f$) a better ground range resolution (see $\delta_{rg_n}$ and $\delta_{rg_f}$) is achievable. Thus, a general improvement of range resolution is theoretically possible by using large off-nadir look angles or by shortening $\tau$, but both require a higher transmission power, which is limited due to technical and safety reasons. In practice, the bandwidth is considered instead of $\tau$ because by frequency modulation – chirping and frequency shifting of the emitted pulses ($\tau \cdot BW = \text{const.}$) – an improvement in resolution while reducing the mandatory power can be reached. The extended radar pulse length enables the transmission of more signal energy leading to higher signal response and better signal-to-noise ratio (SNR).

The spatial resolution in azimuth $\delta_{ra}$ is deduced by diffraction theory as a linear function of $r$:

$$\delta_{ra} = r \cdot \varphi_{ra} , \quad \text{with} \quad \varphi_{ra} = \frac{\lambda}{L_{ra}} , \tag{2-3}$$

where $r$ denotes the slant range distance and $\varphi_{ra}$ the angular aperture of the 3 dB antenna beam in azimuth direction given by the used wavelength $\lambda$ and the length of the real aperture $L_{ra}$. Since diffraction effects lead to a widening of the radar beam, it is common use within remote sensing applications to take advantage of a long real aperture $L_{ra}$ in order to obtain a narrow beam and a better spatial resolution in azimuth direction for large $r$. Moreover, the dependence on object position gives rise to a worsening of $\delta_{ra}$ with increasing $r$, which is also visible in Fig. 2.1a for $\delta_{ra_n}$ and $\delta_{ra_f}$. An improvement of $\delta_{ra}$ is restricted because the necessary enlargement of $L_{ra}$ is technically constrained by a practical antenna size and an applicable transmission power. Additionally, a decrease of $\lambda$ is less helpful because of the increasing atmospheric attenuation of the radar signal. These limitations of RAR led to the development of SAR.

## 2.1.2    Synthetic Aperture Radar

The principle of SAR is shown in Fig. 2.1b with image axes azimuth and range similar to RAR imaging. The desired improvement of $\delta_{ra}$ is realised by multiple illuminations of the object thanks to a high pulse repeat rate and motion of the SAR sensor. Three beams cover the object starting with beam $n_s$ at time $t_s$, crossing zero-Doppler plane with beam $n_z$ at time $t_z$, and ending with beam $n_e$ at time $t_e$. The decrease in the range between sensor and object from $n_s$ to $n_z$ and then the increase from $n_z$ to $n_e$ results in a relative movement between both. The radial component of this movement leads to a Doppler shift in the received signals. The changing of this shift over integration time ($t_s$ to $t_e$) is called Doppler history and characterised by the range position of the object. To realise the SAR principle the radar sensor has to operate fully coherent, which means the phase relation between different transmit and receive pulses has to be stable. The subsequent SAR processing [72] starts with the range compression. Afterwards, an azimuth compression also called azimuth focussing – a convolution between the received echoes and the range dependent correlation functions (Doppler histories) – is carried out to achieve the real azimuth position. In practice, more time-efficient processing algorithms rather than 2D-convolution are used for azimuth focussing, for example, chirp scaling algorithms, Omega-K algorithm, and SPECAN algorithm, which are de-

scribed and compared in [33]. If very high precision is required (e.g. very high spatial resolution data), then more time consuming algorithms have to be considered [21], and additional processing steps like estimation of Doppler centroid and Doppler rate are necessary [72]. However, the result of any of them is a complex SAR image $S$ characterised by two dimensions: either in Cartesian (real part $s_i$ and imaginary part $s_q$) or in polar coordinates (amplitude $A$ and phase $\varphi$). The mathematical definitions of $S$, $A$, and the intensity $I$ are:

$$S = s_i + j s_q = A(\cos\varphi + j\sin\varphi) = A \cdot e^{j\varphi} , \quad A = \sqrt{s_i^2 + s_q^2} , \quad \text{and} \quad I = s_i^2 + s_q^2 . \tag{2-4}$$

Additionally, this concept, using the motion of the real antenna to achieve a long synthetic antenna according to the recorded range history of the tracked object, assumes a stationary world during the object observation. Hence, the velocity components of a moving object (e.g. car, train, and ship) affect the geometric SAR signature in comparison to a static object. Movements in flight direction lead to a blurring of the object signature in azimuth direction. In contrast, a radial component of the velocity vector results in a displacement in azimuth, for example, observable for moving cars with a displacement to the left or right of the road.

The following equations establish the requested enhancement of the spatial resolution in azimuth direction as consequence of azimuth focussing. Based on the multiple illumination of the object, a longer antenna is synthesised, and its length is equal to the distance moved on ground between $t_s$ and $t_e$. This distance is called the synthetic aperture $L_{sa}$, which is a function of range distance $r$ and angular aperture $\varphi_{ra}$:

$$L_{sa} = r \cdot \varphi_{ra} = r \cdot \frac{\lambda}{L_{ra}} . \tag{2-5}$$

The SAR specific angular aperture $\varphi_{sa}$ is given in (2-6) as a function of the real aperture $L_{ra}$ and the slant range distance $r$. The factor $\frac{1}{2}$ results from the SAR specific multiple illuminations from different positions, leading to phase gradients on the way to and back from the object [72] different to the RAR measurement. Furthermore, the spatial resolution in azimuth direction of SAR $\delta_{sa}$ is half of the antenna length $L_{ra}$, thus independent from the object position compared with $\delta_{ra}$. Note that (2-6) does hold for stripmap mode only (Subsection 2.1.4).

$$\varphi_{sa} = \frac{\lambda}{2 \cdot L_{sa}} = \frac{L_{ra}}{2 \cdot r} \quad \text{and} \quad \delta_{sa} = r \cdot \varphi_{sa} = \frac{L_{ra}}{2} \tag{2-6}$$

### 2.1.3    SAR Image Formation

In practice, however, the final geometric resolution in azimuth and range direction is more interesting than the angular aperture $\varphi_{sa}$ and the spatial resolution in azimuth direction $\delta_{sa}$. Therefore, in the following the SAR image formation is described containing range and azimuth compression. These are usually carried out in frequency domain. The equivalent convolution steps in spatial domain are realised by a correlation with a 2D matched filter. This is characterised in range by the envelope of the transmitted radar pulse (chirp) and in azimuth by the antenna pattern. The resulting complex signature of a normalised point target is the impulse response function (IRF) of the

SAR system serving as quality measure of SAR images. The ratio between main and side lobes is important in particular since high side lobes of a strong target can obscure other targets nearby. This is important for applications focusing on objects (e.g. buildings and cars) with a large RCS.

Hence, weighting functions $w(n)$ are applied to achieve an apodization of the side lobes, whereas the reduction of the first side lobe level, the smoothing of the remaining side lobe levels (octaves), and the 3 dB width $k$ of the main lobe are the most characterising features. A detailed description of common weighting functions is given in [62]. Here the rectangle function (uniform weighting), and a "raised cosine" function are presented.

$$\text{Rectangle window:} \quad w(n) = 1 \qquad\qquad\qquad\qquad k_{\text{rect}} = 0.89$$

$$\text{Hamming window:} \quad w(n) = \nu + (1-\nu) \cdot \cos\left(\frac{2\pi}{N} \cdot n\right) \tag{2-7}$$

$$w(n) = 0.54 + 0.46 \cdot \cos\left(\frac{2\pi}{N} \cdot n\right), \quad \nu = 25/46 \qquad k_{\text{Hamm}} = 1.30$$

The resulting IRF of a single point target applying uniform weighting is the sinc function characterised by a reduction of the first side lobe of 13 dB, an ongoing side lobe fall-off of 6 dB per octave, and a 3 dB main lobe width of 0.89. In comparison, using a real weighting function such as a Hamming window, the first side lobe undergoes a suppression of 43 dB and decreasing envelope of 6 dB per octave is achievable. On the other hand, the 3 dB main lobe width is increasing up to 1.30 and the general width (null-to-null) of the main lobe is twice as wide as that of uniform weighting. The final geometric resolution in azimuth $\delta_a$ and range $\delta_r$ direction as given by the 3 dB main lobe width of the IRF is defined by the parameter $k$ depending on the applied functions $w(n)$.

$$\delta_a = k_a \cdot \frac{L_{\text{ra}}}{2} \quad \text{and} \quad \delta_r = k_r \cdot \frac{c}{2 \cdot B} \tag{2-8}$$

Despite the loss of resolution, for image interpretation the resulting differences on object signatures are much more important, especially if a high density of detailed structures characterise the appearance of an object (e.g. buildings, bridges, and vehicles). The expected variation of signatures is given in [94] for a synthetic image considering ideal point scatterer, dihedral and trihedral corner for instance. An asymmetric weighting is applied by focusing on uniform, Hamming, and autoregression functions. The comparison points out that Hamming weighting leads to wider azimuth and range response, but on the other hand best side lobe apodization can be achieved. The oscillating side lobes are only observable for the rectangle window and the trihedral corner reflectors give the strongest target response. Real image examples of an airborne sensor are presented in [119] by the use of a symmetric weighting with uniform, spatially variant apodization (SVA) and Taylor function. The comparison of the weighting results focus on the analysis of a single point scatterer and a clutter area. The SVA shows a high side lobe apodization without increasing the width of the main lobe. Furthermore, a good preservation of clutter details and texture information is given, and in addition, clutter speckle patterns are better maintained compared to applying Taylor weighting.

In general, the challenge is to develop interpretation algorithms working for all data constellations or for at least the majority. The realisation of this requirement is difficult due to the high signature

variability, which will be shown for buildings in Section 3.2. Two well-established ways to open approaches for general use are the choice of parameters of image processing and interpretation algorithms according to characteristics of the scene at hand (Section 4.4) or from SAR sensor and processing parameters (Section 4.6).

### 2.1.4 SAR Imaging Modes

In this subsection, the most common imaging modes of SAR data are described. The investigated airborne data sets (e.g. AeS-1 [111] and MEMPHIS [106]) have mostly been recorded in Stripmap mode and the spaceborne data (e.g. TerraSAR-X) in Spotlight mode. Then two specific configuration types are discussed: the polarimetric and the interferometric SAR, which are independent from the chosen imaging mode.

### Stripmap Mode

The Stripmap mode, the most common SAR imaging mode, is used by both airborne and spaceborne SAR sensors. The antenna beam illuminates the target on ground with a fixed look angle, as described previously for the standard SAR principle. The Stripmap images show a constant slant range resolution and may cover seamless stripes of arbitrary length. Stripmap spaceborne data are applicable for monitoring tasks such as detection of land use changes (e.g. sealing areas). High resolution airborne data are even usable for object detection as discussed in detail in this thesis (e.g. building reconstruction).

### ScanSAR Mode

The burst mode ScanSAR, as used by spaceborne SAR sensors, enables the largest spatial coverage, however with reduced geometric azimuth resolution. During the acquisition, the look angle of the antenna beam is periodically changing to cover different subswaths in range direction. Hence, an increase of the stripe width is realised at the expense of azimuth resolution, as each scatterer is imaged not as often as in Stripmap mode. Due to this low geometric resolution, these SAR data are mainly used for large scale monitoring applications such as the detection of environmental pollution (e.g. oil slicks).

### Squint Mode

A SAR system operating in Squint mode illuminates the target by looking tilted forward or aft, however not in the zero-Doppler plane marked grey in Fig. 2.1. In the past, especially airborne systems applied squint angles up to 60 degrees for tactical safety reasons. Nowadays, real Squint mode data are rare, the majority of SAR data show squint angles only up to some degree due to flight conditions of airborne platforms or because of earth rotation with respect to spaceborne systems. During SAR data processing and geocoding, this squint angle has to be taken into account. Additionally, the tilting of the SAR sensor can be accomplished mechanically by a real tilting of the whole antenna or electrically by phase differences between different parts of the phased array antenna. In practice, the electrical solution is preferred due to technical restrictions of the mechanical solution (e.g. trigger time and signs of wear).

## Spotlight Mode

The Spotlight mode provides the highest geometric resolution to the disadvantage of limited spatial coverage. During the acquisition, the orientation of the antenna beam is adapted such that a site of interest is illuminated exclusively. This steered tracking leads to a longer synthetic aperture and consequently results in a better azimuth resolution. These spaceborne or airborne data show a very high level of detail allowing the detection of individual objects and even their identification and reconstruction (e.g. vehicle identification and building reconstruction).

## Polarimetric SAR

In contrast to standard single-polarimetric SAR data, the acquisition of dual- or full-polarimetric data makes use of transmitting and receiving different polarised waves. In general linear (horizontal or vertical) and circular (right or left) polarised waves are distinguished, whereby for remote sensing applications the linear polarised waves (horizontal $H$ or vertical $V$) are preferred. Using these two polarisations, four different backscatter components can be formed by considering the potential reversal of wave orientation at scattering object. The co-polarised channels $HH$ and $VV$ on the principal diagonal and the cross-polarised channels $HV$ and $VH$ on the secondary diagonal define the resulting scattering matrix $[S]$. For monostatic acquisitions, this scattering matrix is symmetrical and has only three independent components since $S_{HV} = S_{VH}$. Usually the first index refers to the polarisation of the received wave and the second one to the emitted wave [12].

$$[S] = \begin{bmatrix} S_{HH} & S_{HV} \\ S_{VH} & S_{VV} \end{bmatrix} \qquad\qquad (2\text{-}9)$$

The information benefit concerning polarimetric data is based on the effect that the individual elements of the scattering matrix $[S]$ are affected differently by the scattering properties of illuminated objects [82]. Based on different comparisons between these four components, distinctions between even- and odd-numbered reflections as well as the degree of depolarisation are possible. A combined analysis of this phase characteristic along with the received amplitudes improves the results of object segmentation and classification like the analysis of soil moisture and land use [31]. Other applications based on high resolution data are the classification of different tree species [80] or the interpretation of line signatures (e.g. bridges and buildings) by characterising direct and double-bounce reflections [81].

## Interferometric SAR

The interferometric SAR processing comprises either repeated or simultaneous recording of at least two SAR images of a scene. The difference in the phase measurements between the acquisitions is the signal of interest. The interferogram $S$ of two images is calculated by a complex valued multiplication of the two received signals $S_1$ and $S_2$ given in (2-10), where $A_1$ and $A_2$ are the signal amplitudes and $\Delta\varphi$ is the phase difference proportional to the range difference $\Delta r$ and signal runtime difference $\Delta t$. The parameter $p$ (either 1 or 2) depends on the transmit/receive mode of the sensor configuration. For example, the ping-pong mode, where two transmitters and two receivers operate, requires $p$ to be 2.

$$S = S_1 \cdot S_2^* = A_1 e^{j\varphi_1} \cdot A_2 e^{-j\varphi_2} = A_1 \cdot A_2 \cdot e^{j(\Delta\varphi)} \text{ , with } \Delta\varphi \approx p \cdot \frac{2\pi}{\lambda} \cdot \Delta r \text{ , and } \Delta r \propto \frac{c \cdot \Delta t}{2} \qquad (2\text{-}10)$$

The recorded image pair is characterised by its temporal and spatial baseline. The size of the temporal baseline depends on acquisition mode and sensor platform, which may operate in single-pass or repeat-pass mode. Single-pass acquisition means that the images are acquired simultaneously, usually from airborne platforms. Form space, only the former Shuttle RADAR Topography Mission (SRTM) and the recently launched TanDEM-X along with TerraSAR-X can provide nearly single-pass interferometric data. Repeat-pass acquisitions are achievable by airborne and space-borne platforms, but the temporal difference between the two recording dates varies from seconds up to weeks. Depending on the availability, different applications in the field of change detection can be supported, such as moving target identification (short term) and monitoring of surface deformation (long term).

In addition to the temporal baseline, the orientation of the spatial baseline defines what kind of displacement is measured. In an along track configuration, where the spanned baseline is parallel to flight path, the calculated phase difference of a mapped object is proportional to its velocity component orthogonal to flight direction. This mode is useful for moving target identification and monitoring (e.g. iceberg tracking and traffic monitoring) with preferred single-pass acquisition. An across track configuration allows the computation of height differences between adjacent pixels and will be discussed in more detail since such data are an important element of this thesis. For the setup visualised in Fig. 2.2a, the interferometric baseline is orthogonal to the flight path formed by two antennas (single-pass) or two tracks of a sensor equipped with a single antenna (repeat-pass).

The phase differences, also called interferometric phases $\Delta\varphi$, are proportional to the object height and can be characterised by the wrapped sum of different contributions defined between $-\pi$ and $+\pi$:

$$\Delta\varphi = \varphi_{\text{flat}} + \varphi_{\text{topo}} + \varphi_{\text{dist}} + \varphi_{\text{scat}} + \varphi_{\text{noise}} \text{ .} \qquad (2\text{-}11)$$

The first term, the flat-earth phase proportion $\varphi_{\text{flat}}$, is independent from the imaged area. Only the increase of the off-nadir look angle $\theta$ from near range to far range leads to this contribution. The second, the topographic phase contribution $\varphi_{\text{topo}}$, results from the actual surface topography. The third term contains a group of physical and mainly deterministic effects (e.g. surface displacements, orbit errors, and atmospheric conditions), which are summarised as distortion contribution $\varphi_{\text{dist}}$ here. Depending on the interferometric sensor configuration, several up to all of these distortion effects are negligible. For example, a single-pass InSAR dataset is unaffected by any surface displacement and change of atmospheric conditions. The fourth term, the scatterer's phase contribution $\varphi_{\text{scat}}$, depends on the backscatter properties of the illuminated object and the sensor configuration. However, at best this term can be neglected if coherent scatterers are observed. The phase of an image cell has to be defined by one or a group of dominant scatterers and the chosen baseline has to enable the superposition of the signal of the same scatterers in both images. Hence, the temporal and spatial baselines should not be too long to prevent the decorrelation of the spectra and, as a result, the phases $\varphi_1$ and $\varphi_2$. The last phase contribution, $\varphi_{\text{noise}}$, refers to noise effects (e.g. thermal noise).
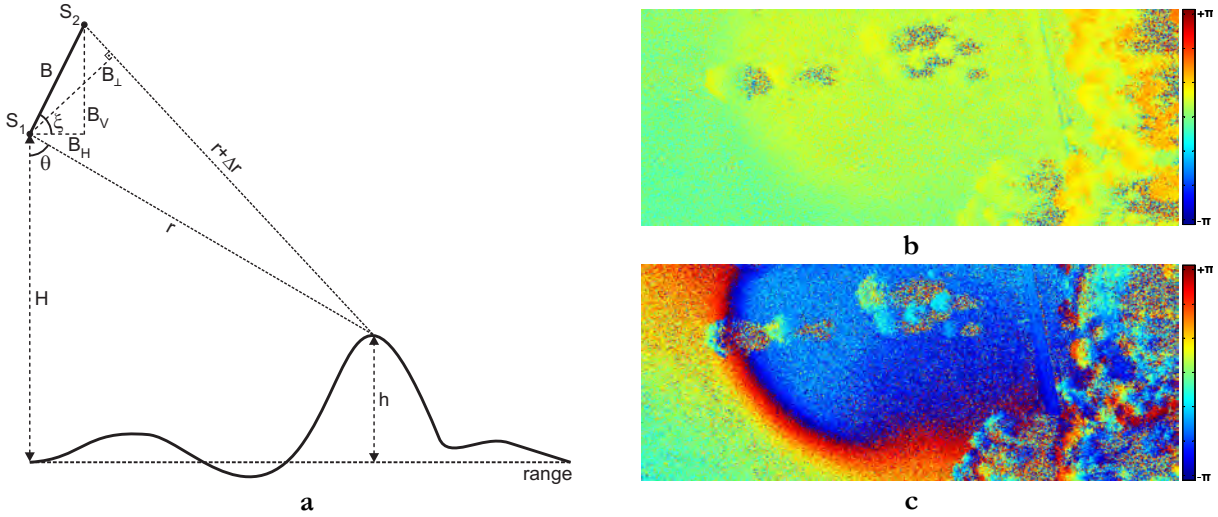
**Figure 2.2:** Principle of across-track SAR interferometry (a), flat-earth corrected InSAR phase images showing the same scene but with different unambiguous ranges $\Delta h_i$; short baseline (b) and long baseline (c)

In general, the quality and thus the usefulness of $\Delta\varphi$ can be characterised by the interferometric coherence. In terms of interferometric SAR, the coherence $\gamma$ is used to determine the level of correlation between the two received signals $S_1$ and $S_2$. It is required that these signals are ergodic, which is usually the case according to [17]. Due to this fact and as mentioned in Subsection 2.1.2, a SAR system operates entirely coherent during the integration time. The coherence is the magnitude of the complex cross-correlation coefficient $C$ between the InSAR images $S_1$ and $S_2$ by considering an image patch of $n$ pixels:

$$\gamma = |C| = \frac{\left|\sum_{i=1}^{n} S_{1_i} \cdot S_{2_i}^*\right|}{\sqrt{\sum_{i=1}^{n}\left|S_{1_i}\right|^2 \cdot \sum_{i=1}^{n}\left|S_{2_i}\right|^2}} \tag{2-12}$$

The interferometric coherence takes values in the interval [0,1]. Zero reflects total incoherent (colour coded black) and "1" implies full coherent signal (colour coded white). For repeat pass InSAR tracks, this measure is mainly used to assess the quality of the interferometric phase, but furthermore very detailed information concerning the scattering process of single objects is delivered. For example, complete coherent scattering is given for dihedral corners (e.g. at building locations), a decreasing coherence value is observable for growing vegetation (from fallow land to cropland to forest), and fully decorrelated signals are obtained for water surfaces and temporal changes. Hence, the interferometric coherence is later on used for classification (Section 4.4), height calculation (Section 4.5) and InSAR phase filtering (Subsection 4.10).

The mathematical relation between across-track interferometric phase $\Delta\varphi$ and relative object height $h$ is given by:

$$h \approx \frac{1}{p} \cdot \frac{\lambda \cdot r \cdot \sin\theta}{2\pi \cdot B_{\perp}} \cdot \Delta\varphi, \quad \text{with} \quad B_{\perp} = B \cdot \cos(\theta - \xi), \quad \text{and} \quad \xi = \arctan\frac{B_{\mathrm{V}}}{B_{\mathrm{H}}}, \tag{2-13}$$

where $r$ is the range distance between sensor and object, $\theta$ the off-nadir look angle, and the so-called normal baseline $B_{\perp}$ is the perpendicular part of the spatial baseline $B$, such as shown in Fig. 2.2a.

Furthermore, the relation between $B_{\perp}$ and $B$ is characterised by the vertical baseline $B_{\mathrm{V}}$ and the horizontal baseline $B_{\mathrm{H}}$ as parts of $B$ and by the angles $\theta$ and $\xi$. As interferometric phases are phases wrapped into the interval $[-\pi, +\pi]$, the corresponding object heights are restricted too. The unambiguous range $\Delta h_i$ (2-14), which is a function of the constant values wavelength $\lambda$ and $p$ and the values $B_{\perp i}$, $r_i$ and $\theta_i$ are related to the range position $i$.

$$\Delta h_i \approx \frac{1}{p} \cdot \frac{\lambda \cdot r_i \cdot \sin\theta_i}{B_{\perp i}} \tag{2-14}$$

Hence, $\Delta h_i$ is increasing from near to far range. An increasing length of baseline gives a decreasing $\Delta h_i$. If the relative height difference of an imaged area is larger than $\Delta h_i$, phase jumps, also called fringes, appear in the interferogram and in the final height model. There are two approaches to a solution: configuration and algorithm oriented ones. New sensor systems (e.g. MEMPHIS) equipped with a group of transmitters and receivers, provide data of multiple-baselines within a single-pass acquisition [89]. The various possibilities of combining transmitters and receivers allow to obtain different lengths of baselines. The unwrapping process starts with the shortest baseline interferogram featuring the largest $\Delta h_i$ according to (2-14) and showing ideally no phase jumps (Fig. 2.2b). By this gradient information, the ambiguities in the next longer baseline interferogram are eliminated. At the end of this process the interferogram of the longest baseline (Fig. 2.2c) is unwrapped incrementally and the best height accuracy is retained. With this configuration oriented solution, it is also possible to unwrap spaceborne data, since varying baseline lengths between the repeat-pass acquisitions are given. In addition to this multi-baseline solution, also algorithms incorporating mathematical constrains (e.g. residue-cut method and least-squares method [61]) have been developed to eliminate ambiguities in interferograms. The general idea of these phase unwrapping algorithms is the determination of the gradient, the local phase shift between neighboured pixels. This is realised by 1D or 2D integration over an interferogram area to assemble the correct integer-number ratio of phase cycles in order to unwrap the interferogram.

Applications for across-track InSAR data are characterised by the temporal baseline and the geometric resolution or the size of the imaged area. Based on single pass acquisitions, DSMs of high quality are extractable, and depending on the geometric resolution, large scale surface deformations up to individual object changes are observable in repeat pass InSAR data.

## 2.2    Imaging Properties

In the following subsections, the radiometric relations between sensor and object properties are discussed with respect to their effect on the magnitude signature. Furthermore, the designations of

the radar-frequency bands are introduced. Geometric distortions at elevated objects due to the SAR imaging properties are featured in the last subsection.

### 2.2.1 Radiometric Properties

The radiometric signature in SAR images is affected by the physical imaging principle and the object properties. First, a phenomenon caused by the SAR imaging principle is described that dominates the SAR image texture in general. Subsequently, the focus is on the texture variance defined by the observed scene, whereby the resulting magnitude value of a single image cell depends on type and number of contributors summed up over the pixel area. The signature of the cell can be dominated either by a strong scatterer alone or by an unknown number of different scatterers. In the following, the signature of single objects is analysed through the interaction of sensor wavelength, object material, and object roughness. Then, the occurrence and appearance of distributed scatterers (clutter areas) are characterised and common statistical distributions describing different kinds of SAR signatures are presented. Additionally, we focus on the sensor wavelength presenting the designations of the radar-frequency bands.

### Radiometric Properties in General

In general, the radiometric appearance of SAR images is dominated by a texture or signal distribution perceived as a grainy "salt and pepper" pattern. In the following paragraph, this phenomenon called *speckle* is physically and statistically characterised. Also the most common speckle reduction method and a few more advanced speckle reduction filters are presented.

### *Speckle*

Speckle is no special electromagnetic phenomenon; it is also observable for sound waves and particle streams showing wave properties. The requirements for this phenomenon are coherent illumination and rough surfaces in comparison to the used wavelength (see equation (2-18)). Irregularities of a surface, in the SAR domain called scatterers, reflect the emitted radiation in form of waves that might be in phase or out of phase. The interference (also called *fading* [101]), the superposition of the different wave fronts, leads to cancellation or reinforcement effects appearing as randomly distributed intensity values in the SAR image. Hence, the brightness of a single pixel is not only determined by the physical properties of the scatterer, but also by the relative phase interaction between the contributing scatterers. In general, the speckle is modelled as a multiplicative random signal with circular Gaussian statistics leading to a *probability density function* (pdf) of the intensity $I$ (2-15) and uniform distribution for $\varphi$ in the interval $[-\pi,+\pi]$.

$$\mathrm{pdf}\left(I\right) = \frac{1}{\sigma_I} \cdot e^{\left\{-\frac{I}{\sigma_I}\right\}} \tag{2-15}$$

This common description implies some simplifications, for example, the statistical independence of the signal received from different scatterers, which makes it inappropriate for some real situations. The requirements for this so-called "fully developed speckle" are summarised in [57] by pointing out the necessity of large number of scatterers, which contribute to the measured signal. Concern-

ing open and rural areas, these restrictions are fulfilled for spaceborne and airborne data. For radiometric image interpretation and for methods of automatic image analysis, such as segmentation and classification, speckle is a limiting factor. Hence, in the following paragraphs the most common speckle reduction method and more advanced speckle filters are described.

### *Multilooking*

The easiest way to reduce speckle is given by averaging over different independent sub-images [101]. This so-called *multilooking* is realised in SAR processing by frequency partitioning to generate sub-images, whereby the number of sub-images, also termed looks, describes the level of averaging. In practice, the number of looks is not really important, but rather the reduction of speckle variance in comparison to the expectation value. Therefore, the defining criterion is the *equivalent number of looks* (ENL) calculated from a homogeneous image region $X$ in the intensity SAR image:

$$\text{ENL} = \frac{\text{E}\{X\}^2}{\text{Var}\{X\}} \tag{2-16}$$

Assuming that SAR data are already processed, the described multilooking in the frequency domain is equivalent to a linear filtering in the image domain. The filtering is usually implemented by incoherently averaging pixel values inside a square window of $N \times N$. In general, the achieved ENL is lower than the number of averaged pixels due to the correlation of neighbouring image cells. For both approaches, the reduction of speckle variance results in a decreasing spatial resolution because of the shorter synthetic aperture per look or the spatial averaging. To avoid this drawback, more advanced speckle filters have been developed, which better maintain the high spatial resolution of the SAR data.

### *Other Speckle Filters*

Instead of averaging, more sophisticated schemes are necessary to reduce or remove the speckle in a more effective way. In principle, the variation of the image magnitude is estimated by considering a small image area first. Then the original pixel value is replaced by a new one derived from the local statistics to reduce the image speckle. The filters can be subdivided into non-adaptive and adaptive ones according to their ability to adjust their weighting coefficients to the local image statistics. Preference is given to the adaptive approaches because of better preserving structural and textural information. Matured and well-known adaptive speckle reduction filters, as the Lee-Filter [77], the Frost-Filter [51], and the Kuan-Filter [75], were presented in the 1980s and are characterised by a high level of speckle reduction while preserving the expectation value of the magnitude. Later, these filters were refined in order to preserve signatures of point targets in a better way. One representative of this group of maximum a posteriori probability (MAP) speckle reduction filters is the Gamma MAP-Filter [87].

These filters can be classified by requirements deduced from the respective application, whereby a differentiation between radiometric and geometric features is useful. Such a comparison of adaptive speckle reduction filters is given in [149] for the Lee-, Kuan-, Frost-, Enhanced Lee-, Enhanced Frost-, and the Gamma MAP-Filter. The validation of the radiometric enhancement is based on the features "maintenance of average mean" and "capability of speckle reduction". The dependency

and the effect on geometric properties are assessed by considering different image scenes, from homogeneous areas to edges, point targets, lines, and angular structures. Focusing on the last two with respect to the SAR building signatures, the Frost-filter delivered the best results.

Furthermore, as the generation of speckle is not random, it can contain information useful for texture analysis, for example, in oceanography and forestry. Additionally, the spatial resolution from one metre down to only some centimetres gives rise to the question of appropriate statistical models, because the assumptions of fully developed speckle might no longer be fulfilled. New filters like those recently presented in [139] have to consider this as well as the increasing density of fine structures and their radiometric and geometric preservation.

SAR data of urban areas will not fulfil the above-mentioned requirements of fully developed speckle [57]. The most important conditions, large number of contributors and non-dominance of single scatterers, are not realistic because of the very high spatial resolutions and the material properties of man-made structures. Thus, other statistical models/distributions are mandatory to describe the statistical properties of such SAR data (see e.g. [130]). A short overview on single and mixed scatter signatures is given in the following subsections.

## Radiometric Properties of Single Objects

Beside the geometric properties (see Subsection 2.2.2), the physical sensor and the object properties characterise the radiometric signature of an object deduced from the received power $P_R$ in sensor direction. This power is defined as a function of transmitted power $P_T$, the antenna gain $G$, the wavelength $\lambda$, the RCS $\sigma$, sensor losses $L$, and the range distance $r$ between sensor and object. For RAR systems the received power is defined by the radar equation:

$$P_R = \frac{P_T \cdot G^2 \cdot \lambda^2}{(4\pi)^3 \cdot L} \cdot \frac{\sigma}{r^4}$$

(2-17)

Concerning SAR systems, the dependency on $r$ is reduced to $1/r^3$ [72]. The interaction effects characterising the radiometric appearance of objects in SAR data are dominated by $\sigma$ and $\lambda$. $P_T$, $G$, and $L$ are sensor specific parameters, which are almost uncorrelated with the object properties. The effect of decreasing $P_R$ by diminishing the ground range pixel size due to increasing $r$ is observable in uncalibrated data. Normally, this is compensated within the SAR data processing of calibrated image data. $\sigma$ aggregates the object properties – size, orientation, shape, surface material and roughness define the radiometric signature of an object depending on $\lambda$. In the following, the effects of the surface material and roughness are described since they affect the amount of transmission and reflection of the incident radiation. Moreover, effects caused by different object sizes, orientations, and shapes are discussed briefly; their influence on the appearance of buildings will be presented in more detail in Section 3.3.

### *Surface Material of Objects*

The scattering of the incident radiation is characterised by the ratio between transmission, reflection, and absorption at the given surface layer. The relative permittivity $\varepsilon_r$ of the material is the relevant physical parameter describing the amount of transmission and the penetration depth into
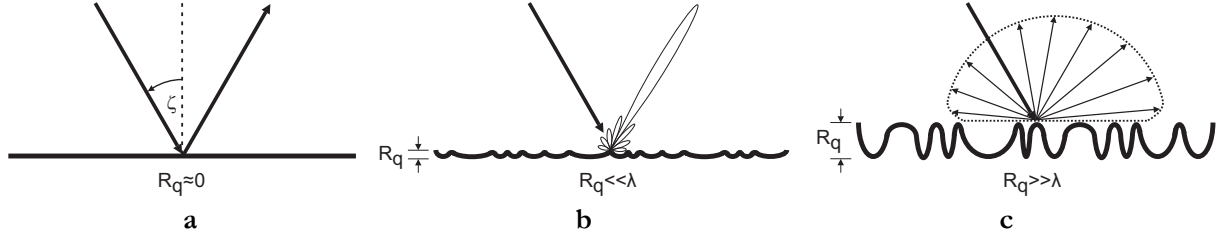
**Figure 2.3:**  Schematic view of reflection properties depending on the roughness of ground material (e.g. plane surface (a), smooth to medium rough surface (b), and rough surface (c) – showing Lambertian reflection) [72]

the material as a function of wavelength $\lambda$ and some conditional parameters (e.g. temperature of material). Concerning different wavelengths, the penetration depth is increasing with rising $\lambda$. In extreme cases, total transmission without reflection is given (e.g. for forest canopy when using L-band). Focusing on $\varepsilon_r$, a small value leads to a high transmission and consequently to a low reflection of the incident radiation. Such areas appear darker in the SAR magnitude data. High $\varepsilon_r$ values minimise transmission and lead to a nearly total reflection of the incoming radiation. In SAR data, these areas show either very low or high intensity depending on the local incidence angle $\zeta$ with a maximum intensity value for $\zeta = 0$.

### Surface Roughness of Objects

In addition to the material of the surface, also the roughness of the surface defines the amount of reflection. It further describes the type of reflection. A discrimination between specular and diffuse reflection is usually made, characterised by the interaction of surface roughness $R_q$ and $\lambda$. In Fig. 2.3, three types of surface scattering are visualised by considering a plane (a), a smooth to medium rough surface (b), and a rough surface (c). The first example shows specular (mirror like) reflection occurring for example at smooth water. As no signal is reflected towards the sensor (except for $\zeta = 0$), these objects appear dark and thermal noise dominates the SAR image. The decision, whether a surface is smooth or not, can be derived from the Rayleigh roughness criterion [143] given in (2-18). This defines the average roughness $R_q$ depending on the local incidence angle $\zeta$ of the radar waves with reference to the surface normal and $\lambda$.

$$R_q < \frac{\lambda}{8 \cdot \cos\zeta} \tag{2-18}$$

The second example visualises smooth to medium rough surfaces dominated by specular reflection occurring for example at streets, water surfaces, and also building roofs. Concerning magnitude data, such horizontal planes appear nearly black since only a low amount of the signal is backscattered towards the sensor. Thus, also SAR phases are dominated by thermal noise. The third example shows the scattering process for rough surfaces, which is featured by diffuse reflection. The Lambertian scattering, the most common model for diffuse reflection, describes the reflection of energy in all directions by the Lambertian cosine law. It implies that the reflected power towards the sensor is defined by the product of power of incident radiation weighted by $\cos\zeta$. The magnitude signature of such objects (e.g. roof areas) varies from dark to bright depending on $\zeta$.

**Radiometric Properties of Clutter**

In addition to the scattering of a single dominant object, a resolution cell can also contain information about a group of contributors (e.g. vegetation). The coherent sum over these random scatterers leads to a mixed signature, so-called clutter, with random phase and amplitude values. Usually, clutter areas are areas of no interest surrounding the target object. In this context, other widely used terms are background clutter, volume clutter, and surface clutter, whereby, depending on the application, the first one describes the proportion between primary target (e.g. car and tank) and background signal, and the latter terms are used to classify the backscatter characteristics of objects and areas. Since most clutter objects are natural, an exact characterisation in the above mentioned form (e.g. roughness, material, and form) to determine the backscatter coefficient is virtually impossible. Hence, different ways to model the backscatter signature of designated types of clutter are presented in the literature (e.g. statistical models derived from product model and empirical models deduced from real SAR data). As the signal distributions refer to highly varying parameters (e.g. clutter type, look angle, sensor polarisation, and sensor ground resolution) and the steady progress in the sensor technology led to a high variability of SAR data, the number of published models and distributions is tremendous. In the following, only the most common distributions to describe amplitude and phase signatures of radar clutter are summarised. More details of statistical modelling of SAR images can be found in [54].

*Amplitude Distributions*

The most common probability distributions to describe the SAR amplitude signatures of radar clutter are Rayleigh- and K-distribution as the representatives of the statistical models, and Weibull [113], Log-normal, and Fisher distribution of the empirical ones. Exemplarily, the description of the Weibull distribution is given in (2-19), where $\psi$ is the *scale parameter* and $\eta$ is the *shape parameter*.

$$g(u,\psi,\eta) = \begin{cases} \dfrac{\eta}{\psi} \cdot \left(\dfrac{u}{\psi}\right)^{\eta-1} \cdot e^{-(u/\psi)^{\eta}}, & u > 0, \psi > 0, \eta > 0 \\ 0, & \text{otherwise.} \end{cases} \tag{2-19}$$

The exponential distribution for SAR intensities and the Rayleigh distribution for SAR amplitudes are special cases of the Weibull distribution with $\eta = 1$ and $\eta = 2$. Considering homogeneous areas and low sensor resolution, the exponential distribution fits to the statistics of single-look intensity images, and the Rayleigh-distribution filter to single-look magnitude images. With the availability of better resolutions, distributions that are more flexible were required due to a smaller amount of scatterers per image cell. Beyond this effect caused by the change in resolution, the backscattering of clutter also changes through sensor and processing parameters (e.g. apodization function – Subsection 2.1.3 – and wavelength) and time. Concerning heterogeneous areas such as urban regions, the quantity of bright scatterers is strongly increasing and cannot be described by exponential distributions. More flexible models have to be introduced such as the Fisher model. In [130] the suitability of this distribution to model the statistics of high resolution SAR images of urban areas is proven for the example of real airborne SAR data of AeS-1, which will be investigated later on.

Such statistical modelling of SAR amplitude data is necessary to support developments in the domain of SAR specific segmentation, classification, or object detection algorithms (Section 4.6).

### *Phase Distributions*

In addition to the statistical modelling of amplitude and intensity signature of circular Gaussian scattering, also the characterisation of the phase and the interferometric phase signature in particular are of concern. The phase can be modelled as a uniformly distributed signal in the interval $[-\pi, +\pi]$ since the phase value of a single pixel results from a quasi-random summing-up over a large group of contributing scatterers. The information content of SAR phases becomes apparent by interferometric SAR (Subsection 2.1.4). The quality of the interferometric phase is affected by decorrelation, for example, due to view-dependent reflection properties, temporal changes between the two SAR acquisitions, system noise and phase aberration. The corresponding behaviour of interferogram statistics was investigated in [70]. Similar to the filtering of speckle-affected amplitude images, the noise on interferometric phase signatures is also reduced by applying different filters. Frequently used filters are the conventional multilook-filter [78], and the filters presented in [56] and [6] investigating the frequency spectrum of InSAR patches to reduce the high frequency noise.

Concerning data that are of better resolution than one metre, the phase modelling has to be adapted – similar to the amplitude modelling – because the assumption of random phase behaviour is no longer valid. Based on the analysis of real InSAR data of RAMSES [37] and AeS-1, a new model was introduced in [99] to handle spatial correlations as observed for strong reflectors and medium rough surfaces in the InSAR phase data. These correlation effects in the InSAR phase signature have to be considered in subsequent processing steps (e.g. filtering). An adaptive orientation filter based on local noise level in the InSAR phase data was first shown in [79], where sixteen orientations, local weighting, the number of looks, and the local variance were taken into account. This filtering adapts to the fringes to preserve the phase gradient. Additional information and a new InSAR phase filter suitable for building signatures are presented in Section 4.10.

### Wavelength

One of the most descriptive features of a SAR sensor is the used wavelength $\lambda$. The frequency range of radar waves is subdivided in to the different bands listed in Tab. 2.1. The abbreviations HF-, VHF-, and UHF-band stand for High, Very High, and Ultra High Frequency bands. The most common and available frequency bands for remote sensing applications are L, C, and X due to their low atmospheric extinction. Depending on the application, the following phenomena resulting from the wavelength have to be taken into account: with shorter wavelength the RCS of an object is increasing, the atmospheric effects on radar waves are rising, and due to the Rayleigh roughness criterion (2-18) more object surfaces appear to be rough. Furthermore, short wavelengths are more sensitive against view changes and object motion so that an increasing decorrelation of repeat-pass data is given, which is important for InSAR applications. In addition, the unambiguous range $\Delta h_i$ of an interferogram (2-14) is influenced by $\lambda$ resulting in better height accuracy for shorter wavelengths. In contrast, longer wavelengths lead to increasing penetration depths into special surface materials (e.g. ice and dry soil) and into vegetation. Thus, depending on the application, different wavelengths are preferable, for example:

**Table 2.1:**   Designations for Radar-Frequency Bands [67], [84]

| Band Designation | Frequency Range | Wavelength | Band Designation | Frequency Range | Wavelength |
|---|---|---|---|---|---|
| HF-band | 3–30 MHz | 100–10 m | X-band | 8–12 GHz | 3.75–2.50 cm |
| VHF-band | 30–300 MHz | 10–1 m | Ku-band | 12–18 GHz | 2.50–1.67 cm |
| UHF-band | 300–1000 MHz | 1–0.30 m | K-band | 18–27 GHz | 1.67–1.18 cm |
| P-band | 220–390 MHz | 1.36–0.77 m | Ka-band | 27–40 GHz | 1.18–0.75 cm |
| L-band | 1–2 GHz | 30–15 cm | V-band | 40–75 GHz | 0.75–0.40 cm |
| S-band | 2–4 GHz | 15–7.5 cm | W-band | 75–110 GHz | 0.40–0.27 cm |
| C-band | 4–8 GHz | 7.5–3.75 cm | mm-band | 110–300 GHz | 0.27–0.01 cm |

- P-band for archaeological and geological applications,

- L-band for sea ice monitoring and mapping of deforestation,

- C-band for atmospheric water vapour and soil moisture measurements and

- X-band for deformation measurements, object detection and reconstruction.

Furthermore, this short overview underlines the versatility of radar remote sensing supported by the large amount of available SAR sensors (Section 2.3).

### 2.2.2   Geometric Properties and Influence on Radiometry

The SAR imaging principle is characterised by a side-looking distance measurement. As mentioned before, the resulting image coordinate system is defined by the range axis orthogonal to the sensor flight direction and the azimuth axis parallel to it. An object position in image space is given by its minimal distance to the sensor (range coordinate, "fast time") and the position of the sensor at acquisition time (or the perpendicular intersection with the azimuth axis - azimuth coordinate, "slow time"). Due to this acquisition geometry, the appearance of objects is characterised by different phenomena (see [108]), where for example elevated objects show a displacement away from nadir axis.

In the following, SAR phenomena related to elevated objects are analysed in detail. The different phenomena are visualised in Fig. 2.4 by considering three objects of different slopes. We focus on the range coordinates within this context (azimuth axis is oriented orthogonal to the sheet). The sensor located in the upper left corner transmits and receives the signal; the circles refer to wave fronts. The upper bar diagram termed *slant range* shows the expected magnitude profile in the SAR image given in slant range geometry. The chosen grey values and altitudes match the expected SAR signal brightness or magnitude, respectively. A similar profile called *ground range* is shown in the lower part of Fig. 2.4. This change from slant to ground range geometry requires a projection (Section 4.7).
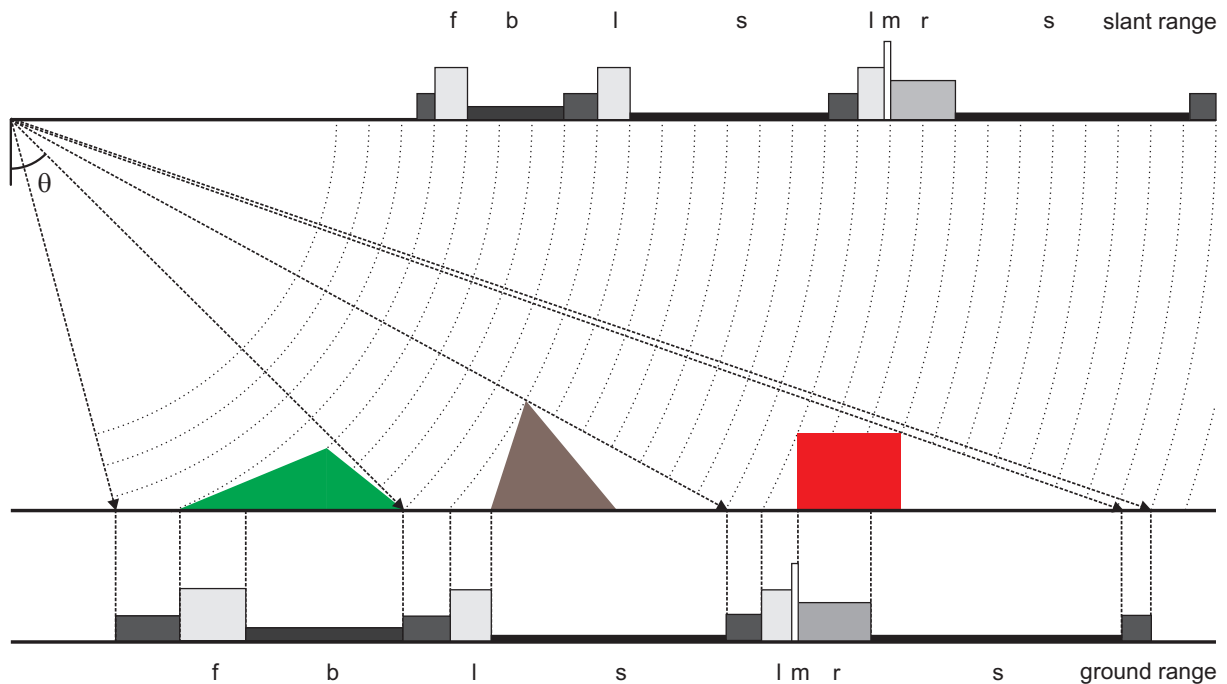
**Figure 2.4:** Schematic view of radar mapping phenomena in ground and slant range projection for the three examples: hill (green), mountain (brown), and building (red); $f$ – foreshortening, $b$ – backscattering of area oriented away from sensor, $l$ – layover, $m$ – multi-bounce reflection, $r$ – backscattering of roof, and $s$ – shadow

### Foreshortening / Stretching

The foreshortening phenomenon $f$ is observable in hilly landscape on terrain facing towards the sensor. In Fig. 2.4 the hill marked in green visualises this imaging geometry, whereby the terrain gradient is less than the off-nadir look angle $\theta$. The gradient and the SAR imaging geometry lead to a shortening of the front slope in the slant range profile. Additionally, the magnitude appears brighter in the slant and ground range profile due to the compressed mapping of the backscatter signal. The foreshortening effect occurs stronger with increasing terrain gradient or decreasing $\theta$. At the extreme case, a match of terrain gradient and $\theta$, the backscatter signal is compressed theoretically into one range pixel cell and appears very bright.

The stretching, the reverse effect to the foreshortening, is visible in the SAR data if the slope of the mountainside turned away from the radar sensor is smaller than the off-nadir look angle $\theta$. For the constellation given in Fig. 2.4, this assumption is only fulfilled by the hill marked in green. Hence, this mountainside is stretched in comparison to the side facing towards the sensor (see low backscatter magnitude $b$). In case of stronger slope, no return is received from the mountainside; a shadow area will appear in the SAR data (see brown mountain).

### Layover

Foreshortening changes into the layover phenomenon $l$ if the terrain gradient is greater than the off-nadir look angle $\theta$, as often apparent in mountainous areas. Again, terrain sides facing towards
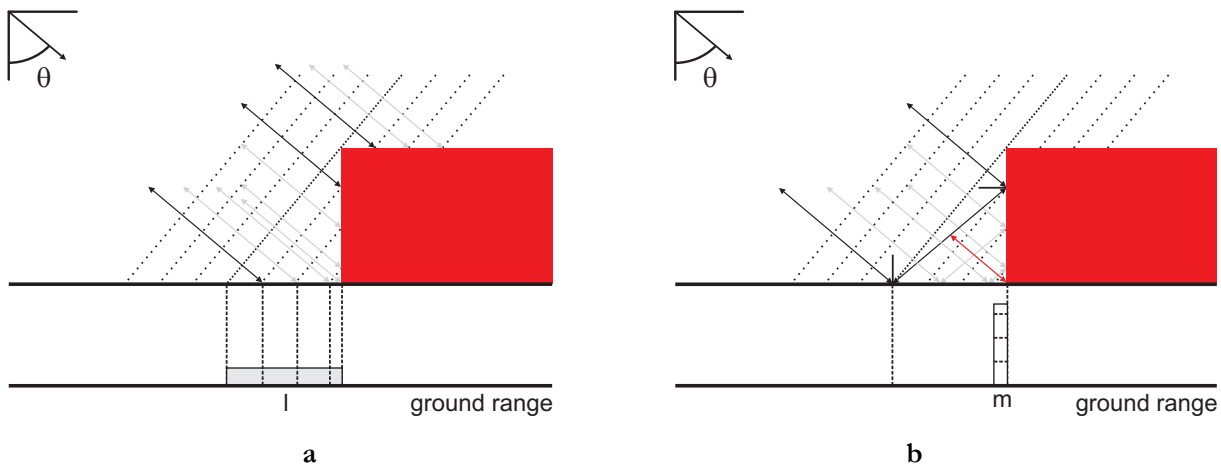
**Figure 2.5:** Illustration of direct backscattering (a; e.g. $l$ – layover) and multi-bounce scattering (b) at building location

the sensor are affected. Additionally, the back of mountains can also contribute to the layover area if their slope is smaller than $\theta$. In Fig. 2.4 the layover is visualised on the object marked in brown and red. The range distance between sensor and mountain peak is shorter than that of the base point. Hence, the backscatter signal of the mountain peak is received earlier and will be mapped in the SAR image in front of the signal of the basepoint. This fall-over effect towards the sensor position is exactly the opposite of the displacement effect in optical remote sensing images.

Moreover, the backscatter signals of different object points showing the same distance to the sensor are integrated to the same image cell. This is shown in more detail in Fig. 2.5a, where the parallel dashed lines visualise in a simplified manner the wave fronts. The arrows coloured in black mark terrain and object points of similar range distance. The superposition of these various contributors (e.g. terrain, wall, and roof) leads to a very bright magnitude in the SAR image.

**Multi-bounce reflection**

In addition to the direct backscattering of objects, also multi-bounce scattering $m$ is observable in SAR data, especially the appearance of urban areas is dominated by double-bounce scattering. This is caused by the dihedral corner reflectors formed by vertical building walls shown in Fig. 2.5b. In addition to the orthogonal geometry, also the smoothness of the surfaces is relevant. The surface materials (Subsection 2.2.1) must feature a dominating mirror-like reflection to give rise to such multi-bounce scattering. The geometric image position of the multi-bounce signal is characterised by a displacement away from the sensor due to the longer signal runtime, which is equal to twice the length of the red arrow in Fig. 2.5b. The magnitude value at this position depends on object height because the wave front hitting this structure and undergoing double-bounce reflection has same run-time and is thus added up. Hence, a higher object leads to a brighter magnitude value at this position in the SAR image.

The multi-bounce phenomenon is not limited to double-bounce reflections. Even more reflections are possible and sometimes observable, for example, at artificial trihedral corners used as calibration objects, at L-shaped building corners, or at bridges over smooth water. However, since reflec-

tions at non-perfectly smooth surfaces lead to signal spread, such multi-bounce usually rapidly decays. Typically a mixing of the phenomena foreshortening, layover, and multi-bounce reflections arises for more complex objects (e.g. ships and skyscrapers), thus complicating their signature interpretation.

### Shadowing

The shadow phenomenon $s$ is found at elevated objects, if the terrain gradient of the back of the object is more than $(90° - \theta)$. Otherwise, a low backscatter magnitude $b$ is received (e.g. green object Fig. 2.4). Shadow is given for the brown and red object, where an area behind the object cannot be illuminated by the transmitted radar beam due to its slope. This region, also called radar shadow, appears dark in the magnitude image and contains the system noise only. The distinction of such no-return areas from smooth areas of low return depends mainly on the so-called Noise Equivalent Sigma Zero (NESZ), which describes the reflectivity level equivalent to the noise level of a SAR sensor [93]. A small NESZ eases the detection of radar shadow and thus the detection of objects and targets.

## 2.3    Sensor Systems

In the following subsection, an overview of the state-of-the-art spaceborne and airborne SAR sensors is given considering commercial and experimental systems in civil and military operation. Furthermore, the characteristic parameters of these systems are compared by focusing on wavelength, spatial and temporal baseline, spatial resolution, and availability.

### 2.3.1    Spaceborne Sensors

The evolution of spaceborne SAR sensors for civilian purposes started in the 1970s and saw a significant boom in the last ten years. Especially the spatial resolution and the range of products were improved during that period. A summary of SAR satellites and their main features such as field of activity, frequency used, and spatial resolution are listed in Tab. 2.2. The seeming dominance of civilian sensors is misleading, the trend is given for civilian and defence systems equally, whereby the latter are listed incompletely due to classified specifications. The evolution shows the improvement by one order of magnitude in spatial resolution (e.g. from RADARSAT-1 to RADARSAT-2 [65]) and an increase of X-band satellite systems. Furthermore, the interferometric capability (Subsection 2.1.4) of the systems is continuously enhanced by reducing the repeat cycle, i.e. the time span between two acquisitions achieved under similar sensor geometry (also referred to as temporal baseline for SAR interferometry). This can be achieved by additional satellites identical in construction on the same orbit close behind one another as practiced by COSMO-SkyMed 1-4 [32]. However, a tandem constellation of two satellites imaging an area simultaneously is the neat solution successfully realised by the pair of TerraSAR-X [25] and TanDEM-X [74]. Moreover, the number of systems capable of collecting full polarimetric data (e.g. RADARSAT-2 and TerraSAR-X) is increasing. However, this mode is not available for all products.

**Table 2.2:** System parameters of satellites with SAR sensors

| Satellite-Sensor (Company/Owner) | Activity | Launch | Frequency | Repeat Cycle | Best Spatial Resolution |
|---|---|---|---|---|---|
| ERS-1 and ERS-2 (ESA/AMI) | civil | 1991–1995 | C-band | 35 days | 25m |
| RADARSAT-1 (CSA/MDA) | civil | 1995 | C-band | 24 days | 8m |
| Envisat-ASAR (ESA) | civil | 2002 | C-band | 35 days | 30m |
| ALOS-PALSAR (JAXA/JAROS) | civil | 2006 | L-band | 44 days | 10m |
| SAR-LUPE 1-5 (BMVg/BWB) | defence | 2006–2008 | X-band | - | < 1m |
| COSMO-SkyMed 1-4 (ASI/e-GEOS) | civil/defence | 2007–2008 | X-band | 1(multi)/16 days | 0.9m |
| TerraSAR-X (BMBF/DLR/Astrium) | civil | 2007 | X-band | 11 days | 0.6m/1.1m |
| RADARSAT-2 (CSA/MDA) | civil | 2007 | C-band | 24 days | 3m |
| TanDEM-X (BMBF/DLR/Astrium) | civil | 2010 | X-band | 11 days | 0.6m/1.1m |
| Sentinel-1 (ESA) | civil | 2013 | C-band | 12 days | 5m |

With regard to civilian applications of object recognition and, in particular, on building reconstruction data availability, spatial resolution and interferometric capability are decisive for the sensor choice. Hence, the civil and dual-use systems (e.g. TerraSAR-X and COSMO-SkyMed) are the most suitable ones for this purpose. The new single-pass configuration of TerraSAR-X and TanDEM-X is of particular interest, not only because of the very high spatial resolution, but also a high coherence is ensured by the simultaneous acquisition. The relatively small wavelength as well as the large baselines lead to high resolution and accurate DEMs [18].

This positive sensor development continues with focus on higher temporal coverage to support monitoring applications (e.g. TerraSAR-X-2), and other frequencies for environmental applications (e.g. Sentinel-1 in C-band and TanDEM-L in L-band).

### 2.3.2 Airborne Sensors

In addition to spaceborne SAR sensors, also airborne sensors underwent an impressive evolution in the last ten years. A short selection of airborne SAR sensors is given in Tab. 2.3 by summarising the same sensor features as considered for SAR satellites. Before going into detail, the main pros and cons of spaceborne and airborne systems are discussed. By focusing first on the feature "activity" it becomes obvious, that since most of the airborne sensors are experimental and defence related, the availability of freely accessible data is limited. Furthermore, such systems require more lead time, for example, to fit the sensor on the platform or to obtain flyover approvals. Beside this, the most established SAR advantage, the weather independency, is also only partly correct for airborne systems due to aviation safety reasons. Additionally, their area of operation differs because satellites enable coverage of almost the whole world while airborne systems are limited to regional areas.

On the other hand, airborne systems are characterised by high flexibility concerning sensor setup and flight planning. These SAR sensors allow the operation on different platforms, in different

**Table 2.3:**   System parameters of airborne SAR sensors

| Sensor (Company) | Activity | Frequency-Band | Baseline [m] | Resolution [m] |
|---|---|---|---|---|
| STAR-3i/4/5/6 (Intermap Technologies) | commercial | X | 0.9/0.98 | 1.25 |
| TopoSAR (Intermap Technologies) | commercial | X | 0.6/1.8 | 0.5 |
| X-band radar sensor (MetaSensing) | commercial | P/L/X/Ku | not specified | 0.15 |
| E-SAR (DLR) | experimental | P/L/C/X | repeat-pass | $0.25\text{-}1.5 \times 2/4$ |
| PAMIR (Fraunhofer FHR) | experimental | X | multi, max. 1.0 | < 0.1/0.3 |
| MEMPHIS (Fraunhofer FHR) | experimental | Ka/W | multi, max. 0.3 | 0.2/0.8 |
| RAMSES (ONERA) | defence | P/L/S/C/X/Ku/ Ka/W | multi in X/Ku | 0.1 |
| SETHI (ONERA) | defence | UHF-VHF/ P/L/C/X | single-pass in X | <0.45 |
| Lynx/MiniSAR (Sandia National Laboratories) | defence | L/S/C/X/Ku/Ka | not specified | 0.1-3 |

wavelengths, and with varying antenna configurations. The same flexibility is given for flight planning by adjustment of flight height, flight direction, look angle, and flight path (e.g. straight or circular). In comparison, the flexibility of satellite configurations is restricted to ascending or descending orbit, and choice of off-nadir look angles. The most significant differences between spaceborne and airborne configurations are given for achievable spatial resolution and interferometric capability. Spatial resolutions up to one metre have been realised in airborne data 20 years ago, so that today data in decimetre scale are the rule rather than the exception. In comparison to SAR satellites, most of the airborne sensors enable operation in single-pass interferometric mode with two or more antennas acquiring data simultaneously. Hence, atmospheric and temporal decorrelation (Subsection 2.1.4) between InSAR images is excluded. Airborne repeat-pass InSAR is also operated for applications such as change detection. A comparison between single- and repeat-pass experiments is given in [21] regarding investigations on coregistration of very high resolution data over urban areas.

Concentrating first on the commercial sector, the market leader Intermap Technologies was founded in 1996 with focus on wide area campaigns to provide InSAR DEM data. For example, England was mapped in 2002 and Germany in 2006 [85]. Since 2009, the company MetaSensing has been providing very high resolution InSAR data for detailed analysis and offering leasing or purchasing of their airborne SAR sensors [90]. The listed experimental and defence related systems provide data of spatial resolutions from some decimetres up to some centimetres. The magnitude signature of single targets (e.g. Lynx [141]) as well as the InSAR appearance of urban areas (e.g. PAMIR [21] and MEMPHIS [106]) shows an impressive level of detail. Moreover, these systems stand out due to their high flexibility to offer different wavelengths, special flight configurations (e.g. bistatic experiment of RAMSES and E-SAR [28]), and antenna configurations (e.g. multi-baseline interferometry with MEMPHIS [89]).

# 3    Buildings in Multi-Aspect InSAR Data

In this chapter, the signature of buildings in InSAR data is analysed by focusing on different groups of parameters that can affect the appearance of a building. First, the main attributes of buildings in magnitude and interferometric phase data are described in detail. Then, the dependency of the building signature on sensor platform and sensor configuration is discussed. The influence of data processing is addressed in the third subsection. Finally, the influence of real building geometry is analysed by considering buildings of various type, size, orientation, and surrounding. For that, real and simulated building signatures of airborne and spaceborne sensor platforms are shown.

## 3.1    Basics of Building Signature

In principle, the building signature is characterised by the SAR mapping phenomena described in Subsection 2.2.2. In the following, the magnitude signature of buildings in real InSAR data is analysed in more detail by considering slant range profiles. Beside the magnitude signature, the interferometric phases also show characteristic attributes at the building location. Those attributes are also specified in the following.

### 3.1.1    Magnitude Signature

We start the discussion of the characteristics of buildings in SAR magnitude data for the simple case of a prismatic flat-roofed building. In Fig. 3.1 an optical image (a) and the schematic view of the considered SAR magnitude signature (b) of the building are depicted. The real SAR magnitude signature is shown in (c), and for detailed information, the magnitude profile of the slant range line marked in orange is given in (d). The outer bounds of the building are 210 m and 60 m, the height of the two parts is 10 m and 20 m, respectively. The front superstructure has a width of 15 m and a height of 10 m. The building is part of an industrial area dominated by flat halls and sparse vegetation.

The simplified 3D model is given in (b), neglecting substructures on the roof and in the neighbourhood of the building. The expected grey value distribution in the magnitude data corresponds with the bar diagram of the slant range profile below. The first received signal at the sensor results from the contributors: ground, building wall, and building roof. All of them show the same distance to the sensor leading to superposition of their backscatter signal in the same image cells. This effect is called layover, as introduced in Subsection 2.2.2. In contrast to elevated terrain, at building locations a subdivision of the layover area is possible due to various contributor groups depending on building outline and illumination geometry (Section 3.3). The given example shows such a subdivision in schematic view. In the real magnitude signature, this effect is not as clearly visible due to the low sensor resolution. In addition to the layover, bright lines are characteristic building features. In simplified terms, a group of many dihedral corner reflectors spanned by ground and building wall (Subsection 2.2.2) cause these lines, which are called corner lines in the following. By
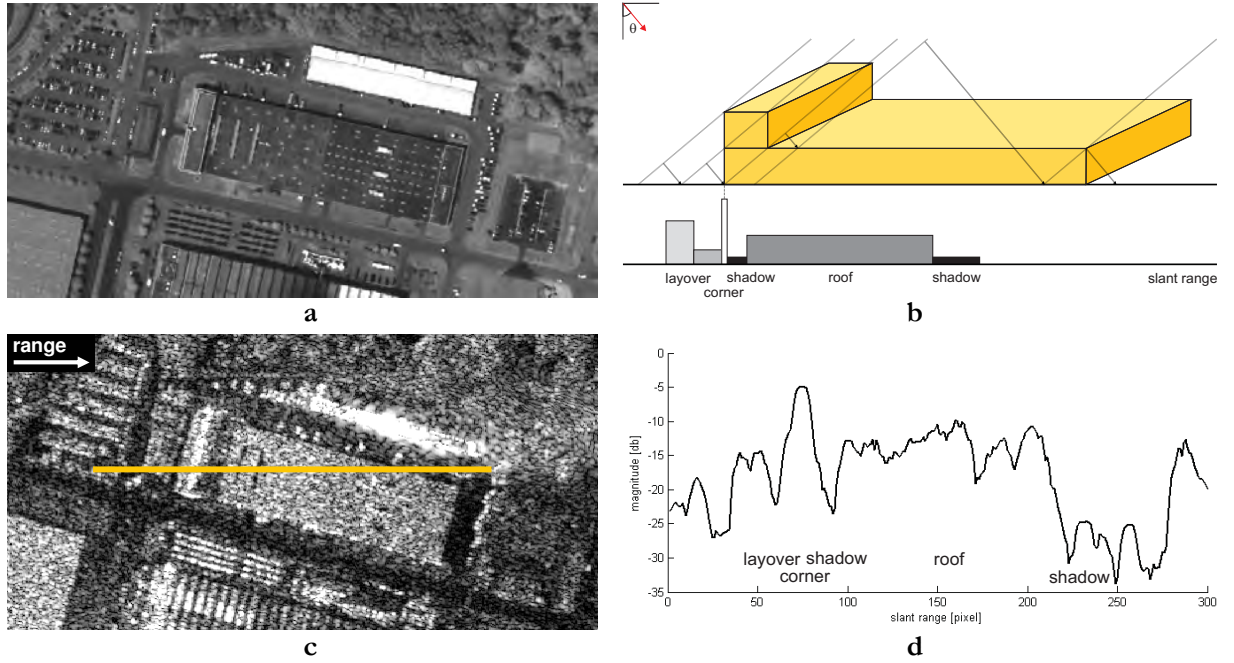
**Figure 3.1:**   Signature of a flat-roofed building in an optical image (a), schematic view of SAR magnitude signature (b), real SAR magnitude signature (c), and corresponding magnitude profile (d)

assuming right-angled buildings, the plane configuration of ground and wall leads to a superposition of all signals that hit this structure and undergo double-bounce propagation back to the sensor. Hence, this part of the signature appears very bright in the magnitude data due to integration of the signal. Moreover, the corner line occurs along the side of the building facing the sensor and is located at the base of the building. Usually behind this corner line, an area of homogeneous amplitude distribution is observable resulting from the direct backscatter of the building roof. The intensity in this area can take an arbitrary value in the full range of no up to a very bright signal depending on roof structure, roof material, wavelength, and illumination geometry. In contrast to the majority of buildings, in the example in Fig. 3.1, a short shadow region appears between the corner and the roof area that is caused by a superstructure. At least, the ground behind the building is partly occluded by the building shadow leading to a low signal magnitude.

A closer look at Fig. 3.1c reveals that the real magnitude signature of the building differs from the schematic signature because unmodelled substructures on the building roof, signals from adjacent objects, and the speckle phenomenon interfere with the signature. The short layover area in front of the building is observable followed by high intensity values of double-bounce scattering forming a corner line along the building front. Subsequently, as already mentioned, a small shadow region caused by the height difference of 10 m is visible. The magnitude values are low due to missing signal response while only noise dominates. Additionally, single bounce reflection of the roof appears as a large parallelogram with bright homogeneous amplitude. The shadow area behind the short building side looks very dark compared to the shadow region along the longer building side. Adjacent elevated substructures, which are also observable in the optical image, appear as bright spots in the shadow area. The real SAR magnitude profile, orange marked, is given in Fig. 3.1d. For visualisation purposes, $9 \times 9$ multilooking and logarithmic scaling were carried out. The layover starts

at slant range pixel 60 and the building corner is located at position 80. The shadow behind the corner caused by the substructure can be distinguished as local minimum. From slant range pixel 95 up to 215, the single backscatter of the building roof is shown. Inside this area, local maxima and minima are extractable due to small substructures (e.g. constructions of ventilation) on top of the building. At last, the main shadow behind the building is recognisable as low amplitude area interspersed with higher amplitudes of adjacent substructures. This simplified description of the SAR magnitude signature of buildings will be filled with more detail in the following subsections by focusing on signature changes affected by sensor configuration, data processing, and illumination as well as building geometries.

### 3.1.2 Phase Signature

The phase value of a single cell contains a mixture of signals of different contributors just as is the case for the magnitude value. The calculated interferometric phase value considering across track configurations is proportional to the contributor heights – see equation (2-14). Hence, the resulting InSAR height for an image pixel can be interpreted as a function of heights from all objects contributing to the particular range cell. The interferometric phase signature is characterised by layover, double-bounce reflection, direct reflection from the roof, and shadow. In Fig. 3.2, we focus on the same building as investigated for magnitude description to point out the characteristics of the InSAR phase signature.

In the LIDAR data (Fig. 3.2a) elevated objects (e.g. building and vegetation) show brighter grey values than the mean ground level. The steplike architecture of the building and the regular groups of substructures on top of the building are clearly visible. A simplified building profile and corresponding simulated InSAR phases based on the simulation approach described in Section 4.9 are given in Fig. 3.2b. The real interferometric phase image (c) as well as the phase profile (d) is calculated by the use of a 9×9 windowing. Analogous to the LIDAR signature the grey value in the phase image corresponds to the object height. Additionally, the coherence of the InSAR data is depicted in (e) and (f).

Starting with the signature part closest to the sensor, the layover, also called front-porch region [9], is characterised by heights of three contributors - terrain, building wall, and building roof. The typical downward trend of this part results from the superposition of the three contributions, whereby the height values of ground and roof are constant in contrast to the building wall. Its value decreases from roof to terrain height. Hence, the longer the range distance to the sensor becomes, the lower the local height of the reflecting point at the wall will get. Similar to the magnitude signature, the corner is located next to the layover. In the profile, this point shows a phase value similar to local terrain phases (d). That is caused by the sum of the double-bounce reflections between ground and wall having the same signal runtime as a direct reflection at the building base point. For the given example, the phase value of local terrain is at zero level. The fact that the corner shows this characteristic phase value enables the discrimination of corner lines from other lines of bright scattering. The mean terrain height can usually be estimated reliably making these corner lines useful as significant building features. Additional lower phase values are given in the real phase profile (d) corresponding to the dark shadow area in the magnitude data. In this shadow area, no backscatter signal is received so that the measured phase represents phase noise. In the simulated phases
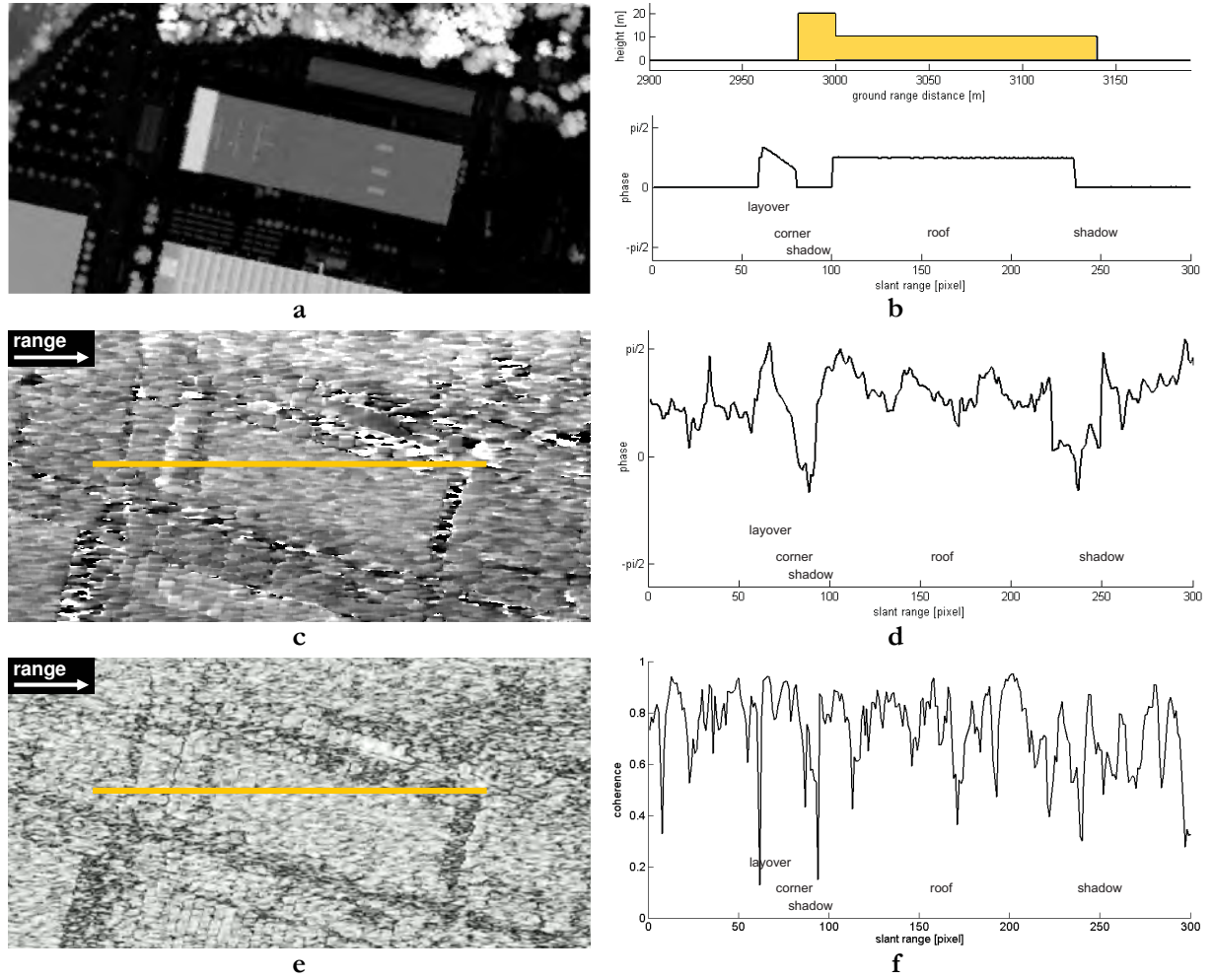
**Figure 3.2:** Signature of a flat-roofed building in LIDAR data (a); simulated interferometric phase profile (b), real signature in InSAR phase image (c), corresponding phase profile (d), coherence of In-SAR data (e), and corresponding profile (f)

(b), this part is defined by phase value zero, because in InSAR data we can easily detect and filter such an area according to the poor coherence (Fig. 3.2e,f). Hence, this effect is neglected here for the sake of focussing on more relevant features for the given task. Single response of the building roof will lead to a constant trend in the interferometric phase profile. Of course, the simulated profile follows this assumption (Section 4.9); however, the real phase profile appears less constant due to noise and small substructures on top of the real building. Behind the roof signature, the building shadow area coincides with a noise-dominated InSAR phase distribution appearing with phase jumps in the real profile (d).

The interferometric phase signature enables building height extraction. This is described on the simplified simulated phase profile for the two building heights. First, the height of the superstructure dominating the shape of the layover area can be specified by extracting the maximum at the layover area. Second, the height of the main building characterises the roof shape in the phase profile, enabling a direct extraction of this height value from the full area of phases "roof" [115]. In

a                                     b                                     c
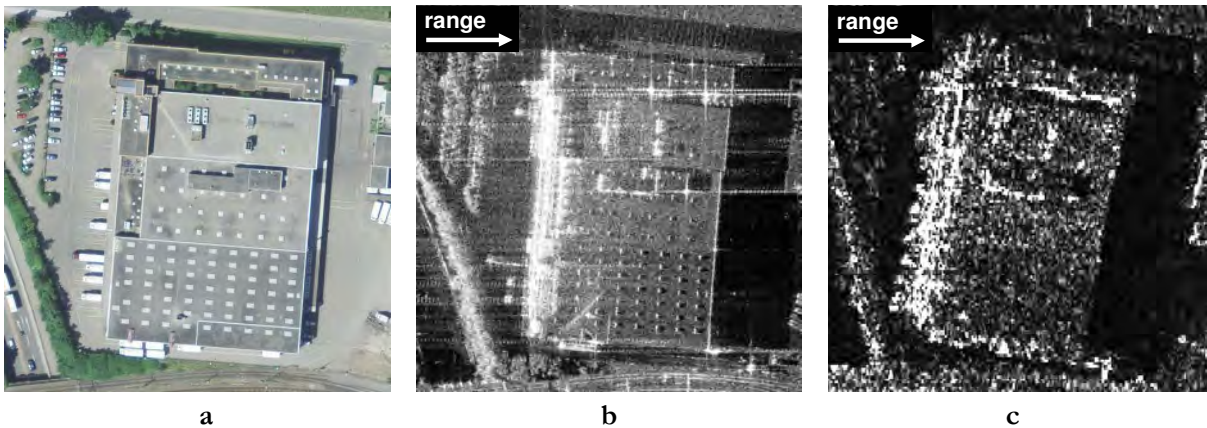
**Figure 3.3:**  Influence of sensor and processing parameters: industrial hall in optical (a, screenshot from map.geo.admin.ch, ©swisstopo), and in SAR magnitude data of MEMPHIS (b, Fraunhofer FHR) and TerraSAR-X (c, DLR)

case of a simple flat-roofed building, both locations, "layover" and "roof", will provide information for the extraction of building heights.

In the following, the analysis of the interferometric phase signature of buildings will be deepened by considering different sensor configurations and illumination and building geometries. Interferometric signature changes affected by viewing direction and various types of roofs are investigated in particular.

## 3.2    Influence of SAR Sensor and SAR Processing

Real building signatures can differ a lot from the previous general description of building appearance in interferometric SAR data, as can be seen in Fig. 3.3. The magnitude data of two different SAR sensors imaging the same industrial building are shown. The SAR magnitude signatures recorded by the airborne sensor MEMPHIS and the spaceborne sensor TerraSAR-X and an optical image are given in Fig. 3.3a to c. In general, the appearance of buildings and their surroundings is characterised by internal system and mission parameters such as wavelength, bandwidth, polarisation, baseline, revisit time, and look angle, and by data processing parameters as, for instance, image resolution, sampling rate, and applied apodization function. In the given example, the visible differences are caused by an interaction of many parameters, such as SNR (b – airborne, c – spaceborne), wavelength (b – Ka-band, c – X-band), off-nadir look angle (b – $\theta = 65°$, c – $\theta = 54°$), data resolution (b – approx. $0.2 \times 0.2 \, m$, c – approx. $0.6 \times 1.1 m$), and applied apodization function (b – Kaiser window, c – Hamming window). A clear assignment of signature changes to single parameters is difficult since some effects result from the interaction between sensor parameters, processing parameters as well as building parameters. In the following subsections, we describe only four key parameters, which are most characteristic for the considered InSAR data from our point of view; these are system wavelength, baseline configuration, image resolution, and windowing function.

### 3.2.1 SAR Sensor Parameters

From the group of SAR sensor parameters, in the following we focus on effects caused by the varying wavelength and interferometric baseline length. Information concerning different polarisations and bandwidths can be found in [96] and [105], for example. The impact of different off-nadir look angles and aspect angles is described subsequently in Section 3.3 because of the direct relation with the building orientation and position.

### Wavelength

The wavelength of the radar system is one of the most important parameters. From the radar equation (2-17) it follows that for extended objects of direct backscattering the RCS $\sigma$ of an object is usually dominated by the wavelength $\lambda$ (3-1).

$$\sigma \sim \frac{1}{\lambda^2} \tag{3-1}$$

For image areas resulting from single backscattering such as building layover and roof, a longer wavelength leads to decreasing magnitude values. The inverse effect is observable for magnitude values at building corner locations, because double-bounce reflections between ground and wall benefit from longer wavelengths. These effects are partly visible in the data of the Ka-band sensor MEMPHIS ($\lambda \approx 1\,cm$) and the X-band sensor TerraSAR-X ($\lambda \approx 3\,cm$) given in Fig. 3.3. The roof signatures are much brighter in Ka-band (b) than in X-band data (c) due to an intensified Lambertian backscattering. Changes of corner intensities due to different wavelengths are hardly visible. The expected effect is shown on simulated and real SAR data in [45], [48]. The perceptibility of isolated roof structures will be highest, if the surrounding roof material appears smooth in comparison to the wavelength due to contrast maximisation in the SAR magnitudes. Real RCS measurements of materials of different roughness at a fixed wavelength can be found in [96].

### Baseline Configuration

As the magnitude signature, the interferometric phase signature of buildings is mainly characterised by geometric parameters. The components of the spatial baseline specified either by the antenna configuration or by the track geometry and the length of the temporal baseline of especially repeat-pass InSAR image pairs are the most important parameters.

The temporal baseline affects the level of coherence between the two SAR images. Focusing on buildings, their stability leads to good coherence values in areas of direct backscattering (e.g. from façades and roof) and of multi-bounce scattering at building structures alone. The continuous growth of vegetation and other changes in the building neighbourhood (e.g. parking lots) lead to a decorrelation of their direct backscattering and multi-bounce scattering between them and buildings (e.g. corner reflector). Nevertheless, this decorrelation of phases can also happen to the layover signature of buildings due to the superposition of direct backscatterer of ground, façade, and roof. As a rule of thumb, for buildings as well as for all other objects it can be stated that the shorter the temporal baseline, the better the quality of the interferometric phase.
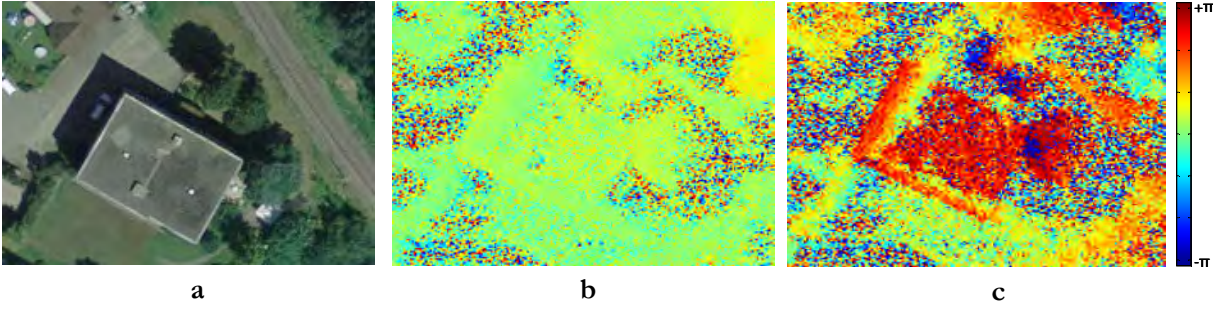
**Figure 3.4:** Influence of sensor baseline: example Hinwil (Switzerland) given in optical (a, screenshot from map.geo.admin.ch, ©swisstopo), 2 cm baseline (b), and 14 cm baseline InSAR data (c)

The spatial baseline of InSAR configurations can be separated into along and across track components. As mentioned in Subsection 2.1.4, the across track component is crucial for the interferometric phase signature of buildings. Equations (2-13) and (2-14) define the unambiguous range based on the length of the baseline and some local parameters. This is characterised by the maximal height difference clearly detectable in the phase data without requiring phase unwrapping. The change in the unambiguous range is observable for the building shown in Fig. 3.4. For the smallest baseline of the MEMPHIS configuration with a length of 2 cm (Fig. 3.4b) an unambiguous range of approx. 190 m is achieved, while the unambiguous range drops to 27 m for the longest baseline of 14 cm (Fig. 3.4c). The previously described front porch slope in the layover region of the building (c - colour transition from red to yellow to light green) is more visible in the long baseline than in the short baseline example due to the difference in the unambiguous range. Beyond this effect, a longer across-track baseline leads to a lower interferometric height error. Assuming that the phase noise is the crucial factor, the standard deviation $\sigma_h$ of these heights can be determined by propagation of error, such as deduced in [115]:

$$\sigma_h \approx \frac{1}{p} \cdot \frac{\lambda \cdot r \cdot \sin\theta}{2\pi \cdot B_\perp} \cdot \sigma_\varphi \tag{3-2}$$

where $\sigma_\varphi$ is the standard deviation of phases considering an interferogram of distributed scatterers [70]. Furthermore, the local $\sigma_h$ is a function of range distance $r$ and off-nadir look angle $\theta$ as well as perpendicular baseline $B_\perp$. Hence, with constant $\theta$ and flat terrain, a better $\sigma_h$ is obtainable by shorter $r$ and larger $B_\perp$. The first is limited by the sensor platform, but airborne configurations enable a height accuracy that is better by one order of magnitude compared to SAR satellites [115]. An unlimited increase of the latter is also not possible due to two reasons: the critical baseline $B_c$ and physical or technical conditions. In detail, $B_c$ donates the baseline, where the interferometric coherence $\gamma$ between the two SAR signals gets lost and the resulting interferometric phases are random. The perpendicular proportion $B_{c\perp}$ such as shown in [88] is defined by:

$$B_{c\perp} = B_c \cdot \cos(\theta - \xi) = \frac{r \cdot \lambda \cdot \tan\theta}{p \cdot \delta_{rs}}, \quad \text{with} \quad r = \frac{(H - h)}{\cos\theta}. \tag{3-3}$$

where $H$, $h$, and $\delta_{rs}$ are the height of sensor over ground, the height of the object, and the spatial resolution in slant range direction. The chosen baseline has to be a good compromise between necessary height accuracy and feasible baseline length. Nevertheless, with a bigger unambiguous range

$\Delta h$ the standard deviation $\sigma_h$ increases, too, because $\Delta\varphi$ as well as $\sigma_\varphi$ are scaled in the same way. Furthermore, phase unwrapping has to be considered for longer baselines.

### 3.2.2    SAR Processing Parameters

Besides sensor parameters, the signature of buildings in InSAR data is also characterised by processing parameters, whereby a precise distinction of effects is sometimes impossible. In the following, the impact of using different windowing functions and the relation between data resolution, sampling rate, and pixel spacing are described.

### Windowing (Apodization Function)

The richness of details visible in SAR building signatures depends on geometric and radiometric data resolution as well as on the applied apodization function. As described in Subsection 2.1.3, the IRF of a single point target is characterised, amongst others, by the suppression of the first side lobe, the ongoing side lobe fall-off per octave, and above all by the 3 dB width $k$ of the main lobe. Furthermore, the detectability of two close-by targets is a very important parameter also determined by the chosen windowing as presented in [62] comparing the most common choices of windowing functions.

In general, the reduction of side lobes in range and azimuth direction is required in order to facilitate image interpretation. However, it leads to a degradation of image resolution (i.e., a trade-off between sharpness and low side lobes). Some signatures resulting after applying different windowing functions on synthetic SAR images are presented in [94] by considering symmetric as well as asymmetric weighting in range and azimuth.

Focusing on the SAR data used in this thesis, different filter windows are considered in the data processing. Similar weighting schemes on range and azimuth spectra were applied to MEMPHIS and TerraSAR-X data. For the first, a Kaiser window with a coefficient $\nu = 2.12$ was used and for the second, a Hamming window with coefficient $\nu = 0.6$ was applied [19]. The AeS-1 data are processed by applying different windowing functions, in azimuth a Hamming with coefficient $\nu = 0.54$ and in range a Hamming with coefficient $\nu = 1$, i.e. a uniform weighting or rectangular window.

The SAR signature of an industrial building recorded by MEMPHIS and TerraSAR-X is given in Fig. 3.3. The used filter windows show similar values for $k$ leading to the same level of resolution loss of the SAR image. Such a main lobe widening gives rise to broadening and blurring effects at building corners and it also hampers the separation of close-by structures (e.g. layover region). This has to be taken into account later, when the detection of double lines is investigated (Section 4.6). Moreover, the suppression of the first side lobe is stronger if a Hamming window is applied, but the side lobe decay per octave is higher for the Kaiser window. Hence, strong scatterers show a more star-shaped signature in the MEMPHIS data. The Hamming weighting applied to the AeS-1 data leads to a strong suppression in azimuth, in contrast to the uniform weighting applied in range. This asymmetric signature is observable in Fig. 3.7f.
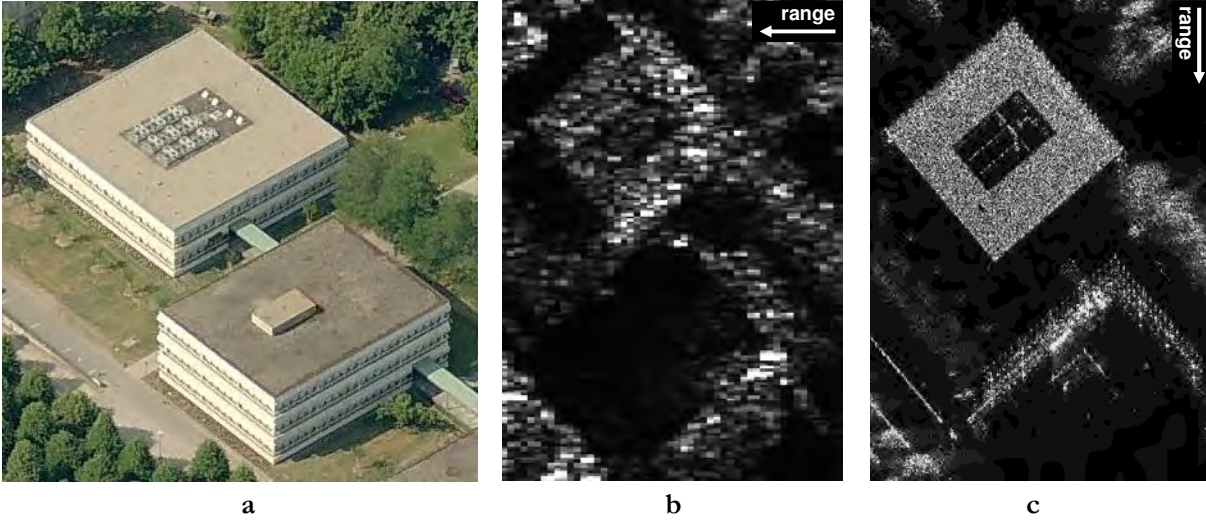
**Figure 3.5:** Influence of sensor resolution: example Karlsruhe (Germany) given in optical (a, screenshot from bing, ©2011 Microsoft Corporation), 1 m resolution (b – STAR-3i), and 0.1 m resolution data (c – PAMIR)

In addition to the visible effects on building signatures, which have to be considered in image interpretation and object detection (Section 4.6), the resolutions $\delta_a$ and $\delta_r$ depend on the apodization functions. For instance, the theoretically highest range resolution of TerraSAR-X (single polarisation and 150 MHz bandwidth) is 0.89 m, if no weighting is utilised. In practice, both the range and the azimuth spectrum are filtered using the mentioned Hamming window, resulting in a worsened range resolution of 1.2 m [50]. Since object analysis and detection are carried out in image data, not only the resolution but also the pixel size is of interest; their relation is described in the following.

### Sensor Resolution and Pixel Spacing

The signature of buildings and especially the level of detail depend on the SAR data resolutions $\delta_a$ and $\delta_r$, which are defined by the equations (2-8). The resolution cell size is determined by the length of the real aperture $L_{ra}$, the system bandwidth $BW$, and the 3 dB width $k_a$ and $k_r$ of the azimuth and range filter windows. In Fig. 3.3 and Fig. 3.5, image pairs acquired by SAR sensors of different resolutions are given. In detail, MEMPHIS data [89] of approx. 0.20 m ($BW = 800\,\text{MHz}, k_{a,r,\text{Kaiser}} \approx 1.0$) and TerraSAR-X data [19] of approx. 0.6 m in range and approx. 1.1 m in azimuth ($BW = 300\,\text{MHz}, k_{a,r,\text{Hamm}} \approx 1.2$) are presented in the first figure. The level of detail visible in the MEMPHIS data is much higher than in the TerraSAR-X data because of various sensor parameters (e.g. frequency, operational height, and look angle). In the second figure, airborne X-band data of STAR-3i [85] with resolutions up to 1.25 m ($BW = 135\,\text{MHz}$) are compared to PAMIR [21] with a resolution better than 10 cm ($BW = 1.8\,\text{GHz}$). This tenfold finer spatial resolution is especially observable in the detailed structuring of layover and roof areas, where point patterns resulting from building façades are detectable. Differences due to various viewing directions are minimised, since similar façade structures are given around the two buildings. In both data sets the remarkable magnitude offset between the two roof areas resulting from different materials is visible.

For applying image interpretation methods to SAR data, the SAR signal conversion from analogue to digital signal is required to finally receive an image representation in the form of a pixel matrix. This is realised by sampling of an analogue signal and taking into account the Nyquist criterion. This implies that for a lossless digitalisation and for avoiding aliasing effects, the sampling frequency has to be higher than the signal bandwidth $BW$. For most SAR data processors, this requires signal oversampling leading to a correlation between neighbouring image pixels [61]. Hence, the image pixel spacing $\Delta$ does not match the SAR data resolution $\delta_a$ and $\delta_r$ [101]. To give an example, the high resolution spotlight data of TerraSAR-X have resolutions of $\delta_a = 1.1\,\text{m}$ and $\delta_r = 0.6\,\text{m}$ and pixel spacing of $\Delta_a = 0.87\,\text{m}$ and $\Delta_r = 0.45\,\text{m}$.

The described relations between sensor resolution, apodization function, sampling rate, resulting pixel spacing, and the accompanying variations in the building appearance have to be taken into account, since image analysis by means of pixel based operations is applied such as object segmentation (e.g. Section 4.4), image based measurements (e.g. Section 4.6), and image correlation (e.g. Section 4.11).

## 3.3 Influence of Building Geometry

In addition to sensor and processing parameters, the building appearance is mainly determined by the individual 3D shape and by orientation and position of the building. Furthermore, building material, façade and roof structures affect the signature significantly also. In the following, these effects are discussed and image examples are shown pointing out the high complexity of building signatures in InSAR data due to these parameters.

### 3.3.1 3D Shape

The variation of the building signature due to 3D shape can be described as a function of three parameters - length, width, and height of the building. First, effects on the magnitude and interferometric phase signature caused by increasing building height are discussed. Second, we focus on the relation between building width and height. As third, the appearance of different roof types is taken into account; especially changes due to gable-roof variations are investigated.

### Building Height

The effect of increasing building height on the magnitude and interferometric phase signature of an isolated building is schematically shown in Fig. 3.6. Four different height levels $h_i$ are considered for this analysis. The expected magnitude profiles in slant range geometry are indicated with the marked layover $l_i$ and shadow $s_i$ in Fig. 3.6a. The length of the layover area in the slant and ground range geometry is given by:

$$l_{\text{slant}} = h \cdot \cos\theta \qquad \text{and} \qquad l_{\text{ground}} = h \cdot \cot\theta \tag{3-4}$$

Additionally, the length of the radar shadow in slant and ground range geometry is also a function of object height $h$ and off-nadir look angle $\theta$.
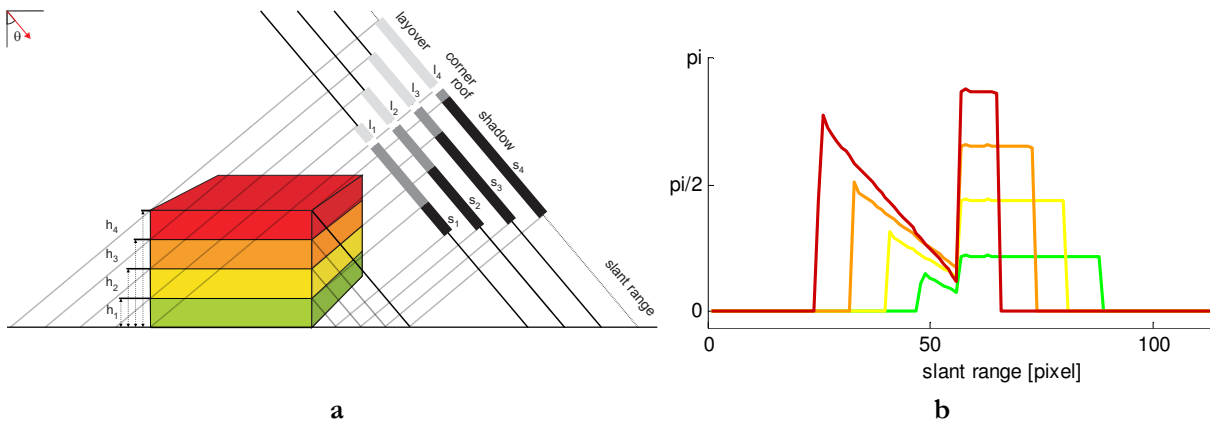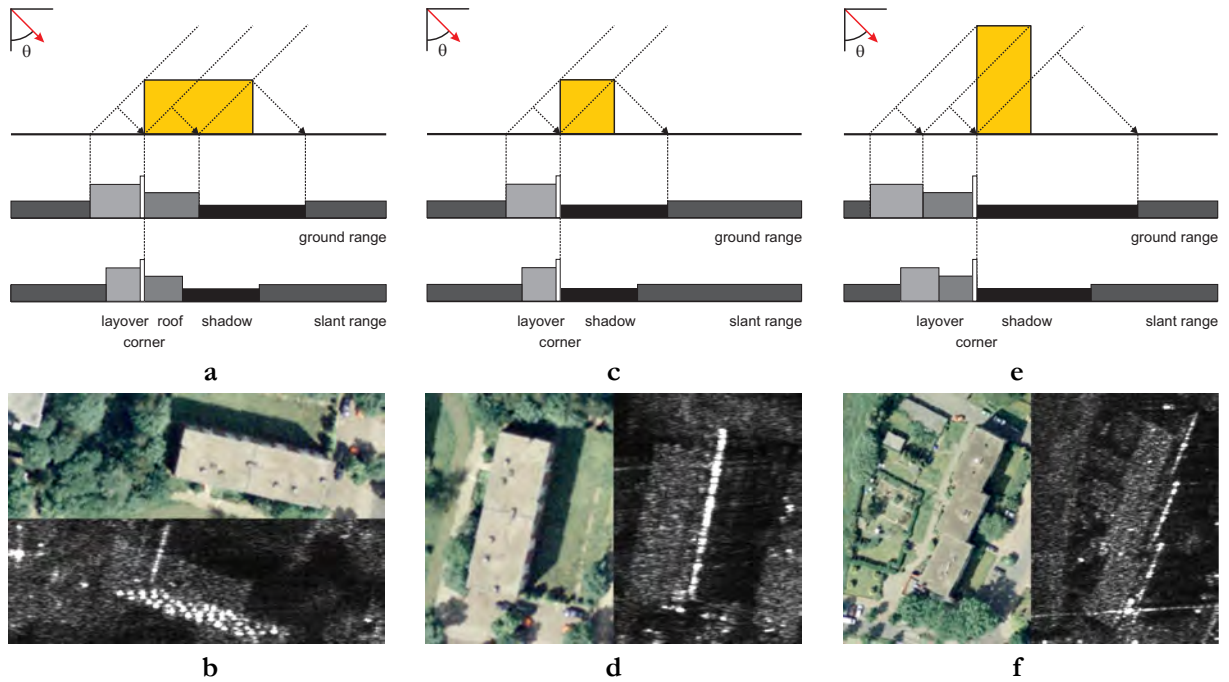
**Figure 3.6:** Influence of building height: schematic view of varying SAR magnitude signature (a) and simulation results of InSAR phase signature (b) by increasing building height

$$s_{slant} = \frac{h}{\cos\theta} \qquad \text{and} \qquad s_{ground} = \frac{h}{\sin\theta \cdot \cos\theta} \qquad\qquad (3\text{-}5)$$

If we consider a constant off-nadir look angle $\theta$, larger building height $h_i$ gives rise to increasing layover and shadow areas. This is accompanied by less single roof backscattering clearly observable in Fig. 3.6a. The single roof backscattering would disappear with further increasing building height. The corner appears for all four models at the same position, because the distances between sensor and building base point are identical. In real SAR magnitude data, the corner would show higher intensity values with growing building height due to larger planes (wall and ground) spanning up the right-angled structure. Overall, the extent of the building signature in the magnitude image increases radically. This conclusion is important for building reconstruction in urban and dense urban areas, where interaction effects between neighbouring buildings could be possible (Subsection 3.3.2).

The interferometric phase signature (Fig. 3.6b) is also affected by a rising building height. The coloured profiles show simulated interferometric phases corresponding to the models $h_i$ of Fig. 3.6a. Just as magnitude values, every interferometric phase value of a single range cell results from the mixture of signals of all contributors. Hence, the InSAR phase is proportional to the contributor heights. Moreover, the InSAR height can be interpreted as a function of heights from all objects contributing to the particular range cell. Consequently, in the layover area heights from terrain, building wall, and roof contribute to the final InSAR height. In detail, the shapes of the given InSAR phase profiles are characterised by a maximum value at the beginning of the layover area followed by a downwards oriented ramp. This is caused by the contribution mixture, whereby ground and roof deliver constant heights, whereas the building wall height values decreases. The lowest point in the InSAR phase profiles corresponds with the corner position in the magnitude data. This phase value is defined by nearly zero height values of ground and building walls and by the roof height. In real InSAR data, this minimum value is almost equal to local terrain phases, since strong double bounce between ground and wall marginalises the other contributions resulting in further pull-down on terrain-level. Behind the minimum position, the single response of the building roof leads to a constant trend in the phase profile. The subsequent shadow region shows a value of zero

**Figure 3.7:**  Influence of ratio building width to building height: schematic view and real SAR magnitude signature of ratio 2:1 (a,b), ratio 1:1 (c,d), and ratio 1:2 (e,f)

in the simulations, because no signal is received for this area. In real InSAR data, this area is only characterised by noise.

Summarising this effect, the overall signature of a building is increasing with rising height. The utilisation of the full signature is not advisable, because in suburban and urban areas overlapping effects due to near-by trees and other buildings are very common. Moreover, the layover, roof, and shadow area will appear not as homogeneous in real SAR data making their extraction more difficult. In comparison, the corner shows stability in most cases, which will be further emphasised in the next subsections.
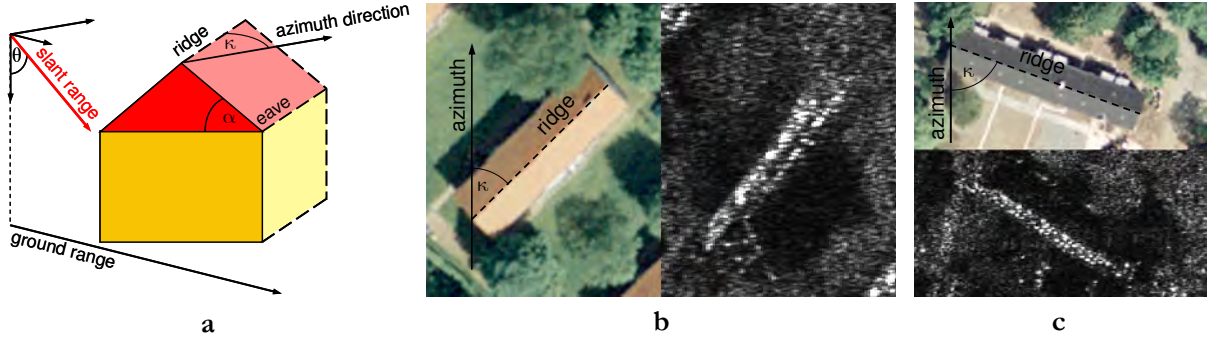
**Building Width-to-Height Ratio**

The relation of building width to building height is described in the schematic view and the real SAR magnitude of Fig. 3.7. The sketches visualise three building hypotheses showing width-to-height ratios of 2:1, 1:1, and 1:2 illuminated at an off-nadir look angle $\theta$ of 45 degrees. All three real building signatures are acquired by the same SAR sensor with nearly identical $\theta$.

An example of a low-rise building (e.g. industrial buildings) is visualised in the first column (Fig. 3.7a,b). For a width-to-height ratio of 2:1, all parts discussed in the previous sections – layover, corner, roof, and shadow – of the building signature appear in the image clearly. The bright point pattern in the lower part of the real SAR signature results from multi-bounce scattering on the building façade. An additional corner at this building side is not observable due to poor ray intersection geometry and façade structures. For smaller buildings or buildings with a ratio of 1:1, such as often given in residential areas, the signature looks different. As presented in Fig. 3.7c,d, the layover and corner of the building signature are still observable in contrast to the isolated part
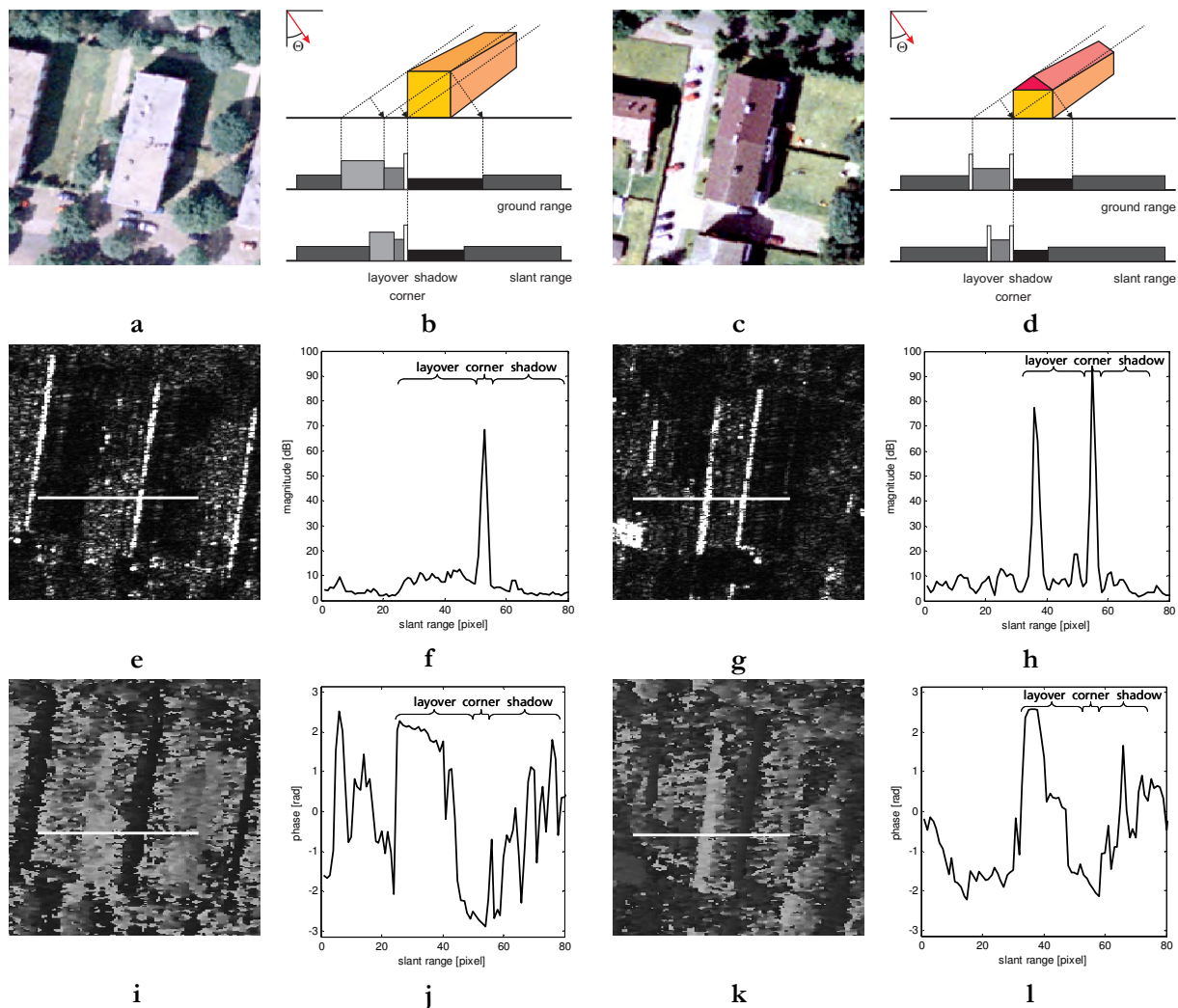
**Figure 3.8:** Influence of the building roof type: a flat-roofed building - optical signature (a), schematic view of SAR phenomena (b), real InSAR magnitude (e) and phase (i) signature and corresponding range profiles (f,j); a gable-roofed building – optical (c) and schematic magnitude (d) signature and real InSAR signature (g,k) with corresponding profiles (h,l)

of the direct backscattering of the roof. This is caused by the decreased building width leading to a full mixture of roof signal with signal of wall and ground in front of the building. Building corner and building shadow are clearly visible in this case. The third set-up is tailored for narrow buildings, which are much higher than wide (e.g. skyscraper). The signature in Fig. 3.7e,f shows the differences to the standard case a,b. The layover occurs subdivided into two parts, with a brighter one caused by summing up of the contributions ground, wall, and roof and a darker part resulting from ground and wall contribution only. In the real SAR data, the stepped building shows three parallel short corner lines in accordance with the building edges in the optical image. The variation of the magnitude values along the corner lines result from heterogeneous façade structures. With rising range the next feature is the radar shadow, whose length is reduced by the amount of the darker layover part.

**Figure 3.9:** Influence of span angle $\kappa$: schematic view (a), increasing span angle from 45° (b) up to 70° (c)

Summarising these three width-to-height constellations, differences are observable for layover, roof, and shadow part of the building signature. The corner line is the only invariant feature.

## Building Roof Type

In addition to the building size, the roof type significantly affects the building signature. In Fig. 3.8, the appearance of flat-roofed and gable-roofed buildings is shown. Comparing first the schematic view of SAR phenomena (Fig. 3.8b,d), a subdivision of the layover area occurs at both building examples. At gable-roofed buildings, this effect is caused by backscattering of the tilted roof planes. For the given example, the strong compression of backscatter from the roof plane facing the sensor to only a few or even a single pixel in range direction leads to the line structure in the layover area. The following darker part results from the superposition of backscatter from ground and façade only. Subsequent to the layover area, a bright line appears in the flat- and gable-roofed signature (Fig. 3.8e,g) caused by the dihedral corner reflector spanned by ground and building wall. Hence, a *double line* signature in the image and two peaks in the range profile (Fig. 3.8h) are observable for the gable-roofed building. Single backscatter signals of gabled roofs only become visible for relatively wide buildings with small pitch angles. In Fig. 3.8e,g, no single roof area is visible for both examples since the building width is too small. A shadow area directly next to the corner appears for both of them.

Similar to magnitude signatures, the interferometric phase signatures of flat- and gable-roofed buildings show interesting differences, too. The interferometric phase images and corresponding slant range profiles are given in Fig. 3.8i,k and j,l. The layover region is characterised by a downward slope in range and a constant trend along building orientation. The slope of flat- and gable-roofed buildings is caused by two constant (ground and roof) and one varying (wall) height contributors or one constant (ground) and two varying (roof and wall) contributions, respectively. The layover pixel closest to the sensor has the highest phase value in the layover area since backscatter signals of wall and roof are prevalent. For flat-roofed buildings, this phase value corresponds roughly to the building height. This is not assignable to gable-roofed building, which will be discussed in Subsection 4.8.2.

Depending on the building width, a flat roof phase profile has a constant gradient in the layover part or a weaker gradient at the beginning of the ramp than at the end (e.g. Fig. 3.8j). The minimum of the profile corresponds to the corner position in the magnitude profile because the sum of the
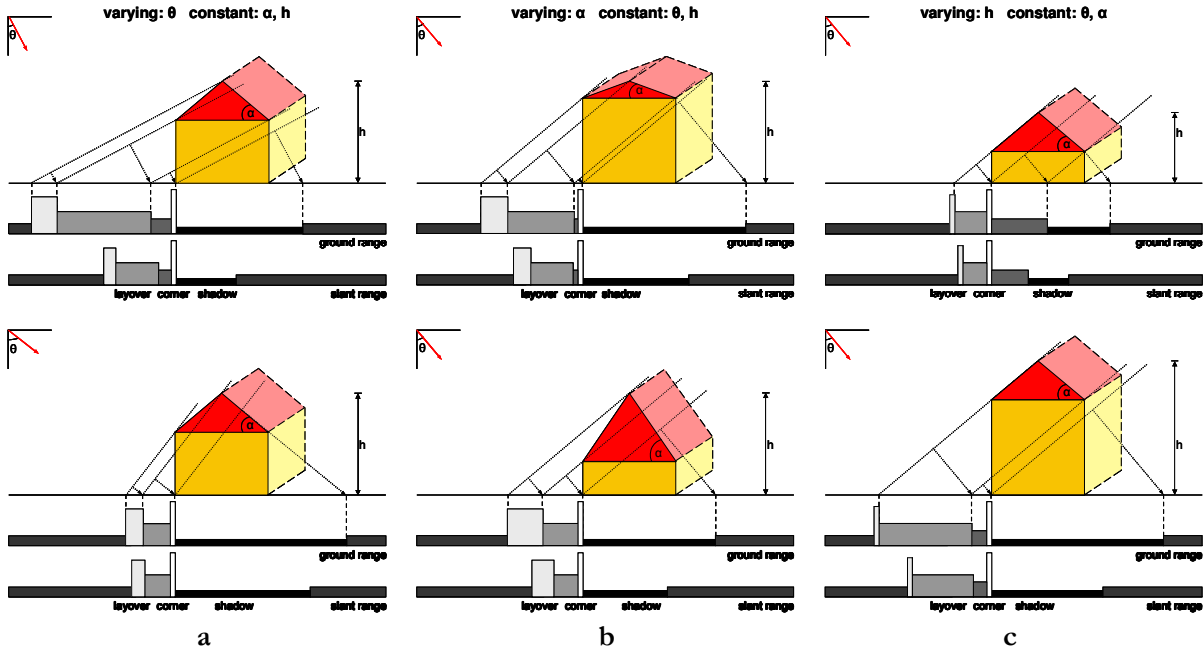
**Figure 3.10:** Influence of three different illumination and object parameters: schematic views of varying off-nadir look angle $\theta$ from close-range to far-range positions (a), of varying roof pitch angle $\alpha$ from flat to steep roofs, and of varying building height h from low to high buildings (c)

double-bounce reflections between ground and wall has the same signal runtime as a direct reflection at the building corner point. In average, phase values at this position are equivalent to the local terrain height. A constant trend in the phase profiles due to single response of the building roof is not visible in Fig. 3.8j because of the too narrow width. The phase values in the subsequent shadow region are random since no suitable signal is received.

The phase profile of the gabled roof (Fig. 3.8l) shows the same sequence – layover, corner, and shadow. The stepwise shape in the layover results from different groups of contributors, the building roof adds to the first part (high phase values), but not to the second (low phase values). In the magnitude profile, the first part corresponds to the bright line closer to the sensor that is caused by direct backscattering of the pitched roof plane and the second part to the dark area between the parallel lines. As with the flat roof profile, also the corner position of the gable-roofed building is characterised by a phase value proportional to local terrain height, and the shadow phases are randomly distributed. The remarkable signature of gable-roofed buildings is of course subject to viewing parameters, which is specified in the following paragraphs.

The occurrence of the *double line* signature of gable-roofed buildings depends on the geometric constellation of azimuth direction to local ridge orientation described by the span angle $\kappa$ visualised in Fig. 3.9a. A parallel alignment $(\kappa = 0)$ is the most favourable case to achieve well-separated double lines. With increasing $\kappa$, a widening of the layover line, a shortening of the distance between the two lines, and a decreasing intensity of the corner line is observable (Fig. 3.9b). The gable roof signature resembles more and more that of a flat-roofed building (Fig. 3.9c). This becomes clear considering the extreme case, the orthogonal configuration $(\kappa = 90)$. Then, the roof height in a single range line is approximately constant. The same applies to interferometric phases. If the building is

not completely oriented in range direction, the single response of the building roof starts at high level and shows a weak trend downwards. With a ridge orientated precisely in range direction of the sensor, the phase profile will show a constant trend, such as for the flat-roofed building.

In addition, the perceptibility of the parallel line signature depends on sensor and building parameters, for example, off-nadir look angle $\theta$, pitch angle $\alpha$, and building height $h$. In Fig. 3.10, double line signatures achieved by different parameter configurations are visualised considering parallel alignment $(\kappa = 0)$. The columns show changes caused by $\theta$ (a), $\alpha$ (b), and building height $h$ (c).

The analysis focuses first on the sensor-close magnitude maximum. Assuming Lambertian reflection, this feature appears as a bright area of different width. A larger difference between the angles $\theta$ and $\alpha$ results in a wider projection of the roof plane. This coincides with diminished brightness, because the roof signal is spread out over a larger area. Specular reflection results in case of illumination in the normal direction of the roof plane $(\alpha = \theta)$. Consequently, the entire signal is imaged into a thin line; the brightest signal appears (Fig. 3.10c). The second magnitude maximum, the corner line, is always located at the position of the building footprint. As the position of the sensor-close maximum depends on $\theta$, $\alpha$ and $h$, the distance between both maxima is a function of these parameters. Decreasing distance is caused by increasing $\theta$ (a) and $\alpha$ (b) as well as decreasing $h$ (c).

Summarising this section, it can be stated that the most stable and dominant feature of InSAR building signatures are the corner lines, while geometric information of a building is mainly contained in its layover region. Especially the analysis of magnitude and phase profiles of non-flat-roofed buildings seems to be useful and is considered in the Subsections 4.6.2 and 4.11.1.

### 3.3.2    Position and Orientation

In this subsection, effects due to changes in the relative position of sensor and object are discussed, caused for example by varying look angles and different viewing aspects. Additionally, the interaction effects between close-by objects such as neighbouring buildings are described.

### Building Position

Signature variations due to different distances between sensor and object or due to different look angles are similar to effects caused by various width to height ratios (Subsection 3.3.1). The schematic magnitude signature of a building imaged from three different off-nadir look angles is given in the first row of Fig. 3.11. For a small look angle or for a building in near range (a), the subdivision in the layover area is observable due to the various groups of contributors – ground/wall/roof and ground/wall. A middle range look angle (b) leads to homogenous layover and subsequent shadow areas for this building. Single backscatter signals of building roof appear only for the example of large look angle (c). The building corner is observable in all three examples and again constitutes the most stable feature.

In addition to the schematic view, three simulated SAR signatures are shown containing the same variation of sensor illumination. The purpose of this simulation is not to model the entire SAR processing incorporating object features; the focus is rather on the discussion of the impact of geometric features. This allows simplifying the simulation by assuming Lambertian backscattering
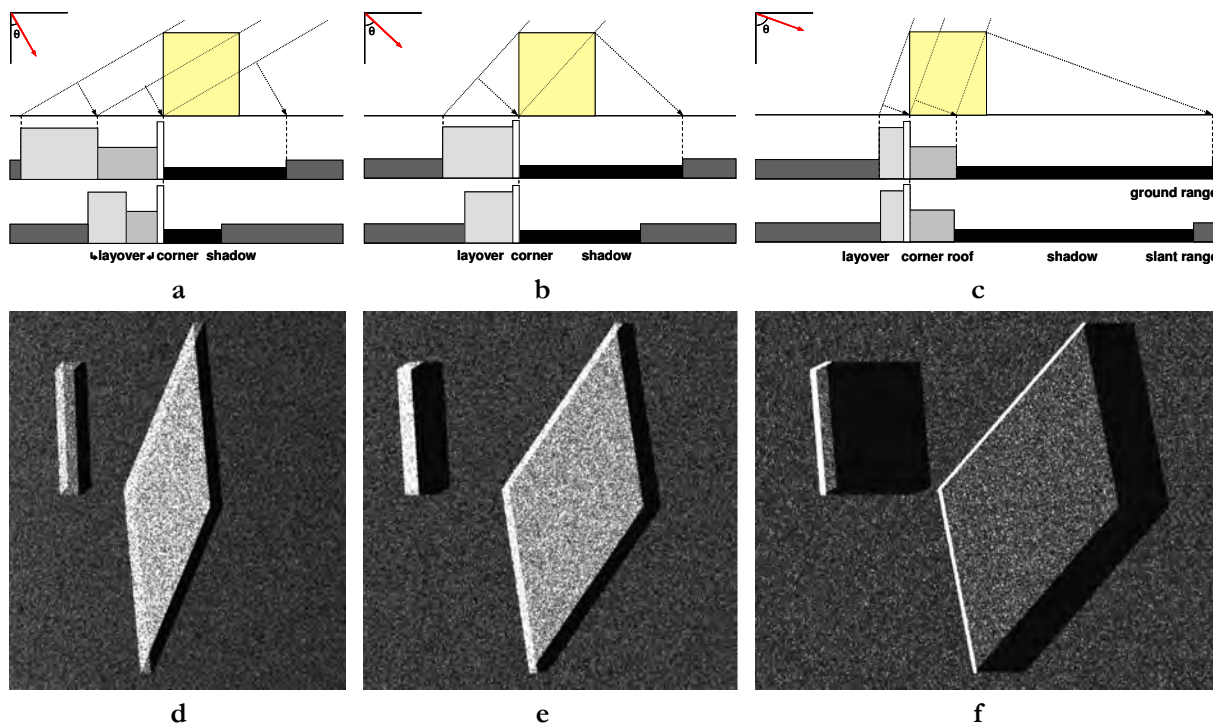
**Figure 3.11:** Influence of off-nadir look angle and building position: schematic views of varying look angles and close-range, middle-range and far-range position (a,b,c), corresponding SAR magnitude simulation results (d,e,f) for a small and a large building

properties only. For this, the basic version of the software SAR-View [112] was used. The small building shows the mentioned states of change in the signature with increasing off-nadir look angle $\theta$ – from a subdivided layover to a homogenous layover to a fully developed layover and roof area. In contrast, the signatures of the large building do not feature these variations; fully developed layover and roof areas are visible in all cases. With rising $\theta$, the brightness of the roof area falls off due to a larger local incidence angle at the roof plane. The increase of the shadow length in range direction is observable for the small as well as for the large building example. Moreover, the overall length of the building signature increases, which is especially relevant in dense urban area.

## Building Orientation

Due to the side-looking geometry, the off-nadir look angle, the viewing direction and the building orientation have a strong impact on the appearance of the building in the SAR data. Depending on the SAR sensor system considered, these parameters are more or less variable. The majority of the SAR satellites is fixed to right or left look direction limiting the choice to ascending or descending orbit. Furthermore, the crossing angle of these orbits is limited; it is defined by the satellite specific inclination and the geographic latitude of the scene. The expected variations in the building signature are shown in Fig. 3.12b,c for the example of an image pair of TerraSAR-X imaging part of Frankfurt airport. The viewing directions of both aspects are visualised in yellow and red on an optical image (Fig. 3.12a). In the $a_1$ signature recorded from ascending orbit (Fig. 3.12b), a fully developed layover is given, characterised by pointwise façade scattering, the subsequent corner line, the roof part, and a shadow area. The flight direction of the satellite and the building main axis are
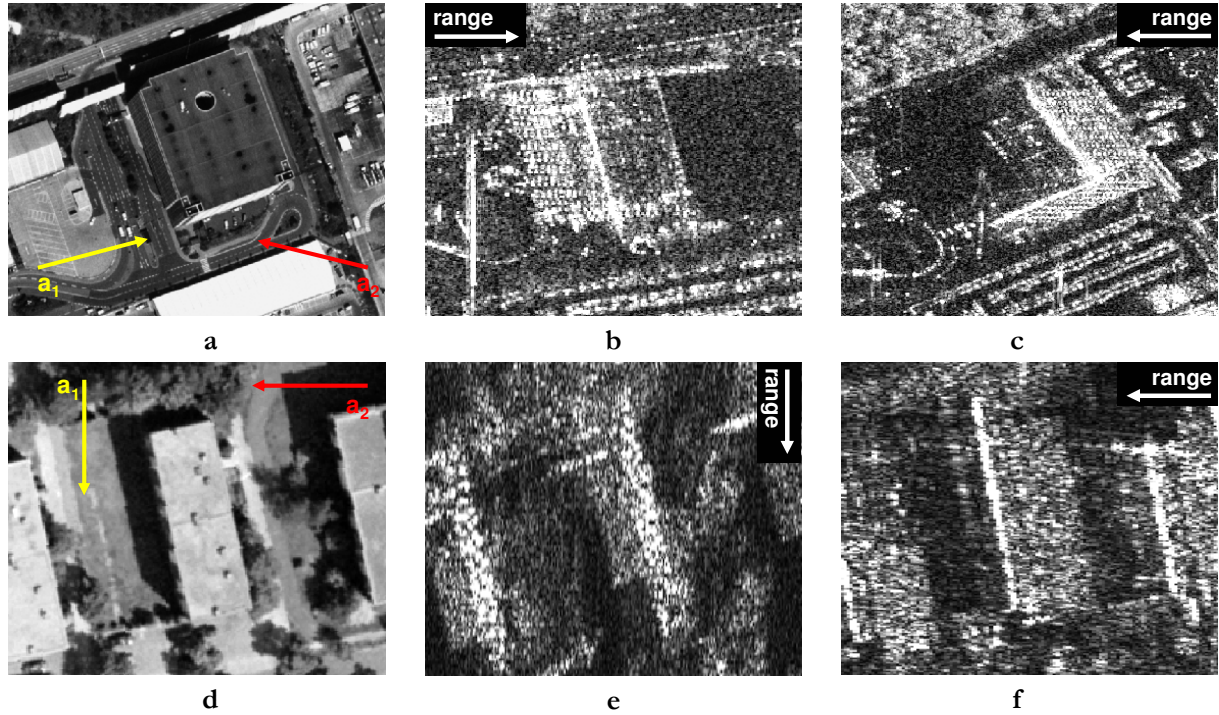
**Figure 3.12:** Influence of viewing direction and building orientation: optical signature of buildings (a,d) with marked aspect 1 (yellow) and 2 (red), SAR magnitude signature under aspect 1 (b,e) and aspect 2 (c,f)

nearly parallel. Hence, only the façade facing towards the sensor is illuminated and seen in the image. The signature $a_2$ (Fig. 3.12c) of the building contains the same regular scatter points in the layover area caused by regular structures at the building façades. Two building corners forming a mirrored L are visible in this amplitude signature, which is due to a greater heading angle between sensor flight direction and building orientation. The brighter spots on the roof signature are related to superstructures on the building top. Neighbouring objects such as other buildings and vegetation do not affect the SAR signature of this building, as it is the largest.

In most cases, the use of an airborne SAR system enables more flexibility by optimising flight height and flight direction according to a given purpose. An airborne multi-aspect building signature achieved by an orthogonal flight configuration is given in Fig. 3.12d,e,f. Since airborne configurations provide better geometric resolutions, the recognition and analysis of smaller objects becomes possible. The given long but thin building appears very different in the two amplitude signatures (Fig. 3.12e,f). First the L-shaped layover area and one corner line in $a_1$, and second a straight layover and corner line in $a_2$ are visible. In contrast to the first building example, the analysis of this multi-aspect signature is more complicated, because nearby trees and the chosen aspect angle hamper the recognition of all standard phenomena. This refers especially to the lack of a second corner line at the short building side in the $a_2$ data. A single backscatter part of the building roof appears only in $a_1$. In the case of $a_2$, the entire signal of the roof is obscured by layover. Moreover, the distinction between building signature and surroundings is more difficult for this building since close-by buildings and trees lead to signal superposition. This is observable for the shadow and layover part.
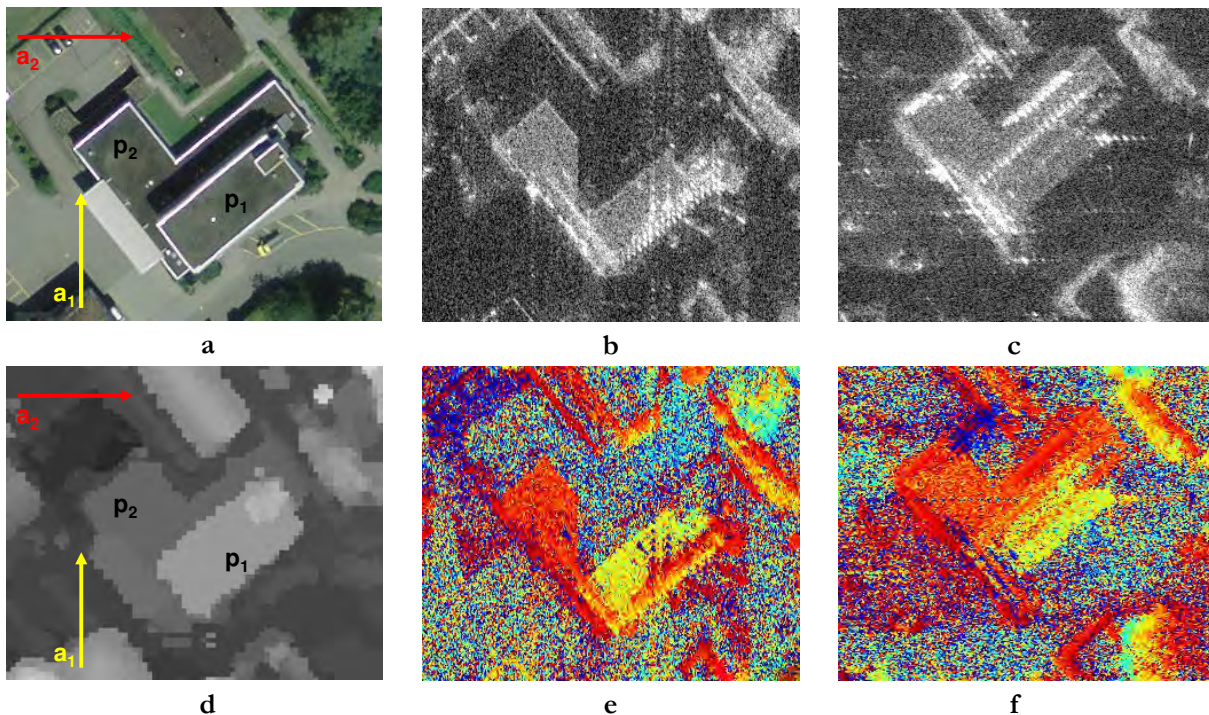
**Figure 3.13:** Multi-aspect InSAR signature of complex buildings: optical signature of a stepped building (a, screenshot from map.geo.admin.ch, ©swisstopo) with marked aspect 1 (yellow) and 2 (red), SAR magnitude signature under aspect 1 (b) and aspect 2 (c); LIDAR signature (d); corresponding InSAR phase signatures of building (e,f)

The phase signature of buildings is subject to similar changes. For more complex buildings, the interpretation of the magnitude and phase signature is more difficult. This is visualised for a stepped building in Fig. 3.13, where superposition effects between superstructures appear. The given airborne SAR data of the MEMPHIS sensor are recorded at 94 GHz frequency in an orthogonal flight configuration with a resolution of approx. 20 cm. Focusing first on signature $a_1$ (Fig. 3.13b,e), the higher building part $p_1$ shows a bright layover area in the magnitude data interspersed by regular façade scatterers and a front porch slope in the phase data. Due to the large off-nadir look angle, a long shadow appears. Hence, occlusion of the lower building part $p_2$ is observable in the magnitude (b) as well as in the phase signature (e). The signature of part $p_2$ is characterised by a very thin layover area, a wide homogenous roof, and a remarkable shadow extent. In the lower part of the magnitude signature two parallel bright lines are observable resulting from the signal superposition of building part $p_2$ and the short side of part $p_1$. The layover areas at the long and at the short side of $p_1$ occur different in width and lowest phase value since the relative height steps are different. The $a_2$ InSAR signature of the building bears more similarity to the optical (a) and the LIDAR signature (d) thus making the interpretation easier. The layover at the long side of $p_1$ is thinner than in $a_1$ due to the subjacent building part $p_2$. Furthermore, the signatures of $p_1$ and $p_2$ are not affected by shadow. This leads to a homogenous L-shaped roof area in the magnitude image (Fig. 3.13c). In the phase data (Fig. 3.13f) the two different height levels ($p_1$ - yellow, $p_2$ - red) are clearly recognisable.

These multi-aspect examples once more make clear the high variability of building signatures. The final selection of the most reliable features is given in the next section.
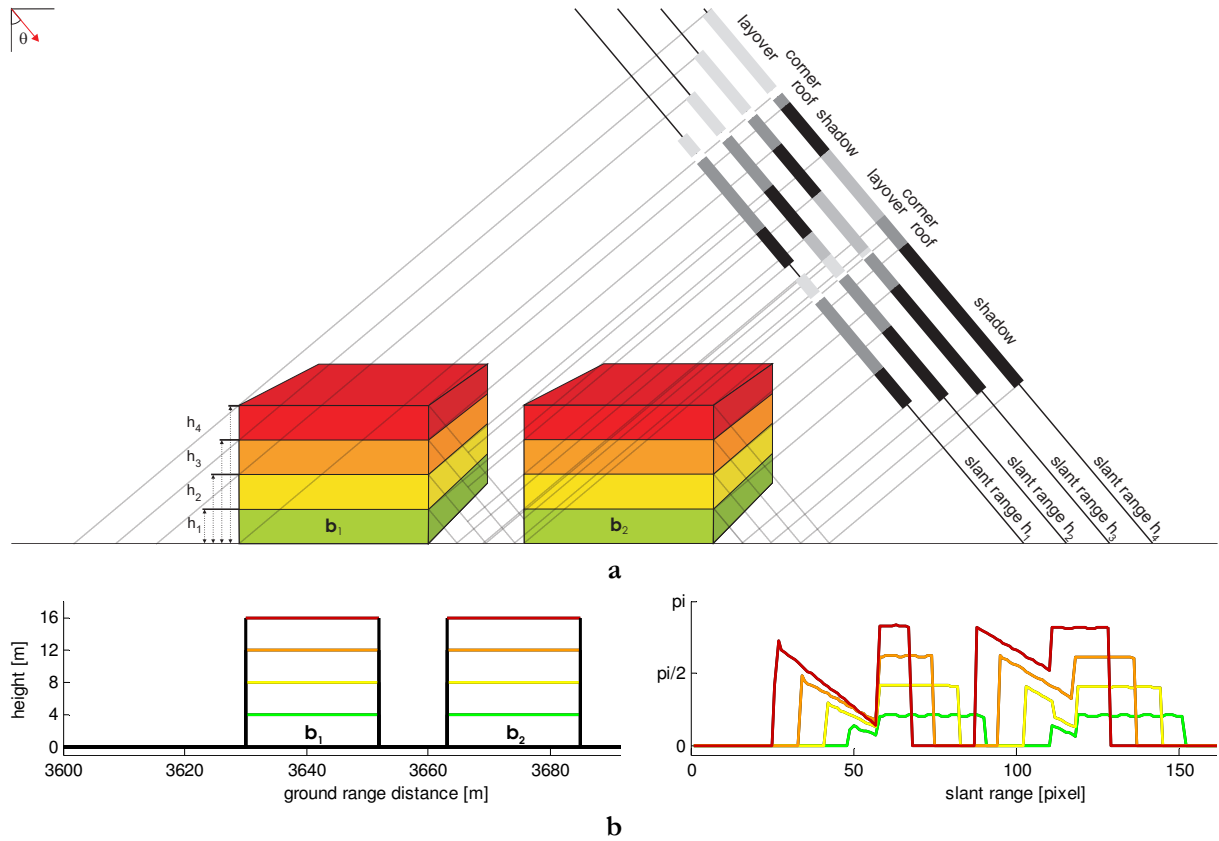
**Figure 3.14:** Influence of building height in case of neighbouring objects: schematic view of varying SAR magnitude signature (a) and DSM profiles with corresponding simulation results of InSAR phase signature (b) by increasing building height

## Building Neighbourhood

In addition to the sensor flight parameters and the building orientation, effects caused by neighbouring or nearby buildings are also of interest. As mentioned in Subsection 3.3.1, for rising height larger layover and shadow areas are observable. When buildings interfere, the layover part of the first building is increasing in contrast to its shadow part. Vice versa, this is visible for the second building. This is shown in the simple example of Fig. 3.14 considering two similar buildings $b_1$ and $b_2$ with a small distance between each other. Four slant range profiles resulting from different height assumptions are visualised.

In the lowest constellation $h_1$ (green in Fig. 3.14a), the buildings do not affect each other leading to classical SAR magnitude signatures - layover, corner, roof, and shadow. Starting with the height assumption $h_2$, coloured yellow, the expected interaction effects between the buildings occur. This is noticeable on the shortening of the $b_1$ shadow and on the subdivision of the $b_2$ layover. Those effects become even more pronounced with rising building height. Beyond the length and the amplitude of the $b_2$ layover, also the brightness of the building corner line is decreasing due to a smaller effective dihedral area between ground and wall. The worst case is shown in red in the example, where double-bounce scattering between ground and wall can no longer appear. Consequently, no corner is observable for $b_2$. With increasing heights and height differences between
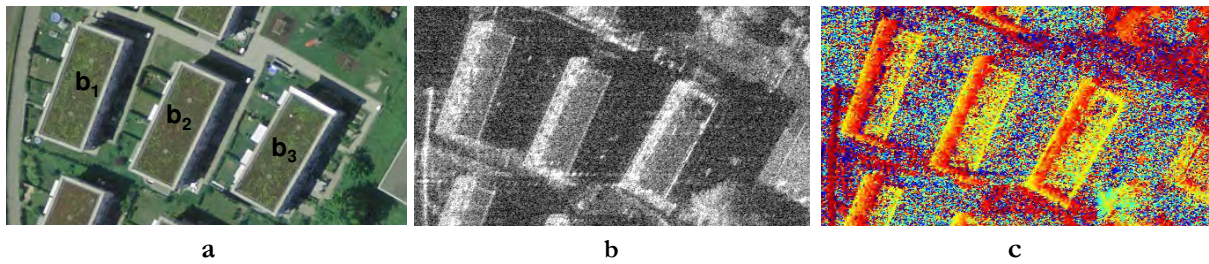
nearby buildings, such as given in metropolises, a rising complexity of these effects is noticeable, whereby complete intermixture in the layover or complete occultation in the shadow are possible.

The interferometric phase signature reveals that larger building heights lead to increasing interferometric phases. All four profiles are characterised by two maxima, which signalise the beginning of the building layover followed by a downwards oriented ramp. The continuous mixture of ground, building wall, and building roof causes this trend, whereby the building wall contributes a decreasing portion. The subsequent local minimum of the profile corresponds to the building corner in the magnitude data (except for the second building in red profile). The additional single-bounce response of the building roof leads to the constant trend in the phase profile. Differences between layover shapes are observable first for the second constellation (Fig. 3.14b yellow) due to different contributor groups similar to the magnitude signature. The bend in the phase shape of $b_2$ marks the point, where the contribution of ground is added additionally to the contribution of wall and roof. The third example coloured in orange shows further differences in the layover shape of both buildings. The phase values in the layover area of $b_2$ are constantly higher. A bend like shown in the yellow profile is not observable, since the increasing shadow of $b_1$ hampers the illumination of the ground totally. Focusing on the red profile $h_4$, phase values at the beginning of the $b_2$ layover areas are higher than values of $b_1$. The different contributor groups cause this, such as for the orange case $h_3$ and the yellow case $h_2$. Furthermore, the length of the $b_2$ layover is different, because now the building $b_1$ in front also occludes the lower part of the wall of $b_2$. Hence, even the minimum of the $b_2$ phase profile is shifted and no longer identical with the base point of the building. In addition, the single backscattering area of building $b_2$ is growing in comparison to $b_1$.

The appearance of these superposition phenomena between neighbouring buildings in the real InSAR data is given in Fig. 3.15. In the optical image (a), a group of three close-by buildings of same size is shown. The analysis of the magnitude signature (b) shows the shortening of the building shadows for $b_1$ and $b_2$. The layover areas of $b_2$ and $b_3$ are thinner than that of $b_1$, which is accompanied by a wider roof area. Furthermore, a subdivision of the layover is not visible in the real data. Hence, this example corresponds to the height assumption $h_4$ of Fig. 3.14, which is also supported by the phase signatures (c). In the phase signature of $b_1$, the local minima show values similar to the terrain height coloured in dark blue. These values are not given in the signatures of $b_2$ and $b_3$ since double-bounce scattering between ground and building wall does not take place. This potential missing of building corners is the most important effect occurring due to neighbouring buildings.

## 3.4 Summary

In summary, the InSAR signature of buildings is characterised by magnitude features - layover, corner line, roof, and shadow - and by significant interferometric phase profiles featured by the following variations:

**Layover Area:** Small building sizes, gabled roofs, complex façade structures, high sensor resolutions, or superposition effects with nearby objects, lead to a non-homogeneous appearance of building layover. In SAR amplitude images, a subdivision into different parts of brightness or a total decomposition into multiple point scatterers and line structures is observable making reliable layover detection difficult.

**Corner Line:** The line of bright scattering caused by a group of many dihedral corner reflectors spanned by ground and building wall is a distinctive feature that is invariant to, for example, building size and structure, roof type, and sensor resolution. Only unfavourable illumination configurations, large surface roughness, and shadowing effects of close-by objects can cause a reduction or vanishing of corner lines in the worst case. Moreover, interferometric phase and coherence values at corner position support their detection and delimitation from other bright lines.

**Roof Area:** The occurrence of a roof part is mainly dependent on the building size and sensor off-nadir look angle, viewing direction, and roof type. For example, if the look angle falls below a certain value, the entire signal of the roof is obscured by layover. Furthermore, the appearance of the roof is mainly characterised by roof material and sensor wavelength used. Hence, a bright homogeneous amplitude signal as well as a very dark noisy signal can be achieved. Since for smaller buildings single backscattering from the roof might not be present in the building signature, this feature will not play an important role in the reconstruction algorithm.

**Shadow Area:** The distinction of building shadow areas from adjoining smooth areas (e.g. parking places) depends on the NESZ of the SAR sensor (Subsection 2.2.2). Hence, in some SAR data clear shadow detection is not possible due to a high NESZ. Moreover, mostly the shape of observable shadow areas does not fit to the building geometry since close-by elevated objects (e.g. vegetation and buildings) lead to signal superposition. Therefore, the building shadow is an inappropriate feature for the reconstruction of small buildings.

**Phase Signature:** The phase signature of buildings is characterised by mostly the same effects as the magnitude signature, allowing the support of the classification of ambiguous magnitude features by exploiting corresponding interferometric phases. For example, bright areas of layover caused by signal superposition show the front porch shape in the phases, and corner lines in contrast to other lines are characterised by a phase level similar to mean terrain height. These possibilities highlight that the consideration of InSAR phases is helpful for building detection.

In summary, it can be stated that concerning SAR magnitudes, the corner lines are the most stable and dominant building feature appearing at almost all building locations. Additionally, the phase signature permits the separation of these corner lines from other bright lines, and by considering multi-aspect data the missing of features due to occlusion effects can be reduced. These three main conclusions will be taken into account in the following chapter concerning building recognition and reconstruction.

# 4    Reconstruction of Buildings

This chapter contains a detailed description of the developed approach. First, the considered building model is described (Section 4.1). Second, the overall workflow is briefly summarised (Section 4.2) followed by a systematic characterisation of all steps of the approach (Sections 4.3-4.11).
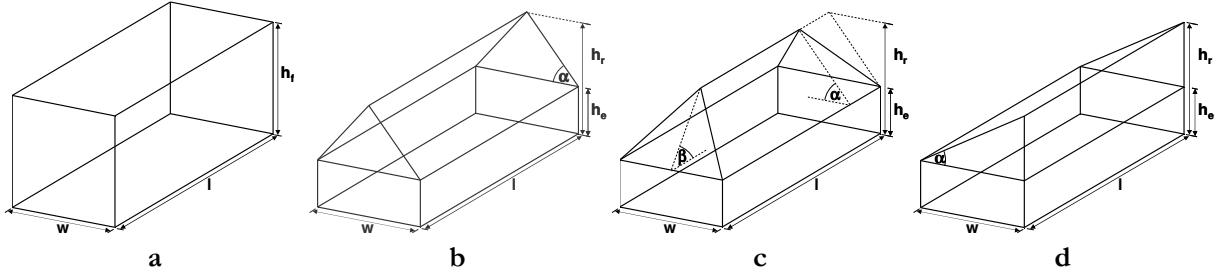
## 4.1    Building Modelling

A detailed introduction to building detection and building reconstruction based on SAR data was given in Subsection 1.2.2, where Bolter [13] and Soergel [115] only comprised investigations on 3D reconstruction utilising multi-aspect InSAR data. Their algorithms started with the extraction of building hypotheses based on single-aspect data. The exploitation of the multi-aspect information was realised by comparing and fusing these single-aspect hypotheses. Such strategies are restricted to buildings, which are detectable and reconstructible in single-view data.

Considering the new generation of airborne and spaceborne InSAR systems, spatial resolutions of up to one decimetre and up to half metre are possible, respectively. Due to this technological progress, the feasibility of analysing urban areas from multi-family up to one-family houses is given. However, the signature of such small buildings is extremely sensitive to changes of illumination geometry (Section 3.3). Therefore, their extraction based on merely single-aspect data is very often unsuccessful as presented in [123]. An improvement is achievable by using the following approach, whereby initial building hypotheses are generated on multi-aspect building features. The choice of suitable and sufficient building features is significantly determined by the summary of chapter 3. Furthermore, the combination of features based on SAR magnitude and interferometric phase leads to an improvement of the reconstruction result.

Since this algorithm is not intended to be an all-in-one solution, which supports the architectural variety of arbitrary building shapes, the focus is on reconstructing isolated buildings of simple shape. Hence, constraints due to building geometry and InSAR signature are defined and subsequently described.

### 4.1.1    Geometric Building Constraints

The algorithm is tailored for isolated buildings typically found in many towns outside the historical centres. The chosen model-based reconstruction method requires the introduction of prior knowledge regarding buildings that are reconstructed. The building footprint is modelled to be of rectangular shape. Building walls are required to be plane and orthogonally oriented to the building ground plate. The considered roof types are flat, gable, hipped, and monopitch roofs, however only symmetric shapes of the roofs are assumed. The resulting four basic models defined by the parameters width $w$, length $l$, flat roof height $h_f$, eave height $h_e$, ridge height $h_r$, pitch angle $\alpha$, and hip pitch angle $\beta$ are depicted in Fig. 4.1. All four models show the same ground plane and maximum building height ($h_f = h_r$). For the examples of gable- and hipped-roofed models, the angle $\alpha$ is

**Figure 4.1:** Geometric description of considered building models: flat-roofed (a), gable-roofed (b), hipped-roofed (c), and monopitch-roofed building (d)

similar. Assuming the same building height $h_f$, the angle $\alpha$ for the monopitch-roofed model is smaller than for the other building models. Moreover, minimum building extensions of $5\,\mathrm{m} \times 5\,\mathrm{m} \times 5\,\mathrm{m}$ $(w \times l \times h_f)$ are required due to the object detection methods used, InSAR data resolution, and InSAR specific constraints, which are discussed in the following.

### 4.1.2   InSAR Specific Constraints

Regardless of the pre-defined building models the result of building reconstruction depends on the properties of the InSAR data (e.g. resolution and wavelength – see Section 3.2) and on the individual characteristics of the buildings (e.g. size, shape, material, and neighbourhood – see Section 3.3). An ideal InSAR signature of the four geometric building models is given in Fig. 4.2 by making use of the simulators CohRaS [60] and an advanced version of the simulator described in [125] (Section 4.9). These magnitude and interferometric phase signatures given in slant range geometry contain all described building features, whereby the azimuth direction is chosen parallel to the long side of the building. The building corner, the bright line adjacent to the building shadow, is well visible for all four models and represents the most important feature of the building detection. To discriminate between the four different roof types, the characteristics of the building layover in magnitude and interferometric phase have to be analysed. A double line signature due to the pitched roof planes appears for the gable-, hipped-, and monopitch-roofed buildings. Differences are observable in width and length of the additional bright line and especially in the slope of the interferometric phases. Changes between flat, gable, and monopitch roof are visible along the whole length of the signature, but differences between gable and hipped roof signatures occur only at both ends of the building making their distinction more difficult.

Focusing on the acquisition of real InSAR data, the same constraints related to the sensor parameters and the building neighbourhood have to be taken into account. First, the occurrence of corner lines depends on sensor wavelength and material roughness, i.e., this feature is more pronounced for longer wavelengths. Second, the detailed analysis of layover areas requires high geometric resolution in order to allow parameter extraction as described in Section 4.6. Third, a fully developed layover area is needed, too. Hence, occlusion effects due to adjacent buildings or high vegetation can diminish the correct interpretation of the signature. The consideration of multi-aspect data mitigates this limitation, but cannot prevent shadowing entirely.

In addition to the building signature, data-related constraints are necessary to realise building reconstruction in such a way as described in the following sections. First, across-track interferometric
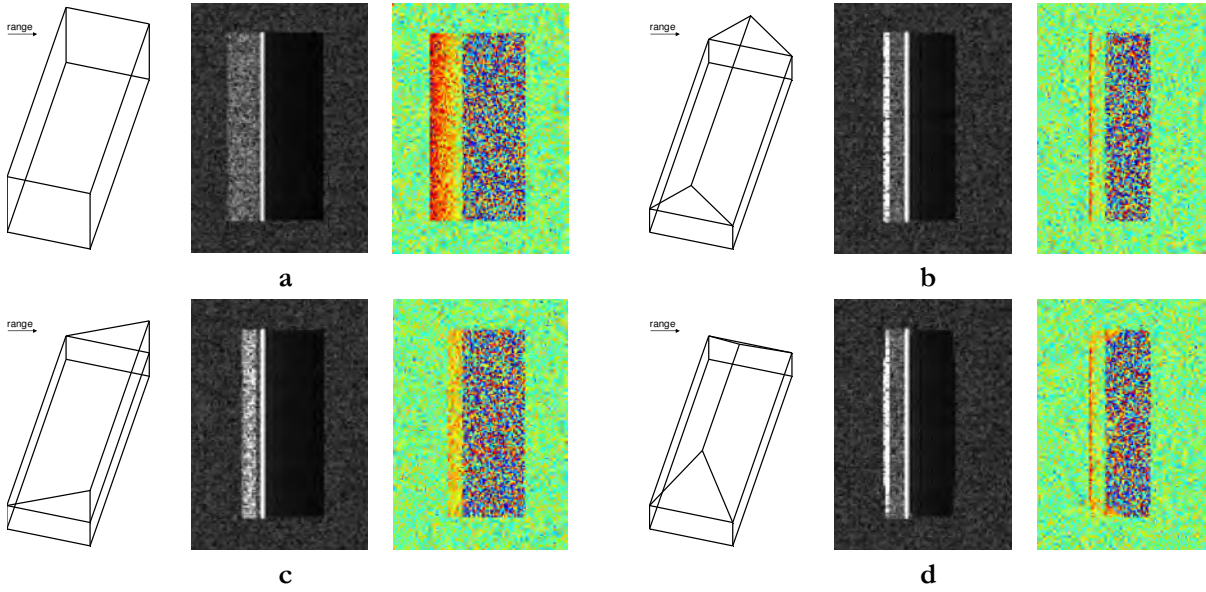
**Figure 4.2:** Simulated InSAR signature of considered building models: flat-roofed (a), gable-roofed (b), monopitch-roofed (c), and hipped-roofed building (d), range from left to right and $\theta = 50°$

image pairs in slant range geometry given as Single Look Complex data (SLC) are requested enabling interferometric height processing, feature extraction, and avoidance of interpolation effects. Short temporal baselines are advantageous to minimise decorrelation effects. Second, the transformation of building features from slant range into ground range geometry requires precise flight parameters to achieve best positional accuracy. An assembly to appropriate building hypotheses is only possible based on well geocoded features of different viewing directions. The same applies to the step of back projection, which enables the post-processing of building hypotheses in a loop. Third, the goal of reconstructing small buildings requires data from different flight tracks. In detail, the recorded InSAR data have to consist of acquisitions from at least two aspects spanning an angle of 90 degrees in the optimal case in order to benefit from complementary object information.

Requirements concerning geometrical and temporal baseline as well as flight geometry are easier fulfilled by airborne configurations due to their high flexibility. By contrast, new spaceborne configurations score with their highly accurate orbit geometries and recently with small temporal baselines. Their main limitation is given by restricted flight configurations referring to only ascending or descending orbits.

## 4.2 Overview of Building Reconstruction Approach

For clarifying the general structure of the developed approach, a brief overview is given before describing all processing steps in detail. By use of two interferometric image pairs, nine algorithmic parts have to be completed successfully to obtain 3D building models. Structure, order, and dependencies of the steps are illustrated in Fig. 4.3.

The approach can be subdivided into two main parts consisting of the analysis of magnitude and interferometric data. Findings presented in Sections 4.4 and 4.6 rely mainly on the analysis of mag-
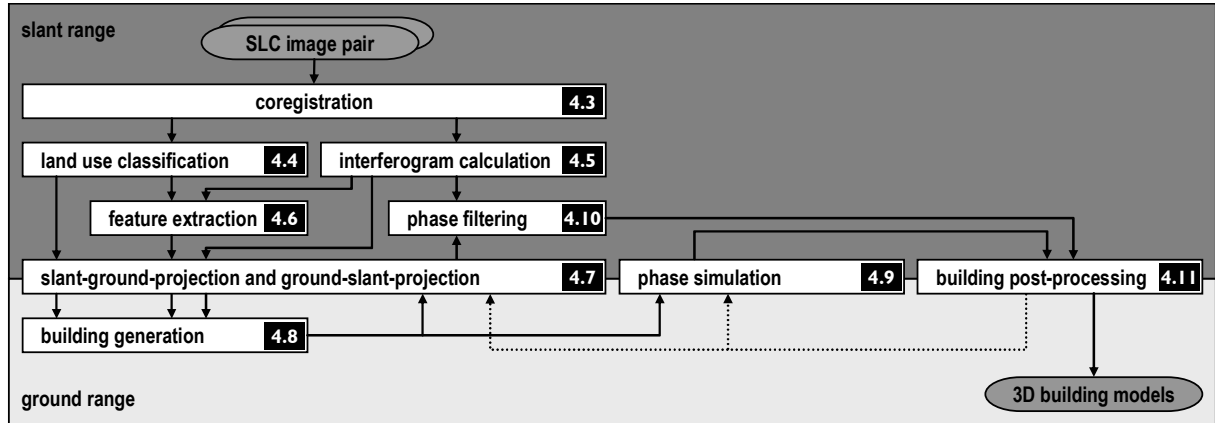
**Figure 4.3:**  Workflow of building reconstruction approach

nitude data. The steps of interferogram calculation 4.5, phase simulation 4.9, and filtering 4.10 exploit the interferometric phases. In Fig. 4.3 an additional subdivision is visualised by using different background colours denoting the applied geometry. Processing in slant range refers to the individual acquisition geometry of each image pair. Steps arranged at the transition of slant to ground range enable the transformation between both or work with data given in both geometries. The step of building generation and the phase simulation are the only ones, which require input arguments.

In detail, the processing starts in slant range geometry with sub-pixel registration of the interferometric image pairs as a prerequisite for land cover classification and interferogram calculation. The classification delivers an urban and a vegetation mask to assist the feature extraction and the building generation. In parallel, the interferogram calculation provides input in the form of normalised interferometric phases and interferometric heights to the processing steps of feature extraction, phase filtering, and building generation. Since feature extraction – individually processed for each image pair – is carried out in slant range geometry, the building generation requires a slant to ground range projection. Moreover, the generation step contains the fusion of the multi-aspect features supplemented by the height estimation and the assessment of building hypotheses due to classification results and specified model constraints. All remaining building hypotheses are tested and post-processed by comparing their simulated phase signature and corresponding real interferometric phases. The steps of phase simulation and filtering have to be run on each building individually. Eventually, sufficient correlation between simulated and real phases terminates processing and delivers the final 3D building shape.

The implementation of the approach is accomplished using different commercial products as well as freely accessible and own software sources. Moreover, the software package Definiens Developer assists in the classification step. Feature extraction and generation of hypotheses are realised by building up a graphical processing chain in the KBV platform [83] comprising already implemented as well as self implemented tasks. The interferometric processing steps of filtering, simulation, and post-processing consist for the most part of own Matlab implementations. More information concerning workflow realisation are given in the following sections.

## 4.3 Coregistration

In practice, interferometric image pairs – whether recorded in single-pass or repeat-pass mode – show an offset of at least a few up to a hundred pixels. Since some processing steps (e.g. interferogram calculation) require subpixel matching of the images, precise coregistration is essential. Detailed information concerning SAR image registration is presented in [86], so only a brief description is given here. The general strategy, similar for all datasets, contains a two-stage procedure consisting of coarse and fine registration. First, the coarse offset between the interferometric pair is calculated by measuring a tie point or by utilising orbit and baseline information. Second, the fine registration comprises the determination of displacement vectors at tie points, the calculation of transformation coefficients, the transformation as well as the interpolation of the slave image onto the master image. In this building reconstruction approach, the coregistration is carried out differently for airborne and spaceborne data, because the first shows higher variations in flight path accuracy and their processing is less supported by commercial software.

The coregistration of airborne data is realised as follows: the coarse offset is estimated by measuring one tie point manually. Coefficients and degree of the transformation equation for fine registration are derived from x- and y-component of shift vectors. These are determined for the slave image based on a regularly distributed field of tie points. To reach a coregistration on subpixel level an eightfold over-sampling of the data is implemented. For the investigated airborne data, a simple transformation comprising translation and scaling in range direction is successful. The final determination of the transformation parameters can be achieved, for example, by fitting a transformation polynomial to the shift vectors or by using an iterative optimisation of the parameters. Since the fitting can fail due to a low density or poor distribution of the shift vectors, the second solution is realised in this thesis. In detail, we consider a coarse-to-fine parameter testing to reach coherence maximum between master and slave image. The initial transformation values (translation $a_0$ and scaling $b_0$) are tested in predefined intervals of $-u_0 < a_0 < u_0$ and $-v_0 < b_0 < v_0$ by use of the step widths $i_0$ and $j_0$. The resulting best parameter combination $a_1$ and $b_1$ is used as new initial solution to start the second iteration with finer step widths $i_1$ and $j_1$ in a smaller search intervals $[-u_1, u_1]$ and $[-v_1, v_1]$. The process stops when no appreciable improvement of correlation is reached or the maximum level of correlation or iterations is passed.

Similar strategies are implemented in commercial software, for example, SARscape modules for ENVI and ERDAS IMAGINE, to coregister spaceborne SAR data. If master and slave image show equal pixel spacing, the ERDAS IMAGINE software is an appropriate tool. Otherwise, SARscape has to be utilised, whereby an additional down sampling of the resulting coregistered images is necessary. The results of the coregistration step will be assessed in Subsection 5.2.1, focusing on the airborne data.

## 4.4 Land Cover Classification of InSAR Data

In view of the fact that the exploitation of large scenes and a reduction of false detections are requested, a simple pre-classification into built-up and open land is very useful. For this purpose, many different strategies described in [10] can be utilised such as Maximum Likelihood Classifier, Bayesian Networks, Support Vector Machines, MRFs, and CRFs. Focusing on high resolution SAR

data covering urban areas, for example, Markovian classification was applied by Tison [130], and CRFs to fuse optical and SAR features by Wegner [140].

In this thesis, fuzzy logic is used to formulate a classification concept, which enables creating an appropriate rule set containing expert knowledge about InSAR relevant image content. Fuzzy rule sets [122] in general are similar to the human mind, comprehensible, simple to handle, and uncertainties in class memberships can be modelled easily. Beside the selection of a classifier, appropriate information features have to be chosen or calculated, if necessary. Intensity based classification of urban areas was presented in [130]. In addition to the SAR intensity, in [16] also the interferometric coherence was investigated to extract bio- and geo-physical parameters in ERS data. Within this work, three information layers are considered, which were introduced in the CoVAmCoh analysis [109] – a method to improve mainly the visual interpretation of high resolution InSAR images. In the following, these classification input layers, the classification process focussing on the creation of the fuzzy rule set as well as the fusion of the multi-aspect classification results is described.
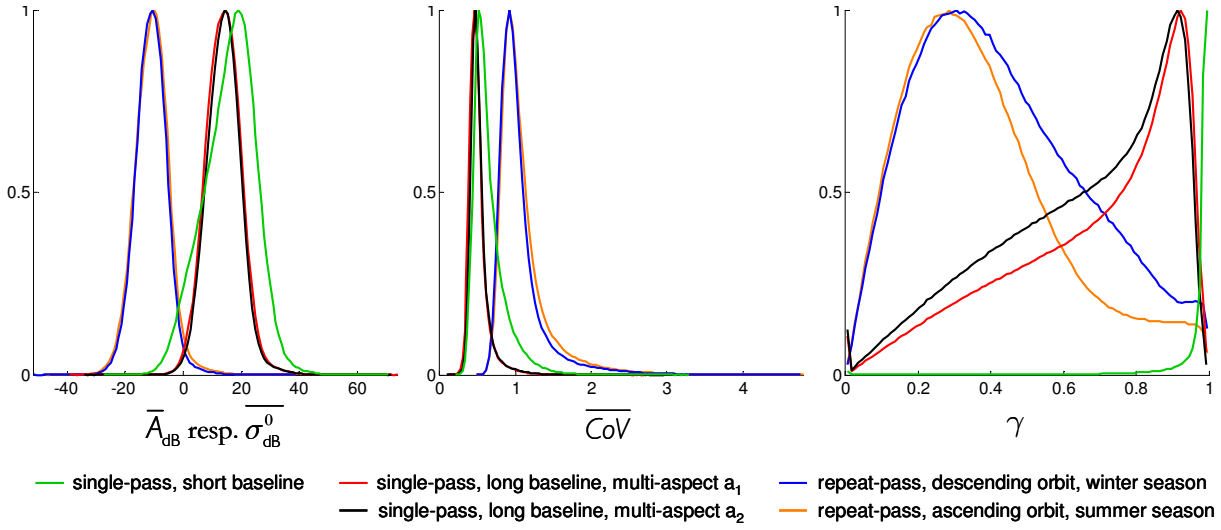
### 4.4.1    Feature Layers

The selection of classification input layers is based on the already mentioned CoVAmCoh-RGB composition usable to colour-code InSAR data. The three layers mark different attributes of InSAR data making the interpretation much simpler. Below, their calculation and characteristics are described as well as their variability with regard to the spatial and temporal length of baseline is addressed.

### SAR Magnitude

The SAR magnitude contains the backscatter intensity, which depends on the radiometric properties of the illuminated object on ground (Subsection 2.2.1). If uncalibrated airborne data and calibrated spaceborne data are used, two different equations have to be introduced. In equation (4-1), appropriate to uncalibrated data, amplitudes $A_1$ and $A_2$ of the two acquisitions are used to compute the arithmetic average $\overline{A}$. Moreover, dB-scaling is applied to enable a similar parameter range for different datasets particularly important to define a general classification rule set.

$$\overline{A} = \frac{A_1 + A_2}{2}$$
$$\overline{A}_{dB} = 20 \log_{10} \cdot \overline{A} \qquad\qquad (4\text{-}1)$$

Working with calibrated data is preferred since such data enable the transfer of derived parameter settings to additional datasets, which is an advantage when utilising multi-aspect data. Beyond Sigma Naught $\sigma^0$ and Beta Naught $\beta^0$ calculation, the data preparation contains the same averaging and scaling steps to obtain the calibrated backscatter layer in this case. In equation (4-2), $\beta^0$ is determined by the product of the processor scaling parameter $k_s$ and the square of the pixel amplitude value $A$. $\sigma^0$ results from $\beta^0$ corrected by the local incidence angle $\zeta$ [68].

**Figure 4.4:** Different data distributions of feature layers: dB-scaled averaged SAR magnitude $\overline{A}_{dB}$ resp. $\overline{\sigma^0_{dB}}$ , averaged Coefficient of Variation $\overline{CoV}$ , and coherence $\gamma$

$$\sigma^0 = \beta^0 \cdot \sin\zeta, \quad \text{with} \quad \beta^0 = k_s \cdot |A|^2$$
$$\overline{\sigma^0} = \frac{\sigma^0_1 + \sigma^0_2}{2} \tag{4-2}$$
$$\overline{\sigma^0_{dB}} = 10\log_{10} \cdot \overline{\sigma^0}$$

The resulting dB-scaled mean amplitude values $\overline{A}_{dB}$ and Sigma Naught coefficients $\overline{\sigma^0_{dB}}$ follow normal distributions. This is depicted in Fig. 4.4, where histograms of five different InSAR image pairs mapping the same area are plotted. All show the same behaviour that is advantageous for the classification step. Differences are given only in the position of the mode of the distributions and in the spread of the distribution due to different sensor properties. In general, this feature layer contains information about object roughness used, for example, to distinguish between vegetated (appears bright) and sealed land (appears dark).

## Coefficient of Variation (CoV)

The second input layer comprises the Coefficient of Variation ($CoV$) that enables the differentiation between homogeneous and heterogeneous areas. This value is defined by the ratio of standard deviation and arithmetic average in a local neighbourhood of intensity, amplitude, or Sigma Naught coefficients. In equation (4-3) all three variations are given, where exemplarily $\mu_A$ is the local mean amplitude and $\sigma_A$ the standard deviation. In a second step, the $CoV$ values $CoV_1$ and $CoV_2$ of the two InSAR images are combined by averaging.

$$CoV_I = \frac{\sigma_I}{\mu_I}, \quad \text{here} \quad CoV_A = \frac{\sigma_A}{\mu_A} \quad \text{and} \quad CoV_{\sigma^0} = \frac{\sigma_{\sigma^0}}{\mu_{\sigma^0}}$$
$$\overline{CoV} = \frac{CoV_1 + CoV_2}{2} \tag{4-3}$$

In general, the local $CoV$ values are utilised in frameworks of adaptive SAR filtering (e.g. [87]); here they are used as evidence of locality. For a single-look intensity image, the pdf of an ideal homogeneous backscattering area is an exponential distribution with $\sigma = \mu$, which leads to $CoV_I = 1$. The same takes effect for Sigma Naught coefficients, with Beta Naught coefficients proportional to square of amplitudes. Homogenous areas in single-look amplitude data show Rayleigh distribution (see also Weibull distribution (2-19)):

$$g(u,s) = \frac{u}{s^2} \cdot e^{-(u^2/2s^2)}, \quad \text{with} \quad s = \psi / \sqrt{2}$$

$$\mu = s \cdot \sqrt{\frac{\pi}{2}} \quad \text{and} \quad \sigma^2 = \frac{4-\pi}{2} \cdot s^2 .$$

(4-4)

Hence, the $CoV_A$ of a speckle dominated homogenous area is approximately equal to 0.523. Moreover, local structures such as point scatterers, edges, or lines give rise to higher $CoV$ values, whereby urban areas appear much brighter in the $CoV$ layer than rural areas. As can be seen in Fig. 4.4, the five distributions show high similarity. Depending on whether amplitude values or Sigma Naught coefficients for the $CoV$ calculation are taken, different mean values ($\overline{CoV_A} = 0.523$ and $\overline{CoV_{\sigma^0}} = 1$) result. The spread of the distributions differs slightly, which can be caused by different data resolutions.

## Coherence

The third layer contains a measure of temporal stability – the coherence $\gamma$. As described in Subsection 2.1.4, $\gamma$ shows the level of correlation between the two received signals $S_1$ and $S_2$. Low values arising from more independent signals appear, for example, at noise dominated areas (e.g. water surface) and at temporally unstable areas (e.g. growing vegetation). Coherence values near 1 denote completely coherent scatterers such as point scatterers and urban structures. Besides the object properties, data specifics – temporal and spatial length of baseline – influence the level of coherence. This variability is depicted in Fig. 4.4 by taking the example of three single-pass (coloured red, black, and green) and two repeat-pass InSAR image pairs (coloured orange and blue). Their mean values show high differences due to a temporal baseline of 11 days in case of the latter. Additional variations in the distributions of the two repeat-pass datasets result from seasonal changes (e.g. summer = orange and winter = blue) as well as from different viewing directions. Similar effects occur for the three single-pass examples because the viewing directions and the length of the interferometric baselines differ. Shorter baselines (e.g. green distribution) lead to less geometrical decorrelation, which results in higher coherence values.

In summary, it can be stated that in comparison to the two other feature layers the coherence layer shows the highest level of variability. With regard to the achieved image classification, this complicates the derivation of general rules discussed in the following.

### 4.4.2    Classification Process

The classification process can be subdivided into a segmentation step, the structuring of the fuzzy rule set, and a classification step [8]. This process was realised with Definiens Developer [35].

Starting with the generation of segments, the three input layers are used in a multi-resolution segmentation. This contains a bottom up region-merging technique starting on one-pixel objects. Moreover, the subsequent clustering process comprises an optimisation procedure minimising the layer-weighted heterogeneity of the image object. Since the clustering is based on three layers, the segmentation result can be influenced by the processing parameters – layer weight and scaling. The former defines suitability or significance of each individual layer during the segmentation step. The second describes the maximum level of heterogeneity, conceded in image segments. In addition, this requires a specification of the term heterogeneity also called "composition of homogeneity criterion", which is realised with two additional parameters - colour and shape. The latter relies on the sub-parameters smoothness and compactness. A more detailed description on these parameters can be found in [8]. For classifying high resolution SAR data, a low scaling factor and equally weighted input layers are chosen, since small urban structures have been imaged. Moreover, the composition of the homogeneity criterion contains colour and shape information in equal shares, because in contrast to optical data, the shape criterion is especially helpful in strongly textured imagery such as SAR data [35].

For the final segments, object features building the base for formulating the fuzzy rule set are calculated. Those features comprise, for example, maximum, minimum, mean values, and standard deviations. In the implemented land cover classification, only the three mean values ($\overline{A}_{dB}$ resp. $\overline{\sigma^0_{dB}}$, $\overline{CoV}$, $\overline{\gamma}$) of the image segments are considered as object features.

In general, the fuzzy classification consists of the steps of fuzzification, fuzzy logic combination, and defuzzification. The former contains the definition of fuzzy sets on an object feature. Fuzzy sets are membership functions (MF), which define how each point in the feature space is mapped to class specific membership values (or degree of membership) between 0 and 1. These MFs are different curves (e.g. linear ramp and sigmoid curve) that are exemplarily shown in Fig. 4.5 and explained in the next paragraphs. The combination of several fuzzy sets characterising the same object class in different feature spaces is realised by fuzzy logic concerning "and", "or", and "not". The result of this classification process is an *n*-dimensional vector of membership degrees describing the level of class assignment of an image object to *n* classes. The highest membership value or the distance between first and second maximum of the membership vector can be used to derive the reliability and the stability of the classification. For achieving a crisp classification result ("true" or "false"), defuzzification is required. In general, the maximum membership degree determines the affiliation of an object to a class. Supplementary, a maximum membership level can be introduced to ensure minimum reliability. Objects showing lower membership degrees are referred to the group "unclassified" objects. In addition to this short description, more detailed information can be found in [8] and [122].

If we assume that each of the three feature layers ($\overline{A}_{dB}$ resp. $\overline{\sigma^0_{dB}}$, $\overline{CoV}$, $\gamma$) have only two states [low, high], $2^3$ different classes of segments are possible. Eight combinations result corresponding to the main colours (red, green, blue, yellow, cyan, magenta, white, and black), when additive colour mixing is applied onto the three feature layers (see Tab. 4.1, [109]). Beyond these eight combinations, a ninth subclass (petrol coloured) is listed and characterised by low $\overline{CoV}$, medium $\overline{A}_{dB}$ resp. $\overline{\sigma^0_{dB}}$, and $\gamma$, which is often represented in the CoVAmCoh-images. The appropriate assignment of real world objects to this CoVAmCoh colour description depends on InSAR data properties and especially on

**Table 4.1:**    CoVAmCoh-Analysis of single-pass and repeat-pass InSAR data

| CoVAmCoh-Image | | $\overline{CoV}$ | $\overline{A}_{dB}$ resp. $\overline{\sigma}_{dB}^{0}$ | $\gamma$ | CoVAmCoh-Characteristic | Example |
|---|---|---|---|---|---|---|
| | 🟥 | high | low | low | local changes of low return | small shadows |
| | 🟩 | low | high | low | areas of volume scatterers | dense bushes |
| | 🟦 | low | low | high | persistent areas of low return | sport fields |
| | 🟦 | low | high | high | persistent areas of high return | building roofs |
| | 🟪 | high | low | high | persistent (local) scatterer of low return | street borders |
| | 🟨 | high | high | low | local changes of bright backscattering | moving cars |
| | ⬜ | high | high | high | persistent (local) scatterer | lamp poles |
| | ⬛ | low | low | low | areas of no return | lakes |
| | 🟦 | low | medium | medium | areas of medium scattering and stability | fallow land |

the level of coherence. In detail, highly coherent objects in single-pass data (see Tab. 4.1 first column, first image - fallow land, lower right corner) do not necessarily show a high coherence in repeat-pass data (see second image). Furthermore, red and yellow coloured local changes are only observable in repeat-pass data. Hence, the general description of an object signature can be difficult because of different InSAR configurations, which becomes more obvious when focusing on the wanted object classes.

In total, two superclasses shall be discriminated by the implemented fuzzy rule set; the classes of urban and vegetated areas. The classification contains three fuzzy sets due to the three input layers, which are combined by the fuzzy logic "and". Moreover, the fuzzy sets comprise two (low, high) or three (low, medium, high) MFs adapted for describing the nine-colour subclasses (see Tab. 4.1). In Fig. 4.5 the MFs specified as sigmoid and Gaussian curves are shown, where the curves coloured green, yellow, and red correspond to low, medium, and high mean values, respectively. The black dashed curves show the original layer distributions of the repeat-pass summer season InSAR pair (curves coloured orange in Fig. 4.4). The borders and the mode of the MFs are derived from the particular layer statistics of $\overline{A}_{dB}$ resp. $\overline{\sigma}_{dB}^{0}$, $\overline{CoV}$, and $\gamma$. The classification delivers for each segment a vector containing nine membership degrees. The maximum value of these denotes the final subclass assignment during the step of defuzzification. From the more abstract subclasses, two superclasses are generated. The superclass *vegetated areas* ($C_{veg}$) is especially marked by a high level of homogeneity leading to low $\overline{CoV}$ values. Furthermore, vegetation is characterised by medium up to high $\overline{A}_{dB}$ resp. $\overline{\sigma}_{dB}^{0}$ values due to volume scattering, and their temporal variability results in medium to low $\overline{\gamma}$ values. Hence, the green and the petrol coloured subclasses can be easily assigned to the superclass $C_{veg}$. The cyan coloured areas are critical *vegetated areas* since homogenous building parts (e.g. layover and roof) as well as low vegetation show these feature values. Nonetheless and with regard to high resolution SAR data, more detailed structures are observable in building signatures that lead to rising $\overline{CoV}$ values and minor risk of confusion. Furthermore, all other subclasses are assigned to the superclass *urban areas* ($C_{urb}$). The major part of segments showing high $\overline{\gamma}$ values comprises man-made objects. The same applies to areas of local changes (coloured yellow and red in Tab. 4.1). Only areas appearing black in CoVAmCoh-images are difficult to assign since water
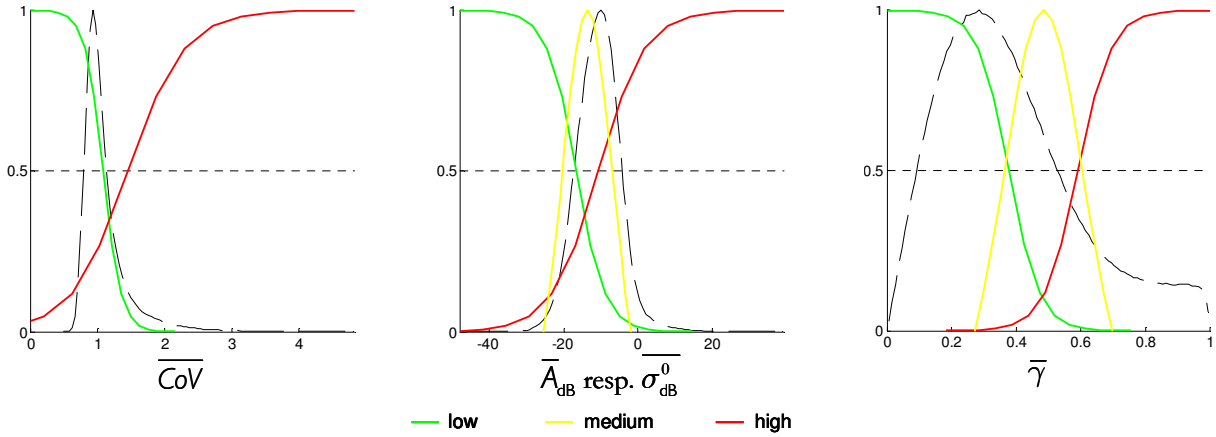
**Figure 4.5:** Membership functions of the nine CoVAmCoh classes used in fuzzy classification

surfaces and building shadow show low values in all three feature layers. Finally, for each InSAR image pair the classification into *vegetated* and *urban areas* is accomplished by reasonable adjustment of the fuzzification step.

As high vegetation shows the same layover effect as buildings, adjacent objects can be occluded by vegetation signatures. Hence, a fusion of multi-aspect classification results is carried out to work against this occlusion effect. First of all, this requires an individual geocoding of the classification results to a common coordinate system followed by a fusion step calculating the intersection between the classified *vegetated areas*. Only those areas are considered as final *vegetated areas* that belong to this class in all InSAR data. First results on this multi-aspect classification were presented in [123]. The final results as well as the assessment of the classification results by comparison with electro-optical data are presented in Subsection 5.2.3. In the following steps of building reconstruction, the classification result is used to support feature extraction (Section 4.6) and the generation of building hypotheses (Section 4.8).

## 4.5 Calculation of Interferometric Heights

In this section, the procedure to derive heights from interferometric image pairs is described. The fundamentals and equations of the interferogram calculation have already been given in Subsection 2.1.4, so that only data specific topics are treated.

The steps of the interferometric height calculation are summarised in Fig. 4.6a, all carried out in slant range geometry. The coregistration of the image pair as well as the estimation of the interferometric coherence has already been discussed in the previous subsections. The interferogram $S$ is calculated by complex multiplication of the two images $S_1$ and $S_2$ (see (2-10)). Then only the phase difference $\Delta\varphi$ is taken further into account showing a uniform distribution and a "sawtooth" fringe pattern in range direction. This linear phase variation is called flat earth contribution $\varphi_{flat}$ and is specified by the parameters ping-pong value $p$, wavelength $\lambda$, range distance $r$, off-nadir look angle $\theta$, the spatial baseline $B$, and its orientation $\xi$:

$$\varphi_{flat} = -p \cdot \frac{2\pi}{\lambda} \cdot \left( \sqrt{r^2 + B^2 + 2 \cdot r \cdot B \cdot \sin(\xi - \theta)} - r \right) \qquad (4\text{-}5)$$

The next processing step contains the subtraction of $\varphi_{\text{flat}}$ to obtain the so-called flat earth corrected phase. This correction can easily be accomplished using commercial software (e.g. ENVI or ER-DAS IMAGINE) as long as the appropriate sensor model is implemented. The quality of the provided configuration parameters (e.g. rapid or science orbit) determines whether or not post-processing is necessary. If post-processing is required, for example, ground control points (GCPs) are utilised. Since InSAR data of the new generation of satellites are provided with high precision orbit information, no additional processing has to be considered (see Fig. 4.6a, step "flat earth correction"). This is different for airborne data, because these platforms show higher variations in track geometry than satellites on orbits. Furthermore, commercial software tools do not support the processing of airborne data in general because of their limited data accessibility and individual specifications. Considering that, for the interferometric processing of airborne data, in-house solutions are used.

The flat earth correction of airborne data underlies some assumptions: first, the length of the baseline is constant as the antennas are rigidly fixed. Second, the flight height over ground is steady and third, the flight geometry is stable during recording time. For a scene dominated by flat topography close to the mean height chosen for flat earth correction, a phase distribution with a significant narrow maximum is expected. The result of flat earth correction achieved with the original parameter set is given in Fig. 4.6b. The phase distribution (left) shows a wide curve rather than a significant narrow maximum. The reason for that is a linear phase trend observable in a corresponding range profile (right). This can be caused by imprecise configuration parameters or a natural slope of topography. Taking into account additional information about the topography of the recorded scene, a flat terrain can be assumed. Therefore, the goal of an improved flat earth correction is the reduction of this linear phase trend. This improvement of the flat earth correction contains a refinement of the two angles $\xi$ and $\theta$, whereby the latter is specified by sensor height over ground $H$ and range distance $r$. In detail, $\xi$ is corrected by varying the vertical $B_{\text{V}}$ and horizontal $B_{\text{H}}$ parts of the baseline, and $\theta$ by testing $H$, respectively. The estimation of optimal values is realised by a coarse-to-fine parameter search similar to the coregistration. The aim is to reach a narrow phase distribution with a minimum standard deviation. The reduction of the linear trend is visible in Fig. 4.6c. The numerical results are summarised in Subsection 5.2.2.

The resulting absolute phase values (c) are random and the Gaussian-like phase distribution can show a high $\sigma$. The latter can be caused by hilly topography or by insufficient motion compensation during the SAR processing. To find out how strong this effect is, range histograms are calculated from the InSAR phases considering phase values of several neighboured range lines. A linear drift of the distribution maximum becomes visible in the plot of all histograms (Fig. 4.6d left), indicating residual motion effects in the InSAR data. Since the fusion of multi-aspect InSAR data is one of the main goals of this approach, this aspect specific effect has to be taken into account. The subsequent phase centring can mitigate this motion effect in an easy way, and additionally a phase distribution with zero mean can be achieved. The centring is implemented as a simple rotation of the complex interferogram values into zero position. Thus, from the interferogram $S(x,y)$ with $x$ and $y$ as range and azimuth coordinates, the one-dimensional function $S_y(y)$ is calculated:

$$S_y(y) = \sum_{\text{all } x} S(x,y) \tag{4-6}$$
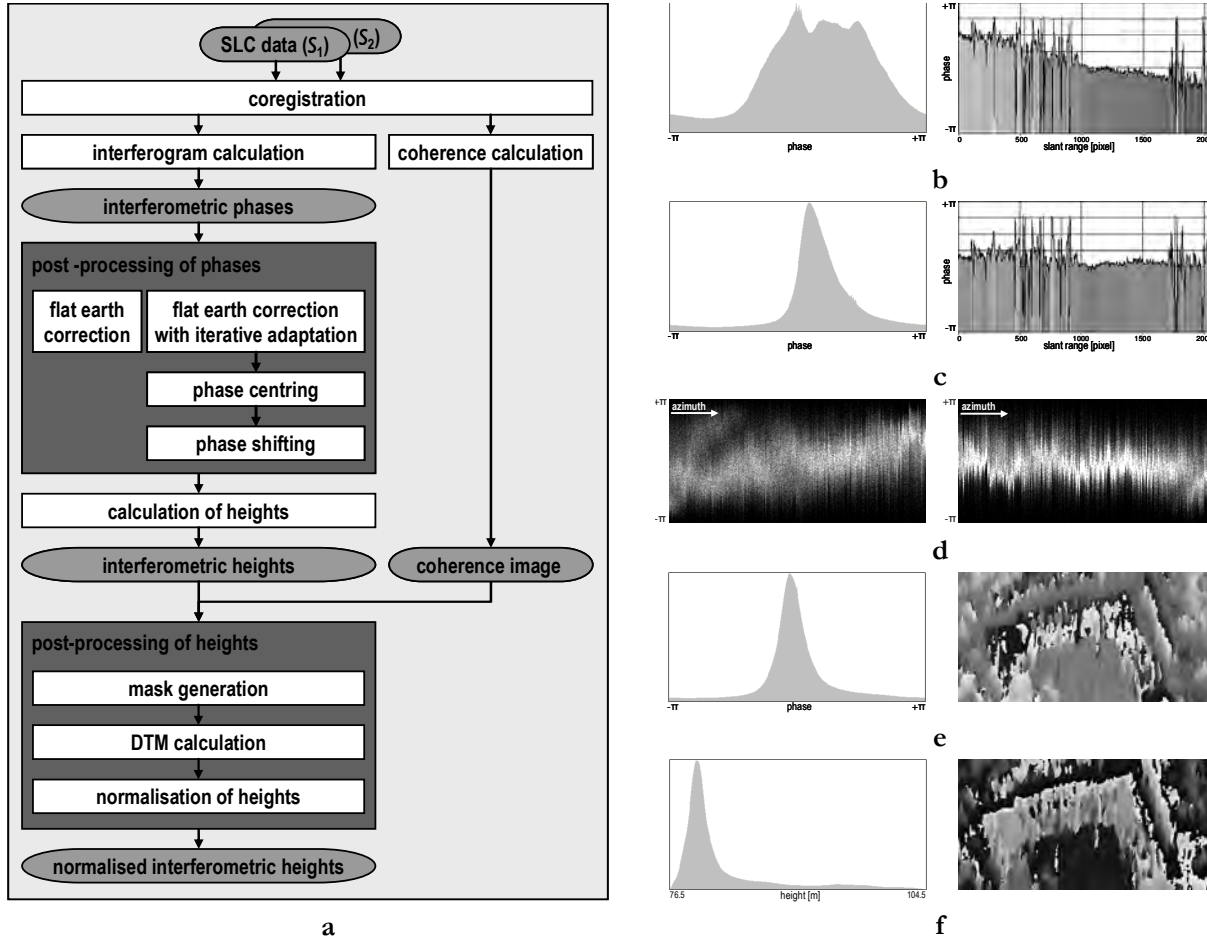
**Figure 4.6:** Workflow of interferometric height calculation (a); histograms of InSAR data and corresponding slant range profile – result of "flat earth correction" (b), result of "flat earth correction with iterative adaptation" (c), histogram plot of azimuth drift (d), histogram of "phase centring" and image patch (e), result of "calculation of heights" with "phase shifting" (f)

This azimuth profile is filtered by averaging values in the range of $\gamma' = -\delta, ..., +\delta$. In the following, this result is termed as $\overline{S_y(y)}$. The parameter $\delta$ has to be chosen large enough to avoid effects on the phase of objects. The final zero-centred interferogram results from:

$$S_{zero}(x,y) = S(x,y) \cdot \frac{\overline{S_y(y)}^*}{\left| \overline{S_y(y)} \right|} \tag{4-7}$$

where $\overline{S_y(y)}^*$ denotes the complex conjugate of $\overline{S_y(y)}$. In Fig. 4.6e the centred phase distribution (left) is narrower than the one in (c – left). Also the linear trend in the plot of the range histogram is not longer visible (Fig. 4.6d – right). Of course, care has to be taken for hilly topography as this centring can eliminate topography portions.

Before converting the interferometric phases to height values, phase unwrapping has to take place. Since many unwrapping algorithms fail in urban areas, a simple step of phase shifting is integrated. That means phase values significantly below the phase average are shifted upwards by $2\pi$. As the
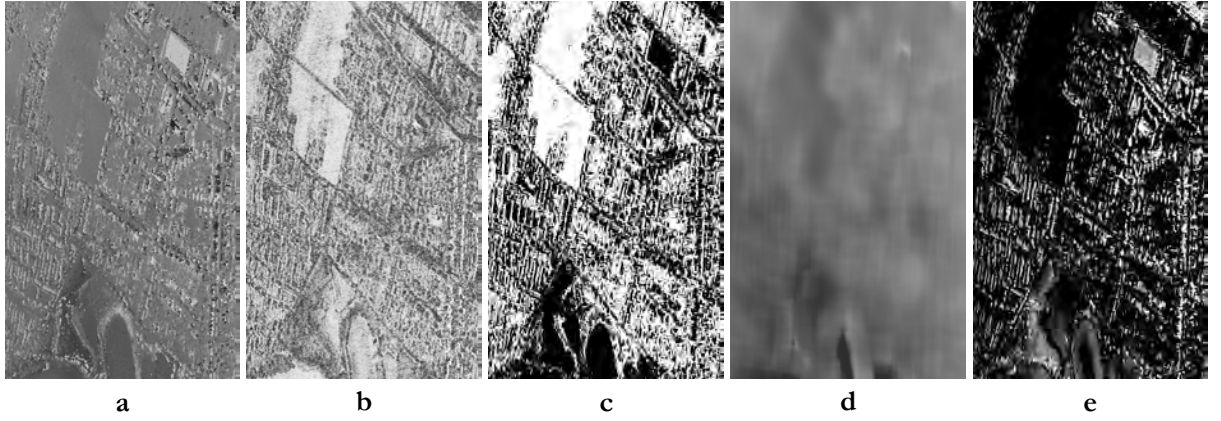
**Figure 4.7:** Post-processing of an extended region: InSAR heights (a), coherence (b), mask (c), DTM (d), and normalised InSAR heights (e)

mean of the phase distribution corresponds to the local terrain height, this step leads to an enlargement of the unambiguous range over ground. Hence, phase jumps (i.e., the transition between $+\pi$ and $-\pi$) at elevated objects, for example buildings, are reduced at the cost of possible exaggeration of sinks in the terrain. Results of the InSAR height estimation without and with considering the phase shifting step are shown in Fig. 4.6e (right) and f, respectively. In the given example, the $2\pi$ unambiguous range corresponds to approximately 30 m and therefore phase ambiguity issues arise at buildings taller than 15 m. With an offset value of $\frac{3}{4}\pi$, the unambiguous range of the height is shifted from [66.1 m , 94.0 m] to [76.5 m , 104.5 m]. The phase shifting effect is visible at the U-shaped building (Fig. 4.6e,f right) that is featured by roof heights of 16 m up to 23 m. Obviously, less discontinuities (i.e., transitions from black to white) are observable in the roof area of this building. If no abrupt steep descents are present in the scene, this step of phase shifting compensates phase jumps at building roofs in a proper way.

Considering larger areas with slight topography, the global phase shifting can fail due to varying local terrain heights. For that reason, normalised InSAR heights are generated, which are essential for the subsequent filtering of building primitives (Subsection 4.6.2). The processing of these heights contains the following steps, whose intermediate results are shown in Fig. 4.7.

First, a binary filter mask ($mask_i$) is computed to define image pixels used for the Digital Terrain Model (DTM) generation. Only pixels of coherence value ($\gamma_i$) above a minimum coherence threshold ($\gamma_{min}$) and an InSAR height value ($h_i$) close to the global mean terrain height ($\bar{h}$) are considered, as given in (4-8). Thus, this mask contains the value 1 for objects like fallow land and rough man-made areas showing high coherence and mean terrain height. Elevated objects such as trees and buildings as well as areas of low coherence (e.g. shadow areas) are assigned to the value 0. The definition of the parameter $\gamma_{min}$ depends on the temporal and spatial length of the InSAR configuration. For the given example $\gamma_{min} = 0.5$ was chosen. Additionally, the parameter $\sigma_{\bar{h}}$ can be estimated directly from the InSAR heights. In case of rising topography, $\sigma_{\bar{h}}$ will also increase possibly affecting low building signatures. A solution would be the determination of local $\sigma_{\bar{h}}$.
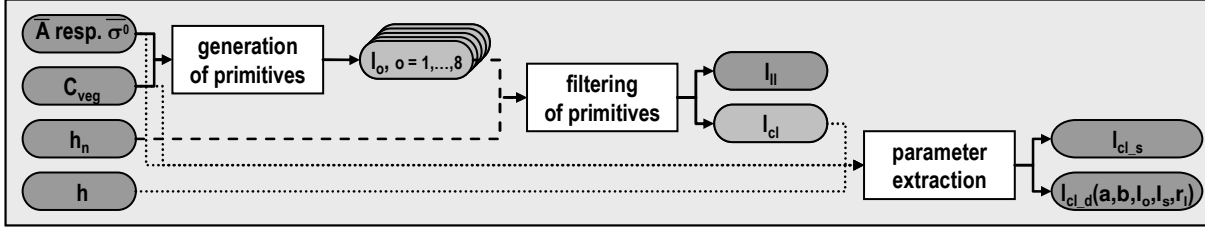
**Figure 4.8:** Workflow of building feature extraction

$$mask_i = \begin{cases} 1, & \text{if } \gamma_i \geq \gamma_{\min} \text{ and } \left| h_i - \bar{h} \right| \leq \sigma_{\bar{h}} \\ 0, & \text{else} \end{cases} \tag{4-8}$$

Second, based on the filtering of the InSAR heights (a) with the binary mask (Fig. 4.7c), the DTM (d) is calculated. The pixel values of this DTM result from a weighted averaging of height values over an area of $50\text{m} \times 50\text{m}$ in ground range resolution. Such a large area is mandatory for smoothing local structures probably included due to a high $\sigma_{\bar{h}}$.

Finally, the height differences, the normalised InSAR heights (e) using the InSAR heights (a) and the DTM (d), are calculated. In the following, these heights are investigated to filter building primitives (Subsection 4.6.2) and to extract building heights (Subsection 4.8.2).

## 4.6 Extraction of Building Features

The extraction of appropriate features sketched in Fig. 4.8 is made up of three processing steps: first, the generation of structure elements is treated considering the magnitude data ($\bar{A}$ resp. $\overline{\sigma^0}$) and the classification result ($C_{\text{veg}}$). Second, the filtering of these so-called primitives is accomplished to classify them in layover and corner lines with the aid of the normalised interferometric heights $h_n$. Third, building parameters are extracted from the corner lines and their surroundings by taking into account $\bar{A}$ resp. $\overline{\sigma^0}$, the mask $C_{\text{veg}}$, and the interferometric heights $h$. Subsequently, these three steps are described in more detail including input and output arguments as well as intermediate processing steps. The feature extraction is carried out in slant range geometry to avoid interpolation effects or signature changes due to resampling effects after geocoding in ground range geometry. Hence, this part of the workflow is realised separately for each single InSAR image pair.

### 4.6.1 Generation of Primitives

The generation of building primitives focuses on the detection of bright lines because the appropriate signature part *corner line* is characterised by high magnitude values. Since the surrounded signature parts – layover, roof, or shadow – show lower values, a line detector should deliver good results. For this purpose, many different kinds of line and edge detectors may be used. There exist two main categories of line detectors: detectors that are specifically designed for the statistics of SAR imagery and detectors designed for optical data. Examples for non-SAR specific operators are the Canny [27], and the Steger operator [120], needing radiometrically pre-processed SAR magnitude images (e.g. speckle reduction and logarithmic rescaling). Touzi [133] and Tupin [137], for in-
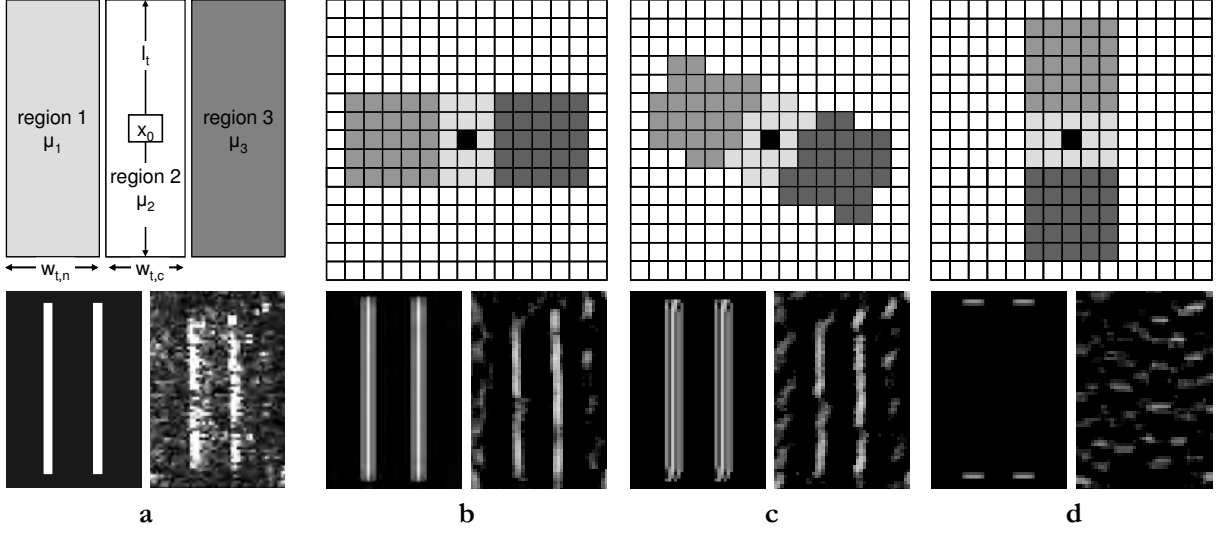
**Figure 4.9:** Detection of primitives: schema of line detection (a – top), synthetic and original SAR ampli-
tude image (a – bottom); results of line detection – window orientation 1 (b), 2 (c) and 5 (d)

stance, have developed SAR specific operators considering the statistics of magnitude images. Since
we prefer to work as closely as possible to original data, the SAR specific detectors are preferred.

In this thesis, the two SAR specific operators mentioned in the last paragraph are taken as exam-
ples to implement a line detector tailored to the task. The detectors of Touzi and Tupin determine
the probability of a pixel to belong to an edge or line, respectively, using different template orienta-
tions. Focusing first on the edge detection, we assume that two considered regions are homogenous
and their intensity values are similar, variations to this assumption are caused only by *speckle*. Due
to the multiplicative behaviour of *speckle*, operators based on pixel differences will deliver results
that depend on intensity. To avoid this, the Touzi detector takes the quotient of the mean values
$(\mu_m, \mu_n)$ of both regions. That leads to probability values for the detector that depend only on the
ratio of $\mu_m$ and $\mu_n$, not on the measured intensity values themselves. This kind of detector is called
a detector of Constant False Alarm Rate (CFAR). Since the pdf for false detections is characterised
by a quotient of $\frac{\mu_m}{\mu_n} = 1$, thresholds for a given false alarm rate can be deduced that are independent
of the image. The line detection by Tupin, an enhancement of the Touzi edge detection, is based
on a template consisting of a central region and two neighbouring regions of equal size such as
shown in Fig. 4.9. By applying the edge detector two times, the probability at pixel $x_0$ is deter-
mined to belong to a line. As given in (4-9), the two probability values $r_{1,2}$ and $r_{2,3}$ are calculated
from the mean values $\mu_1$, $\mu_2$, and $\mu_3$. The detector value $r_{line}$ is defined by the minimum of the two
real values $r_{1,2}$ and $r_{2,3}$.

$$r_{m,n} = 1 - \min(\frac{\mu_m}{\mu_n}, \frac{\mu_n}{\mu_m}), \quad \text{with} \quad (m,n) \in \{(1,2),(2,3)\}$$

$$r_{line} = \min(r_{1,2}, r_{2,3})$$

(4-9)

Since edges and lines in the images may have arbitrary orientation, templates of different orienta-
tions are used during the step of line detection. Commonly, the number of template orientations is
set to eight directions. Three of these templates are given in Fig. 4.9b-c (first row). In the original

approach of Tupin, a second detector D2 is implemented to increase the detection probability and to fuse the different probability images of the first detector D1 (4-9). D2 takes into account the homogeneity of the two neighbouring regions by calculating the $CoV$ values, too. Subsequently, the results of D1 and D2 are combined and the maximum value at position $x_0$ is finally searched in the set of probability images according to the number of tested orientations. The fusion of the probability images is necessary for applications considering curved paths such as road extraction. As this is rather unfavourable for building models as described in Section 4.1, the applied line detector shows the following modifications.

- The detection of lines is restricted to bright lines only, since building structures such as corner lines are looked for. Thus, the relations $\mu_1 < \mu_2$ and $\mu_2 > \mu_3$ have to be fulfilled.

- The D1 detector of Tupin is implemented only because the homogeneity assumption of D2 could be critical in some cases. For instance, if layover and roof areas show regularly distributed bright point scatterers, the level of homogeneity will be low.

- No fusion of the probability values of different orientations is carried out since the searched buildings are assumed to be rectangular objects, and consequently lines are supposed to be straight. Moreover, they are believed to show their maximum in the probability image whose template orientation is closest to the real line orientation.

Hence, the applied detector delivers for each template orientation a single probability image; three of those are shown in Fig. 4.9 (second row) using a synthetic and an original SAR amplitude image as input.

The generation of primitives contains besides the described line detection also the segmentation, the fitting and the merging of lines, which is sketched in Fig. 4.10a. This short workflow is realised eight times in accordance with the number of template orientations. The magnitude data ($\overline{A}$ resp. $\overline{\sigma^0}$) and the vegetation mask $C_{veg}$ are the general input images. In the following, the details of the generation of primitives are discussed.

First, the line detection is accomplished providing the oriented probability images $p_o$ with $o = 1,...,8$. Furthermore, the three parameters $w_{t,n}$, $w_{t,c}$, and $l_t$ have to be defined to specify the widths and the length of the detector template (see Fig. 4.9a). The choice of these parameters is determined by SAR-processing parameters and building model assumptions. The width of a corner line depends on the applied weighting function specifying the geometric resolution $\delta_r$ and on the image pixel spacing $\Delta_r$ in range (see Subsections 2.1.3 and 3.2.2). Thus, $w_{t,c}$ defined in image pixels results from the ratio of $\delta_r / \Delta_r$. Since odd numbers are preferred, $w_{t,c}$ is often set to 3 pixels. Determining $w_{t,n}$ and $l_t$ implies information about the expected building size and the geometric resolution in azimuth. The detection results presented in this study are obtained by the settings $w_{t,n} = 5$ pixel and $l_t = 7$ pixel. Exemplarily, one of the eight probability images, for the vertical template orientation, is provided in Fig. 4.10b.

Second, the segmentation comprises a peak search and filtering of the probability images to achieve thinned out binary maps $b_o$. The thinning of the probability images $p_o$ takes place first by applying non-maximum suppression on every image row. As this has to be done orthogonally to the template orientation, all $p_o$ are individually rotated. Also, a probability threshold has to be defined that
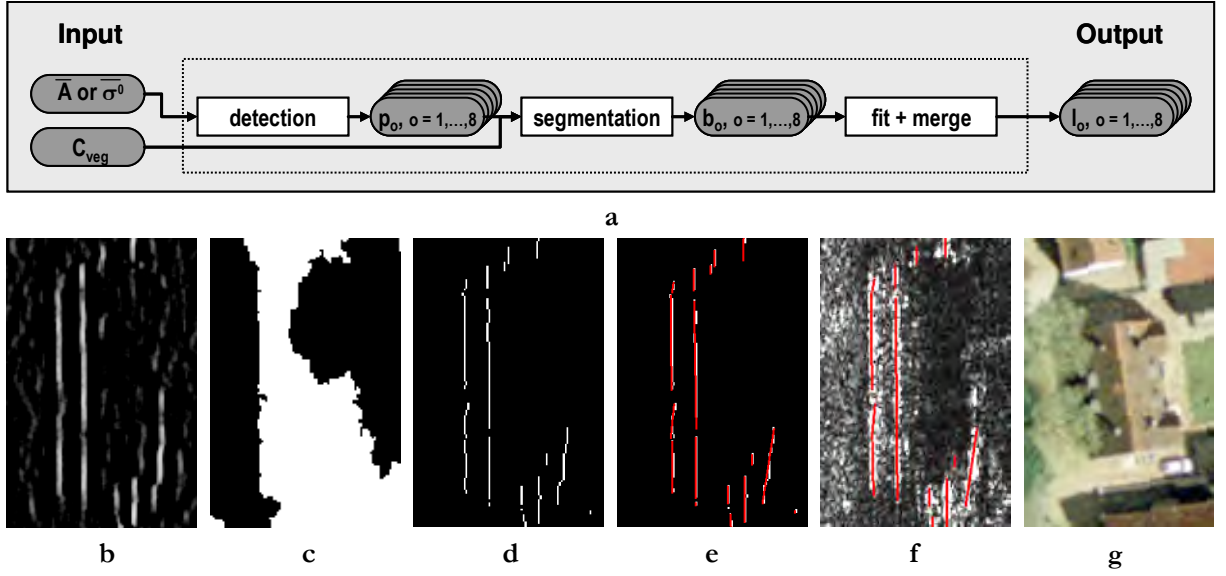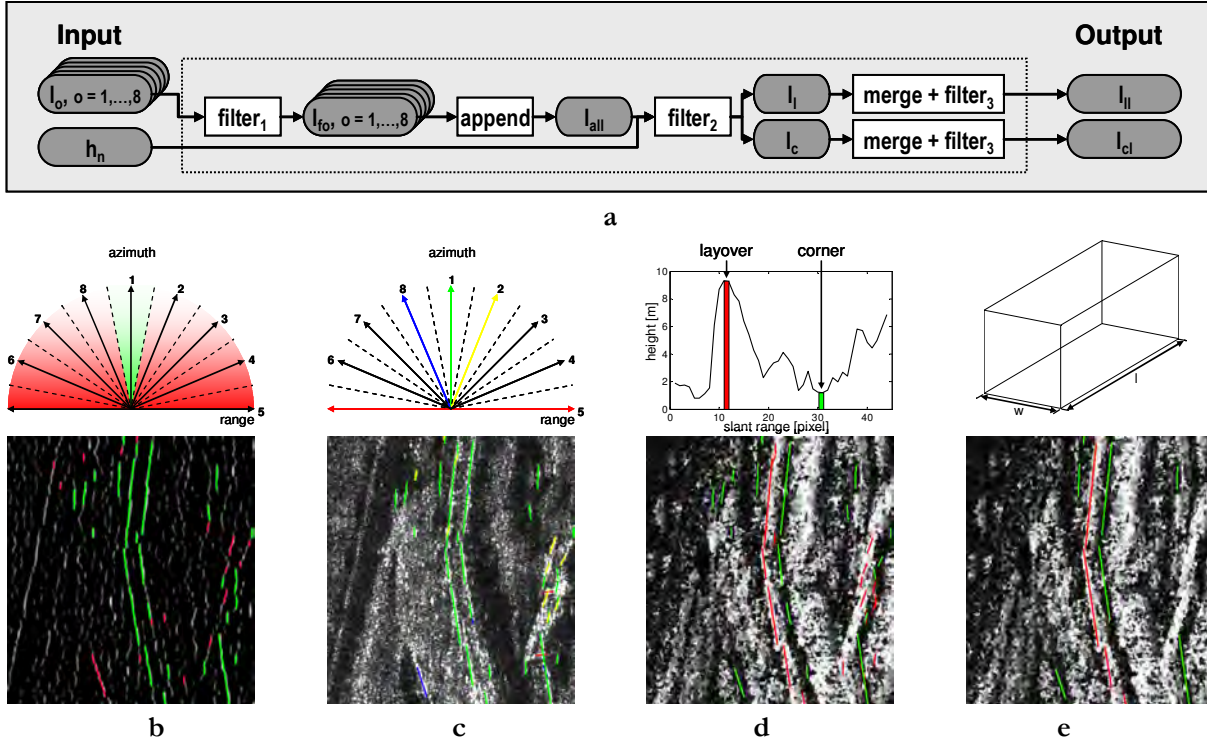
**Figure 4.10:** Generation of primitives: workflow (a), result of line detection $o = 1$ (b), vegetation mask (black = vegetation, c), line segments (d), fitted (e) and extended lines (f), optical signature of building (g)

corresponds to an acceptable false alarm rate. At this early stage of primitive extraction, a low probability threshold is preferred because subsequent filter steps reduce the number of false alarms in a proper way. Additionally, the vegetation mask $C_{veg}$ shown in Fig. 4.10c is used in the segmentation step. The intersection between white pixels, which are assigned to non-vegetated areas, and detected local maxima forms the binary outcome $b_o$ given in Fig. 4.10d.

In the third and last step, straight lines are fitted to each binary image $b_o$. Moreover, adjacent lines showing small distances are merged to longer ones with regard to the following three criteria: the lines have to fulfil constraints in terms of orientation and in the size of the gap between them. In Fig. 4.10e and f, the binary image $b_1$ and the magnitude image $\overline{A}$ are overlaid by the group of generated primitives $l_1$. The image patch contains two remarkable vertical lines that are caused by single and double-bounce reflections of the gable-roofed building (Fig. 4.10g). Both are successfully detected and primitives (lines) are generated. In summary, the advantages of this way of generating primitives are the integration of the CFAR detector and the restriction to straight lines matching the building model assumption.

### 4.6.2    Filtering of Primitives

The filtering of the generated groups of primitives $l_o$ comprises three individual filter steps carried out on only several or all primitives. In addition to the primitives $l_o$ also the normalised interferometric heights $h_n$ are used as input (see Fig. 4.11a). The first filtering applied on all groups of $l_o$ restricts the permissible orientation of primitives: only lines that match the template orientation of the underlying probability image are retained. The valid orientation interval and the resulting filtered primitives $l_{f1}$ of the vertical template are coloured green in Fig. 4.11b. The green lines shown on the lower part of Fig. 4.11b fulfil this orientation assumption; the red lines fail. This procedure ensures that all bright lines given in the magnitude image are only extracted once (i.e., in the prob-

**Figure 4.11:** Filtering of primitives: workflow (a), orientation based filtering (b), append primitives (c), height based filtering (d), merging and filtering of layover and corner lines (e)

ability image showing the maximum $r_{line}$ value). Subsequently, all groups of filtered primitives $l_{fo}$ are added to $l_{all}$. The magnitude image overlaid with these primitives is shown in Fig. 4.11c with the four most frequent orientations $o = 1, 2, 5, 8$ marked in green, yellow, red, and blue. The reason for the disproportionate number of primitives in the orientation intervals 1, 2, and 8 is the relative position of SAR sensor and ground object. With an increasing span angle $\kappa$ the corner lines decrease in intensity and disappear eventually (see [45] and [48]). Hence, bright lines with an orientation range in the intervals 3, 4 , or 6, 7 are rarely observed. In contrast to this, primitives belonging to the interval 5 are often caused by very strong scatterer side lobes.

The second filter step rates two features, the orientation of the primitives $l_{all}$ and the mean height along each primitive. For that, the normalised interferometric heights $h_n$ are used to calculate the necessary height feature by averaging over all pixel values belonging to the respective primitive. Only a subset of the whole group of bright lines $l_{all}$ is caused by double-bounce reflections. To distinguish those from bright lines resulting for instance from direct reflections, additional polarimetric information or interferometric heights are necessary. Since the first is not focused in this study, the second solution is utilised in this filter step. The expected differences in the height information are visualised on the signature of a gable-roofed building (Fig. 4.11d). This building complex is characterised by pairs of parallel lines, with the sensor close lines caused by direct reflection from the roof (coloured red) and the sensor far line caused by double-bounce propagation between façade and ground (coloured green). In the graph, a normalised height profile is given along range direction with marked layover and corner position. Moreover, the zero level of these normalised heights corresponds to the local terrain height (see Section 4.5). Focusing on the two lines, it is ob-

servable that the layover value is significantly higher than zero level because the direct reflection results from the building roof. In contrast, the corner value obtained by double-bounce reflection between ground and wall is much lower and close to zero level. In addition to the height, also the orientation of the primitives is used as filter criterion because, as already mentioned, primitives belonging to the interval 5 are no corners. In summary, this filter step comprises two features to derive corner lines and layover lines from the primitives $l_{all}$. Corner lines $l_c$ fulfil the height threshold ($h_n(l_c) \leq 2.5\,\text{m}$) and their orientation is within the interval $[-70°,+70°]$ with respect to the azimuth direction. For the layover lines $l_l$, the height value is set to $h_n(l_c) > 2.5\,\text{m}$ and the allowed orientation interval to $[-80°,+80°]$. The increase of the interval is due to the reason that some roofing materials can lead to direct reflection even under these unfavourable geometric conditions.

Before the third filter is applied, a merging is necessary since close-by lines assigned to successive orientations (e.g. $o=8$ and $o=1$) are not fused so far. The merging has to take place after the splitting into $l_l$ and $l_c$ because any mix among them is expressly undesired. Similar to the generation step, the lines have to pass an orientation tolerance and gap tolerances in range and azimuth direction. Subsequently, a filter criterion is deduced from the introduced building model: the final lines have to show a length longer than $\tfrac{2}{3}$ of the defined minimum building extensions (see Subsection 4.1.1). In Fig. 4.11e, the outcome ($l_{\parallel}$ coloured red and $l_{cl}$ coloured green) of this processing part is depicted that represents also the input of the building generation (Section 4.8).
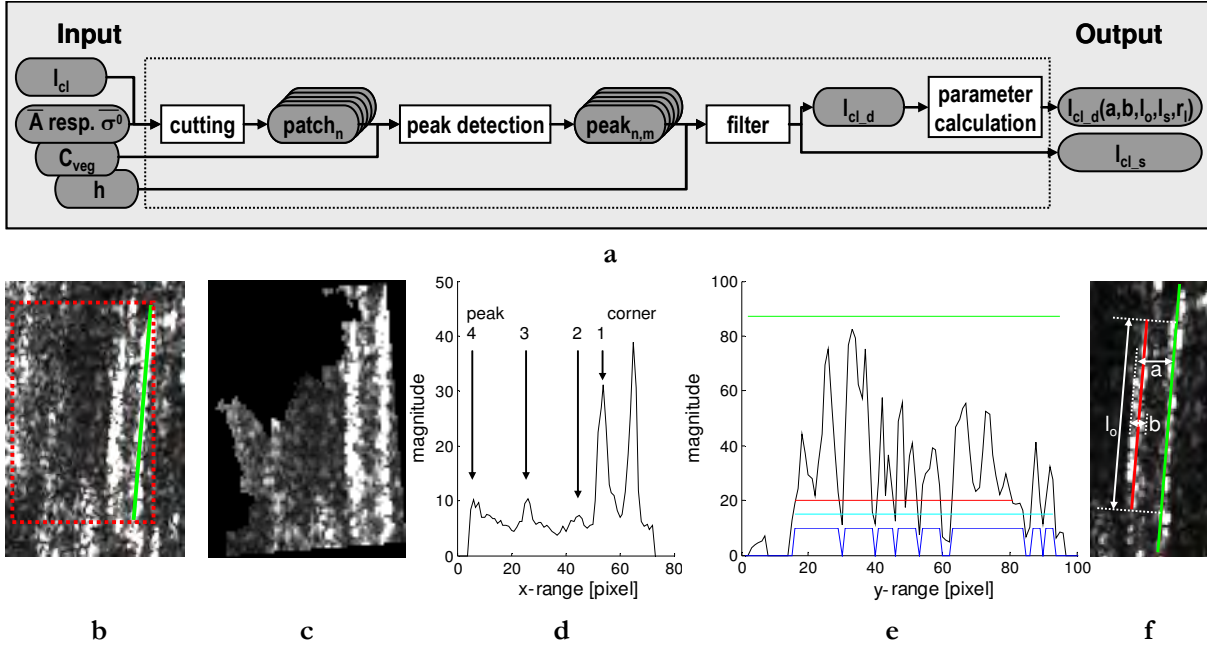
### 4.6.3    Extraction of Building Parameters

After discriminating corner from layover lines, additional building parameters are extracted from these primitives and the surroundings: the signature of parallel lines is searched that supports the determination of the building roof type. The strategy is depicted in Fig. 4.12a using the magnitude data ($\overline{A}$ resp. $\overline{\sigma^0}$), the vegetation mask $C_{veg}$, the interferometric heights $h$, and the corner lines $l_{cl}$ as input data.

First, a patch is extracted from the magnitude data containing a corner line $n$, with $n=1,...,\#l_{cl}$ and its sensor close surroundings (see dotted red line in Fig. 4.12b). In azimuth, the patch size is defined by the corner endpoints. The definition in range is independent of the corner; here the ambiguity interval $\Delta h_n$ and the off-nadir look angle $\theta_n$ are decisive. Since the interpretable building height is restricted to only half of $\Delta h_n$ (see Section 4.5), the maximum layover width can be calculated using equation (3-4). This width is also the maximum distance between a potential layover line and the corner line $l_{cl,n}$. By considering phase shifting during the calculation of the interferometric heights, the patch size can be enlarged in range.

Second, peak detection is carried out. The extracted $patch_n$ is filtered with the vegetation mask $C_{veg}$. Thus, potential layover lines are not searched for in vegetated areas. Furthermore, the masked $patch_n$ is rotated to achieve a vertically oriented corner line, which simplifies the subsequent analysis. From the resulting patch shown in Fig. 4.12c, an averaged range profile is calculated and magnitude peaks are detected. The group of $peak_{n,m}$, with $m=1,...,4$ in the given example of Fig. 4.12d, is analysed by starting with the peak closest to the corner.

Third, the different criteria considered to evaluate a $peak_{n,m}$ are summarised in the filter step. The azimuth profile at peak position (Fig. 4.12e) is rated to estimate the amount of pixels contributing

**Figure 4.12:** Extraction of building parameters: workflow (a), input information (b), rotated and masked corner patch (c), averaged profile of peak detection (d), filtering of parallel lines (e), and sketch of parameter extraction (f)

to the high magnitude value of the peak. Azimuth pixels are considered as potential line pixels (marked blue in Fig. 4.12e) when showing a magnitude value higher than half of the peak value (see Fig. 4.12d). Additionally, a line (coloured cyan) is fitted to these pixels. This line will be very short, if only a bright scatterer leads to the peak in the range profile, but long if an extended layover line exists. Hence, the first criterion is specified by the overlap of the potential layover line (cyan) and the corner line (green): a minimum overlap of 40 percent is requested. Higher values would diminish the extraction of layover lines caused by hipped roofs (see Subsection 4.1.2, Fig. 4.2). The second criterion evaluates the height-distance relation that can be deduced from equation (3-4). It states that the height difference between potential layover line and corner line has to fit with the range distance in the mean profile (Fig. 4.12d). Since noisy height values can distort the averaged height value along the potential layover line, the height difference is only required to be greater than half of the height obtained from the range distance between the lines. As third point, the line detection (Subsection 4.6.1) is carried out by testing different detector template widths $w_{t,c,u} = 2u+1$ (see Fig. 4.9) with $u = 1,2,...$. The resulting detection values along the layover line are averaged in y-direction to obtain $r_{line,u}$. If at least one element of $r_{line,u}$ is greater than the defined probability threshold, we assume that the tested magnitude peak in the range profile is a layover line. This described three-stage analysis is done one by one for each peak, but will stop immediately if one peak fulfils all three criteria.

At least five final parameters are calculated and assigned to the corner line $l_{cl\_d}$ by analysing the range and the azimuth signature of the extracted double line. From the range signature, four different groups of building hypotheses can be generated (Fig. 4.13a-d) showing the same layover width (parameter $b$) and distance between layover and corner (parameter $a$). For the gable-roofed build-
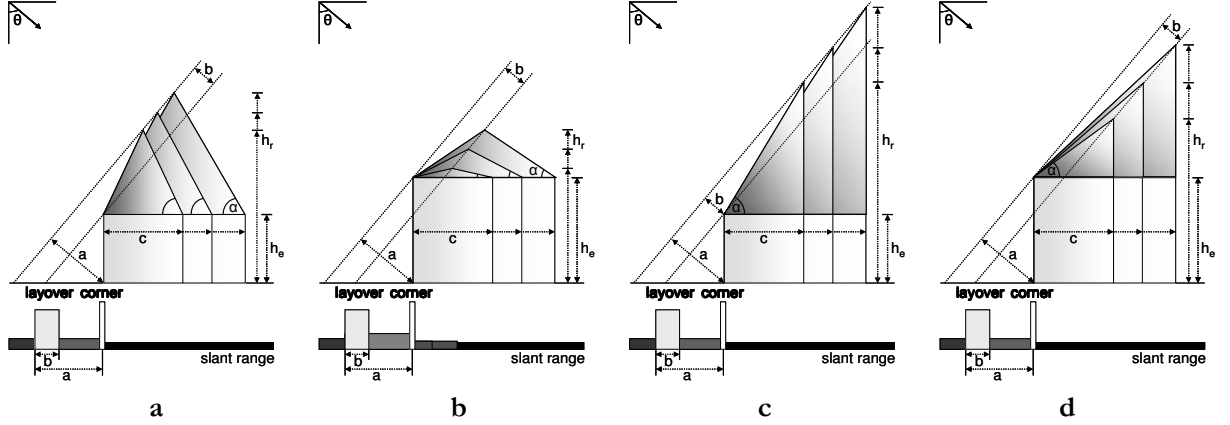
**Figure 4.13:** Schema of building hypotheses: gable- (a – $\alpha > \theta$, b – $\alpha < \theta$) and monopitch-roofed hypotheses (c – $\alpha > \theta$, d – $\alpha < \theta$) derived from only one primitive $l_{cl\_d}(a,b)$

ing group (Fig. 4.13a), defined by a roof pitch angle $\alpha$ greater than the off-nadir look angle $\theta$, the layover maximum results from direct signal reflection of roof and ground. The corresponding monopitch-roofed group of hypotheses is shown in Fig. 4.13c. The other two groups of buildings (Fig. 4.13b,d), leading to the same magnitude profile, are characterised by $\alpha$ smaller than $\theta$. Hence, the bright layover part contains signal from roof, wall, and ground. A reduction of these four groups of hypotheses can be achieved by considering another aspect direction enabling the extraction of the parameter $c$, the width of the building in range direction (see Subsection 4.8.2). Beyond the range signature, the azimuth signature can be used to decide whether a gable or a hipped roof contributed to the layover line. As described on simulated data (see Fig. 4.2), the first will show layover and corner lines of similar length, where the hipped roof will lead to a symmetric shortening of the layover line. Thus, the overlap $l_o$ between layover and corner line as well as the symmetry measure $l_s$ between both is extracted from the azimuth signature.

All of the parameters ($a$, $b$, $l_o$, $l_s$) are derived from the best line detection result $r_l = \max(r_{line,u})$: $b$ is given by the layover width $w_{t,c}$, and $a$ is defined by the sum of half of the layover width $w_{t,c}/2$ and the distance between layover and corner line (see Fig 4.12f). Since $w_{t,c}$ and the distance between $peak_m$ and corner $l_{cl\_d}$ are extracted in the rotated magnitude image, the values have to be corrected. Furthermore, a conversion from pixel space to metric slant range values is necessary by taking into account the range pixel spacing. Additionally, effects due to SAR processing (e.g. apodization function) are corrected, so that for example the parameter $b$ only contains the widening component (see Subsection 4.8.2). The parameters $l_o$ and $l_s$ are derived from the line detection values of $r_l$ in y-direction. All y-positions showing a value higher than the probability threshold are used to fit the layover line (marked red in Fig. 4.12e,f). The overlap $l_o$ is defined by the ratio of layover and corner length, and takes at best a value of 1. The y-offsets between the layover and corner endpoints specify the symmetry parameter $l_s$ taking values in the interval [0,1]. For optimal hipped roof signatures showing symmetric shortening of the layover line, this value $l_s$ will become 1. Finally, $r_l$ is recalculated by averaging only line detection values along the fitted layover line (coloured red line in Fig. 4.12f).

To summarise this section, the final output objects are layover lines $l_{\parallel}$, single corner lines $l_{cl\_s}$, and double corner lines $l_{cl\_d}$ (see Fig. 4.8), whereby only the last group provides detailed information concerning the roof type.

## 4.7 Slant to Ground and Ground to Slant Projection

The extraction step delivers building features (i.e., layover and corner lines) in the individual slant range geometry of every InSAR image pair. Since a fusion of the multi-aspect building features is requested, a projection, also known as geocoding or orthorectification, is necessary. In this step, all features of each aspect are transformed from slant range to ground range geometry into a common world coordinate system. In the following, only the specific points due to the projection of the building features are discussed, and selected projection results are presented. More information concerning SAR geocoding can be found in [104].

In general, for the geocoding the 3D position of each image pixel has to be specified to project them to a reference plane in the chosen ground range coordinate system. Thus, two main steps have to be carried out: the calculation of the 3D coordinates of each image pixel relative to the centre of the earth ellipsoid and the orthogonal projection of the imaged surface to a reference plane. For the coregistration of InSAR image pairs (Section 4.3), the orthorectification is implemented in commercial software (e.g. SARscape modules for ENVI and ERDAS IMAGINE) and free software like the Next ESA SAR Toolbox. As input, the image data, acquisition specific parameters (e.g. track points of the sensor, velocity vectors of the sensor, and sensor flight height over ellipsoid) and a height model are required. In general, these products do not support airborne data, for which an in-house solution was used.

The investigated geocoding tool supports the projection from slant to ground geometry by use of external height data, or, more interesting, by use of slant range interferometric heights. Hence, the processed interferometric heights can be utilised to enable the geocoding of the building features. The preparation of a suitable height image is visualised in Fig. 4.14. A local InSAR height $h_l$ is assigned to each building feature by averaging all pixel values along the corner or layover line sketched by the dotted white rectangle in Fig. 4.14b. Then, a height mask of size similar to the SAR image is generated. This mask is filled by a constant height value preferably equal to mean terrain height. At the endpoints of the features, the individual feature height $h_l$ is inserted (Fig. 4.14c). To avoid overlapping effects between corner and layover lines, the preparation of the height mask is done separately for each feature group. The subsequent geocoding requires as input the sensor track coordinates and the height mask. As result, shift vector fields containing the x- and y-offsets of the image transformation are obtained. These offsets are used to project the building feature from slant to ground range geometry. A geocoding result of two corner lines is shown in Fig. 4.14e, where local heights $h_l$ are assigned to the yellow corners (c) and mean terrain height to the green corners (d). In this overlay of LIDAR DSM and geocoded corner lines, a shift inside the building is clearly visible due to the difference between local feature and mean terrain height. Furthermore, it is observable that the building corner line is directly located at the building footprint, if the local feature height is considered.
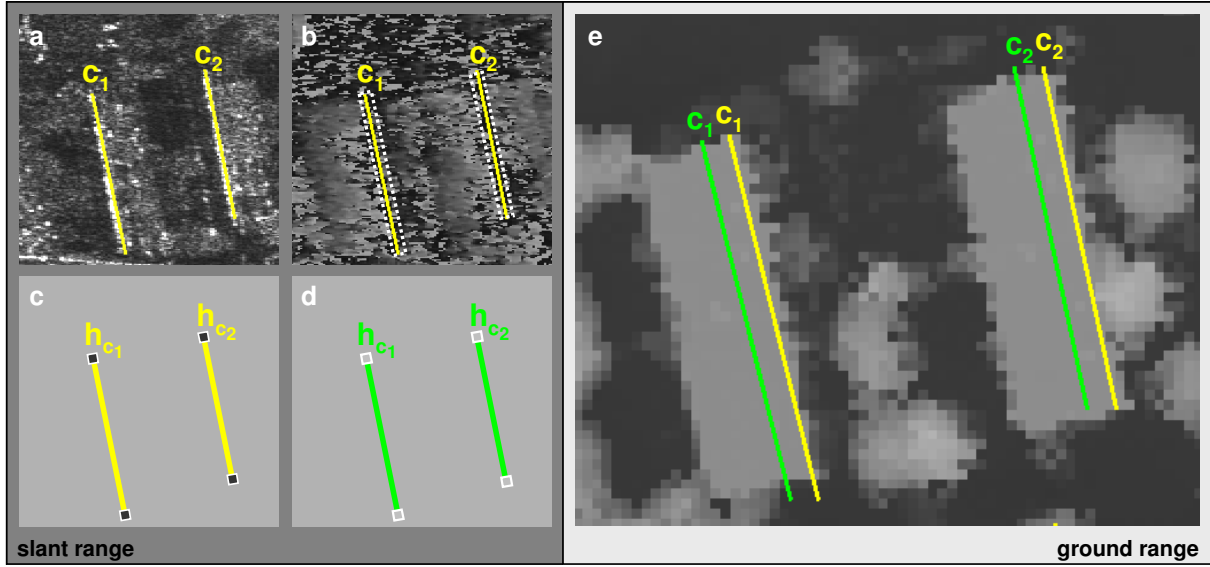
**Figure 4.14:** Projection of building features: magnitude (a) and interferometric height data (b) overlaid with two corner lines, height layer considered for geocoding using local corner height at endpoints (c) or constant terrain height (d), LIDAR DSM overlaid with geocoded corner lines (e)

Additionally, the geocoding result of two orthogonal flight tracks superimposed onto a LIDAR DSM is given in Fig. 4.15a. The corner lines of the first flight direction, corresponding to top-down illumination, are marked in red, the corner lines of the second direction in yellow. The set union of these corner lines reveals the benefit of multi-aspect views that is further discussed in the next section. Both views complement one another resulting in much more accurately detected parts of the building outlines. Beyond the corner lines, also the layover lines are geocoded by use of the averaged local InSAR height. The layover and corner lines of three hipped-roofed buildings are shown in Fig. 4.15b. From the first data ($r_1$), no corner lines but four layover lines ($l_1$, $l_2$, $l_3$, $l_4$ – marked blue) are extracted. The same is observable for the second view ($r_2$), only the three layover lines ($l_1$, $l_2$, $l_3$ – marked green) are fully detected. The missing corner lines in both images are marked in magenta and cyan. The geopositions of the layover lines show a shift to the inside of the building footprint. This offset depends on the calculated feature height specified by the contribution mixture in the layover area. For gable- and hipped-roofed buildings, it is often the case, that the layover line selected at the side of the sloping roof (marked green) is shifted towards the building ridge line. On the other building side, layover lines ($l_1$, $l_2$, $l_3$ – marked blue) are mostly characterised by a smaller offset. In the following, these different geopositions and feature constellations are analysed and first building hypotheses are generated.

In addition to the geocoding of the building features, the classification result $C_{veg}$ is projected from slant to ground geometry. As height information, the mean terrain height is taken into account. If this is done for all multi-aspect data individually, the fusion step – calculating the intersection between the classified *vegetated areas* – can be accomplished (Subsection 4.4.2). Only those areas are considered as $C_{veg\_fus}$, which belong to $C_{veg}$ in all InSAR aspects. This mask will be used to reduce the number of false alarms in the following processing step.
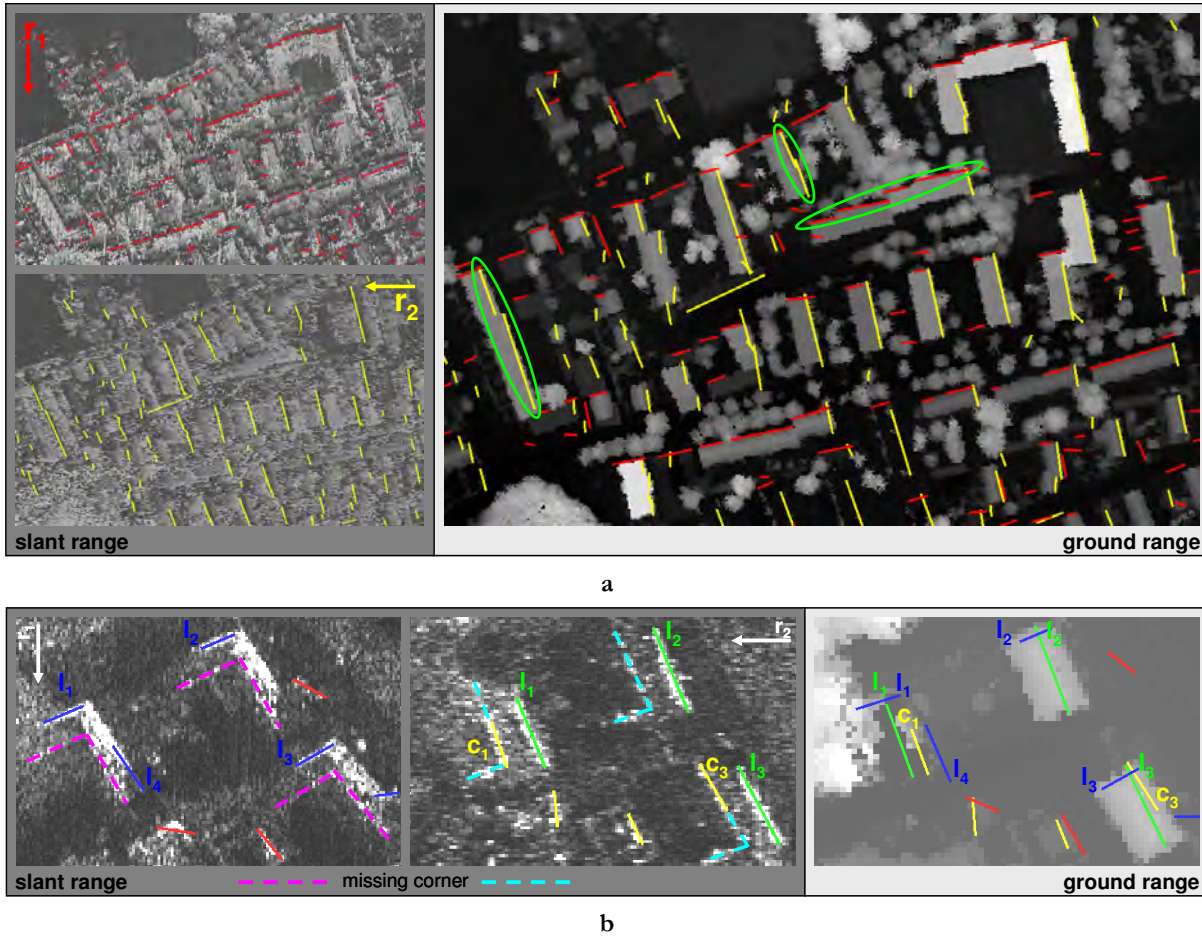
**Figure 4.15:** Geocoding result of two orthogonal flight tracks: slant range – height image overlaid with corner lines, ground range – LIDAR DSM overlaid with geocoded corner (a); slant range – magnitude image overlaid with all extracted features, ground range – LIDAR DSM overlaid with geocoded features (b)

Besides the slant to ground projection, the reverse ground to slant projection takes place. This back projection is used within the step of extracting the building height, which is described in detail in Subsection 4.8.2. Similar to the slant to ground projection, a height image is generated by using In-SAR height information. For this, the extracted feature heights $h_l$ are assigned to the corner points of the generated building parallelograms. Based on the projected building footprints, the average building height is calculated. Thus, a projection of the InSAR heights can be skipped to avoid interpolation effects. Furthermore, by using one height value for all four building corners, the shape of the building footprint is preserved. Results of the back projection and some further remarks are given in Fig. 4.19 and Subsection 4.8.2.

## 4.8     Generation of Building Hypotheses

This section is subdivided into two parts. The step of generating 2D building hypotheses is described making use of the previously extracted corner lines $l_{cl\_s}$ and $l_{cl\_d}$ and layover lines $l_{\parallel}$. Fre-

quently appearing constellations of corner and layover lines spanning orthogonal L, T, or X-shaped structures are exploited. The utilization of such simple geometric structures was also published, for example, in [114] and [148]. In [114], L- and T-shaped bright features are extracted from multi-view SAR data. The detection of L-structures from multi-aspect SAR data was presented in [148]. Beyond the generation of the building footprint, the building roof type is selected, considering flat-, gabled-, hipped-, and monopitch roofs. At the end the building heights and roof angles are derived from the normalised interferometric height $h_n$ and the parameters $a$, $b$, $l_s$ and $l_o$.

### 4.8.1    Building Footprint

Before starting the grouping of right-angled structures, the flat-roofed assigned corner lines $l_{cl\_s}$ and the layover lines $l_{ll}$ are combined to longer lines. This is especially helpful for the reconstruction of stepped buildings (marked green in Fig. 4.15a), where a separation of the corner lines is visible. This is performed in ground range geometry because a fusion in slant range would lead to an imprecise $h_l$ and thus to worse geocoding results. Since the prolongation step should not mix line features from different aspects, it is accomplished individually for each viewing direction.

In the next step, the generation of potential building footprints starts with the search of right-angled crossings of lines taking layover and corner lines of all aspects into account. The pairs of lines have to fulfil orientation, bridging, and gap tolerances. As result, L-, T-, and X-shaped line structures are derived, which deliver as potential building footprints one, two or four parallelograms (Fig. 4.16b). The set $pg_{all}$ of parallelograms is divided in to three subclasses ($pg_{cc}$, $pg_{cl}$, and $pg_{ll}$), which are specified by the type of combined building features (corner or layover lines). Furthermore, different assumptions in terms of parallelogram orientation and position are applied depending on the type of features that are combined. Since the main data set of this study is taken by flying two orthogonal tracks, some constraints are related to this configuration (see Section 5.1).

### Building Footprint from Corner-Corner Pairs

The class $pg_{cc}$ of parallelograms results from L-, T-, and X-shaped structures of two corner lines. For the generation of these parallelograms all $l_{cl\_s,i}$ and $l_{cl\_d,i}$ are taken into account with $i = 1,2$ specifying the aspect direction. In the next steps, the set $pg_{cc}$ are filtered by utilising flight geometry and feature properties. In Fig. 4.16a, the different orientations of resulting parallelograms $pg_{cc}$ are visualised by black angles. Lines dotted in black show the extension to a full parallelogram. In dense urban areas, where many building corners are located close-by, it may happen that corner lines of different buildings are combined to parallelograms $pg_{cc}$. However, under the condition that corner lines appear only on the sensor facing sides of a building, not all of the black angles are present in multi-aspect data of orthogonal flight geometry. This is illustrated by colouring potential building corners of track 1 and track 2 in red and yellow. From this, it is observable that permitted corner combinations cover only a subset of orientations (segment marked in dark grey). By exploiting this orientation segment, it is possible to eliminate false alarms in the group of $pg_{cc}$. To summarise this for orthogonal flight directions, only those $pg_{cc}$ are suitable, which form an angle of corners with the exterior to the two flight paths.
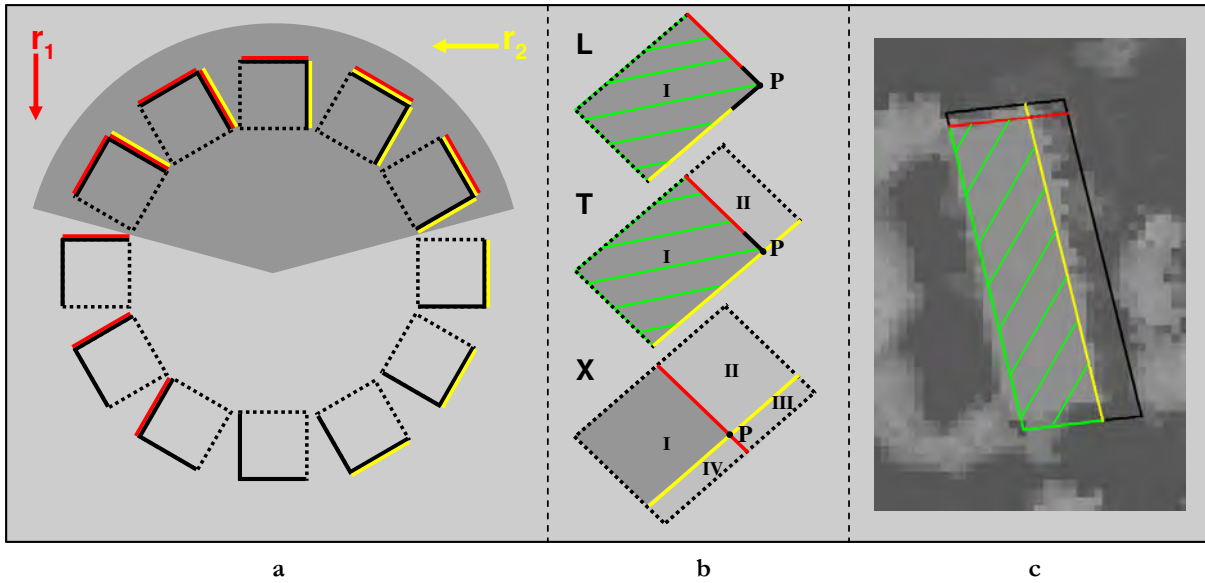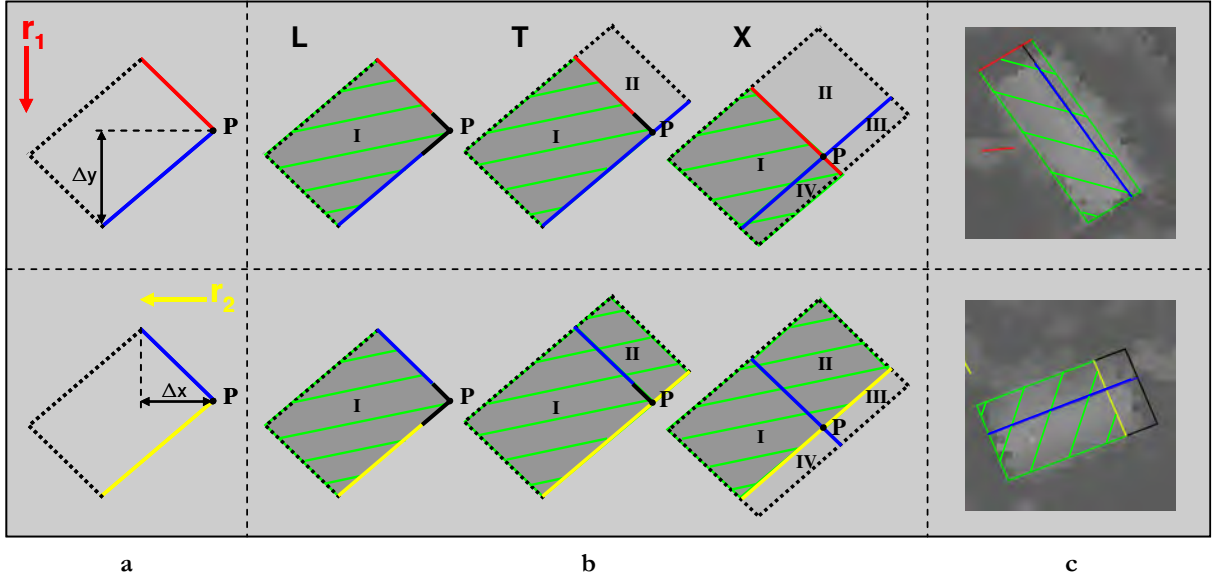
**Figure 4.16:** Generation of parallelograms $pg_{cc}$ from two corner lines: filtering of $pg_{cc}$ by considering view direction (a), filtering of formed $pg_{cc}$ (L-, T-, and X-structure) by considering span area (b), $fp_{cc}$ – result of footprint generation based on X-structure(c)

In Fig. 4.16b, three examples of crossing corner pairs are shown, where $P$ marks the crossing point of the two lines. The first figure shows the L-shape forming one $pg_{cc}$ (I). The second, spanning a T-structure, delivers two $pg_{cc}$ (I, II). Additionally, the third figure showing are X-shape leads to four parallelograms (I-IV). To reduce the $pg_{cc}$, first the orientation assumption is used, which is only fulfilled by the $pg_{cc}$ (I) (marked in dark grey). In a second filter step, the size of the remaining $pg_{cc}$ is analysed. Since corner lines describing the outer boundary of the building are searched, the $pg_{cc}$ has to take most of the area spanned by the T- or X-structure. That is the case if $P$ is located on the half of the corner lines closer to the sensor for both flight directions. This is true for the example of a T-structure in Fig. 4.16b, but not for the exemplary X-structure. In the algorithm, as filter criterion an area ratio $r_{area}$ is introduced evaluating the proportion of $area_{pg_{cc}}$ and $area_{struct}$ with $struct = L, T, X$: only $pg_{cc}$ showing $r_{area} > 0.5$ are considered. For the visualised three examples, only two $pg_{cc}$ accomplished this area constraint (shaded green in Fig. 4.16b) and are treated as potential building footprints termed $fp_{cc}$. A real building example of an X-shaped corner structure is shown in Fig. 4.16c. Here the parallelogram shaded in green fulfils the orientation and area constraints.

## Building Footprint from Corner-Layover Pairs

The class $pg_{cl}$ of parallelograms results from L-, T-, and X-shaped structures composed by one corner and one layover line. For that, all corner lines ($l_{cl\_s,i}$, $l_{cl\_d,i}$) and all layover lines ($l_{ll,i}$) are taken into account with $i = 1, 2$ specifying the aspect direction. Similar to the first group $pg_{cc}$, it may happen that also in the group $pg_{cl}$ line features of different buildings are combined. To reduce these false alarms, the position of the layover line in relation to the corner line is analysed. In Fig. 4.17a, two parallelograms are visualised containing a corner of track 1 or track 2 (coloured in red and yellow). With respect to the SAR geometry, the corner line has to be found at the sensor close build-

**Figure 4.17:** Generation of parallelograms $pg_{cl}$ from corner and layover lines: filtering of $pg_{cl}$ by considering the $\Delta x$ and $\Delta y$ part of the layover line (a), parallelograms formed by L-, T-, and X-structure (b), $fp_{cl}$ – results of footprint generation based on T- (top, c) and X-structure (bottom, c)

ing side. Hence, the orthogonal layover line forming the potential building footprint has to be located at the sensor far side of the corner line. This location constraint can be tested by evaluating $\Delta x$ and $\Delta y$ between the crossing point $P$ and endpoint of the layover line (see Fig. 4.17a). For the two considered aspects, $\Delta y > 0$ has to be fulfilled for track 1 and $\Delta x > 0$ for track 2. Parallelograms $pg_{cl}$ of an L-, T-, and X-structure are given in Fig. 4.17b. Since for the T- and X-structure more than one parallelogram $pg_{cl}$ complies the location constraint (coloured dark grey), the remaining $pg_{cl}$ have to be fused. The final parallelograms, the potential footprints $fp_{cl}$, are shaded green. In Fig. 4.17c, real building examples are shown for track 1 (T-structure) and track 2 (X-structure).

### Building Footprint from Layover-Layover Pairs

The last of the three classes contains parallelograms $pg_{ll}$ formed by L-, T-, and X-shaped structures of two layover lines, considering $l_{ll,i}$ with $i = 1,2$. In contrast to $pg_{cc}$ and $pg_{cl}$, no filtering can be applied because layover lines can be located at the sensor close building side, inside the building, or at the sensor far building side. Hence, all $pg_{ll}$ are assumed to be a potential building footprint or a part of them. This is visualised in Fig. 4.18a for all three structures. For the line pairs generating more than one $pg_{ll}$, a fusion step has to take place similar to the $pg_{cl}$ generation. The final bounding parallelograms, the footprint hypotheses $fp_{ll}$, are shaded green in the schematic view (a) and in the real building example (b).

### Post-processing of Building Footprints

The three groups $fp_{cc}$, $fp_{cl}$, and, $fp_{ll}$ of potential building footprints are post-processed by utilising the processed vegetation mask $C_{veg\_fus}$ and by using the constraints to the building model defined in Section 4.1. First, an enclosing rectangle is assigned to the potential footprints. Second, the inter-
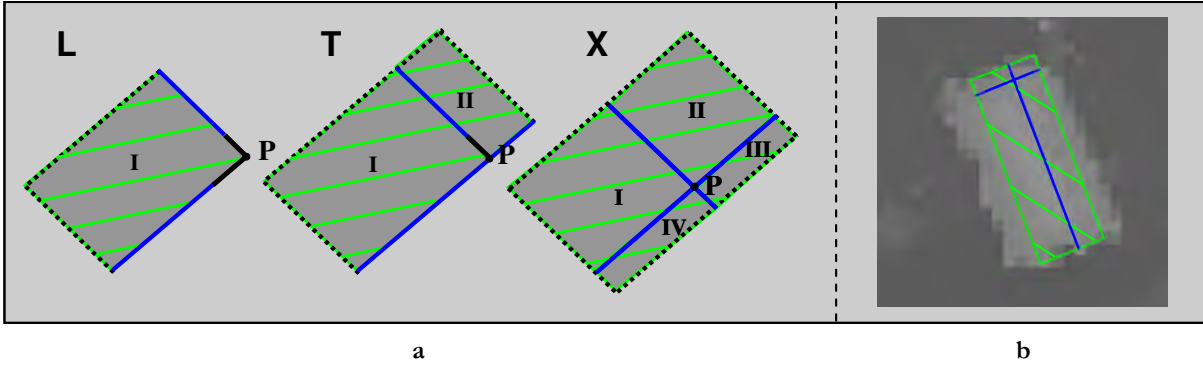
**Figure 4.18:** Generation of building footprints from layover lines: parallelograms formed by L-, T-, and X-constellations (a), $fp_\parallel$ – result of footprint generation based on X-structure (b)

section between the generated footprints and the vegetation mask is determined. A threshold $th_{veg}$ is introduced, filtering out candidates whose overlap with the classified vegetated area is more than $\frac{1}{3}$ of the footprint size. Third, the lengths of the parallelogram sides as well as the footprint size have to meet model constraints: the footprint sides have to be longer than $5\,\text{m}$ and the area of the footprint larger than $25\,\text{m}^2$. The result of these steps are filtered groups of parallelograms $fp_{cc\_f}$, $fp_{cl\_f}$, and, $fp_{\parallel\_f}$. These groups are divided in three different reliability levels, whereby $fp_{cc\_f}$ gets the highest since two corner lines define the building footprint at best. The lowest reliability is referred to the group $fp_{\parallel\_f}$ because layover lines probably do not delineate the building footprint. In the last processing step (Section 4.11), these levels are used to handle overlapping building footprints. In the following, based on the three groups of 2D building footprints $fp_{cc\_f}$, $fp_{cl\_f}$, and $fp_{\parallel\_f}$, the roof type and the building heights are calculated.

### 4.8.2 Building Heights

The height of buildings can be extracted by exploiting the SAR magnitude or the InSAR phase signature: the length of the layover and the length of the shadow enable the extraction of the building height. The relevant equations were presented in Subsection 3.3.1. The interferometric phase signature of buildings also contains the height information. In previous studies (see [13] and [115]), the building heights are extracted by averaging the InSAR heights inside the extracted footprint. As quality measure, the interferometric coherence is used to weight the InSAR heights. Multi-aspect InSAR heights are fused in ground range geometry. Additionally, the roof type of the building is extracted by analysing the shape of the building shadow and by fitting oblique planes to the InSAR heights. These strategies are less useful for the reconstruction of smaller buildings because most of the roof signature is superimposed with signature of building wall and ground. Moreover, in dense urban areas intersection with close-by vegetation and neighbouring buildings makes the analysis of shadow areas difficult, if not impossible.

In this thesis, a combination of exploiting the magnitude and the interferometric phase signature is presented. With the exception of the flat roof heights, the analysis of the layover signature provides most information. First, the search for double lines takes place in the magnitude data (see Subsection 4.6.3). Subsequently, from the extracted parameters, 3D building hypotheses are formed. The use of the InSAR phases in the layover area of such hypotheses will be described in the post-

processing (Subsection 4.11). For the calculation of flat roof heights, only the InSAR phase signature is exploited. In the following, first the extraction of the building roof type is briefly outlined. Second, the calculation of the flat-, gable-, monopitch-, and hipped-roofed building heights are described. In the last paragraph, observed ambiguities and challenges of the height extraction are presented to motivate the subsequent processing steps.

**Extraction of Building Roof Type**

Before the building height extraction can be started, the roof type of each building footprint $fp$ has to be determined. For this, the combination of primitives $l_{cl\_s,i}$, $l_{cl\_d,i}$, or $l_{ll,i}$ used to generate the building footprint is investigated. At first, only two different types can be distinguished – the group of flat and non-flat roofs. They are characterised by the following combinations of building features:

$$\text{flat roof}: \qquad (l_{cl\_s,i}; l_{cl\_s,i}) \text{ or } (l_{cl\_s,i}; l_{ll,i}) \text{ or } (l_{ll,i}; l_{ll,i})$$
$$\text{non-flat roof}: (l_{cl\_d,i}; l_{cl\_d,i}) \text{ or } (l_{cl\_d,i}; l_{cl\_s,i}) \text{ or } (l_{cl\_d,i}; l_{ll,i})$$

In a second step, the extracted overlap and symmetry parameters $l_o$ and $l_s$ of the features $l_{cl\_d,i}$ are analysed to discriminate between the groups of gable/monopitch roofs and hipped roofs. To be assigned to the group of hipped-roofed buildings, the analysed double lines (see Subsection 4.6.3) have to fulfil two constraints. The definition of these threshold values is assisted by the analysis of real measured SAR signatures. For the overlap ratio $l_o$, the first constraint, it was observable that the double line signature shows no full overlap for monopitch buildings but as well as for most of the gable-roof buildings. This is caused by nonparallel ridge line and azimuth direction ($\kappa > 0$) or by occlusion effects. Hence, for this parameter the interval $[0.2, 0.6]$ was chosen. The second, the symmetry parameter $l_s$, is also affected by the angle $\kappa$. With rising span angle, the symmetry of the shortening of the layover line is decreasing. To compensate this effect, we decided to accept all double line signatures showing $l_s$ greater than $0.5$. In the following, for each group of roof type the height extraction is described.

**Height of Flat-roofed Buildings**

For the calculation of the flat-roofed building height $h_f$, the normalised InSAR heights are used. Since these heights are given in slant range geometry and a projection to ground range would lead to interpolation artefacts, the building footprints $fp$ are back projected. As described in Section 4.7, a height map is generated by inserting height values at the four building corners. For that, the feature height $h_l$ of the corner primitives $l_{cl\_s,i}$ is used. The building footprints $fp_{ll\_f}$ are back projected by assigning the mean terrain height.

Moreover, the decision has to be made into which slant range geometry of the multi-aspect data the building hypotheses are projected. The aspect facing the shorter building side is taken, as this choice enhances the chance to find an area of single backscattering of the roof. This is required because the building height will be extracted inside the back projected building footprint. In Fig. 4.19 the height map and the projected footprints are visualised for one building hypothesis. The height map containing local feature heights at the building corners is shown in Fig. 4.19a. The
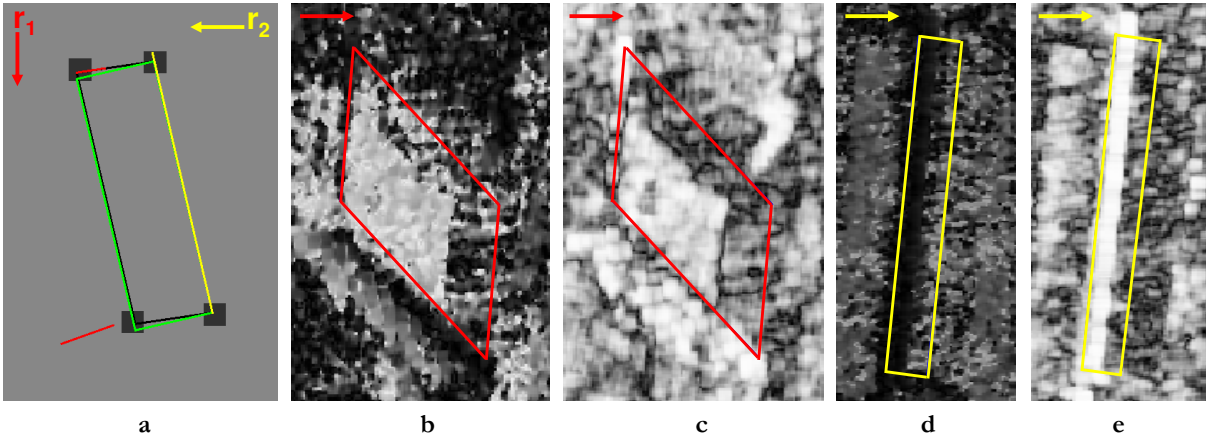
**Figure 4.19:** Calculation of the flat-roofed building height: generated height map overlaid with building footprint and corner lines (a), normalised heights $h_n$ and coherence values overlaid with back projected building footprint – aspect $r_1$ (b,c) and aspect $r_2$ (d,e)

normalised heights of aspects $r_1$ and $r_2$ overlaid with the back projected building footprint are shown in (b) and (d). The homogeneous heights resulting from single backscattering are only observable inside the building footprint of $r_1$ (see Fig. 4.19b). For aspect $r_2$, the backscattering of the roof is fully superimposed with signals of wall and ground in the layover area (see Fig. 4.19d). Hence, the selection of the shorter building side – here aspect $r_1$ – will lead to better height extraction results. Finally, the flat roof height $h_f$ is calculated by averaging all heights $h_{n,j}$ inside the building footprint. Furthermore, all these pixel values are weighted by their coherence $\gamma_j$, which is visualised in Fig. 4.19c,e. The resulting flat-roofed heights $h_f$ are relative height values as the normalised heights $h_{n,j}$ are taken into account.

In the example, a discrepancy between building footprint and real roof height values is apparent due to the displacement of elevated objects. As result, the building footprint contains large areas of shadow characterised by random heights and low coherence. This can lead to an underestimation of the roof height. To compensate this, a post-processing of the building height is implemented that will be described in Subsection 0. Building footprints that are too large due to incorrect building feature extraction show the same effect of underestimation. This will be discussed in Subsection 4.11.3.

### Heights of Gable-, Monopitch-, and Hipped-Roofed Buildings

Similar to the calculation of $h_f$, first the aspect direction has to be chosen in which the height extraction is carried out. If one feature $l_{cl\_d,i}$ is combined with a feature of $l_{cl\_s,i}$ or $l_{\parallel,i}$, then the index $i$ of the $l_{cl\_d,i}$ is used. The combination of two features of $l_{cl\_d,i}$ is rather rare. In this case, the aspect facing the longer building side is chosen.

In order to determine the heights of gable-roofed or monopitch-roofed buildings, the ambiguity problem presented in Fig. 4.13 has to be solved. First, the model parameter $c$ (i.e., the building width in slant range direction) has to be determined from the building width $w$ and the span angle $\kappa$ (see Subsection 3.3.1) using equation (4-10). A building example is depicted in Fig. 4.20a show-
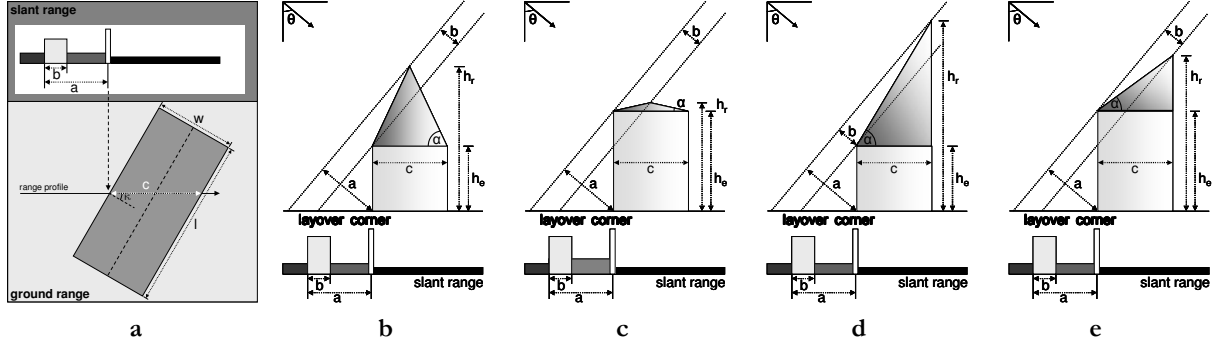
**Figure 4.20:** Height extraction by using model parameters $a,b,c$: extraction of parameter $c$ (a), schema of two gable- (b,c) and two monopitch-roofed (d,e) hypotheses described by one parameter set $a,b,c$, and $\alpha > \theta$ (b,d) and $\alpha < \theta$ (c,e)

ing the right-angled footprint in ground range and a corresponding magnitude range profile in slant range geometry.

$$c = \frac{w}{\cos \kappa} \tag{4-10}$$

With the additional parameter $c$, the groups of hypotheses sketched in Fig. 4.13 can be reduced to one hypothesis per group. In Fig. 4.20b-e, these four hypotheses with $\alpha > \theta$ (b,d) and $\alpha < \theta$ (c,e) are visualised showing an identical magnitude signature in the slant range geometry. Using the three model parameters $a,b,c$ and the off-nadir look angle $\theta$, the three remaining building parameters for 3D reconstruction can be calculated: the pitch angle $\alpha$, the eave height $h_e$, and the ridge height $h_r$ of the hypotheses. For gable-roofed buildings, the corresponding equations are given in (4-11).

$$\alpha_g \geq \theta: \quad h_{e\_g} = \frac{a-b}{\cos\theta} \quad \text{and} \quad h_{r\_g} = h_{e\_g} + \frac{c}{2} \cdot \tan\alpha_g, \quad \text{with} \quad \tan\alpha_g = \tan\theta + \frac{2\cdot b}{c\cdot\cos\theta}$$
$$\alpha_g \leq \theta: \quad h_{e\_g} = \frac{a}{\cos\theta} \quad \text{and} \quad h_{r\_g} = h_{e\_g} + \frac{c}{2} \cdot \tan\alpha_g, \quad \text{with} \quad \tan\alpha_g = \tan\theta - \frac{2\cdot b}{c\cdot\cos\theta} \tag{4-11}$$

For the first case, assuming $\alpha_g \geq \theta$, a low $h_{e\_g}$ and a high $h_{r\_g}$ result. The second case, containing $\alpha_g \leq \theta$, leads to higher $h_{e\_g}$ and lower $h_{r\_g}$. As shown in Subsection 4.6.3, the parameter $b$ contains only the widening component of the layover lines. Thus, if the extracted layover width $w_{t,c}$ is equal to the width of the corner line, then $b = 0$ and consequently $\alpha_g = \theta$. To summarise this, the parameters $a,b,c$ deliver two gable-roofed building hypotheses if $b > 0$, but only one hypothesis if $b = 0$.

The same is given for the monopitch-roofed hypotheses. The parameters $a,b,c$ result in two hypotheses with $b > 0$ and only one with $b = 0$. In (4-12), the equations for the different cases are presented, where $\alpha_m$, $h_{e\_m}$, and $h_{r\_m}$ are the parameters of a monopitch roof. In comparison to the gable roof equations, the factor 2 is missing because for monopitch roofs only one roof plane is extended over the full building width $c$. Hence, the resulting heights of the monopitch-roofed hypotheses are larger than for the gable-roofed hypotheses.

$$\alpha_m \geq \theta : h_{e\_m} = \frac{a-b}{\cos\theta} \quad \text{and} \quad h_{r\_m} = h_{e\_m} + c \cdot \tan\alpha_m , \quad \text{with} \quad \tan\alpha_m = \tan\theta + \frac{b}{c \cdot \cos\theta}$$
$$\alpha_m \leq \theta : h_{e\_m} = \frac{a}{\cos\theta} \quad \text{and} \quad h_{r\_m} = h_{e\_m} + c \cdot \tan\alpha_m , \quad \text{with} \quad \tan\alpha_m = \tan\theta - \frac{b}{c \cdot \cos\theta}$$

(4-12)

The calculated pitch angles $\alpha_g$ and $\alpha_m$ have to be projected from the slant range profile to the ground range geometry similar to the estimation of parameter $c$. The following relation is applied to both roof types.

$$\alpha_{ground} = \arctan\left(\frac{\tan\alpha_{slant}}{\cos\kappa}\right)$$

(4-13)

In the last step, the generation of hipped-roofed buildings is focused. For the parameters $\alpha$, $h_e$, and $h_r$, it is assumed that $\alpha_h = \alpha_g$, $h_{e\_h} = h_{e\_g}$, and $h_{r\_h} = h_{r\_g}$. The hip pitch angle $\beta$ is defined by

$$\beta = \arctan\left(\frac{2 \cdot (h_{r\_h} - h_{e\_h})}{l \cdot (1 - l_o)}\right)$$

(4-14)

where $h_{e\_h}$ and $h_{r\_h}$ are the eave and the ridge height, $l$ is the length of the building, and $l_o$ is the overlap ratio. Since for the hipped-roofed building the same combinations between $\alpha$ and $\theta$ are possible, one ($b = 0$) or two ($b > 0$) hypotheses result.

To summarise the extraction of height information from the primitives $l_{cl\_d,i}$, a parameter set $a,b,c$ delivers four ($b > 0$) or two ($b = 0$) building hypotheses. The same ambiguity problem is observable for hipped-roofed buildings showing $b > 0$. At this stage of the processing, this ambiguity cannot be solved, but by analysing the interferometric phases an evaluation of the different hypotheses can be reached. Therefore, the subsequent steps of interferometric phase simulation and filtering are implemented. The solving of the ambiguity is part of the post-processing of the building hypotheses that will be described in Subsection 4.11.1.

## 4.9    Simulation of InSAR Phases

As mentioned in Subsection 1.2.1, the simulation of interferometric phases came up by concentrating especially on layover areas [142]. The primary objective was to identify and remove such layover mixture areas to improve the generation of digital elevation models (e.g. [26] and [39]) or to support the phase unwrapping at building locations [98], for example. First simulation studies focused on the reproduction and analysis of coherence phenomena, for example coherence loss at steep gradient relief [97]. Later, new high resolution airborne InSAR data enabled a detailed analysis of individual buildings [126] and building substructures [21]. As a result, especially the understanding of how different scattering objects contribute to the layover signal was prerequisite. Hence, new simulation approaches considering interferometric mixture models of more than one contributor were implemented (see e.g. [125] and [42]). In the following subsections, the new mixture model is described, the simulation results are discussed and the influence of varying sensor parameters, building size, roof type and neighbourhood effects on the InSAR phase signature are analysed.

### 4.9.1    Simulation Approach

The simulation approach contains a phase mixture model. This is defined and implemented in the following way: as shown in Fig. 4.21a, the two SAR images are recorded separated by an across track baseline $B$. After SAR processing, the incoming signals gathered by antennas $T_1$ and $T_2$ are mapped into the related range/azimuth resolution cells (pixels) of the complex SAR images $S_1$ and $S_2$, respectively. The signal phasor of a resolution cell is modelled to be the result of coherent superposition of contributions of every individual scattering object inside the related 3D volume.

In a simplified manner, SAR can also be described as distance measurement in horizontal cylinder coordinates with high resolution in radial (range) and azimuth coordinates. However, in look angle (elevation) direction a poor resolution results, which is the reason for the layover phenomenon. An example for a building is given in Fig. 4.21a, where the points $P_A$ (ground level), $P_B$ (building wall) and $P_C$ (building roof) have the same distance ($r_{1,A} = r_{1,B} = r_{1,C}$) to antenna $T_1$. However, the range distances related to antenna $T_2$ differ ($r_{2,A} \neq r_{2,B} \neq r_{2,C}$): $P_A$ is closest to the sensor, followed by $P_B$ and $P_C$. Hence, for the given constellation, the superposition at $S_1$ is defined as follows:

$$
\begin{aligned}
S_1 &= A_1 e^{j\varphi_1} \\
&= A_{1,A} e^{j\varphi_{1,A}} + A_{1,B} e^{j\varphi_{1,B}} + A_{1,C} e^{j\varphi_{1,C}} \\
&= \sum_m \cos\zeta_{1,m} \cdot A_{T,1} e^{j\varphi_{1,m}} , \qquad \text{with} \quad m \in \{A,B,C\} \quad \text{and} \quad A_{1,m} = \cos\zeta_{1,m} \cdot A_{T,1} \qquad (4\text{-}15) \\
&= A_{T,1} e^{j\varphi_1} \cdot \sum_m \cos\zeta_{1,m} , \qquad \text{with} \quad \varphi_1 = \varphi_{1,m} = \varphi_{1,A} = \varphi_{1,B} = \varphi_{1,C}
\end{aligned}
$$

where $A_{1,m}$, $\varphi_{1,m}$, and $\zeta_{1,m}$ are the amplitude, the phase, and the local incidence angle of the contributor $m$, respectively. As no individual surface materials are considered for the different contributors, a general amplitude $A_{T,1}$ is inserted, which is weighted by the cosine of $\zeta_{1,m}$ (see Fig. 4.21b) similar to the model presented in [39]. The phase is derived from the distance to the antenna. Furthermore, $S_1$ is determined as master image, where all contributors show the same range distances $r_{1,m}$, and consequently all $\varphi_{1,m}$ are equal.

The corresponding signal at $S_2$ is then given by:

$$
\begin{aligned}
S_2 &= A_2 e^{j\varphi_2} \\
&= A_{2,A} e^{j\varphi_{2,A}} + A_{2,B} e^{j\varphi_{2,B}} + A_{2,C} e^{j\varphi_{2,C}} \\
&= \sum_m \cos\zeta_{2,m} \cdot A_{T,2} e^{j\varphi_{2,m}} , \qquad \text{with} \quad m \in \{A,B,C\} \quad \text{and} \quad A_{2,m} = \cos\zeta_{2,m} \cdot A_{T,2} \qquad (4\text{-}16) \\
&= A_{T,2} \cdot \sum_m \cos\zeta_{2,m} \cdot e^{j\varphi_{2,m}} , \qquad \text{with} \quad \varphi_2 \neq \varphi_{2,m} \neq \varphi_{2,A} \neq \varphi_{2,B} \neq \varphi_{2,C}
\end{aligned}
$$

Here, the final summing up contains additionally the individual contributor phases $\varphi_{2,m}$. This is required since the range distances $r_{2,m}$ are not equal, and thus neither are the contributor phases $\varphi_{2,m}$. Using (4-15) and (4-16), the interferogram $S$ of the two complex images $S_1$ and $S_2$ is calculated as follows:
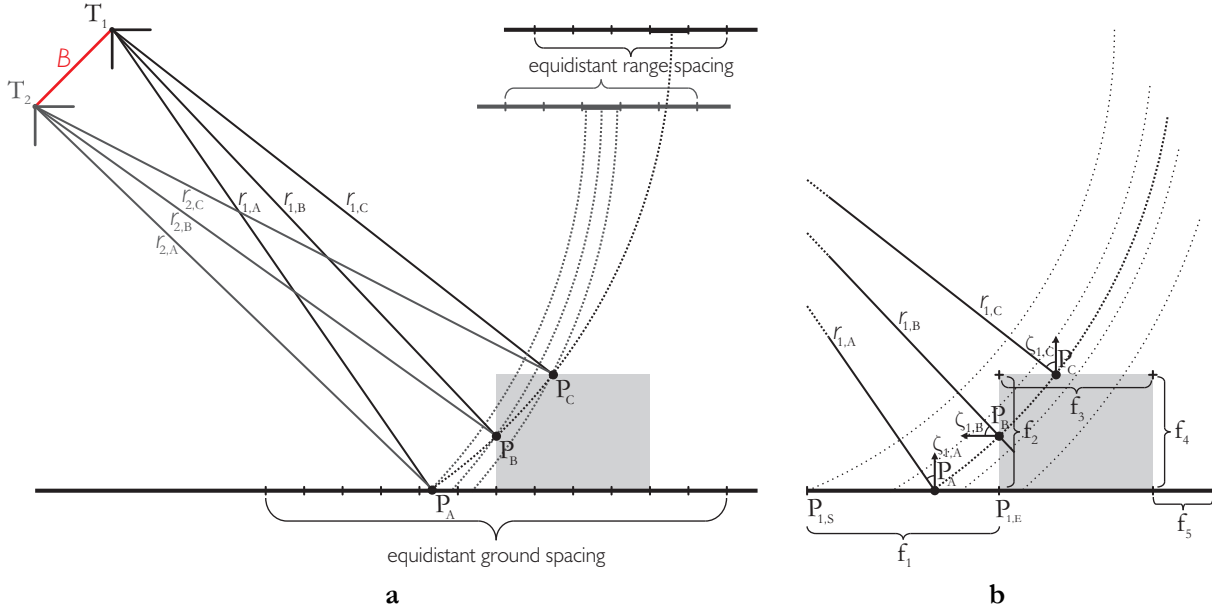
**Figure 4.21:** Simulation principle: contribution distribution of InSAR measurements at building location (a) and DSM profile of a flat-roofed building based on fragments $f_n$ and local incidence angle $\zeta_{1,m}$ of radar signal (b)

$$
\begin{aligned}
S &= S_1 \cdot S_2^* \\
&= \left( A_{T,1} e^{j\varphi_1} \cdot \sum_m \cos\zeta_{1,m} \right) \cdot \left( A_{T,2} \cdot \sum_m \cos\zeta_{2,m} \cdot e^{-j\varphi_{2,m}} \right) \\
&= I \cdot \sum_m \cos\zeta_{1,m} \cdot \sum_m \cos\zeta_{2,m} \cdot e^{j\Delta\varphi_m}, \quad \text{with} \quad I = A_{T,1} \cdot A_{T,2} \quad \text{and} \quad \Delta\varphi_m = \varphi_1 - \varphi_{2,m}
\end{aligned}
\tag{4-17}
$$

Moreover, two additional simplifying assumptions are made concerning the SAR amplitudes. The intensity of the interferogram $I$ is set to 1, and since the range distances $r_{1,m}$ and $r_{2,m}$ are much longer than the baseline $B$, the local incidence angles $\zeta_{1,m}$ and $\zeta_{2,m}$ are almost equal. Finally, we end up with this simpler equation:

$$
S = \sum_m \cos\zeta_m \cdot \sum_m \cos\zeta_m \cdot e^{j\Delta\varphi_m}, \qquad \text{with} \quad I = 1 \quad \text{and} \quad \zeta_{1,m} \approx \zeta_{2,m}
\tag{4-18}
$$

As the superposition of the contributors is modelled to be independent of azimuth position, but the off-nadir look angle rises over the radar beam with increasing range, the simulation is carried out along range profiles (Fig. 4.21b). The process of phase profile simulation starts with the import of the sensor parameters (e.g. wavelength, sensor altitude, antenna configuration, flight direction, and slant range resolution). Considering the result of Section 4.8, from an assembled 3D building hypothesis range profiles are derived (see Fig. 4.22a). The direction of the cut through the 3D building model is orthogonal to the sensor flight track. The number of range profiles necessary to simulate the entire building is obtained from the data resolution and the building size in azimuth direction. In the next step, all range profiles are split up into fragments $f_n$ of approximately constant gradient, with $P_{n,S} := (x_{n,S}, y_{n,S}, z_{n,S})$ as start position and $P_{n,E} := (x_{n,E}, y_{n,E}, z_{n,E})$ as end position.
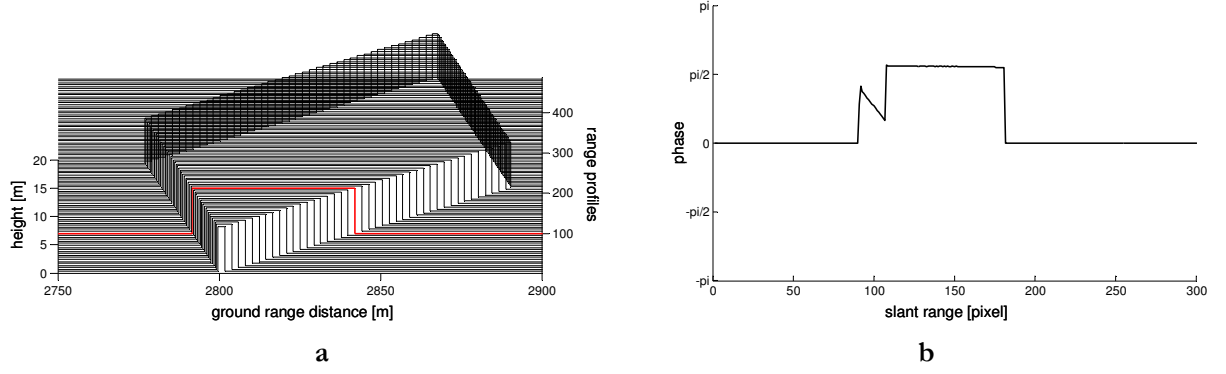
**Figure 4.22:** Assembly of phase profiles: range profiles assembled from the 3D building hypothesis (a) and simulated InSAR range profile (b) corresponding to the DSM profile marked in red

This step also makes the simulation approach applicable to other terrain forms. In Fig. 4.21b, an example of a flat-roofed building is shown assuming flat terrain in the direct neighbourhood.

In addition, the ground fragments $f_n$ are sampled in cells with centre coordinates $P_i := (x_i, y_i, z_i)$. Then for each cell, the following parameters are calculated: the range distances $r_{j,i}$, the difference $\Delta r_i$ of range distance, the phase difference $\Delta \varphi_i$, and the local incidence angle $\zeta_i$ between radar signal path and normal vector $\vec{n}_i$ (see (4-19)). Furthermore, a binary parameter is set by utilizing the orientation of $f_n$. It indicates whether direct line-of-sight between $T_1$ and $P_i$ is given or not, which is important to model shadow effects correctly.

$$
\begin{aligned}
r_{j,i} &= \left| \vec{T}_j - \vec{P}_i \right|, \quad \text{with} \quad j \in \{1,2\} \\
\Delta r_i &= r_{1,i} - r_{2,i} \\
\Delta \varphi_i &= -2\pi \cdot \frac{\Delta r_i}{\lambda} \\
\cos \zeta_i &= \frac{(\vec{T}_1 - \vec{P}_i) \cdot \vec{n}_i}{\left| (\vec{T}_1 - \vec{P}_i) \right| \cdot \left| \vec{n}_i \right|}
\end{aligned}
\tag{4-19}
$$

The simulation is carried out in the slant range grid of the final interferogram, which is identical to the grid of the master image $S_1$. Thus, no co-registration of the two SAR images is required. In the next step, for each ground cell $P_i$ the corresponding slant range cell is determined with regard to the near range distance and the slant range pixel size. For the example shown in Fig. 4.21b up to three entries per slant range cell are gathered. The final interferometric phase results from applying (4-18) – the summing up of all contributions. A sample slant range profile is given in Fig. 4.22b corresponding to the DSM profile marked in red in Fig. 4.22a.

The simulation of a full building signature is realised by connecting all phase profiles. The simulation approach delivers the following products: the phase signature (Fig. 4.23a), the roof mask (b), and the shadow mask (c). The second will be used later to post-process the initial building hypothesis. Focusing on the resulting phase signature, the downwards trend in the layover area as well as the constant trend in the roof area discussed in Subsection 3.1.2 is visible. The shadow area is modelled with a reflectivity of zero without implementing a noise contribution.
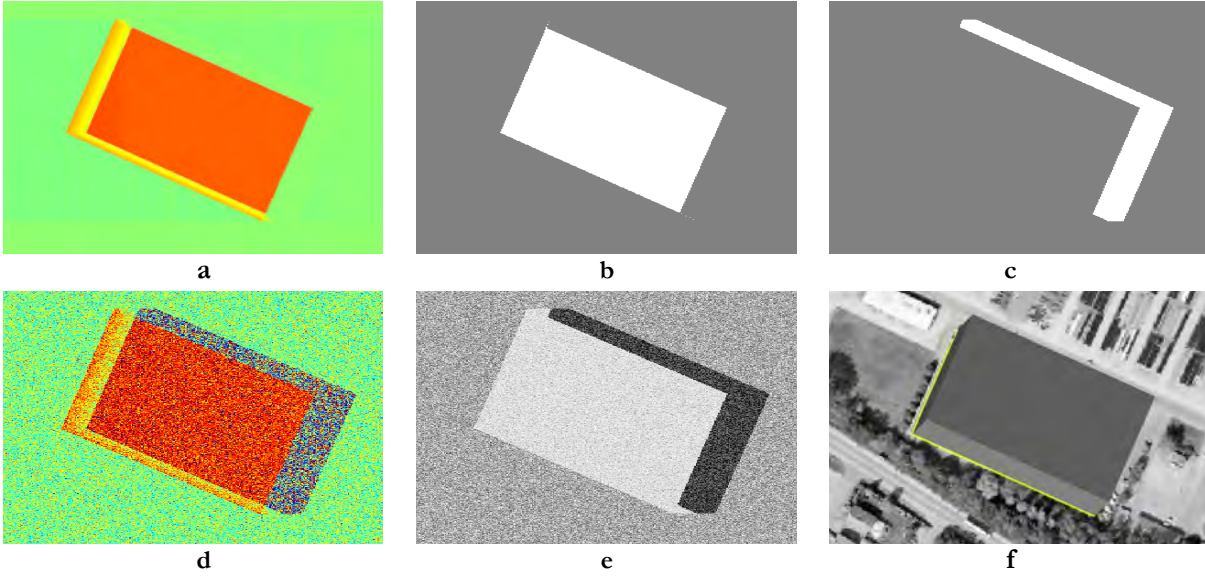
**Figure 4.23:** Result of simulation approach: interferometric phases (a), roof mask (b), shadow mask (c), noisy interferometric phases (d), noisy coherence image (e), and optical image overlaid with considered flat-roofed building model (f)

The modelling of noisy phases concerning all signature parts (i.e., layover, roof, shadow, and neighbourhood) is helpful to test the performance of complex processing steps (e.g. phase filtering). Hence, an additional simple noise model has been implemented. The total correlation $\gamma_{total}$ of interferometric data can be described as a product of six correlation terms [61]:

$$\gamma_{total} = \gamma_{geom} \cdot \gamma_{DC} \cdot \gamma_{vol} \cdot \gamma_{thermal} \cdot \gamma_{temp} \cdot \gamma_{proc} \qquad (4\text{-}20)$$

Since mainly single-pass airborne data are considered in this thesis and especially the analysis of urban areas is focused, some of the decorrelation contributions can be neglected. First, temporal decorrelation $\gamma_{temp}$ will not be considered, due to the negligible temporal baseline of single-pass data. The same is the case for volume decorrelation $\gamma_{vol}$ because of the focus set on buildings. According to [103], for airborne data and after careful InSAR processing, the terms $\gamma_{DC}$ (i.e., decorrelation due to differences in the Doppler centroids) and $\gamma_{proc}$ (i.e., decorrelation caused by the individual processing – e.g. coregistration) can also be neglected. Hence, only the two decorrelation components $\gamma_{geom}$ and $\gamma_{thermal}$ have to be taken into account and are modelled. Since the $\Delta\varphi_{noisy}$ will only be used as test data to compare phase filters (see Section 4.10), the components are estimated in a simplified manner assuming normal distributions. Additionally, the shadow area is modelled by phase values following a uniform distribution in the interval $[-\pi, +\pi]$. The final noisy phases are formed by adding the different noise contributions to the simulated phases $\Delta\varphi_{sim}$:

$$\Delta\varphi_{noisy} = \Delta\varphi_{sim} + \varphi_{thermal} + \varphi_{geom} + \varphi_{shadow} \qquad (4\text{-}21)$$

A resulting noisy phase signature is shown in Fig. 4.23d. In order to enable more filter tests, the simulation of a corresponding coherence map $\gamma_{noisy}$ is carried out. For that, the significant signature parts – layover, roof, shadow, and ground are modelled independently. The layover and roof areas
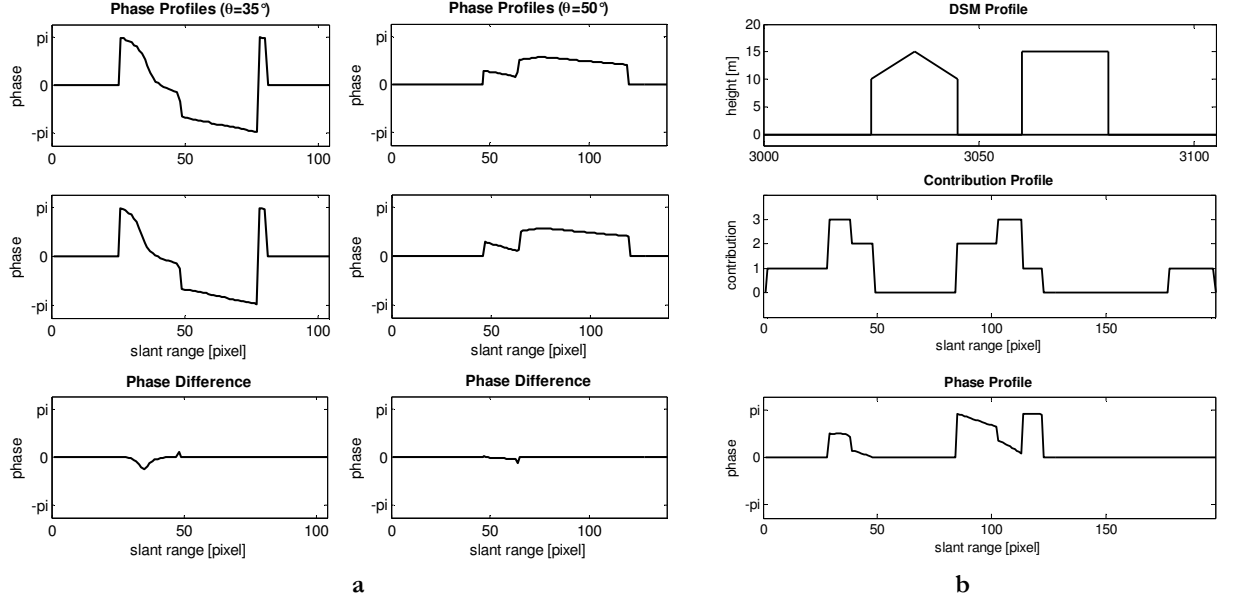
**Figure 4.24:** Simulation characteristics: phases of a gable-roofed building under varying $\theta$ (a) – neglecting (top) and considering local incidence angle $\zeta_i$ (middle) as well as phase differences (bottom); simulation of neighboured buildings under $\theta = 45°$ (b) – DSM (top), contribution (middle) and phase profile (bottom)

are summarised in the variable $\gamma_{\text{building}}$ since their coherence level differs only marginally in measured InSAR data. Hence, $\gamma_{\text{noisy}}$ is defined by:

$$\gamma_{\text{noisy}} = \gamma_{\text{ground}} + \gamma_{\text{building}} + \gamma_{\text{shadow}} + \gamma_{\Delta\varphi} \tag{4-22}$$

where $\gamma_{\text{ground}}$, $\gamma_{\text{building}}$, and $\gamma_{\text{shadow}}$ are assumed to follow normal distributions of different combinations of $\mu, \sigma$ corresponding to measurements in real InSAR data. The last component, $\gamma_{\Delta\varphi}$, is added to make a connection to the noisy simulated phase $\Delta\varphi_{\text{noisy}}$ in pixel space. Fig. 4.23e shows a noisy coherence map. A discussion of these simulation results is given in the next section by taking into account measured InSAR data.

Before discussing the results of simulated in comparison to measured InSAR data, the influence of some parameters on the simulation results are presented. First, the impact of the introduced weighting function $\cos\zeta_i$ is discussed. In Fig. 4.24a two simulated phase profiles of a gable-roofed building are shown assuming off-nadir look angles $\theta = 35°$ (left) and $\theta = 50°$ (right). For the profiles given in the first row, the weighting was neglected. For the profiles in the second row, the weighting was considered and in the third row, the differences between both are visualised. The steeper the look angle the greater the differences. In addition, only in the layover area differences are observed because of the contribution mixture. Therefore, the weighting function is essential for the simulation of steep-looking InSAR configurations.

Second, superposition and occlusion effects between neighbouring buildings can be studied by analysing the contribution map, shown exemplary in Fig. 4.24b: the first row shows the synthetic DSM profile of close-by gable- and flat-roofed buildings. The number of different contributors for the slant range cells is shown in the second row and the resulting phase profile in the third row. The
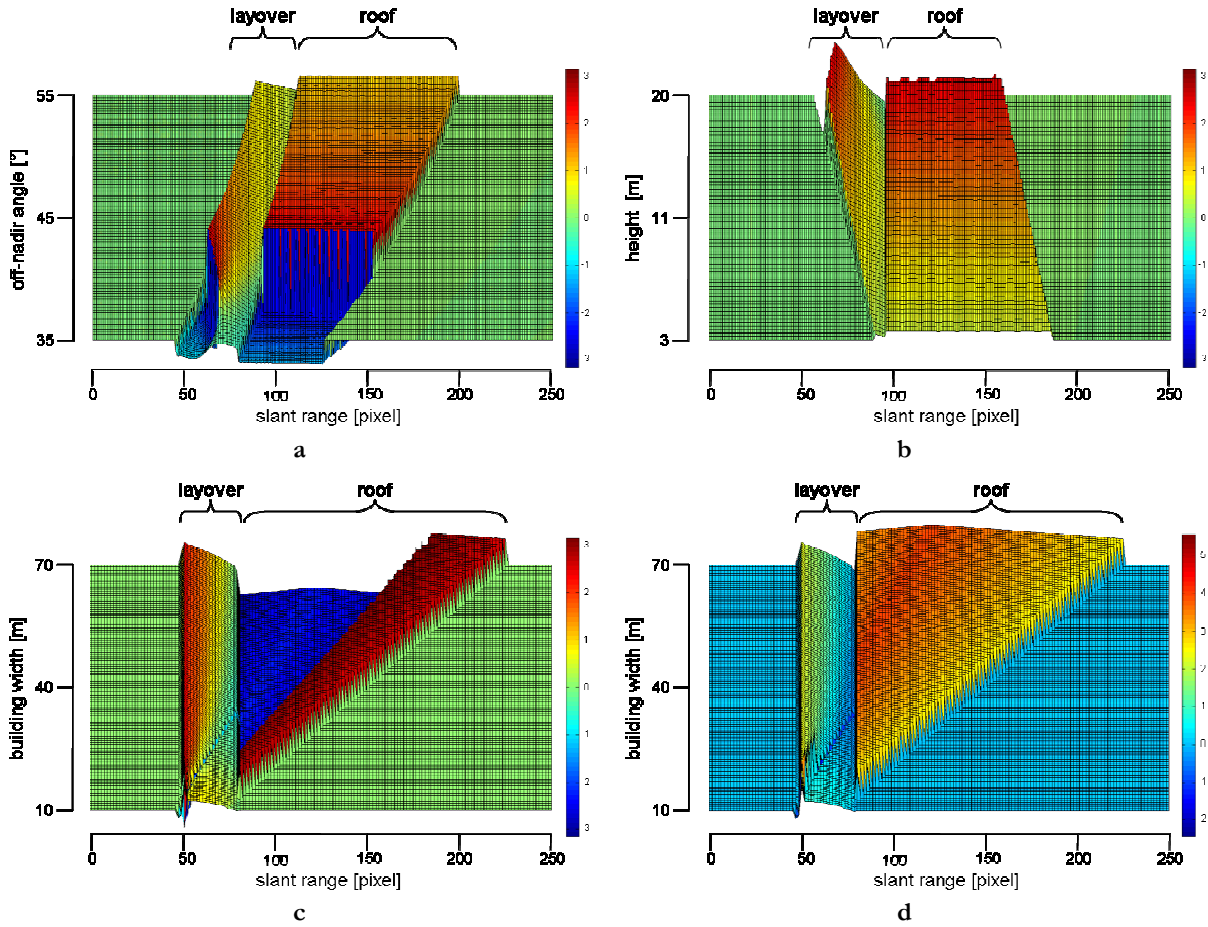
**Figure 4.25:** Changes in simulated phase profiles: flat-roofed building with varying look angle (a) and height (b), gable-roofed building with varying building width (c) and after phase shifting (d)

contribution signature of the gable-roofed building is characterised by three parts – starting with three contributions followed by a part of two and ending with zero contributions. The first two parts correspond to a subdivided layover area with the superposition of ground, wall, roof for the first part and ground, wall for the second part. This subdivision is observable for narrow buildings such as described in Section 3.3 and especially for gable-roofed buildings. Since this is reinforced as in most cases only the sensor facing roof plane is backscattering in sensor direction. The building shadow leads to the part of zero backscatterer.

For the flat-roofed building in Fig. 4.24b, four different contribution parts are visible taking the values $[2,3,1,0]$. In contrast to the gable-roofed building, the flat roof signature starts with two inputs from wall and roof because a part of the ground in front of the building is occluded by the shadow of the gable roof. The subsequent part of the layover then contains the standard three portions – ground, wall and roof. In summary, the stepwise phase slopes in the layover result from a decrease or an increase of contributions for the gable- and flat-roofed building, respectively. Additionally, a part of only one backscatter entry coming from the building roof is given. Furthermore, the shadow of the flat-roofed building leads to a long part of no contribution. At the beginning and at the end of the range profile, the zero entries are set followed by parts characterised by the
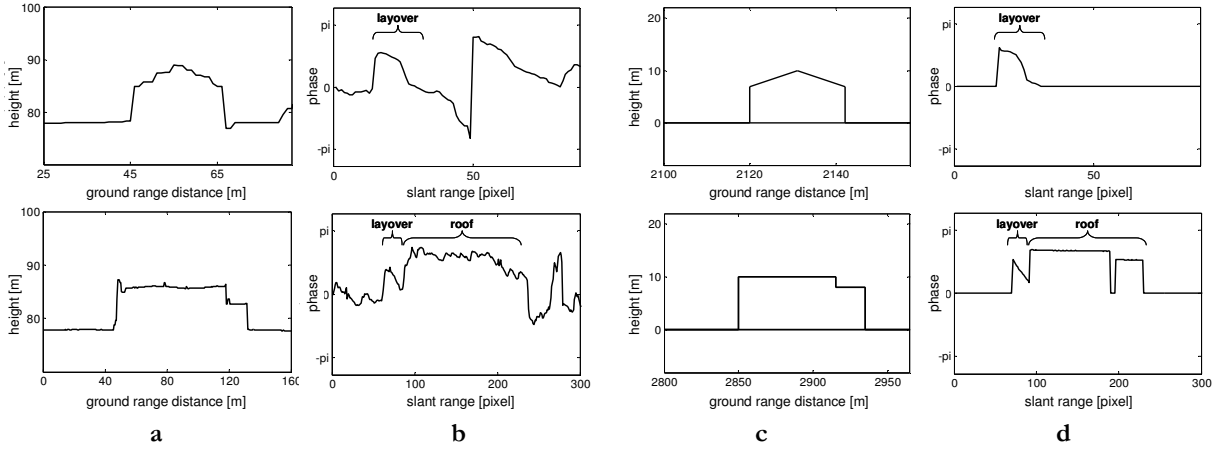
**Figure 4.26:** Comparison of measured and simulated phase profiles: LIDAR DSM profile (a) and measured InSAR phase profile (b), synthetic DSM profile (c) and simulated phase profile (d)

ground portion. The resulting phase profile shows the final interferometric phase already discussed in Subsection 3.3.2. Overall, the contribution map comprises essential information to support the analysis of interferometric phase signatures.

Moreover, with the simulation tool, other influences can be studied affecting the appearance of the InSAR phase profiles such as described in Sections 3.2 and 3.3. These include sensor parameters (e.g. range resolution and antenna configuration), illumination parameters (e.g. range distance and look angle), and building model parameters (e.g. height, width, and roof type). The studies presented here show the impact of varying illumination and building model parameters on the interferometric phase signature.

In Fig. 4.25a simulated phase profiles are shown for a flat-roofed building ($h_f = 10$m and $w = 40$m) as a function of $\theta$ in the range of $[35°,55°]$. The distribution of the phase information of the layover area as well as the roof part includes abrupt phase jumps to negative values (see also Fig. 4.24a, $\theta = 35°$). This is caused by the varying unambiguous range $\Delta h_i$ defined in (2-14). In the given example, $\Delta h_i$ rises from 15 m up to 29 m. Accordingly, with a scaling of $[-\pi, +\pi]$ and terrain definition at phase value zero, only half of the elevation interval can be used for a positive display of building phases. Furthermore, it is visible that the maximum phase value in the layover area is equal to the roof phase. Similar studies on varying look angle and building height have been undertaken for a gable-roofed building [125].

In addition, the building geometry (i.e., height, width, and roof type) is varied; corresponding phase plots are given in Fig. 4.25b and c. The example of building heights spans a range from 3 m up to 20 m steps of 25 cm. In contrast to the increasing $\theta$, incrementing this parameter leads to a decreasing roof area and an increasing layover area. At the end of the variation interval ($h_f \approx 20$m) the simulation results show phase values close to the upper interval border ($+\pi$). Parts of the simulated profiles include abrupt phase jumps. In this case, the unambiguous range is exceeded, but in contrast to example (a) the $\Delta h$ of example (b) is constant.

The variation of the width $w$ from 10 m up to 70 m yields a change of the roof pitch angle from 40° down to 7° (see Fig. 4.25c). The first profile (at 10 m) reveals no single phase signature of the

roof at all; the entire roof signal is compound with other contributions in the layover area. With growing building width, a single roof signature becomes observable, but after a certain width, the already mentioned phase jumps take place.

The observation of phase jumps is confirmed by comparison with real InSAR data; especially in large urban areas with similar building topology illuminated under different off-nadir look angles. Even if the height of the building is smaller than the unambiguous range, this effect may occur due to suboptimal choice of the borders of the elevation interval in the InSAR processing. In such cases, the phase shifting procedure is beneficial (see Section 4.5). The result given in Fig. 4.25d includes such a phase shifting. This step is obviously helpful for this example, but in some cases, the unambiguous range connected to steep look angles is too small for an unambiguous visualisation of the phase values. Then, the phase unwrapping shortly discussed in Subsection 2.1.4 has to take place.

### 4.9.2  Comparison of Simulated and Real InSAR Phases

The assessment of simulated and measured InSAR phases includes the interpretation of phase profiles, the calculation of phase differences, and the comparison of data distributions.

For the first assessment, a suitable LIDAR DSM profile of the scene is selected and generalised (synthetic DSM) for the simulation process, preserving the geometrical size and other key features (e.g. roof type of building). The necessary physical parameters (e.g. wavelength, length of baseline, and sensor altitude) are extracted from the investigated InSAR data set. The two examples given in Fig. 4.26 show a simple gable-roofed building (first row) and a steplike flat-roofed building (second row). The LIDAR DSM profiles (a), the measured phase profiles (b), the synthetic DSM profile (c), and the simulated phase profiles (d) are shown. The simulation yields sharper edges and crisper contours than the real phase profiles. This is caused by the simplification of the model. The measured phases were smoothed by a 9×9-filter matrix. The influence of phase multilooking by applying different window sizes was studied in [125]. The effect of phase filters on the building phase signature will be discussed in the next section.

For the gable-roofed building (Fig. 4.26, first row), the sensor-close part of the phase profiles matches better than the sensor-far part. This difference is caused by interference from adjacent trees. In the layover area, similarities are observable especially at the highest and lowest points. The comparison of phase information in the shadow area is not reasonable, because the simulated phase profile only shows level zero without apparent layover of the trees as observable in the measured phase profile. A more complex signature is given for the flat-roofed building (Fig. 4.26, second row). The layover and roof areas have a high degree of similarity, and even the low step at the sensor-far side of the roof is visible in both profiles. The small gap caused by the height variation in the roof is not observable in the measured phases, since noisy phases arise and multilooking is applied on those. Additional examples are presented in Fig. 3.2 and in [125] containing more complex buildings and building groups. In summary, for all comparisons, high similarities are observable at significant points of the layover and the roof areas as well as in the phase distributions of these areas. Differences are observable when interference caused by trees or other nearby objects has to be taken into account.
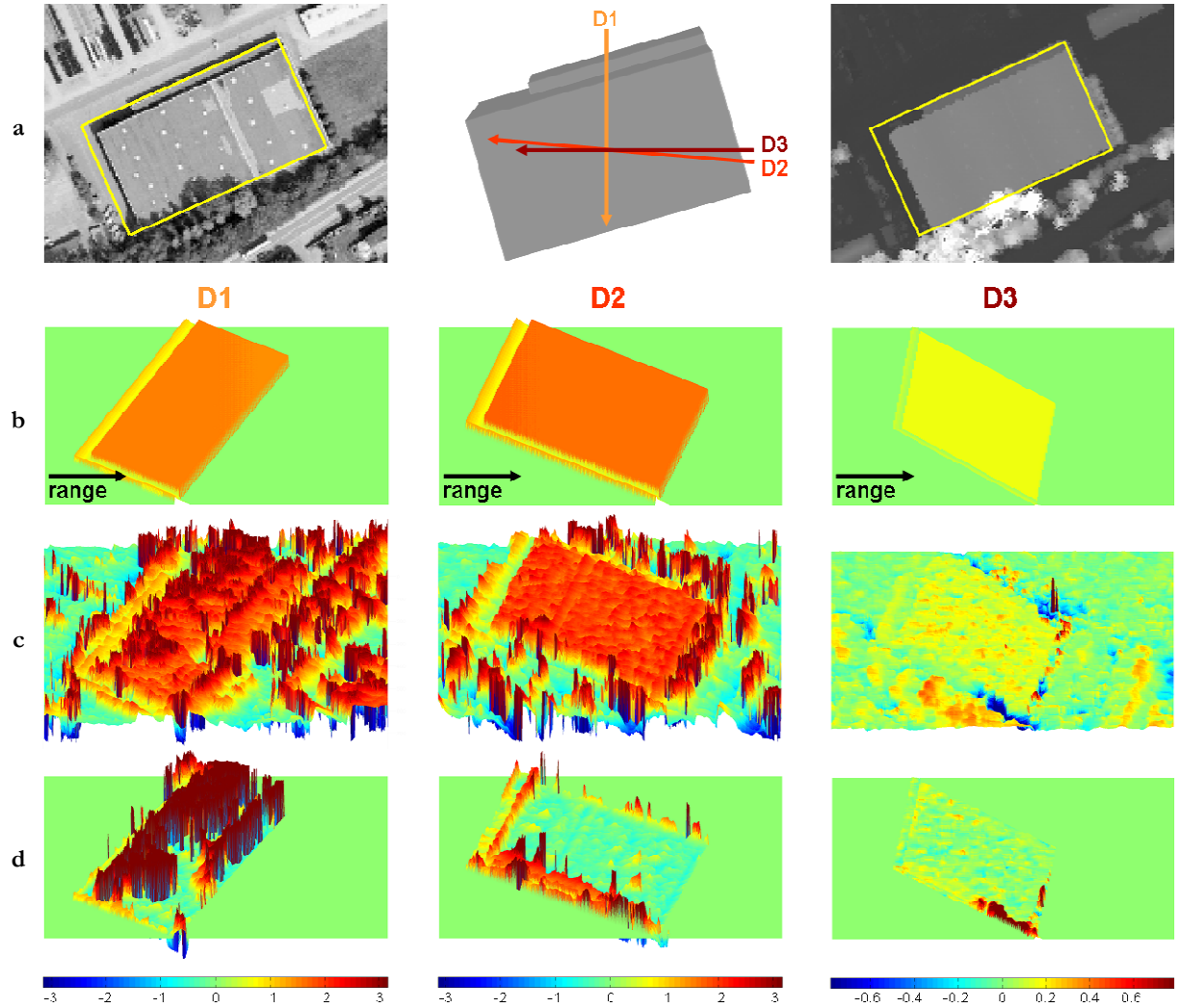
**Figure 4.27:** Comparison of simulated and measured InSAR phases showing three different tracks: 3D building signature (a), simulated phases (b), measured phases (c), and differences between simulated and measured phases (d)

The assessment by calculating phase differences is shown at an industrial hall (Fig. 4.27). The building hypothesis is simulated for three different InSAR configurations containing varying viewing directions, baselines, and data resolutions. In (a), the optical and the LIDAR DSM images are overlaid by the 2D building footprint. The three InSAR viewing directions (D1, D2, and D3) are visualised on the ground truth 3D model. The simulated phases, the measured phases, and their differences containing only layover and roof area are depicted in (b), (c), and (d), respectively. The most obvious differences between simulated and measured phases are due to surrounding objects (e.g. vegetation, fences, and cars) not taken into account during the simulation. Variations between the simulated phases are caused by the individual illumination and sensor parameters leading, for example, to different unambiguous ranges. To improve the visualisation, the phase differences of D3 are scaled in the range of $[-\pi/4, +\pi/4]$, while all other phases and differences are scaled in the range of $[-\pi, +\pi]$. The highest similarities are achieved for the data sets D2 and D3. High differences are observable for D1 especially inside the roof areas due to discontinuities in the measured
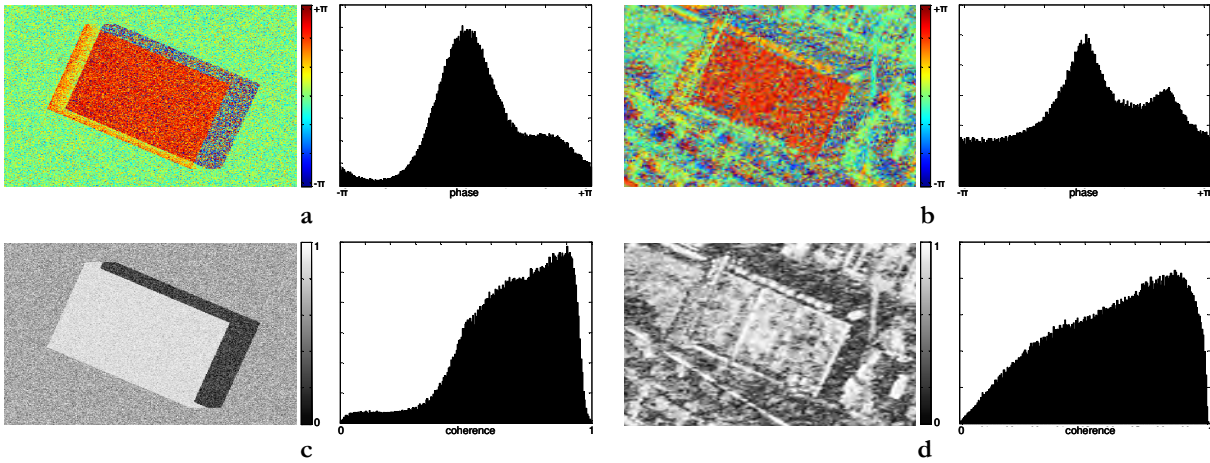
**Figure 4.28:** Comparison of noisy simulated and measured InSAR phase (a,b) and coherence (c,d)

phases, probably because of very strong scatterer side lobes in range direction. Furthermore, for example D3 much smaller differences result than for D1 and D2. The small baseline and consequently the large unambiguous range lead to this misinterpretation. Since $h/_{\Delta h} \sim \Delta\varphi/_{2\pi}$, the conversion of the phase differences to heights delivers comparable results. Ignoring D1, the differences of D2 and D3 are characterised by low values at roof but higher values at layover areas. Since the measured phases have been smoothed, blur effects occur and higher values appear, especially at building edges (see Fig. 4.27d D2). Thus, appropriate filtering of measured phases is discussed in the next section to support the assessment between simulated and measured phases. Additionally, details concerning the numerical assessment are also given in Subsection 4.10.2, where not only the differences but also the correlation between the phase values are considered.

Finally, the results of the noisy simulation are discussed. In Fig. 4.28a,b simulated and measured phases as well as corresponding histograms are shown. High correlations have been reached in the roof and shadow area. Differences are especially visible in the layover area due to occlusion effects caused by adjacent trees. Looking at the histograms, the main peak is more recognisable in the simulated than in the measured phases, because the surrounding is modelled as large open space. The coherence values visualised in Fig. 4.28c,d seem to be less correlated. Especially for the building roof, the values are in some cases lower due to different backscatter properties. Moreover, the decorrelated neighbourhood (e.g. streets and tree shadows) causes differences in the shape of the coherence histograms. Nevertheless, for the testing of the phase filters, the simulated noising phases are sufficient.

In summary, the simulation approach delivers interferometric phases of a 3D building model by considering given sensor specifications. The simulated phases show high correlation with measured InSAR phases independent from building geometry and sensor parameters. Hence, the simulation results are further used to evaluate filter results (Section 4.10) and mainly to enable the post-processing of the initial building hypotheses (Section 4.11).

<div align="center">a                 b</div>
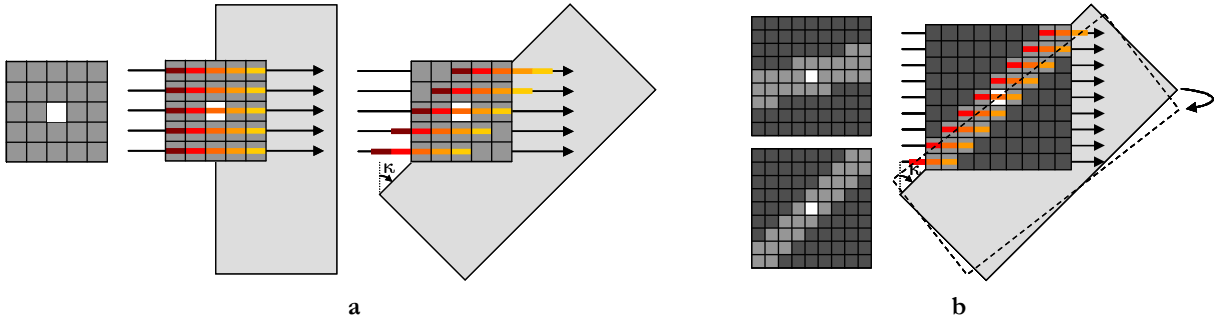
**Figure 4.29:** Schema of conventional filters: area filter (a) and orientation filter (b)

## 4.10  Smart Filtering of Measured InSAR Phases

For the subsequent post-processing, simulated and measured InSAR phases have to be compared. The reliability of the results depends on how well simulation model and real building match, on the quality of the InSAR data (e.g. single-pass or repeat-pass), and on the used pre-processing (e.g. filtering). The latter is described in this section, introducing smart filtering to optimise the smoothing of noisy InSAR phases.

Conventional multilook-filtering [78] yields acceptable results when applied to large homogenous areas, but characteristic phase signatures (e.g. layover areas) are destroyed in particular by the use of large filtering windows. Furthermore, such filters, called area filters in this thesis, are inappropriate if building orientations are not aligned with the sensor flight direction. This is illustrated in Fig. 4.29a, where the 5×5 filter mask is coloured dark grey and the central position is white. The first building coloured in light grey shows flight parallel orientation, while the second building shows a span angle $\kappa$ of 45°. The arrows mark slant range lines and similar phase values are emphasised by same colours. In the parallel-aligned example, the averaging over all pixel values (from dark red to yellow) diminishes the layover ramp and the roof corners. Non-parallel alignment enhances this effect, because not only the five coloured phase values are taken for the filtering (see upper left and lower right pixels). Furthermore, the results depend on the size of the building and the filter size of the window. This is illustrated in Fig. 4.30. A critical increase of smoothing effects is especially visible for the example of the small building (second row). For the largest filter window (25×25), the L-shaped layover area and the roof area are difficult to recognise. This is lesser for the example of the large building (first row).

Other InSAR filters as proposed in [56] and [6] investigate the frequency spectrum of an InSAR patch to reduce high frequency noise in the InSAR phases. In [139], the coherence between so-called non-local image areas is analysed to de-noise image patches by a regularisation-based method. Nevertheless, all area filters blur small structures with rising window size.

An improvement is possible by using adaptive orientation filters. In [79], sixteen orientations are considered and the weighting is characterised by local coherence, number of looks, and variance. A related approach is described in [11] by extending the number of orientation masks. Two different values of line thickness are defined to preserve small signature details. The scheme given in Fig. 4.29b illustrates the principle of orientation filters showing two exemplary orientation masks. The
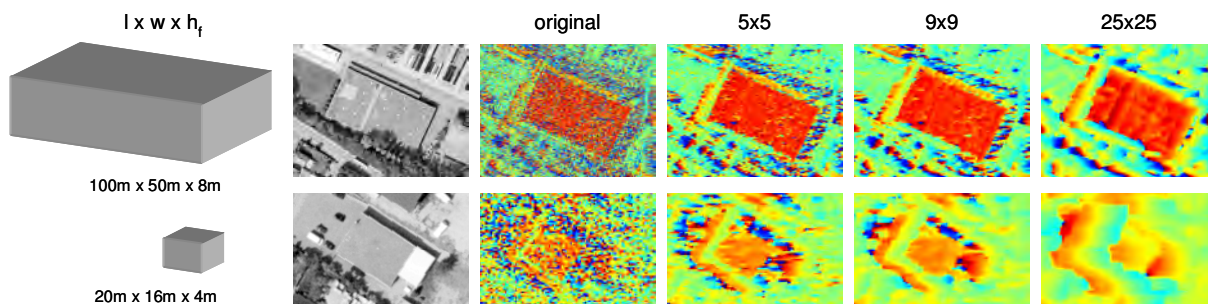
**Figure 4.30:** Result of multilook-filtering applying different sizes of filter windows: example of large building (first row) and small building (second row)

pixels coloured in light grey on the filter mask are considered and the dark grey are neglected in the averaging step. Focusing on the same building geometry ($\kappa = 45°$), only three different phase values (red to orange) are mixed by applying this oriented filter mask. Hence, the blurring of object structures is attenuated, in comparison to area filters. Nevertheless, difficulties may arise for the selection of the appropriate orientation due to a high noise level. Furthermore, only a few orientation angles are supported, so that the actual building orientation may not correspond perfectly to the filter orientation (see for example Fig. 4.29b, dashed line). In that case, building edges and layover ramps are not preserved in the desired way. This can be prevented by using the true orientation obtained by external GIS data (e.g. cadastral building footprint) or by initial building hypotheses. The latter option is implemented in the new filter approach described in the next subsection. Subsequently, different filter results are assessed and compared with the simulated phases (Subsection 4.10.2).

## 4.10.1   Filter Approach

The new filter approach is a modified version of the GIS-supported filter presented in [128] that allows an adaptive fitting of filter masks to achieve best noise suppression at building location. Since in this thesis a basic building model is used, some simplifications due to the model constraint (Section 4.1) are possible to improve the time-consuming adaptive filtering. In the following, the filtering of flat-roofed and non-flat-roofed buildings is described separately since different simplifications are possible.

The schematic description of the filter masks generated to smooth flat-roofed building signatures is given in Fig. 4.31a. Since a simple right-angled building model is assumed, the interferometric signature of a flat-roofed building can be subdivided into zones of similar phase information. These are defined by the roof points $R_1, R_2, R_3, R_4$ and the points of the building footprint $C_1, C_2, C_3, C_4$ in slant range geometry. In total, five different filter zones are observable for an elevated 3D building model, where the zone $Z_r$ contains the roof area and the others ($Z_{l1}, Z_{l2}, Z_{l3}, Z_{l4}$) contain the layover area of the building. The roof zone $Z_r$ is described by the single backscattering of the building roof. Inside this zone, all values are averaged, weighted by the coherence values. The other four zones are characterised by a preferred filtering direction (marked by the arrows), along which all pixels show the same phase value. The subdivision of the layover area is necessary because only the phase values in zone $Z_{l1}$ and $Z_{l2}$ (marked dark grey in Fig. 4.31a) result from the superposition
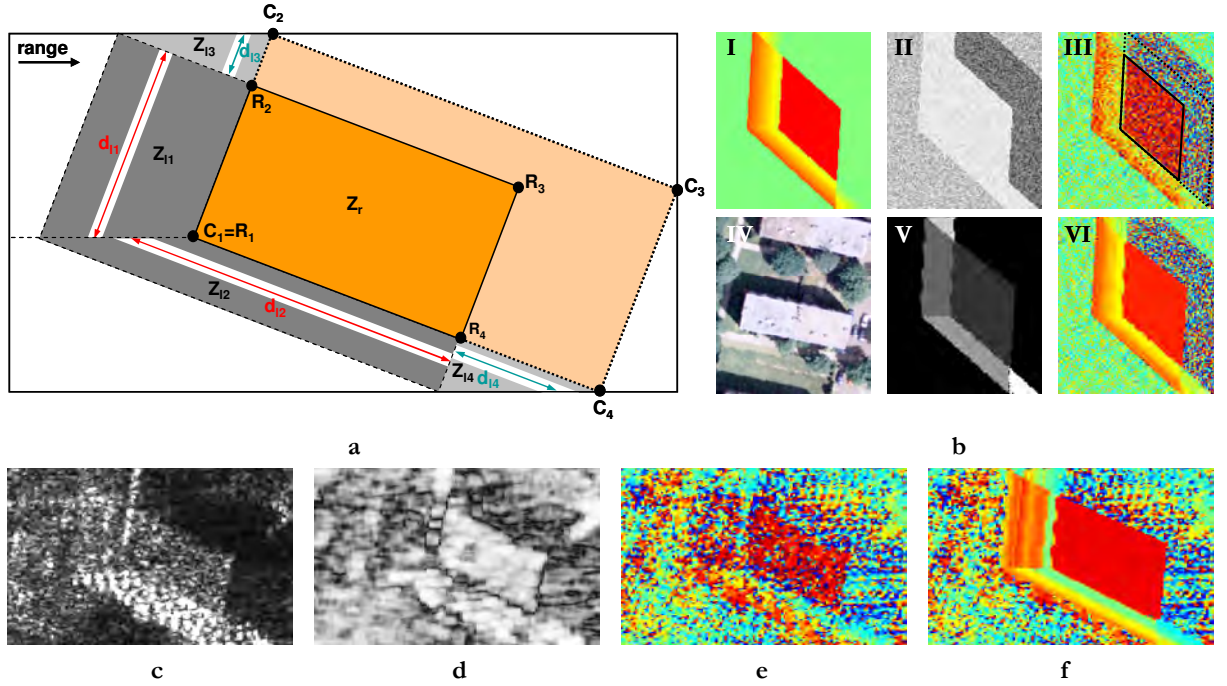
**Figure 4.31:** Smart filtering of flat-roofed building signatures: schematic description of the adaptive filter in slant range geometry (a), input and output arguments of filter step shown on a simulated data set (b); measured InSAR data – magnitude (c), coherence (d), interferometric phase (e), and the filter result (f)

of the signals of ground, wall, and roof. In areas $Z_{l3}$ and $Z_{l4}$, marked light grey in Fig. 4.31a, only the contribution mixture of ground and wall is present. Moreover, in each layover zone, an averaging of phase values is only allowed inside stripes oriented in parallel to the closest building wall, which are moved over the entire zone with adaptive length. Examples of these filter masks can be seen as white stripes in Fig. 4.31a. Similar to the filtering of the roof zone, also a coherence weighted averaging is applied.

In [128] the necessity of local phase unwrapping was pointed out since the weighted averaging is not performed on complex InSAR data. For reducing observed phase underestimation, especially inside the building roof, three different solutions of phase unwrapping were described in [38]. One solution is the calculation of a mean phase level in a neighbourhood as presented in [79]. This is insufficient for data showing a high noise level. The second solution is the extraction of local phase offsets based on the analysis of the local phase histogram. Since noisy phase values are distributed equally over all histogram bins, the largest histogram entry corresponds to the less noisy phase values. The mean value of the phases corresponding to this bin is then calculated to be the desired offset. If no histogram bin shows significantly more entries then the others, the offset is set to zero. The third solution utilises simulated InSAR phases to extract the local offset. Tests on all three methods show best results for the simulation method. Thus, this method is considered in the filtering of flat-roofed buildings.

To summarise, the flat-roofed building filter requires as input the following data: the interferometric phase, the coherence, the corner points of the building footprint, the corner points of the build-
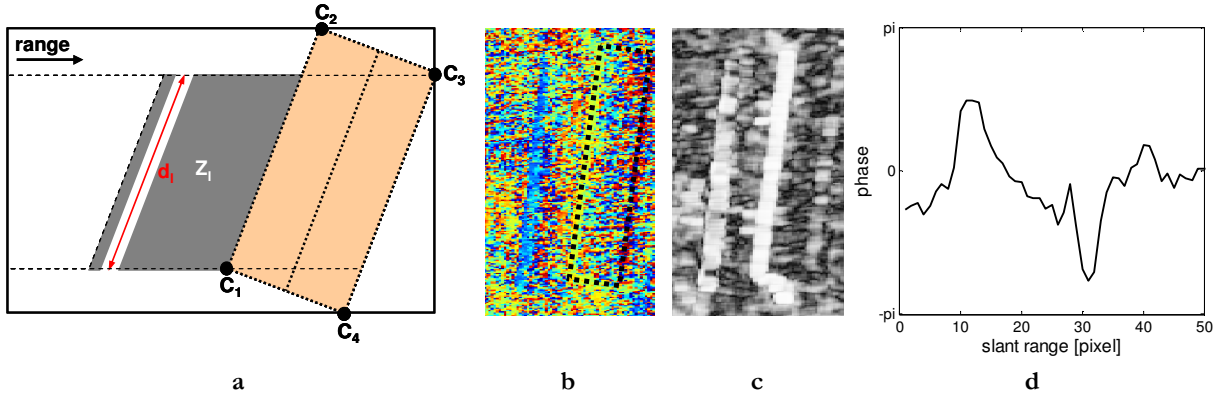
**Figure 4.32:** Smart filtering of non-flat-roofed building signatures: schematic description of the adaptive filter (a), input and output arguments of filter step – measured InSAR phases (b), coherence (c), and filtered phase profile (d)

ing roof signature, and the simulated interferometric phases. Some of the input arguments are visualised in Fig. 4.31b (I-III) based on noisy simulated interferometric phases (see Subsection 4.9.1). The optical signature of the simulated building, the mask marked with the averaging zones, and the filtered InSAR phases are shown in (IV-VI). A visual comparison between simulated (I) and filtered phases (VI) shows that the building phase is not underestimated. Furthermore, the edges of the building and the primary phase ramp in the layover area are preserved. Results on the measured InSAR signature of this building are presented in Fig. 4.31c-f. The shape of the lower layover zone (similar to $Z_{l2}$ in Fig. 4.31a) is better observable than in the original phases (e). The upper layover part does not show the characteristic ramp because these data are disturbed, which is also visible in the coherence data (d). However, the shape of the building is preserved.

In addition to the filtering of flat-roofed buildings in order to avoid underestimation of building heights, a proper phase filtering is also required for solving the ambiguity of non-flat-roofed building reconstruction. This filter is a simplification of the flat-roofed building filter, treating only one layover part $Z_l$ at the sensor facing building side, marked in grey Fig. 4.32a. This area was also investigated to extract building parameters from the magnitude signature (see Subsection 4.6.3). The area of filtering is enclosed by range lines crossing the points $C_1$ and $C_3$ of the building footprint. Pixels along the red arrow feature the same contributors, which results in similar phase values. The area under consideration for the averaging is marked in white. Similar to the filtering of flat-roofed building hypotheses, the stripe-shaped filter mask is moved in range direction. Furthermore, the coherence values are taken into account as weights. As result, the filtering delivers a phase profile in range direction. A local unwrapping of the phase values is also carried out. In Fig. 4.32b,c a building example is visualised by the phase and coherence data. The extracted range profile is shown in Fig. 4.32d with the corner located at position 31. In the following, the filtered phase profiles are used to solve the ambiguity problem in the reconstruction of non-flat-roofed buildings (see Subsection 4.11.1).
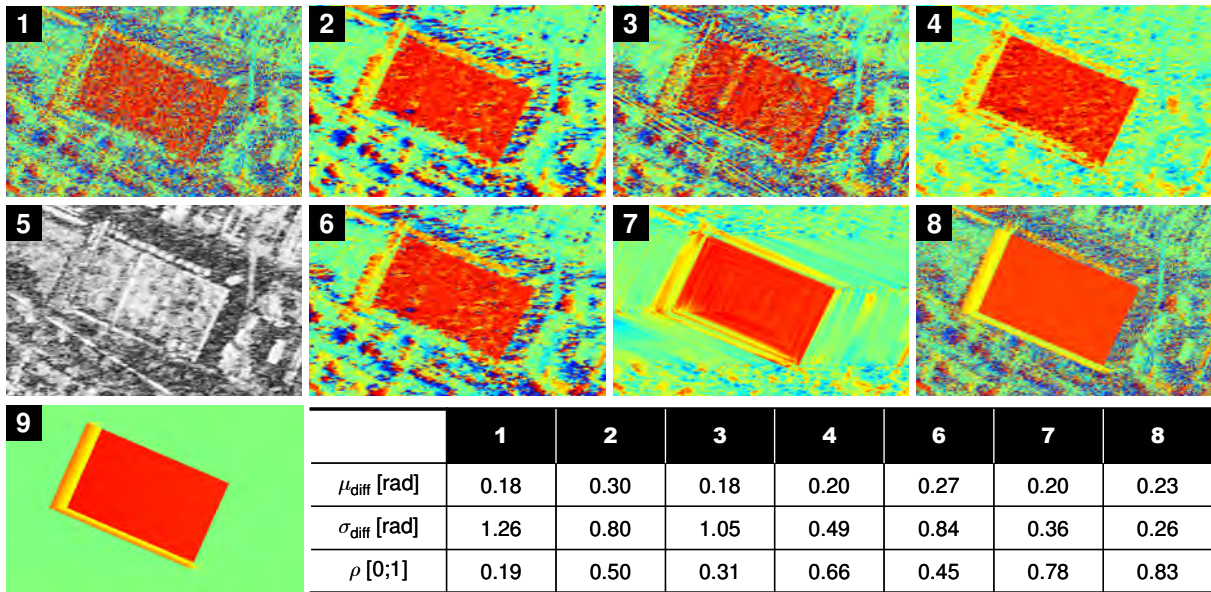
**Figure 4.33:** Assessment of filter results: input data – interferometric phase (1), coherence (5), simulated phase (9), area filter – Multilooking (2), Goldstein (3), and mean-coherence-weighted filter (4), orientation filter – Lee filter (6), GIS supported adaptive filter (7), flat-roofed building filter (8)

| | 1 | 2 | 3 | 4 | 6 | 7 | 8 |
|---|---|---|---|---|---|---|---|
| $\mu_{\text{diff}}$ [rad] | 0.18 | 0.30 | 0.18 | 0.20 | 0.27 | 0.20 | 0.23 |
| $\sigma_{\text{diff}}$ [rad] | 1.26 | 0.80 | 1.05 | 0.49 | 0.84 | 0.36 | 0.26 |
| $\rho$ [0;1] | 0.19 | 0.50 | 0.31 | 0.66 | 0.45 | 0.78 | 0.83 |

### 4.10.2  Comparison of Filtered and Simulated InSAR Phases

In this subsection, the comparison of simulated and filtered InSAR phases is described since the subsequent post-processing of the building hypotheses relies on the assessment of simulated and measured InSAR phases. Results of different filter approaches are compared and evaluated, and three different measures are introduced to support the evaluation of the post-processing.

In Fig. 4.33, the InSAR signature (interferometric phase – 1, coherence – 5) of an industrial building and six different filter results are given. The first row shows the smoothed signature of the building using three different square window filters. Fig. 4.33 (2) arises from a multilook-filtering [78], (3) by applying the Goldstein filter [56], and (4) by considering a weighted mean filter. As the coherence at the building roof is non-uniform, the smoothing effect is also non-uniform. Furthermore, blurring effects at the building edges are observable. The weighted mean filter delivers the best filter result of the area filters: due to the simulation-based unwrapping applied for the weighted mean filter, it shows less phase jumps in the roof area, and the edges are better preserved. Furthermore, quite good noise reduction in the surrounding area is reached. The second row shows the smoothed signature of the building by investigating filter windows of varying orientation. The filter result (6) obtained by the Lee filter [79] is comparable to the ones of the multilook-filtering. From the GIS supported filters [38], the result of the weighted mean filter with adaptive filter masks is shown (see 7 in Fig. 4.33). In comparison to the other filters with fixed window size of fixed or varying orientation, this adaptive filter provides better results. The edges are preserved very well, especially the layover is reconstructed better and the smoothing in the roof is uniform. At the building corner points, high phase values appear that are not observable at real building signatures. This is caused by the small filter windows used in this area that make the filtering suscep-

tible to artefacts. This is improved by the described flat-roofed filter (8). Effects at the building corner are reduced, and due to the filter assumptions, the building roof is represented by one phase value. The downward trend in the layover areas of the building is clearly recognisable. In comparison to the simulated data presented in Fig. 4.23a, the gradient of the layover ramps is lower since trees in front of the building hamper the formation of a full layover ramp. As the surroundings of the building are excluded in this filter approach, the result shows unfiltered values in this area.

The numerical validation of filter results is based on three different evaluation parameters that refer only to the building location (i.e. layover and roof area of the InSAR signature). Hence, the objects around the building that are not simulated (see Fig. 4.33 (9)) do not affect these values. The mean difference $\mu_{\text{diff}}$ between simulated and filtered phase images, the standard deviation of differences $\sigma_{\text{diff}}$ between simulated and filtered phase images, and the cross correlation $\rho$ between filtered and simulated phases are calculated. The value $\mu_{\text{diff}}$ contains the matching of the mean level of both data. Values other than zero report a phase shift between both. The value $\sigma_{\text{diff}}$ enables the assessment of the smoothing level. The similarity between simulated and filtered data is evaluated by $\rho$. The resulting evaluation values of the unfiltered phases and the six investigated filters are summarised in the table of Fig. 4.33. The values support the results of the visual comparison. From the group of area filters (2-4), the coherence weighted filter 4 shows best results. In the group of orientation filters, the GIS supported and the new flat-roofed building filter show the best results. The highest correlation value of 0.83 is achieved for the new flat-roofed building filter. This is due to good fit between building geometry (i.e. industrial building with large roof area) and filtering assumptions. Beyond the evaluation of the filter results, this comparison enables the evaluation of the simulation results as well. Hence, in the following these parameters are used to assess the similarity between simulated and measured interferometric signatures, which is important in the subsequent post-processing of the building hypotheses.

## 4.11   Post-processing of Building Hypotheses

This step of post-processing is integrated in the reconstruction algorithm since the 3D building hypotheses consisting of 2D footprints $fp$ and building heights ($h_f$ or $h_e$, $h_r$) show ambiguities in the building roof reconstruction and underestimation in the building height extraction. The reasons are described in Subsection 4.8.2. To solve the ambiguities and to diminish the underestimation, a detailed analysis of the InSAR phases at the position of the building hypotheses takes place. Using simulated interferometric phases based on the generated 3D hypotheses, an improvement of the building hypotheses can be achieved. The filtering of the InSAR phase described in Subsection 4.10.1 is applied to support the assessment step between simulated and measured InSAR phases.

The first possibility to post-process the building hypotheses is only applicable to non-flat-roofed buildings. Since the ambiguity of the roof reconstruction is given for all hypotheses, the post-processing is applied to all non-flat-roofed hypotheses. The second step enables the possibility to recalculate the height of flat-roofed building hypotheses. To mitigate the underestimation of roof height, this post-processing is carried out on all flat-roofed building hypotheses. As third, an option is presented to correct oversized building footprints due to corner or layover lines that were

extracted too long. This iterative step is only used optionally for the correction of flat-roofed buildings.

### 4.11.1   Ambiguity of Gable- and Monopitch-Roofed Building Reconstruction

The ambiguity in the reconstruction of non-flat-roofed buildings can theoretically be solved by a high-precision analysis of the magnitude or phase signature. In the magnitude signature, the shape of the shadow area can be analysed, as the different heights $h_e$ and $h_r$ of the models will lead to differences between simulated and real data, especially for buildings with a ridge-orientation perpendicular to azimuth direction. However, such an analysis would suppose a clear shape of the shadow without any interference from other objects, which is usually not the case in dense urban areas. Furthermore, the magnitude values of the ridge-parallel layover line would likely also show variations since the signals of different contributors are superimposed.

Hence, the analysis of the phase signature seems more promising. Due to different roof heights of the four remaining building hypotheses, the interferometric phase in the layover area is dominated by different contributors, which results in different phase shapes. This effect is observable in the simulated phase profiles, shown for all four hypotheses in Fig. 4.34a-d. As described in Subsection 4.9.1, in the simulation step the calculated building parameters (e.g. $c$, $h_e$, and $h_r$), the track parameters (e.g. off-nadir look angle $\theta$ and sensor altitude $H$), and sensor parameters (e.g. wavelength $\lambda$ and baseline $B$) are taken into account.

The first row (a,b) of Fig. 4.34 contains the two hypotheses showing $\alpha > \theta$. The two hypotheses with $\alpha < \theta$ are given in the second row (c,d). For all four hypotheses, a phase shifting took place to avoid phase jumps inside the building signature. Thus, the constant terrain phase is moved to approximately $-\pi$. In Fig. 4.34, it is observable that the first phase values in the layover areas of all four hypotheses are different, due to different $h_r$ and distances from sensor to building eave. Focusing first on the models $\alpha > \theta$ (a,b), $h_{r\_g_1}$ and $h_{r\_m_1}$ are higher than $h_{r\_g_2}$ and $h_{r\_m_2}$ (c,d) and the ridge point is the building closest point to the sensor. Hence, the first backscatter information of the building contains the maximal height and leads to the highest point of the layover shape. Additionally, this first layover point allows the direct extraction of the ridge height, if we assume dominant reflection of the roof in comparison to the ground. Comparing gable- and monopitch-roofed hypotheses, $h_{r\_m_1}$ is larger than $h_{r\_g_1}$, which causes a much steeper slope in the layover area for the monopitch-roofed model. The second pair of building hypotheses with $\alpha < \theta$, shows a lower phase value at the beginning of the layover. Thus, the eave point has the smallest distance to the sensor. As a consequence, in comparison to model $\alpha > \theta$, the direct extraction of the ridge height based on the first layover value is not possible. The differences in the phase shape of the layover area are caused by the mixture of heights of the different contributors. The layover part, marked by the parameter $b$, of hypotheses $\alpha > \theta$ is governed by signal contributions of roof and ground. Therefore, the height contribution of the roof is strongly decreasing whereas the ground height stays constant. In comparison, the same layover part of hypothesis $\alpha < \theta$ is caused by the response of roof, wall, and ground. The height contribution of the roof is slightly increasing; the contribution of the wall is decreasing and the ground height stays constant. The mixture of heights shows an increasing trend up to the ridge point position at pixel 13 (see Fig. 4.34c,d.). Other trends can be observed for various $\alpha,\theta$-combinations (see e.g. gable-roofed building in Fig. 4.24b and [127]).
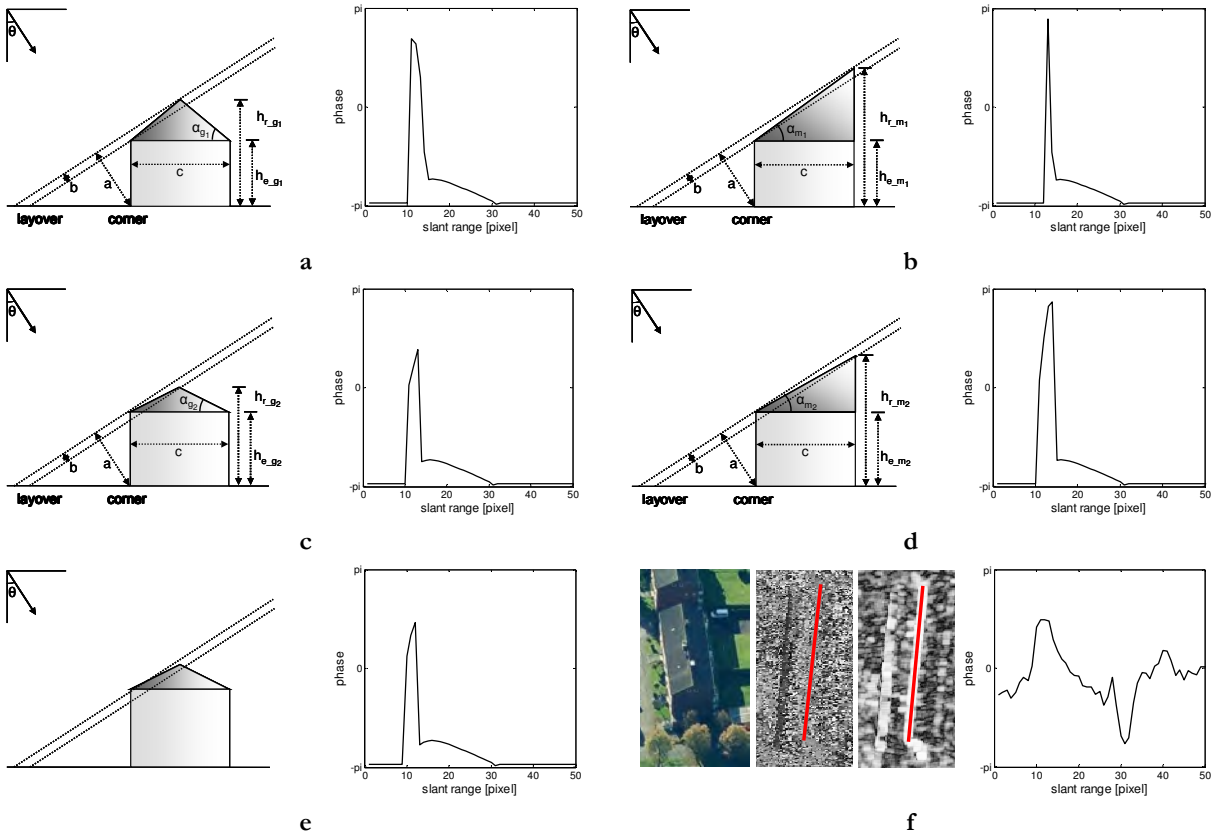
**Figure 4.34:** Ambiguity of the reconstruction of non-flat-roofed buildings: schematic view and corresponding simulated phase profile – $\alpha > \theta$ gable roof (a) and monopitch roof (b), $\alpha < \theta$ gable roof (c) and monopitch roof (d), schematic view and simulated profile considering real building parameters (e); aerial image (screenshot from bing, ©2011 Microsoft Corporation), measured InSAR phases and coherence overlaid with corner line (marked red), and averaged InSAR range profile (f)

The part of the layover area between its maximum and the corner position is characterised by two contributors, wall and ground. It begins at slant range position pixel 13 in the phase profiles of Fig. 4.34a-d and shows a similar trend for all four models. The phase value at the corner position (slant range position pixel 31) is at terrain level in the simulated profiles. Due to the radar shadow of the building, the phase shape behind the layover area contains no further information. In Fig. 4.34e the simulated phase profile of a real building geometry is shown. The heights correlate with the gable-roofed hypothesis $\alpha < \theta$. In comparison, the real InSAR profile resulting from the steps of phase filtering (Subsection 4.10.1) is depicted in Fig. 4.34f. Supplementary, an aerial image, and the phase and coherence image overlaid with the corner line (red) are shown. As observable in the original phase data, the layover line (dark grey) shows lower phase values than the corner line due to a phase jump. Hence, phase shifting took place similar to the simulated profiles, which allows direct comparison between the two. Similarities between simulated and filtered measured phases are harder to observe. The high phase value of both profiles is nearly identical in position and absolute value because for both $\alpha$ is smaller than $\theta$. The short increase at the beginning of the layover is only clearly observable in the simulated phase signature. The strong uptrend in the simu-

|     |     |     |     |     |     |
| :-: | :-: | :-: | :-: | :-: | :-: |
| a   | b   | c   | d   | e   | f   |
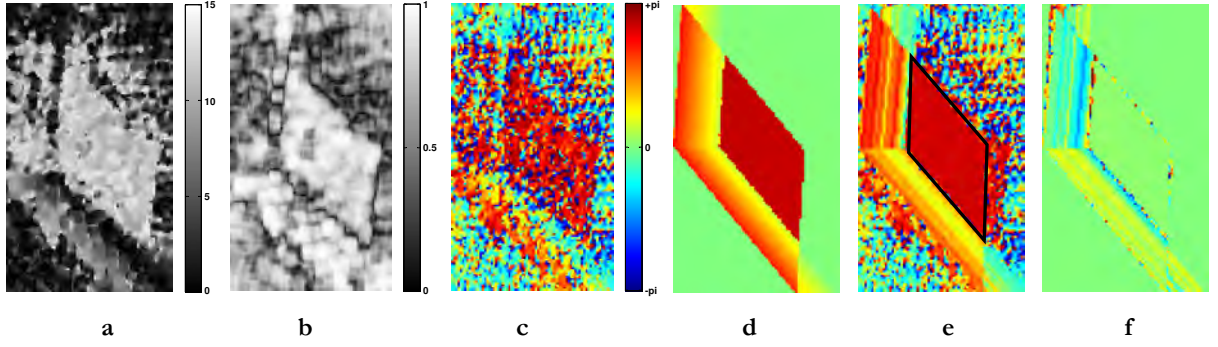
**Figure 4.35:** Correction of underestimated building heights: normalised heights (a), coherence (b), interferometric phase (c), simulated interferometric phases (d), filtered interferometric phases overlaid with roof area (e), difference between simulated and filtered phases (f)

lation of model $\alpha < \theta$ is less pronounced in the real phase profile. The position and the absolute phase value at the corner position (slant range position pixel 31) are again similar in the simulated and in the real phase profile.

For the post-processing of the non-flat roofed building hypotheses, the differences of the layover shapes are investigated and exploited in order to choose the final reconstruction result. First the layover patch of measured InSAR phases is extracted using the back projected building footprint $fp$. Second, the filtering of the measured phases takes place to obtain an averaged phase profile in slant range direction. Third, the simulation is carried out providing phase profiles of all generated hypotheses. Then, the correlation coefficient $\rho$ is calculated to assess the similarity between simulated and measured phases. For this, only profile parts are considered that contain information from wall or roof. Finally, the hypothesis showing the highest correlation coefficient is chosen as reconstruction result. Results and the comparison to reference data are presented in Section 5.3.2.

### 4.11.2  Correction of Underestimated Building Heights

As described in Subsection 4.8.2, the extraction of the height of a flat-roofed building can lead to underestimation due to averaging height values over the entire building footprint. Since this area contains the part of the roof not superimposed by wall and ground signal but also a part of the shadow area, building heights that are too low can result. Thus, a recalculation of the heights is performed by taking into account the simulation (Subsection 4.9.1) and the filtering step (Subsection 4.10.1).

The processing utilises the following data: the normalised heights $h_n$ (see in Fig. 4.35a), the coherence (b), the measured phase (c), and the reconstructed 3D building hypothesis. First, the simulation of the interferometric signature is carried out, whose result is shown in Fig. 4.35d. Based on the generated roof map (i.e., backscattering from roof only, black parallelogram in Fig. 4.35e), a new coherence-weighted averaging is applied to $h_n$. Furthermore, the filtering is also carried out (see Fig. 4.35e). In the last step, the similarity between simulated and measured phases is assessed. The differences are shown in (Fig. 4.35f) using only signature parts relevant to the building (i.e., layover and roof area). For the example an improvement from $h_f = 9.0\,\mathrm{m}$ to $h_{f,c} = 11.1\,\mathrm{m}$ was
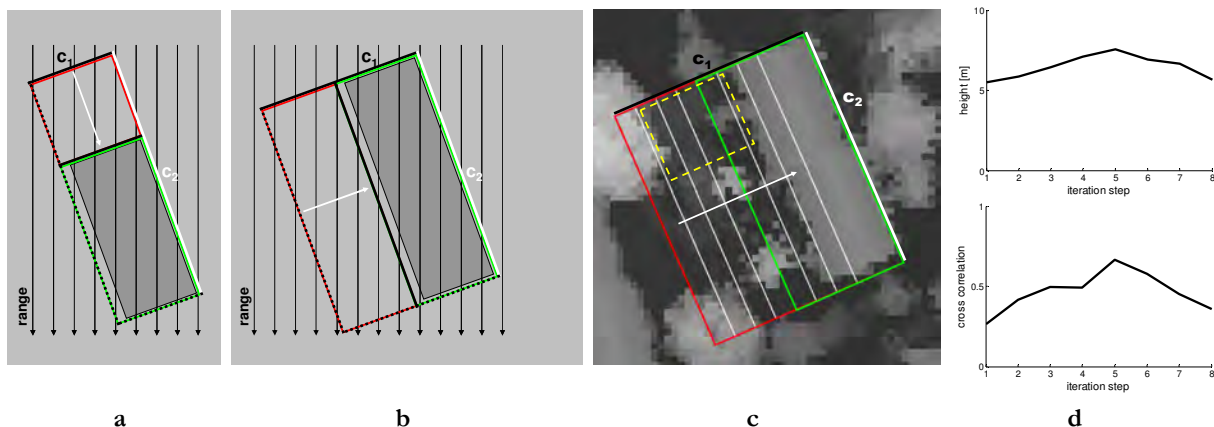
**Figure 4.36:** Correction of oversized building footprints: correction of corner position (a), correction of corner length (b), LIDAR DSM overlaid with initial (red) and final (green) building footprint (c), results of calculating height (top) and cross correlation (bottom) for all iteration steps (d)

achieved obtaining a cross correlation of $\rho = 0.67$. The reference height of this building is $h_{ref} = 12.5\,\text{m}$.

The step of recalculation could be implemented in an iterative manner to recalculate the building height until reaching maximum cross correlation maximum or the maximum number of iterations. This will be discussed in more detail in Subsection 5.4.

### 4.11.3 Correction of Extended Right-Angled Footprints

In addition to the underestimation of the building height described in Subsection 0, an oversized building footprint can also lead to a too low building height. This is mainly caused by signal contributions of adjacent walls, fences, or trees leading to an unfavourable prolongation of the corner or layover lines. The estimated building height is affected by this phenomenon, because surrounding height values of the terrain contribute to the estimation of building height. Similar to the postprocessing of flat-roofed building heights, an improvement can be reached by comparing simulated and measured InSAR phases.

In Fig. 4.36a,b, the corrections of two building hypotheses are visualised. The first example requires a movement of corner line $c_1$. This can be caused by objects in front of the building such as fences. The second needs a correction of the length of corner $c_1$. This can be required due to prolongation of the line resulting from neighbouring objects such as garages. The real building example given in Fig. 4.36c, shows such a case. The correction of the footprint starts, with the simulation of the reconstructed 3D building hypothesis. Second, the measured phases are filtered and the recalculation of the building heights inside the simulated roof map takes place. Additionally, the cross correlation between simulated and filtered phases is calculated. These steps are similar to the procedure to correct underestimated building heights described in Subsection 0. In order to improve the building footprint, a shifting along the building corner lines is performed. The updating of the position is realised by a parallel shift in discrete steps, which is visualised by the white arrow in Fig. 4.36a,b. For each new corner position, the building width or building length are recalculated. As building height, the estimate of the previous iteration step is used. The processing steps

of simulation, height averaging, filtering and assessment are repeated over the full corner length or stopped if reaching a predefined criterion (e.g. maximum iterations or correlation threshold). For the example in Fig. 4.36c, the red outline marks the oversized building footprint. The white lines show the updated building footprints. Finally, the green line highlights the updated footprint achieving the best correlation coefficient $\rho$ and the greatest building height. The trends of the height recalculation and the cross correlation coefficients between simulated and filtered phases are plotted in Fig. 4.36d. In general, the final shape of the building footprint is defined by the maximum of the correlation coefficient. In the given example, the final footprint (green) does not fit the building shape at best. This is due to the neighboured garage (dashed yellow line) and the tree in front of the building, which affect the measured phase signature. This post-processing is implemented as an optional step since not all buildings hypotheses require a correction of the building footprint.

### 4.11.4  Determination of final 3D Buildings

After the post-processing of the reconstructed 3D building hypotheses, the constraints defined for the underlain building model are used to filter false alarms and to rate overlapping hypotheses. The constraint to the building size has already been utilized in Subsection 4.8.1. Hence, only the constraint to the building height is used, retaining all $fp$ showing heights (i.e., corrected flat-roofed height $h_{f,c}$ or ridge height $h_r$) larger than $5\,\text{m}$. In the second step, the groups of building footprints $fp_{cc\_f}$, $fp_{cl\_f}$, $fp_{ll\_f}$, $fp_{cc\_d}$, $fp_{cl\_d}$ are rated independently. For overlapping hypotheses, an intersection of 20 percent at maximum is accepted. If parallelograms still overlap, then the one showing the greatest reconstructed building height is kept. Afterwards, all five groups are fused. In a last step, remaining overlapping hypotheses have to be filtered again. At this point, the different reliability levels and the achieved cross correlation values are taken into account. Since, the reliability level is a more stable feature, it gets a higher priority than the reached similarity between simulated and measured phase. The cross correlation values are only used, if flat-roofed and non-flat-roofed hypotheses of same reliability level overlap. The results of the entire reconstruction process are presented and discussed in the following chapter.

# 5 Results

In this chapter, first the test site is described, specifying the considered interferometric SAR data and the available reference data. Then, the results of the pre-processing steps of coregistration (Section 4.3), classification of land cover (Section 4.4), and calculation of interferometric heights (Section 4.5) are shown. The intermediate results of the reconstruction approach and the final 3D buildings are presented and discussed.

## 5.1 Test Data

In the following, the test site is described focusing on building structures present in the considered area. Furthermore, the specifications of the InSAR data are presented and the reference data consisting of cadastral vector data, orthophotos, LIDAR DSM and DTM are specified. The post-processing of these data is described, which is necessary to utilize them in the evaluation of the reconstruction results.
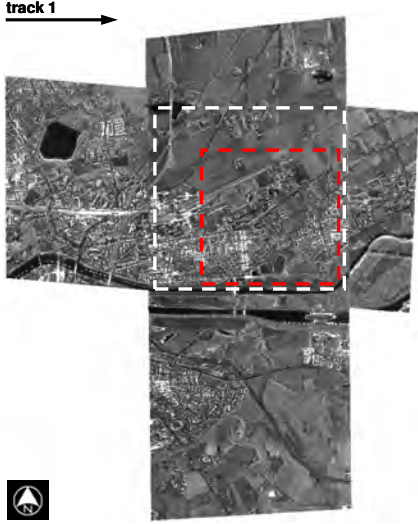
### 5.1.1 Test Site

In this thesis, two interferometric image pairs showing the city of Dorsten, Germany, were used to demonstrate the performance of the approach of building reconstruction described in Chapter 4. The city, located in the Ruhr Area, is characterised by a densely built-up centre with more low-density areas in the surroundings. The covered area contains mainly residential buildings interspersed with few low industrial buildings (e.g. storehouse and petrol station) and some larger buildings for the infrastructure (e.g. school and church). The residential buildings comprise one-family houses with a footprint size lower than $100\,\mathrm{m}^2$ up to multi-family houses showing footprint sizes of more than $400\,\mathrm{m}^2$. The shape of the roofs is highly variable in the considered area. There exist the standard types of flat, gabled, hipped, and monopitch roof, but additionally many mixed forms are observable, as shown in Fig. 5.1. Moreover, most of the buildings are not isolated since many garages, sheds, fences, and walls are built in the direct neighbourhood of buildings. Furthermore, a high level of greening is present in the area (see Subsection 5.2.3).



**Figure 5.1:** Terrestrial photos of Dorsten

**Table 5.1:** Specifications of InSAR data (AeS-1, Intermap Technologies)

| parameter | track 1 | track 2 |
|---|---|---|
| wavelength [cm] | 3.139 | 3.139 |
| polarisation | HH | HH |
| range and azimuth pixel spacing [m] | 0.375 , 0.152 | 0.375 , 0.179 |
| squint angle [°] | 2.88 | 3.16 |
| heading angle [°] | 92.04 | 175.91 |
| sensor altitude [m] | 3203.5 | 3191.4 |
| mean terrain height [m] | 80 | 80 |
| acquiring date | 13-03-2003 | 13-03-2003 |
| look angle (near, middle, far) [°] | 28, 43, 52 | 28, 43, 52 |
| length of baseline [m] | 2.4 | 2.4 |

## 5.1.2 InSAR Data

In this thesis, two single look complex InSAR image pairs are used. The single-pass data provided by Intermap Technologies were acquired by the AeS-1 sensor [111]. The data were taken with different heading angle resulting in an orthogonal flight configuration. Each stripe shows an area of $2,300 \times 5,600\,\text{m}$, depicted in Tab. 5.1 left. The overlapping region marked by the dashed white line, covers approximately $5\text{km}^2$. Additionally, the parameters of both data tracks are listed in Tab. 5.1. The AeS-1 sensor operated in X-band with a wavelength of $3.14\,\text{cm}$ and a bandwidth of $400\,\text{MHz}$. The data show a ground range resolution of approximately $0.5\,\text{m}$. The slant range pixel spacing in range is $\sim 40\,\text{cm}$ and in azimuth $\sim 20\,\text{cm}$. The two interferometric image pairs were recorded with an effective baseline of $2.4\,\text{m}$. The off-nadir look angle increases from $28°$ to $52°$ over swath. Concerning the processing of the SAR data, a Hamming window was applied in azimuth and a rectangular window in range direction. Hence, in the SAR data more side lobes are observable in range direction than in azimuth direction. In the following, only a part of the overlapping area is analysed due to the coverage of the reference data and the size of the SAR data. The area is marked by the dashed line in red that corresponds to a size of $1,700 \times 1,700\,\text{m}$ in ground range and $2,700 \times 10,500\,\text{pixels}$ for track 1 and $2,800 \times 8,400\,\text{pixels}$ for track 2 in slant range geometry.

## 5.1.3 Reference Data

For the evaluation of the reconstruction results, three different kinds of reference data were used. A high resolution optical orthophoto acquired with a Zeiss RMK aerial camera was provided by the State Surveying Authority of North Rhine-Westphalia. The multispectral data show a pixel size of $0.3\text{m}$ on ground. In the following, the data shown in Fig. 5.2a are used to evaluate the result of the land cover classification. For that, a vegetation mask was extracted manually from the optical data. The result can be seen in Fig. 5.2e, where white marks vegetated and black non-vegetated areas.
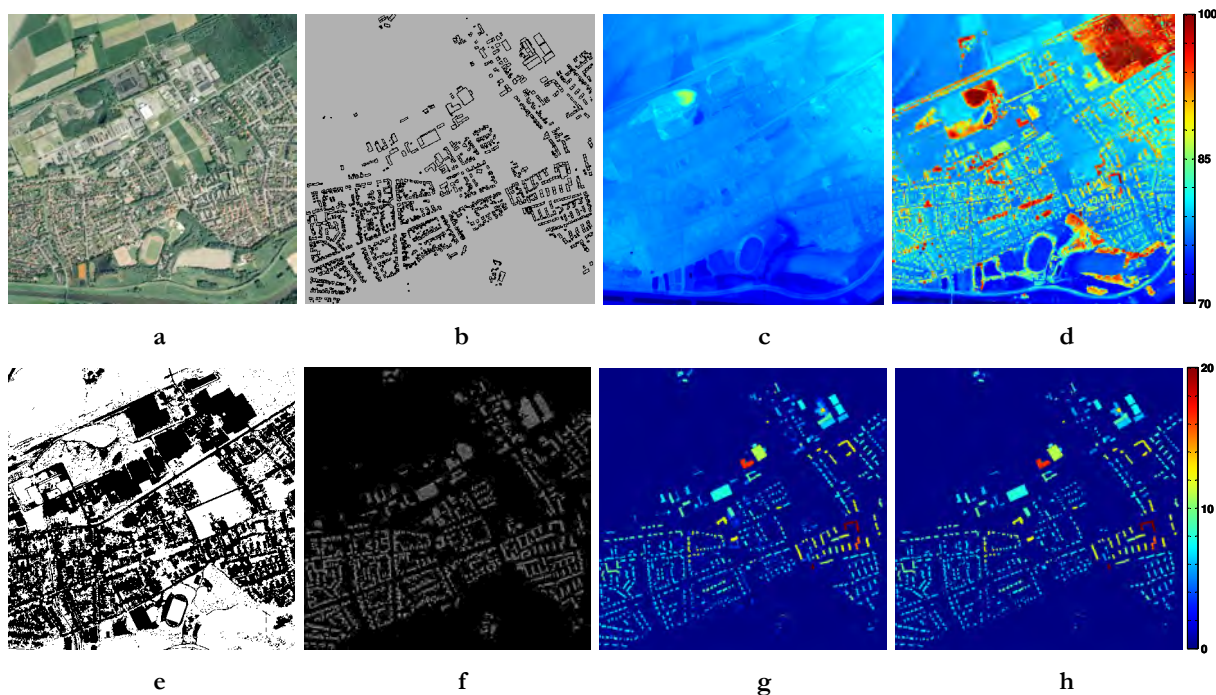
**Figure 5.2:** Reference data: optical image (a), cadastral building footprints (b), LIDAR DTM (c), LIDAR DSM (d); post-processed reference data: vegetation mask (e), mask of building footprints (f), extracted building heights inside footprints (g) and cleaned result building height mask (h)

Cadastral data were used to assess the detected building footprints. The data shown in Fig. 5.2b contain the boundary of the building footprints as well as additional information (e.g. building borders, garages, streets, sub-plot, and plot number). The data were manually processed, extracting only the footprint information, removing very small structures such as sheds, and eliminating virtual building borders, for example, observable for housing terraces. The resulting map is presented in Fig. 5.2f, where grey areas mark building footprints.

As third, the LIDAR DTM and DSM shown in Fig. 5.2c and d were exploited to evaluate the extraction of the building heights. These laser data have a pixel resolution of $1 \times 1\,\text{m}$ . To obtain the relative building height, the differences between DSM and DTM are calculated. The normalised height data are fused with the building map obtained from the cadastral data: the median of all height values inside the building footprint is considered to be the reference building height. The result can be seen in Fig. 5.2g. In Fig. 5.2h, a height map containing only buildings higher than $5\,\text{m}$ (i.e., those that fulfil the model assumptions made in Subsection 4.1.1) is shown. Since this processing delivers only reference heights for flat-roofed buildings, heights for the other roof types were extracted manually for some selected buildings.

## 5.2    Results of Pre-processing

The first results of the developed approach, containing parameter optimisation in the steps of co-registration and interferometric height calculation, are presented in this subsection. Furthermore,

**Table 5.2:**     Results of coregistration and interferometric height calculation



| results of coregistration | aspect 1 | aspect 2 |
|---|---|---|
| translation $a_i$ [pixel] | 6.0 | 6.0 |
| scaling $b_i$ | 1.3 | 1.2 |
| mean coherence | 0.680 | 0.686 |
| mean coherence of Intermap interferogram | 0.696 | 0.706 |

| results of interferogram calculation | aspect 1 | aspect 2 |
|---|---|---|
| original: $B_V$ and $B_H$ [m] | -0.3143 / 2.3640 | -0.3143 / 2.3640 |
| before correction: $\sigma_{\Delta\varphi}$ [rad] | 1.0036 | 1.5754 |
| corrected: $B_V$ and $B_H$ [m] | -0.3123 / 2.3642 | -0.29732 / 2.3662 |
| after correction: $\sigma_{\Delta\varphi}$ [rad] | 1.0024 | 0.9748 |

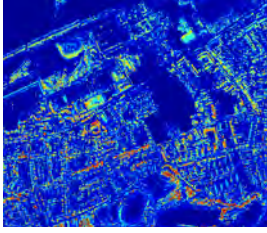the results of the land cover classification are summarised and evaluated by using the generated reference mask of vegetated areas.
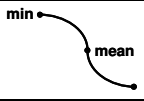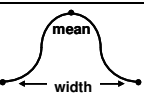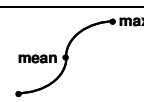
### 5.2.1    Coregistration

The InSAR data were delivered as SLC data. The coregistration of the data was performed by the coarse-to-fine parameter testing described in Section 4.3 to reach maximum coherence between master and slave images (see Section 4.3). As mentioned before, for these airborne data a simple transformation comprising translation and scaling in range direction is successful. The resulting transformation parameters of the InSAR pairs are listed in Tab. 5.2. Furthermore, the reached coherence values calculated by averaging over the whole scene (see Tab. 5.2, upper left image) are given. As reference value, the mean coherence of the additionally delivered downsampled interferograms is listed. These interferograms are not used in the following due to the reduced data resolution. Both coregistration schemes reach a similar level of coherence.

### 5.2.2    Calculation of Interferometric Heights

The calculation of the interferometric heights also contains an optimisation step (see Section 4.5), which aims at reducing unnatural linear trends of the phases in range direction (see Fig. 4.6b). For the given data set, this can be reached by a correction of the baseline angle $\xi$. For that, the vertical and horizontal parts of the baseline ($B_V$ resp. $B_H$) are changed. As criterion of decision, the minimal standard deviation of the phases is chosen since a narrow phase distribution is requested. The results of the correction step are summarised in Tab. 5.2 for both interferograms. The improvement of the standard deviation is especially observable for the second aspect. The achieved standard deviation is comparable to that of aspect 1. Hence, an observable change to the original baseline components is also only given for the second aspect. The differences between the original configuration and the new values correspond to a change of $\xi$ of a half degree. The resulting phases are presented in Fig. 4.6c. Normalised heights are show in Tab. 5.2 left.

**Table 5.3:** Membership functions and interval borders for land cover classification

| low | | Magnitude $\overline{A}_{dB}$ resp. $\overline{\sigma_{dB}^0}$ | Coefficient of Variation $\overline{CoV}$ | Coherence $\overline{\gamma}$ |
|---|---|---|---|---|
|  | min | $\overline{A}_{min}$ | 0 | 0 |
| | mean | $\overline{A}_{mean} - \overline{A}_{std}$ | $\overline{CoV}_{hom} + 0.5 \cdot \overline{CoV}_{std}$ | $\gamma_{mean}$ |
| **medium** | | | | |
|  | mean | $\overline{A}_{mean} - 0.5 \cdot \overline{A}_{std}$ | - | $\gamma_{mean} + 0.5 \cdot \gamma_{std}$ |
| | width | $4 \cdot \overline{A}_{std}$ | - | $2 \cdot \gamma_{std}$ |
| **high** | | | | |
|  | max | $\overline{A}_{max}$ | $\overline{CoV}_{max}$ | 1 |
| | mean | $\overline{A}_{mean}$ | $\overline{CoV}_{hom} + \overline{CoV}_{std}$ | $1 - \gamma_{std}$ |

## 5.2.3 Land Cover Classification

The classification into vegetated and urban areas was implemented to support the extraction of building features (Section 4.6) and the generation of building hypotheses (Section 4.8). A fuzzy classification is applied on the InSAR data. As appropriate information features, the mean amplitude values $\overline{A}_{dB}$ (resp. the Sigma Naught coefficients $\overline{\sigma_{dB}^0}$), the mean Coefficient of Variation $\overline{CoV}$, and the coherence $\gamma$ are taken into account. For the fuzzy rule set eight different membership functions MFs were defined that are specified as sigmoid and Gaussian curves (see Section 4.4). The borders and the mode of these MFs were derived from the InSAR image statistics. The two parameters (i.e., Gaussian curve – {mean, width}, sigmoid curve – {max, mean} or {min, mean}) necessary to specify each MF are listed in Tab. 5.3. For the definition of the three amplitude related MFs, the values $\overline{A}_{min}$, $\overline{A}_{mean}$, $\overline{A}_{max}$, and $\overline{A}_{std}$ are used. The two MFs containing the $\overline{CoV}$ are derived from image statistics – $\overline{CoV}_{hom}$, $\overline{CoV}_{max}$, and $\overline{CoV}_{std}$. In the third column, the MFs of the coherence are summarised that include two statistic values – $\gamma_{mean}$ and $\gamma_{std}$. Based on these eight MFs, nine classes were defined (see Section 4.4) that are assigned to the superclasses $C_{veg}$ and $C_{urban}$. The classification was carried out on both InSAR image pairs. Furthermore, the fusion of the single-aspect classification results was realised to avoid occlusion effects due to the side-looking SAR geometry. For that, the classification results were geocoded, followed by a fusion step calculating the intersection between the classified *vegetated areas*.

The results of the classification step are presented in Fig. 5.3 by taking the manually extracted vegetation map derived from the orthophotos as reference data. In Fig. 5.3a, the reference data and some general information are summarised in the corresponding table. The classification result of the multi-aspect images is visualised in Fig. 5.3b,c together with the corresponding confusion matrix. For both data sets, more than 70 percent of the area is classified correctly. The critical false positives, areas of urban structure classified as vegetated areas, reach values of 16.4 percent and 15.5 percent. In Fig. 5.3d, the fusion result of the multi-aspect data is shown. Less vegetated area is correctly classified, which is visible on the decreasing true positives (32.3 percent) and the increasing false negatives (17.7 percent). The desired improvement, a decreasing of the false positives
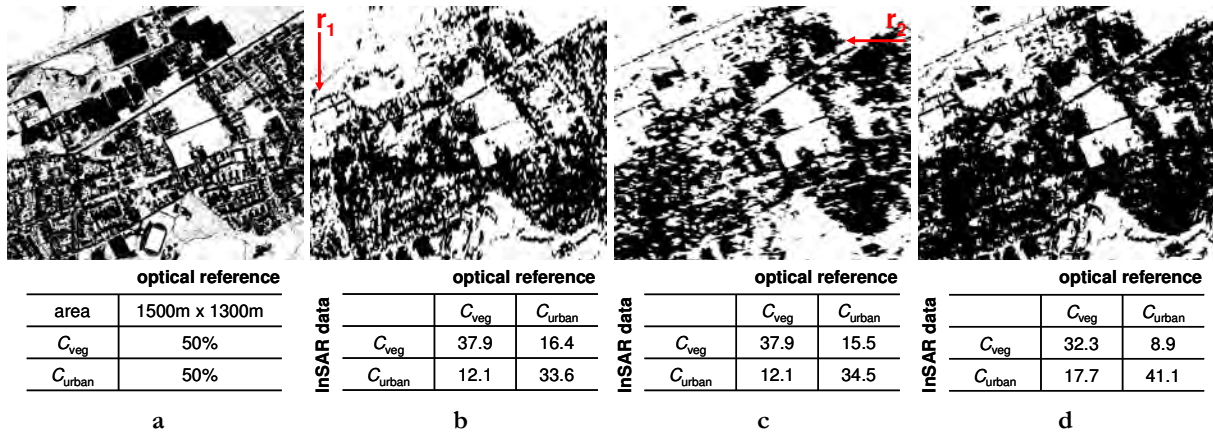
Figure 5.3: and Results of land cover classification: reference mask (a), result of aspect 1 (b) and of aspect 2 (c), result of the multi-aspect fusion (d)

value (8.9 percent), is observable. Thus, false classification due to layover at high vegetation could be reduced by investigating the multi-aspect data. The remaining underestimation of vegetated area could be partly caused by the different acquisition times (InSAR data – March 2003, orthophotos – May 2002).

## 5.3    Results of Building Reconstruction

In this section, the results of the building reconstruction are presented. First, the extraction of the building features is described by investigating the full scene. Second, the generation of the building hypotheses is focused. The results are shown on three subareas of the scene to discuss strengths and weaknesses of the approach.

### 5.3.1    Results of Extracting Building Features

The extraction of building features starts with the detection of lines by using the CFAR line detector described in Subsection 4.6.1. In order to use this detector, the template size has to be defined, taking into account the SAR processing parameters and the pixel spacing. As the detector is used to extract corner lines, which usually appear at building sides oriented parallel to azimuth direction, the centre width $w_{t,c}$ of the template is defined by the range resolution, the applied windowing and the pixel spacing in range direction. As the AeS-1 data are slightly oversampled and to avoid interpolation effects, $w_{t,c}$ is set to 3 pixels. The width of the neighbouring regions $w_{t,n}$ is set to 5 pixels. This value is chosen smaller than proposed in [137] because interaction between close-by double lines should be avoided. The length $l_t$ of the template regions is fixed to 7 pixels. For applications like road extraction, a larger $l_t$ could be helpful to bridge gaps in the searched structures, but this is not desired for the detection of lines in dense urban area. The resulting eight probability images are filtered with the vegetation mask. In the following, line segments are fitted only to high probability values that are not classified as vegetated area (see Subsection 4.6.1). The number of lines extracted in each probability image is listed in the second and third column of Tab. 5.4. For the first image pair more than 245,000 line segments and for the second almost 190,000 segments are detected. In

**Table 5.4:** Results of extracting building features

| orientation of template | aspect 1 | aspect 2 | aspect 1 | aspect 2 | aspect 1 | aspect 2 |
|---|---|---|---|---|---|---|
| | fitting of lines | | merging of lines | | filtering of lines (orientation) | |
| 1 | 30,124 | 24,403 | 14,858 | 11,906 | 5,795 | 4,680 |
| 2 | 42,878 | 36,130 | 9,490 | 7,951 | 1,070 | 611 |
| 3 | 32,047 | 25,715 | 3,802 | 3,139 | 176 | 236 |
| 4 | 19,837 | 17,022 | 2,777 | 2,554 | 79 | 61 |
| 5 | 21,083 | 18,073 | 6,375 | 6,080 | 758 | 701 |
| 6 | 21,057 | 18,916 | 3,069 | 3,145 | 160 | 289 |
| 7 | 36,844 | 31,840 | 4,343 | 4,114 | 84 | 78 |
| 8 | 41,225 | 34,266 | 10,268 | 8,859 | 1,242 | 903 |

| type of line | filtering of lines (height) | | merging of lines | | filtering of lines (model) | |
|---|---|---|---|---|---|---|
| layover | 2,167 | 1,724 | 1,923 | 1,482 | 583 | 542 |
| corner | 6,374 | 4,999 | 5,690 | 4,459 | 1,398 | 1,133 |

| type of line | classification of corners | | merging of lines | |
|---|---|---|---|---|
| corner (single) | 1,192 | 919 | 928 | 875 |
| corner (double) | 206 | 214 | 206 | 214 |
| layover | 583 | 542 | 457 | 506 |
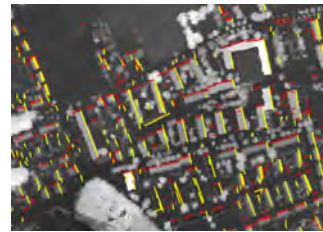


the next step, lines are merged that fulfil constraints in terms of orientation (i.e., orientation difference less than 5 degrees) and in the size of the gap (i.e., up to 5 pixels in line direction and up to 3 pixels sidewise) between them. The definition of these values was assisted by the analysis of the line segments. As a result of this merging step, a significant reduction of lines could be reached (see Tab. 5.4, fourth and fifth column).

Next, orientation based filtering was applied (see Subsection 4.6.2). The resulting lines listed for each orientation interval are shown in Tab. 5.4, columns six and seven. An accumulation in orientation directions 1, 2, and 8 is observable. This is caused by decreasing corner intensity because of an increasing span angle $\kappa$ between building wall and sensor flight direction. The remaining lines in orientation direction 4 are due to signal side lobes in range direction. The subsequent filter step exploits the interferometric heights along the detected lines. Potential layover and corner lines are discriminated in this step. For both aspects, the number of corner lines is three times higher than the number of layover lines (see second part of Tab. 5.4, second and third column). This emphasises the benefit of corner lines for building reconstruction. An additional merging step is carried out using the same values as the last merging step for the orientation and the sideways gap constraint. The allowed gap distance in line orientation is increased since an undesired merging of lay-

**Table 5.5:**     Results of generating building footprints

| input | lines | parallelograms | | type of $pg$ | classification | type of $fp$ | merging | filtering |
|---|---|---|---|---|---|---|---|---|
| aspect 1 | 1,591 | 163 | | $pg_{cc}$ | 1,225 | $fp_{cc}$ | 257 | 200 |
| aspect 2 | 1,595 | 76 | | $pg_{cl}$ | 1,127 | $fp_{cl}$ | 452 | 368 |
| aspect 1 and 2 | 3,186 | 2,759 | | $pg_{\parallel}$ | 407 | $fp_{\parallel}$ | 164 | 144 |



a                                                 b                                                 c
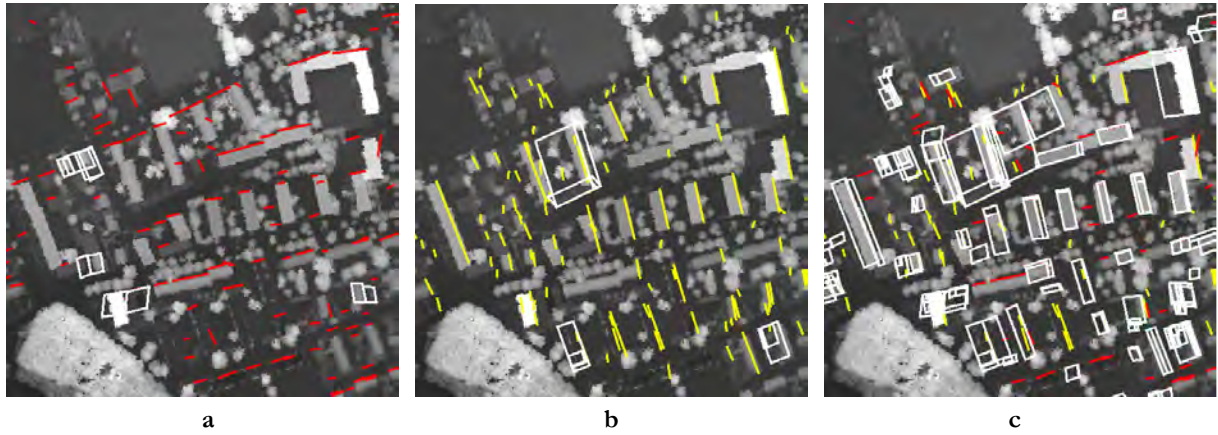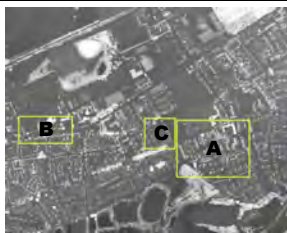
**Figure 5.4:**     Results of generating parallelograms: LIDAR DSM overlaid with generated parallelograms (white) using lines (red) of aspect 1 (a), lines (yellow) of aspect 2 (b), and lines of both aspects (c, aspect 1 – red, aspect 2 – yellow)

over and corner lines is prevented by the previous filter step. Finally, a last filtering is applied that makes use of the geometric model assumptions (see Subsection 4.1.1): lines have to be longer than 5 m. Based on the 1,398 (aspect 1) and 1,133 (aspect 2) corner lines, the extraction of building parameters is accomplished (see Subsection 4.6.3). For less than 20 percent of the corner lines, parallel layover lines are found (see third part of Tab. 5.4, second and third column). In summary, approximately 1,700 (aspect 2) resp. 2,000 lines (aspect 1) are extracted in slant range geometry, which relates well to the about 600 buildings in this scene. The last entries in Tab. 5.4 show the number of lines obtained by a merging in ground range geometry (Subsection 4.8.1). These are overlaid on the LIDAR DSM, where the lines extracted from aspect 1 are coloured in red, and those of aspect 2 in yellow. These lines are used in the subsequent building generation.

## 5.3.2     Results of Generating Building Hypotheses

In this subsection, the results of generating building hypotheses are presented. First, the benefit of exploiting multi-aspect data is emphasised. Then, generation results due to the grouping of different types of lines are discussed on three subareas of the Dorsten scene. Moreover, the extraction of the building roof type is evaluated. At the end of this subsection, the 3D reconstruction results are analysed, focusing on two smaller test sites containing a group of flat- and non-flat-roofed buildings.

**Table 5.6:** Results of generating building footprints

| test site | footprint $fp_{cc}$ | footprint $fp_{cl}$ | footprint $fp_{ll}$ | |
|---|---|---|---|---|
| area A | 37 | 28 | 3 | |
| area B | 10 | 20 | 8 | |
| area C | 1 | 13 | 10 | |
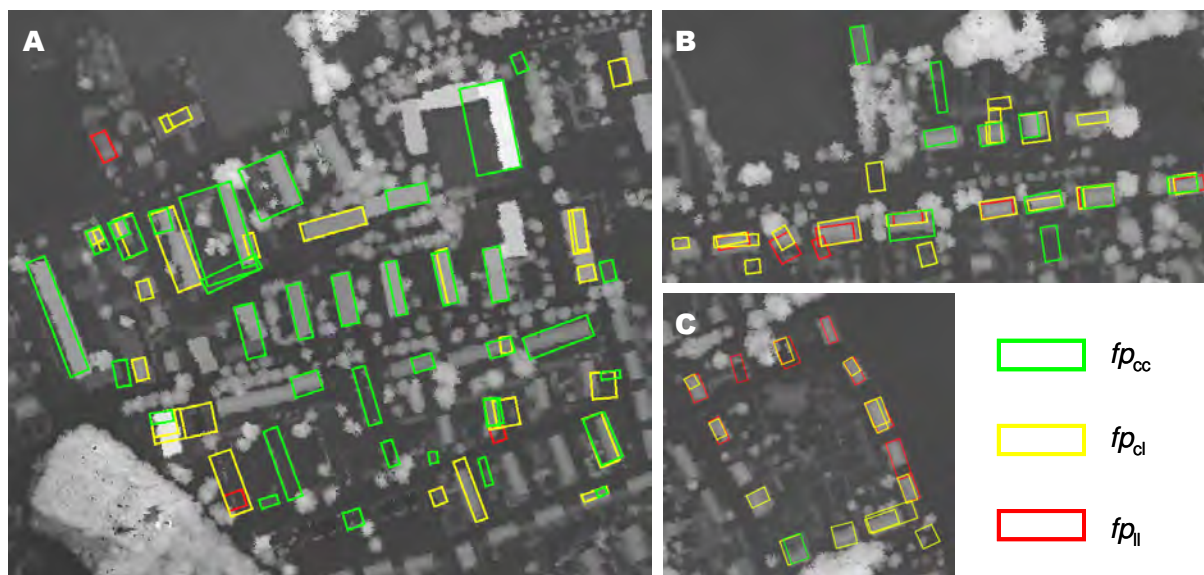


**Figure 5.5:** Results of generating footprints: LIDAR DSM overlaid with parallelograms resulting from corner-corner combinations (green, a), corner-layover combinations (yellow), and layover-layover combinations (red)

## Building Footprint

The results of the parallelogram generation from L-, T-, and X-shaped line structures are summarised in Tab. 5.5. To show the benefit of using multi-aspect data, the number of parallelograms obtained using only lines extracted from single-aspect data is also shown. Additionally, these results are visualised in Fig. 5.4. The classification of the parallelograms $pg_{all}$ into $pg_{cc}$ (corner-corner), $pg_{cl}$ (corner-layover), and $pg_{ll}$ (layover-layover) is shown in the second part of Tab. 5.5. The benefit of considering the extracted layover lines in the grouping step is obvious. Based on the parallelograms, a filtering and merging step is carried out that takes into account the constraints due to the orthogonal flight geometry described in Subsection 4.8.1. The remaining footprints $fp_{cc}$, $fp_{cl}$, and $fp_{ll}$ are filtered using the geometric model assumptions and taking into account the fused vegetation mask (see Subsection 4.1.1), i.e. the width $w$ and the length $l$ of a building have to be larger than 5 m and the overlap with vegetated area has to be less than $\frac{1}{3}$ of the footprint size.

In the following, the benefit of investigating the layover lines in the footprint generation is discussed in more detail, based on three subareas. The remaining potential building footprints are
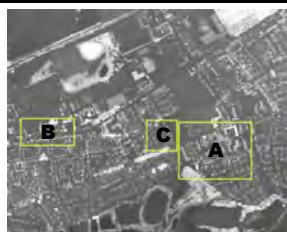
overlaid on a LIDAR DSM in Fig. 5.5. Footprints coloured in green belong to the group $fp_{cc}$, those marked in yellow to the group $fp_{cl}$, and the red footprints belong to the group $fp_{ll}$. The corresponding values are given in Tab. 5.6. In area A, most of the building footprints result from the combination of two corner lines. The second largest group is obtained by corner-layover combinations. Only three footprints are received by grouping two layover lines. This is different for area B, where the group of corner-layover combinations makes up the largest part of the building footprints. The lower detection rate of corner lines, especially from aspect 2, is caused by small distances between the buildings that hamper the appearance of corner reflections between ground and wall. Consequently, only a layover line resulting from roof or façade structures can form a right-angled structure with the line extracted from the first aspect. This effect can be observed even better in area C. Only one footprint results from two corner lines. Almost the same number of footprints is formed by corner-layover and layover-layover combinations. Analysis of the magnitude signature of these buildings shows that only, a weak corner line was visible that could not be detected by the line detector. This low intensity is caused by the closeness of the buildings (relevant for aspect 1) and due to vegetation in front of the buildings (relevant for aspect 2). As these buildings have hipped roofs, layover lines are extractable in both aspects, from which the building footprints can be reconstructed.

In Fig. 5.6, the final building footprints are presented that undergo the steps of building height extraction (see Subsection 4.8.2), post-processing, and the determination of the final 3D buildings (see Section 4.11). Two groups of building footprints are depicted on the cadastral map. The footprints that fulfil the height constraint of 5 m are coloured in green while those showing lower heights are marked in yellow. The same distinction is given for the reference data. Footprints coloured in white show a median height larger than 5 m in the laser data, lower buildings are visualised in grey. Furthermore, reconstructed building footprints that do not coincide with footprints in the reference data are marked with red crosses. The numerical summary of the depicted footprints and the reference data are listed in Tab. 5.7.

Focusing on the largest and most heterogeneous area A, 43 footprints are extracted correctly and only five do not match to reference buildings. Applying the height constraint due to the model assumptions specified in Subsection 4.1.1, only 21 footprints remain that coincide with the reference footprints. Almost all reconstructed footprints match with reference buildings higher than 5 m. Moreover, many footprints marked in yellow also correspond to reference footprints marked in white, but due to an underestimation of the building height, those buildings are not classified as final 3D reconstruction results. Furthermore, due to the simple building model, the extraction of more complex building footprints (i.e., the U- and L-formed buildings in the upper right corner of the area) is not successful. These buildings are often reconstructed only partly or subdivided into smaller building parts.

In area B, a higher detection rate was achieved, the footprints of all 14 buildings could be successfully reconstructed. However, there are also more false alarms. Considering only buildings reconstructed with a height larger than 5 m, 12 correct buildings and 1 incorrect building remain. The lowest number of false alarms was reached for the group of hipped roofed buildings present in area C. 13 of the 17 reference footprints were correctly reconstructed. Only one false alarm occurs, which is eliminated by applying the height constraint. Unfortunately, also five other building hy-

**Table 5.7:**   Results of evaluating building footprints

| test site | fp | | fp ($h_{fp}$ < 5m) | | fp ($h_{fp}$ > 5m) | | reference |
|---|---|---|---|---|---|---|---|
| | correct | incorrect | correct | incorrect | correct | incorrect | |
| area A | 43 | 5 | 22 | 5 | 21 | 0 | 40 |
| area B | 14 | 7 | 2 | 6 | 12 | 1 | 14 |
| area C | 13 | 1 | 5 | 1 | 8 | 0 | 17 |
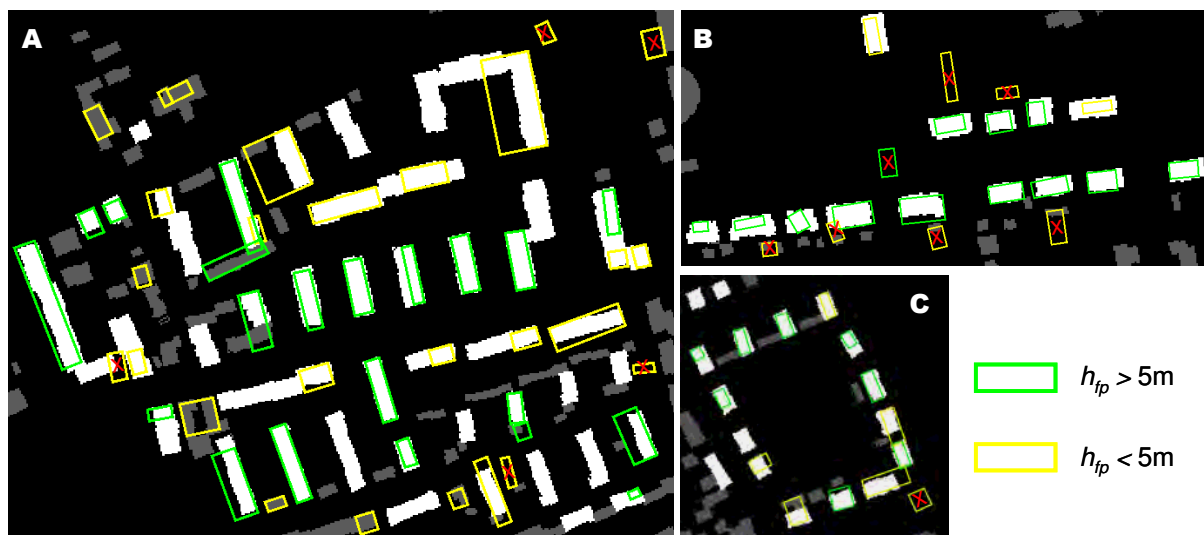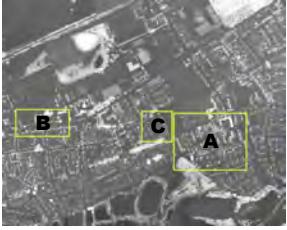




**Figure 5.6:**   Results of evaluating building footprints: cadastral map with buildings showing height > 5m (white) and height < 5m (grey) overlaid with extracted building footprints fp

potheses do not fulfil this model assumption. This is due to a systematic underestimation of the building height discussed further in the next two paragraphs. Numerical results on the building footprint reconstruction are presented in Tab. 5.9 and Tab. 5.10. These will be discussed together with the results of the building height extraction.

### Building Roof Type

In addition to the building footprints, the building roof type was extracted. The results of the classification into flat and non-flat building roofs are listed in Tab. 5.8 and visualised in Fig. 5.7. For this evaluation, only the final 3D buildings are considered. Hence, only 21, 12, and 8 building roofs are assessed of area A, B, and C, respectively. The majority of the building roofs are extracted correctly. Only a few show a mismatch (see Fig. 5.7, footprints marked in yellow), where in most cases a non-flat-roofed building was classified as flat-roofed building. This confusion is mainly caused by double line signatures, which show only a weak corner line. Hence, in many cases only the layover line is detected and combined with a corner or layover line of the other aspect. Furthermore, all footprints resulting from a layover-layover combination were classified to be flat-roofed as the building parameters *a* and *b* are not extractable from such line combinations (see Subsection 4.6.3). Thus, the reconstruction of an eave and ridge height is not possible with the presented

**Table 5.8:**     Results of extracting building roof type

| test site | extraction result | | reference | |
|---|---|---|---|---|
| | flat roof (false) | non-flat roof (false) | flat-roof | non-flat roof |
| area A | 9 (1) | 12 (2) | 10 | 11 |
| area B | 1 (1) | 11 (0) | - | 12 |
| area C | 2 (2) | 6 (0) | - | 8 |
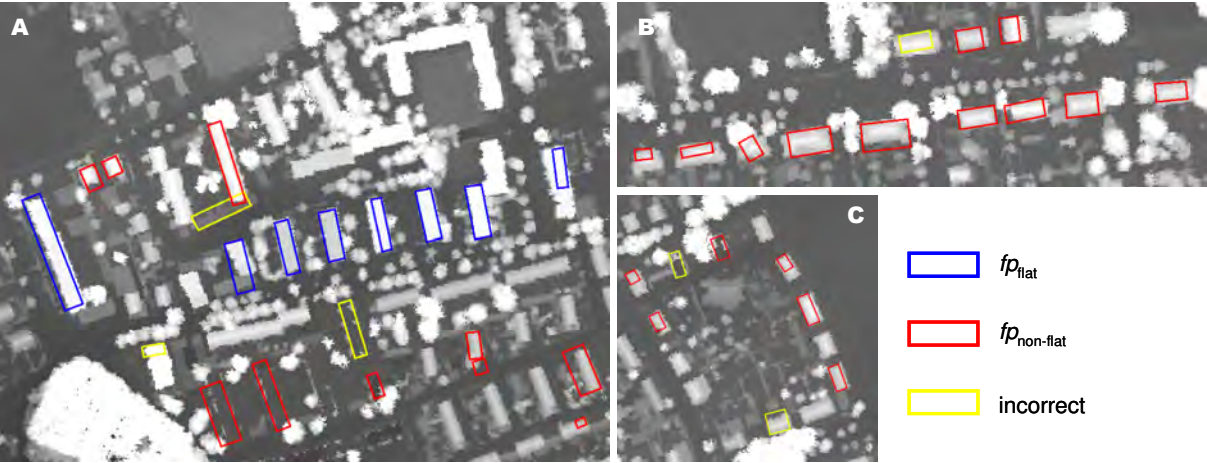


**Figure 5.7:**     Results of extracting building roof type: LIDAR DSM overlaid with building footprints classi-
fied as flat and non-flat

approach (see Subsection 4.8.2). In the next paragraphs, the results of the height extraction are pre-
sented, focusing on the flat-roofed building group in area A (in Fig. 5.7, footprints marked in blue)
and the non-flat-roofed buildings coloured red in area B.

### Building Height

The estimation of the building height is assessed by taking the LIDAR data as height reference. For
the flat-roofed buildings, the processed height map is used. For the non-flat-roofed buildings,
height profiles along building ridge and perpendicular to ridge direction were analysed manually.
Due to the blurring of building edges in the LIDAR data, the extracted heights were defined in
half-metre steps and the estimated pitch angle $\alpha$ in 5 degree steps. In the following, two image
scenes are analysed in detail, containing a group of flat- and non-flat-roofed buildings.
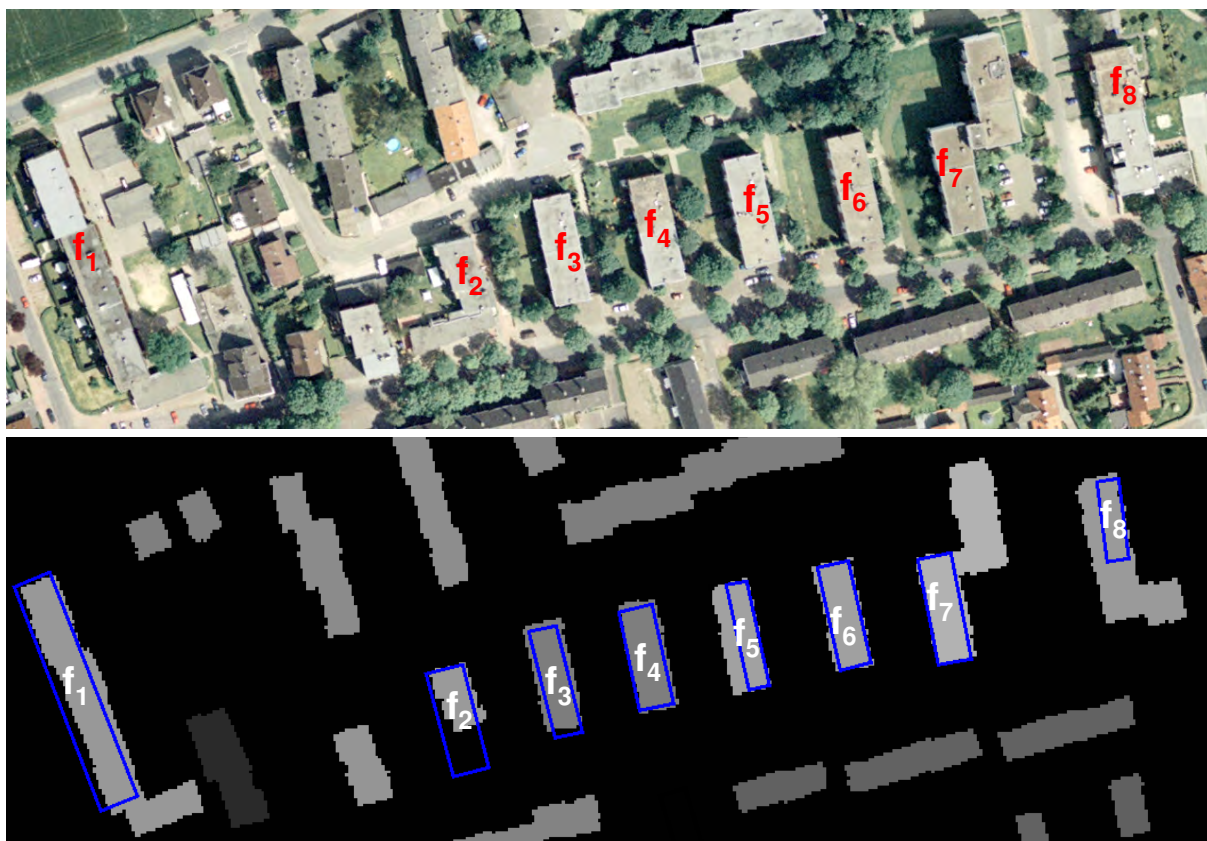
**Figure 5.8:** Results of flat-roofed building extraction: optical image with labelled buildings (top), and median height map of reference data overlaid with extracted building footprints (bottom)

**Table 5.9:** Results of reconstructing flat-roofed buildings

| label | reconstruction result | | | | | reference | | |
|---|---|---|---|---|---|---|---|---|
| | $w$ [m] | $l$ [m] | $h_f$ [m] | $\rho$ | $h_{f\_final}$ [m] | $w$ [m] | $l$ [m] | $h_f$ [m] |
| $f_1$ | 13.1 | 80.0 | 7.2 | 0.64 | 7.2 | 11 | 80 | 11.9 |
| $f_2$ | 12.4 | 35.3 | 6.0 | 0.74 | 6.0 | 10.5 | 23.5 | 12.1 |
| $f_3$ | 9.4 | 36.3 | 6.9 | 0.74 | 6.9 | 12 | 35.5 | 9.8 |
| $f_4$ | 11.3 | 33.5 | 7.5 | 0.71 | 7.6 | 12 | 35.5 | 9.8 |
| $f_5$ | 6.8 | 35.5 | 9.7 | 0.35 | 9.7 | 12 | 35.5 | 12.6 |
| $f_6$ | 10.4 | 34.7 | 9.0 | 0.67 | 11.1 | 12 | 35.5 | 12.5 |
| $f_7$ | 11.2 | 35.8 | 8.7 | 0.52 | 10.4 | 11 | 35 | 14 |
| $f_8$ | 7.3 | 26.7 | 10.3 | 0.59 | 10.2 | 12.5 | 48 | 12 |

*Example 1: flat-roofed buildings*

The reconstruction results summarised in Tab. 5.9 are for the flat-roofed buildings depicted in Fig. 5.8. Analysing first the size of the extracted 2D information, the width $w$ and the length $l$ of the building footprints fit to the reference data quite well. The largest differences are observable for buildings $f_2$, $f_5$, and $f_8$, where the first covers a part of an adjacent building showing a roof height lower than 5 m in the reference heights. The second example, $f_5$, shows shortening of the building width, because the close-by trees at the north of the building mitigate the occurrence of a bright corner line along the full building wall. The building $f_8$ reveals the limitations of the building model used. Stepped buildings can only be reconstructed by a cluster of simple hypotheses, which is visible in Fig. 5.6. The consideration of a more complex building model would solve this problem. For all other buildings, differences smaller than 3 m are shown. This corresponds to approximately 6 pixels difference since the InSAR data have a ground range resolution of 0.5 m. For the extracted building heights, a general underestimation is given. The difference ranges from 1.7 m to 6.1 m (see Tab. 5.9, fourth column), which is much larger than the standard deviation of the InSAR heights ($\sim 0.35$ m). The implemented post-processing including the simulation of interferometric phases (see Section 4.9) and the filtering of the measured phases (see Section 4.10) was carried out for all buildings. This leads to an improvement for the buildings $f_4$, $f_6$, and $f_7$ (see Tab. 5.9, sixth column). The correlation values reached between simulated and filtered measured phases are listed in column five. Largest outlier is $f_2$. Since the footprint of the building contains a higher and a lower building part, only an averaged height could be extracted. The underestimation of the building heights is a crucial problem; possibilities to solve this are discussed in the next section.

*Example 2: non-flat-roofed buildings*

The reconstruction results for non-flat-roofed buildings are presented in Tab. 5.10 and in Fig. 5.9. The extracted footprints of the buildings show a high correlation with the reference data, similar to the flat-roofed examples. Exceptions are only given for the buildings $nf_7$, $nf_8$, and $nf_9$ that show a twisted footprint or a too short building width. This is due to the complex roof structure visible in the optical signature given in Fig. 5.9 and in Fig. 5.1 (right photo shows $nf_8$). Footprint size, roof type, eave height $h_e$, and ridge height $h_r$ as well as pitch angle $\alpha$ and sensor look angle $\theta$ are listed in Tab. 5.10. The extraction of the building roof type was only correct for the buildings $nf_3$, $nf_7$, $nf_{10}$, and $nf_{11}$. All other buildings show also hipped roofs, which could not be detected correctly by the implemented method. An analysis of the building signatures exhibits that the hip pitch angle $\beta$ was too large and therefore the shortening of the layover line too small (see in comparison building $nf_{10}$ – well detected and $nf_2$ – wrong detected). Furthermore, with rising span angle $\kappa$ the assumed symmetry of the layover shortening is decreasing, which makes the extraction more difficult. In this area, the buildings show a span angle $\kappa$ of 5 degrees up to 11 degrees excluding the building $nf_7$. A study on the relation between $\beta$ and $\kappa$ was not possible based on this data; the use of a SAR simulation tool could be helpful.

**Figure 5.9:** Results of non-flat-roofed building extraction: optical image with labelled buildings (top), and LIDAR DSM overlaid with final building footprints and marked ridge orientation (bottom)

**Table 5.10:** Results of reconstructing non-flat-roofed buildings

| label | reconstruction result | | | | | | sensor | reference | | | | | |
|---|---|---|---|---|---|---|---|---|---|---|---|---|---|
| | $w$ [m] | $l$ [m] | type | $h_e$ [m] | $h_r$ [m] | $\alpha$ [°] | $\theta$ [°] | $w$ [m] | $l$ [m] | type | $h_e$ [m] | $h_r$ [m] | $\alpha$ [°] |
| $nf_1$ | 9.0 | 16.1 | g | 5.7 | 10.2 | 45 | 45 | 10 | 19 | h | 7 | 11 | 40 |
| $nf_2$ | 11.6 | 16.6 | g | 5.8 | 11.6 | 45 | 45 | 10.4 | 19.3 | h | 7 | 11 | 40 |
| $nf_3$ | 8.8 | 20.2 | g | 8.5 | 12.0 | 40 | 45 | 8.5 | 19 | g | 7 | 12 | 50 |
| $nf_4$ | 9.5 | 19.5 | g | 6.3 | 11.1 | 45 | 45 | 9.2 | 17.5 | h | 7 | 11 | 40 |
| $nf_5$ | 14.5 | 24.6 | g | 4.3 | 11.6 | 45 | 45 | 10.4 | 22 | h | 7 | 11 | 40 |
| $nf_6$ | 13.4 | 22.2 | g | 5.8 | 11.4 | 40 | 45 | 11.5 | 24 | h | 7 | 11 | 35 |
| $nf_7$ | 10.9 | 7.7 | h | 6.8 | 21.8 | 70 | 45 | 10.5 | 17 | h | 7.5 | 11 | 40 |
| $nf_8$ | 5.1 | 16.6 | g | 3.8 | 6.4 | 45 | 45 | 10.6 | 23 | h | 7 | 12 | 45 |
| $nf_9$ | 5.7 | 8.6 | g | 4.4 | 7.3 | 45 | 45 | 10.6 | 16.5 | h | 8 | 11 | 30 |
| $nf_{10}$ | 11.0 | 13.0 | h | 6.0 | 11.5 | 45 | 45 | 9.5 | 15.3 | h | 7 | 10.5 | 35 |
| $nf_{11}$ | 13.1 | 9.8 | g | 6.9 | 13.5 | 45 | 45 | 11.5 | 13.6 | g | 7.5 | 12 | 40 |

Focusing on the height extraction, for eight buildings no widening of the layover line was found, (see Subsection 4.6.3) resulting in $b = 0$ and consequently $\alpha = \theta$. Hence, only two hypotheses result containing one gable-roofed and one monopitch-roofed building. In the assessment step, correlation values up to 0.9 could be reached between simulated and filtered phase profiles. Since the unambiguous height $\Delta h_i$ rises from 15 m to 29 m over the scene with this baseline configuration, unwrapping problems arise especially for the monopitch-roofed hypotheses during the phase simulation and the assessment steps. Focusing on the achieved results, the extracted heights show a high correlation with the reference heights. The largest differences, similar to the footprint analysis, occur for the buildings $\mathsf{nf}_7$, $\mathsf{nf}_8$, and $\mathsf{nf}_9$. An underestimation such as shown for the flat-roofed height extraction is not observable.

The pitch angle $\alpha$ is given in 5 degree steps similar to the reference. As $\alpha$ depends on the widening parameter $b$ and the building width $c$ in slant range geometry (see equations (4-11), and (4-12) in Subsection 4.8.2), the extraction accuracy of $\alpha$ is directly correlated with those of $b$ and $c$. Since $b$ is extracted on pixel level taking values of $2n \cdot \Delta_r$, the interval steps of gable roofs are $\alpha_g \approx 5°$ and for monopitch roofs approximately half of this if a building width of $c = 10$ m is considered. The comparison between extracted pitch angles and reference data shows a mean difference of 5 degrees, which is in an acceptable range, especially due to the absence of precise reference data.

## 5.4    Discussion

In this section, the new contributions of the approach with regard to the different processing steps are discussed. The main goal of this thesis was the development of an automatic scheme utilising multi-aspect InSAR data to enable the 3D reconstruction of small buildings. This can be reached since the new generation of SAR sensors delivers data, in which in addition to large extended buildings also small buildings down to the size of one family houses become visible. However, these sensors provide huge data sets, wherein the desired urban areas cover only parts of the whole scene. Hence, land cover classification was introduced to limit the application of the building detection to urban areas and to lower the number of false detections during the building generation.

This classification step uses fuzzy logic that contains expert knowledge about image content relevant to InSAR. Three InSAR features were studied to discriminate between vegetated and urban related areas. The applied rule set was formed by membership functions defined by using the InSAR image statistics. In the analysis of the features, four different data sets could be taken into account. Higher variations in the feature distributions were only observable for the coherence, which is caused by temporal decorrelation due to different temporal baseline lengths. Promising results were achieved for the single-pass data and the repeat-pass spaceborne InSAR data that let assume a good transferability, even though the coherence behaviour is related to further criteria (e.g. geometric baseline), which can lead to distribution changes. To prove the presented parameter selection, this feature should undergo further studies by analysing more varying InSAR data sets.

As an additional step, the classification result could be improved by fusing classification results of multi-aspect data. Concerning different flight configurations, the lowest benefit on this fusion is expected for nearly equal viewing angles, most benefit for opposite views. Since for the geocoding

of the classification results the mean terrain height is used, the geometric displacement due to the layover phenomenon is not corrected. This leads to an underestimation of the vegetation areas especially at the vegetation edges. To obtain an improvement, the measured InSAR heights could be taken into account in the future.

The procedure of calculating the interferometric heights is characterised by the behaviour of the utilised airborne data. Looking at other data sets, probably some steps (e.g. phase centring) are not necessary due to sensor configuration, data processing, or scene characteristics. A still existing problem is the limitation of the covered height interval to the height of ambiguity. Hence, only the height of buildings less or equal to the height of ambiguity could be reconstructed in a proper way. For the studied area, this was fulfilled but for other areas or other data configurations, this may not be the case. To solve this issue, a phase unwrapping step should be integrated.

Afterwards, an adapted line detector was applied that delivered line features related to building structures. The features, which were extracted from the magnitude and interferometric phase data, are radiometrically and geometrically stable for large and small buildings. Moreover, these features are to a large extent independent from SAR sensor type and illumination geometry. During the processing, only few parameters have to be defined by the user since model assumptions (e.g. straight lines and minimum building size), data specifications (e.g. apodization function, flight direction, covered height interval), and SAR phenomena (e.g. dependency on building orientation and corner appearance) were taken into account. Parts of the individual parameter setting are the length of template used for line detection, and the orientation and gap tolerances applied for merging of short lines. Those are derivable from the data resolution but also from the individual acceptable false alarm rate. In general, the adaptation to other data sets is quite easy. By using the mentioned parameter settings, the resulting building features (i.e. layover and corner lines) are of high reliability, which was shown in the step of generating the building footprints.

To project the extracted building features from the individual slant range to the common ground range geometry, the InSAR heights were taken into account. Taking the mean height along the building feature as projection information of both line endpoints, very good results were achieved in this relatively flat terrain. An adaptation to consider two feature heights could be necessary for buildings located on a hillside showing up in more hilly landscapes.

The step of building generation benefited from these re-projected lines. The high number and quality of line features enabled the grouping of L-, T-, and X-structures. On the one hand, the benefit of orthogonal multi-aspect data could be shown. On the other hand, the complementary exploitation of the layover and corner lines to achieve a higher detection rate could be demonstrated, especially in dense areas, where likely corners do not appear in all aspects. Problems arose when the real building geometry did not fulfil the defined model constraints. An upgrade to a more complex building model is desirable to improve the reconstruction results. The high number of extracted primitives would provide a good basis for the generation of more complex buildings, because many of them are not used in the building reconstruction yet. Furthermore, the building reconstruction would profit from a more sophisticated rating of the different footprints resulting from the grouping of two lines. Due to the high reliability of the corner position, a high rating for corner-corner configurations such as implemented in this approach is reasonable, but these lines are more af-

fected by occlusion effects than layover lines. Hence, a smart merging of overlapping hypotheses would be helpful.

The discrimination into flat- and non-flat-roofed buildings is robust, if double line signatures are visible for the non-flat-roofed buildings. This is also supported by the orthogonal flight configuration that enables the coverage of two right-angled building sides. Coverage from opposite sides would be less favourable. In the reconstruction approach, the incorrect extraction of the roof type is mostly related to missing corner lines. Hence, most of the building hypotheses containing at least one layover line show no flat roof in the reference data. Since the extraction of the parameters $a$ and $b$ is not possible if the double line signature is missing, probably an additional analysis of the phase signature could improve the roof type extraction for such hypotheses. Furthermore, the aimed differentiation into gable, hipped, and monopitch roofs could not successfully be reached for this scene and data set. A simulation based analysis would help to estimate the relation of $\beta$ and $\kappa$ that affects the assumed symmetric shortening of the layover line.

Beyond the footprint and the roof type, an underestimation of the flat-roofed building heights was observable. This can be mitigated by an iterative update of the building height. First studies on this show promising results [129]. However, this strategy is only successful for buildings that show a roof area in the phase signature superimposed with no other signals. Since this is less the case for high and narrow buildings, an additional analysis of the layover ramp in the phase data has to be implemented. The highest phase value of the layover ramp corresponds in most cases to the flat-roofed building height. Since for most of the buildings the layover ramp is observable at two building sides, a fusion of this redundant height information is recommended, especially if multi-aspect data are used.

For the interpretation and the utilisation of the InSAR phase signature, an InSAR simulation tool was developed. Since most of the related processing steps rely on the comparison between simulated and measured InSAR phases, which suffer from considerable noise, phase filtering is mandatory. The new InSAR phase filter preserves especially the front porch region and is parameterised by considering building hypotheses. The two processing steps, simulation and filtering of In-SAR phases, delivered good results. An enhancement would become necessary, if a more complex building model is defined or the analysis of neighbouring effects is requested to model dense urban scenes.

In general, the presented algorithm delivered good results, especially for the reconstruction of small buildings by using multi-aspect InSAR data. Beyond the improvements on building interpretation and reconstruction, the adaptation on high resolution airborne InSAR data showed the potentials of this topic for the future.

# 6 Summary and Outlook

In this chapter, the thesis is summarised by giving a short overview over the new reconstruction approach and highlighting in particular the most important findings and developments. The benefit is discussed based on three questions. Finally, possibilities to improve and to enhance this approach in the future are mentioned.

## 6.1 Summary

The goals of this thesis were the study of building signatures in InSAR data and the utilization of the new findings to develop an approach to reconstruct the 3D shape of buildings. The three main questions that had to be answered were: is a benefit reachable by exploiting the SAR magnitude and InSAR phase data together? Is there additional information in the InSAR signature that can improve the building reconstruction? Do a higher data resolution and the consideration of multi-aspect data enable the reconstruction of small buildings?

First, the appearance of buildings in InSAR data was analysed in detail by focusing on the identification of characteristic building features. In addition, changes in the building signature due to different sensors, processing modes, illumination properties or building geometries were studied. In the magnitude and the interferometric phase data, the corner line and the layover area were identified as the most distinguishable features. The first, given as bright line in the magnitude and as line of constant value in the InSAR heights, was shown to be the most stable and dominant building feature appearing at almost all building locations. The second showed higher variation, making reliable detection difficult, but was considered to support the determination of the building roof type. Based on these features, a new reconstruction scheme was developed that contains the following processing steps:

- Creation of a vegetation mask used to reduce false alarms
- Extraction of building features based on magnitude and interferometric phase images
- Filtering and fusion of building features by utilising building specific requirements
- Geocoding of building features by using local InSAR heights
- Using building features to group right-angled structures, benefiting from multi-aspect data
- Filtering and merging of parallelograms by considering the flight geometry of the sensor
- Extraction of potential roof types from the building features
- Calculation of building heights from the InSAR heights and the geometric model
- Simulation of InSAR phase signatures based on the potential 3D building hypotheses
- Filtering of measured InSAR phases by investigating the simulated phases

- ▪ Post-processing of building hypotheses by utilising the correlation between simulated and filtered InSAR phases

- ▪ Determination of the final 3D buildings by reducing overlapping hypotheses

The approach was tested on high resolution airborne InSAR data showing a pixel spacing of $\sim 40\,cm$ in range and $\sim 20\,cm$ in azimuth. The two image pairs were acquired on orthogonal flight tracks. The analysis of the intermediate results and the final reconstruction results that contained reference data can be summarised in the following findings.

The extraction of reliable building features benefits from the common exploitation of the SAR magnitude and InSAR phase data. In this way, the extraction of bright lines and their classification into corner and layover lines was possible. Additionally, their position relative to each other was analysed to gain information about the roof type. Furthermore, the InSAR heights could be successfully utilised for the projection of the building features from slant to ground geometry. Especially the positional accuracy of corner lines was improved by considering the local InSAR height. This directly influenced the result of the building footprint generation since corner lines represent the most reliable footprint feature.

In addition, the developed reconstruction approach benefits strongly from the exploitation of high resolution multi-aspect data. This was especially observable in the huge difference between the obtained numbers of parallelograms assembled from single-aspect or multi-aspect features. Moreover, to enable the reconstruction of small buildings and to handle building constellations of weak feature support (e.g. high density of buildings), the fusion of multi-aspect features was realised on a lower level, in contrast to other algorithms. Only in the common ground range geometry, the high number of multi-aspect line features was used to group L-, T-, and X-structures that especially appear due to the orthogonal multi-aspect data. At this point, it could be demonstrated that the combination of layover and corner lines increases the reconstruction rate, especially in dense urban areas. The final step of generating building footprints was applied on the assembled structures considering the underlying building model. This model supports only buildings of rectangular shape with plane building walls that are oriented orthogonally to the building ground plate. Potential roof types are limited to flat, gable, hipped, and monopitch roofs and the minimum extension is restricted to $5\,m \times 5\,m \times 5\,m$. It could be successfully shown that such small buildings are detectable due to the high geometric resolution of the data and the utilisation of the complementary object information present in the multi-aspect data.

Further, the intensive analysis of the interferometric phase signature revealed several possibilities to enhance the reconstruction. The whole post-processing of the intermediate building hypotheses relies on the interferometric phase signature, where a high correlation between simulated and measured InSAR phases is desired. For that, an InSAR simulation tool was developed and since the interferometric phases in real InSAR images suffer from considerable noise, a phase filtering was implemented to assist the exploitation of the measured InSAR phases. This new filter preserves especially the front porch regions and its parameterisation relies on the assembled building hypotheses and the simulated InSAR phases. By applying both tools, the reconstruction of buildings could be improved in several cases. The ambiguity problem in the reconstruction of non-flat roofs was solved by comparing the simulated phase signatures of all possible roof shapes with the meas-

ured InSAR phases. The underestimation of building heights could be decreased by implementing an iterative processing step that recalculates the building height by estimating the similarity between simulated and measured phases. The same strategy was used to correct oversized building footprints by iteratively decreasing the building size.

In general, the presented reconstruction approach enables the 3D reconstruction of buildings considering rectangular footprints and different roof types. The combined utilisation of the magnitude and the interferometric phase signature as well as the usage of high resolution multi-aspect data increases the success rate of the reconstruction of smaller buildings and the reconstruction of buildings in denser areas.

## 6.2 Outlook

In the next paragraphs, possible improvements and enhancements of the presented approach are discussed, following the procedure of processing.

First of all, a more sophisticated building model should be applied to be able to reconstruct more complex buildings. Here, a post-processing step, which makes use of the generated rectangular shaped buildings, could be a start. Furthermore, the pre-classification of the InSAR data in vegetated and urban related areas could undergo a more intensive study including seasonal and configuration effects (e.g. length of temporal and spatial baseline). The processing step of calculating interferometric phases delivers only wrapped phases, thus only height differences in a range of $2\pi$ can be covered. Hence, the development of a strategy that enables the local unwrapping of the building phase signature is necessary to reconstruct buildings showing heights larger than the height of ambiguity. For that, relying mainly on the phase trend in the layover area should help to unwrap building roof phases in a proper way. The detection and segmentation of the building features (i.e. layover and corner lines) are efficiently realised. Only the extraction of the building parameters necessary to model non-flat roofs should be improved to obtain more reliable results. The implemented generation of building footprints delivers very good results for orthogonal flight configurations. For the future, an enhancement by supporting all configurations in the same way would be preferable. In detail, the search of right-angled structures, currently limited to features spanning L-, T-, and X-shape, can be widened to H- and U-shapes. Additionally, the merging of overlapping hypotheses could be handled in a more sophisticated way, in combination with the stated enhancement of the building model. The height estimation of buildings would benefit from fusing multi-aspect height information whereby different contributions (i.e. layover areas and roof areas) have to be combined in a suitable way. For that purpose, sizes of the areas, differences in the height of ambiguity, and neighbouring effects should be taken into account. Generally, the presented approach has to be tested on more data sets covering different sensor configurations and different areas to give proof of a more general applicability.

The presented approach has numerous possible applications, since the demand for detailed cartographic information is growing continuously. One of the main challenges is the monitoring of built-up areas, especially for detecting damaged buildings after a storm or an earthquake. For that, a pre- and post-event data analysis could be applied by attracting attention to changes on the detected reliable building features. Furthermore, a large scale automatic recovering of the 3D shape

of buildings (i.e. building volume and roof type) to support the planning of the energy supply is needed. This could be reached with the new high resolution single-pass space-borne satellite system TanDEM-X, because its data fulfil the requirements of the approach and due to the ascending and descending orbit of the satellites, also multi-aspect data are available. Thus, the application and probably some adaptation of the presented reconstruction approach to this InSAR data would be desirable.

# References

[1]     Auer S, Hinz S, Bamler R (2010)  Ray-Tracing Simulation Techniques for Understanding High-Resolution SAR Images. IEEE Transactions on Geoscience and Remote Sensing, doi: 10.1109/TGRS.2009.2029339, vol. 48, no. 3, part 2, pp. 1445-1456.

[2]     Auer S, Gernhardt S, Bamler R (2011)  Investigations on the Nature of Persistent Scatterers Based on Simulation Methods. IEEE Proceedings of Joint Urban Remote Sensing Event, doi: 10.1109/JURSE.2011.5764719, pp. 61-64.

[3]     Bamler R, Schättler B (1993) SAR Data Acquisition and Image Formation. In: Schreier G.: SAR Geocoding: Data and Systems. Wichmann, Karlsruhe, 1993, pp. 53-102.

[4]     Balz T (2007)  Echtzeitvisualisierung von SAR-Effekten mittels programmierbarer Grafikhardware. University of Stuttgart: Ph.D. Thesis.

[5]     Balz T, Haala N (2003)  SAR-based 3D reconstruction of complex urban environments. International Archives of Photogrammetry, Remote Sensing and Spatial Information Sciences, Workshop on 3-D Reconstruction from Airborne Laserscanner and InSAR Data, vol. XXXIV, part 3/W13, pp. 181-185.

[6]     Baran I, Stewart MP, Kampes BM, Perski Z, Lilly P (2003)  A Modification to the Goldstein Radar Interferogram Filter. IEEE Transaction on Geoscience and Remote Sensing, vol. 41, no. 9, pp. 2114-2118.

[7]     Bennett AJ, Blacknell D (2003)  The extraction of building dimensions from high resolution SAR imagery. IEEE Proceedings of the International Radar Conference, doi: 10.1109/RADAR.2003.1278736, pp. 182-187.

[8]     Benz UC, Hofmann P, Willhauck G, Lingenfelder I, Heynen M (2004)  Multi-resolution, object-oriented fuzzy analysis of remote sensing data for GIS-ready information. ISPRS Journal of Photogrammetry and Remote Sensing, vol. 58, no. 3-4, pp. 239-258.

[9]     Bickel DL, Hensley WH, Yocky DA (1997)  The Effect of Scattering from Buildings on Interferometric SAR Measurements. IEEE Proceedings of International Geoscience and Remote Sensing Symposium, doi: 10.1109/IGARSS.1997.608937, vol. 4, pp. 1545-1547.

[10]    Bishop CM (2006)  Pattern Recognition and Machine Learning. Springer Science+Business Media, LLC, isbn: 978-0387310732.

[11]    Bo G, Dellepiane S, Beneventano G (1999)  A locally adaptive approach for interferometric phase noise reduction. IEEE Proceedings of International Geoscience and Remote Sensing Symposium, doi: 10.1109/IGARSS.1999.773466, vol. 1, pp. 264-266.

[12]    Boerner W-M, Mott H, Lueneburg E, Livingstone C, Brisco B, Brown RJ, Paterson JS (1998)  Chapter 5: Polarimetry in Radar Remote Sensing: Basic and Applied Concepts. In: Principle & Applications of IMAGING RADAR, Manual of Remote Sensing, Third Edition, Volume 2, edited by FM Henderson, AJ Lewis, John Wiley & Sons, Inc., isbn: 978-0471330462.

[13]    Bolter R (2001)  Buildings from SAR: Detection and Reconstruction of Buildings from Multiple View High Resolution Interferometric SAR Data. University Graz: Ph.D. Thesis.

[14]    Bolter R, Leberl F (2000)  Detection and Reconstruction of Human Scale Features from High Resolution Interferometric SAR Data. IEEE Proceedings of the International Conference on Pattern Recognition, doi: 10.1109/ICPR.2000.902916, vol. 4, pp. 291-294.

[15]    Bonin G, Dubois-Fernandez P, du Plessis PDOR, Angelliaume S, Cantalloube H, Oriot H, Coulombeix C (2009) The new ONERA multispectral airborne SAR system in 2009. IEEE Proceedings of International RADAR Conference, doi: 10.1109/RADAR.2009.4976985, pp. 1-3.

[16]    Borgeaud M, Wegmueller U (1996)  On the Use of ERS SAR Interferometry for the Retrieval of Geo- and Bio-Physical Information. Proceedings of the FRINGE 96 Workshop, ESA SP-406, pp. 83-94.

[17]    Born M, Wolf E (1999)  Principles of Optics: Electromagnetic Theory of Propagation, Interference and Diffraction of Light. Cambridge University Press, 7th (expanded) edition, isbn: 978-0521642224.

[18]    Braeutigam B, Martone M, Rizzoli P, Bachmann M, Krieger G (2012) Interferometric Performance of TanDEM-X Global DEM Acquisitions. Proceedings of 9th European Conference on Synthetic Aperture Radar, VDE, ITG, isbn: 978-3800734047, pp. 89-92.

[19]    Breit H, Schättler B, Fritz T, Balss U, Damerow H, Schwarz E (2008) TerraSAR-X Payload Data Processing: Results From Commissioning And Early Operational Phase. IEEE Proceedings of International Geoscience and Remote Sensing Symposium, doi: 10.1109/IGARSS.2008.4778964, vol. 2, pp. 209-212.

[20]    Brenner AR, Ender JHG (2006)  Demonstration of advanced reconnaissance techniques with the airborne SAR/GMTI sensor PAMIR. IEE Proceedings on Radar, Sonar & Navigation, doi: 10.1049/ip-rsn:20050044, vol. 153, no. 2, pp. 152-162.

[21]    Brenner AR, Roessing L (2008)  Radar Imaging of Urban Areas by Means of Very High-Resolution SAR and Interferometric SAR. IEEE Transactions on Geoscience and Remote Sensing, doi: 10.1109/TGRS.2008.920911, vol. 46, no. 10, pp. 2971-2982.

[22]    Brenner AR, Roessing L, Berens P (2010)  Potential of very high resolution SAR interferometry for urban building analysis. Proceedings of 8th European Conference on Synthetic Aperture Radar, VDE Verlag GmbH, Berlin, isbn: 978-3800732722, pp. 1010-1013.

[23]    Brett PTB, Guida R (2011)  Bright Line Detection in COSMO-SkyMed SAR Images of Urban Areas. IEEE Proceedings of Joint Urban Remote Sensing Event, doi: 10.1109/JURSE.2011.5764767, pp. 253-256.

[24]    Brunner D (2009) Advanced Methods For Building Information Extraction From Very High Resolution SAR Data To Support Emergency Response. DISI - University of Trento: Ph.D. Thesis.

[25]    Buckreuss S, Werninghaus R, Pitz W (2008)  The German satellite mission TerraSAR-X. IEEE Proceedings of the International Radar Conference, doi: 10.1109/RADAR.2008.4720788, pp. 1-5.

[26]    Burkhart GR, Bergen Z, Carande R (1996)  Elevation Correction and Building Extraction from Interferometric SAR Imagery. IEEE Proceedings of International Geoscience and Remote Sensing Symposium, doi: 10.1109/IGARSS.1996.516434, vol. 1, pp. 659-661.

[27]    Canny J (1986)  A Computational Approach to Edge Detection. IEEE Transactions on Pattern Analysis and Machine Intelligence, doi: 10.1109/TPAMI.1986.4767851, vol. 8, no. 6, pp. 679-698.

[28]    Cantalloube H, Wendler M, Giroux V, Dubois-Fernandez P, Horn R (2004)  A first bistatic airborne SAR interferometry experiment – preliminary results. IEEE Proceedings of Sensor Array and Multichannel Signal Processing Workshop, doi: 10.1109/SAM.2004.1503033, pp. 667-671.

[29]    Carlotto M (1996)  Detecting Man-Made Features in SAR Imagery. IEEE Proceedings of International Geoscience and Remote Sensing Symposium, doi: 10.1109/IGARSS.1996.516236, vol. 1, pp. 34-36.

[30]    Cellier F (2007)  Reconstruction 3D de bâtiments en interférométrie RSO haute résolution: approche par gestion d'hypothèses. Ecole nationale supérieure des télécommunications: Ph.D. Thesis.

[31]    Cloude SR, Pottier E (1997)  An entropy based classification scheme for land applications of polarimetric SAR. IEEE Transactions on Geoscience and Remote Sensing, doi: 10.1109/36.551935, vol. 35, no. 1, pp. 68-78.

[32]    Covello F, Battazza F, Coletta A, Lopinto E, Pietranera L, Valentini G, Zoffoli S (2008)  COSMO-SkyMed mission status. Proceedings of SPIE Conference on Image and Signal Processing for Remote Sensing XIV, doi: 10.1117/12.803731, vol. 7109, pp. 710918-1-710918-15.

[33]    Cumming IG, Wong FH (2005)  Digital processing of synthetic aperture radar data: algorithms and implementation. Artech House Publishers, isbn: 978-1580530583.

[34]    Dai E, Jin YQ, Hamasaki T, Sato M (2008)  Three-Dimensional Stereo Reconstruction of Buildings Using Polarimetric SAR Images Acquired in Opposite Directions. IEEE Geoscience and Remote Sensing Letters, doi: 10.1109/LGRS.2008.915744, vol. 5, no. 2, pp. 236-240.

[35]    Definiens AG (2007)  Definiens Developer7 Reference Book. Published by Definiens AG, Document Version 7.0.0.843, www.definiens.com.

[36]    Dong Y, Forster B, Ticehurst C (1997)  Radar backscatter analysis for urban environments. International Journal of Remote Sensing, doi: 10.1080/014311697218467, vol. 18, no. 6, pp. 1351-1364.

[37] Dreuillet Ph, Cantalloube H, Colin E, Dubois-Fernandez P, Dupuis X, Fromage P, Garestier F, Heuze D, Oriot H, Peron JL, Peyret J, Bonin G, du Plessis OR, Nouvel JF, Vaizan B (2006) The ONERA RAMSES SAR : latest significant results and future developments. IEEE Proceedings of the International Radar Conference, doi: 10.1109/RADAR.2006.1631849.

[38] Dubois C, Thiele A, Cadario E, Hinz S (2012) Enhancing Building Reconstruction by Adaptive Filtering of Interferometric Phases. Proceedings of 'Fringe 2011 Workshop', Frascati, Italy, ESA SP-697, 6p.

[39] Eineder M (2003) Efficient Simulation of SAR Interferograms of Large Areas and of Rugged Terrain. IEEE Transactions on Geoscience and Remote Sensing, doi: 10.1109/TGRS.2003.811692, vol. 41, no. 6, pp. 1415-1427.

[40] Eineder M, Adam N, Bamler R, Yague-Martinez N, Breit H (2009) Spaceborne Spotlight SAR Interferometry With TerraSAR-X. IEEE Transactions on Geoscience and Remote Sensing, doi: 10.1109/TGRS.2008.2004714, vol. 47, no. 5, pp. 1524-1535.

[41] Ferretti A, Fumagalli A, Novali F, Prati C, Rocca F, Rucci A (2011) A New Algorithm for Processing Interferometric Data-Stacks: SqueeSAR. IEEE Transactions on Geoscience and Remote Sensing, doi: 10.1109/TGRS.2011.2124465, vol. 49, no. 9, pp. 3460-3470.

[42] Ferraioli G (2008) Multichannel SAR Interferometry based on Statistical Signal Processing. Università a degli Studi di Napoli Parthenope: Ph.D. Thesis.

[43] Ferraioli G (2010) Multichannel InSAR Building Edge Detection. IEEE Transactions on Geoscience and Remote Sensing, doi: 10.1109/TGRS.2009.2029338, vol. 48, no. 3, pp. 1224-1231.

[44] Ferro A, Brunner D, Bruzzone L (2010) Building Detection and RADAR Footprint Reconstruction from Single VHR SAR Images. IEEE Proceedings of International Geoscience and Remote Sensing Symposium, doi: 10.1109/IGARSS.2010.5652093, pp. 292-295.

[45] Ferro A, Brunner D, Bruzzone L, Lemoine G (2011) On the Relationship Between Double Bounce and the Orientation of Buildings in VHR SAR Images. IEEE Geoscience and Remote Sensing Letters, doi: 10.1109/LGRS.2010.2097580, vol 8, no 7, pp. 612-616.

[46] Fornaro G, Lombardini F, Serafino F (2005) Three-dimensional multipass SAR focusing: Experiments with long-term spaceborne data. IEEE Transactions on Geoscience and Remote Sensing, doi: 10.1109/TGRS.2005.843567, vol. 43, no. 4, pp. 702-714.

[47] Franceschetti G, Iodice A, Riccio D (2002) A canonical problem in electromagnetic backscattering from buildings. IEEE Transactions on Geoscience and Remote Sensing, doi: 10.1109/TGRS.2002.802459, vol. 40, no. 8, pp. 1787-1801.

[48] Franceschetti G, Iodice A, Riccio D, Ruello G (2003) SAR raw signal simulation for urban structures. IEEE Transactions on Geoscience and Remote Sensing, doi: 10.1109/TGRS.2003.814626, vol. 41, no. 9, part 1, pp. 1986-1995.

[49] Franceschetti G, Guida R, Iodice A, Riccio D, Ruello G, Stilla U (2007) Building feature extraction via a deterministic approach: Application to real high resolution SAR images. IEEE Proceedings of International Geoscience and Remote Sensing Symposium, doi: 10.1109/IGARSS.2007.4423395, pp. 2681-2684.

[50] Fritz T, Eineder M, Mittermayer J, Roth A, Börner E, Breit H, Bräutigam B (2010) TerraSAR-X, Ground Segment, Basic Product Specification Document, CAF – Cluster Applied Remote Sensing. Published by DLR, doc.: TX-GS-DD-3302, issue: 1.7, date: 15.10.2010.

[51] Frost VS, Stiles JA, Shanmugan KS, Holtzman JC (1982) A Model for Radar Images and its Application to Adaptive Dogital Filtering of Multiplicative Noise. IEEE Transactions on Pattern Analysis and Machine Intelligence, doi: 10.1109/TPAMI.1982.4767223, vol. 4, no. 2, pp. 157-166.

[52] Gamba P, Houshmand B, Saccani M (2000) Detection and extraction of buildings from interferometric SAR data. IEEE Transactions on Geoscience and Remote Sensing, doi: 10.1109/36.823956, vol. 38, no. 1, pp. 611-618.

[53] Gamba P, Houshmand B (2000) Digital surface models and building extraction: A comparison of IFSAR and LIDAR data. IEEE Transactions on Geoscience and Remote Sensing, doi: 10.1109/36.851777, vol. 38, no. 4, part 2, pp. 1959-1968.

[54]    Gao, G. (2010)  Statistical Modeling of SAR Images: A Survey. Journal Sensors, doi: 10.3390/s100100775, vol. 10, no. 1, pp. 775-795.

[55]    Gernhardt S, Adam N, Eineder M, Bamler R (2010)  Potential of very high resolution SAR for persistent scatterer interferometry in urban areas. Annals of GIS, doi: 10.1080/19475683.2010.492126, vol. 16, no. 2, pp. 103-111.

[56]    Goldstein RM, Werner CL (1998)  Radar interferogram filtering for geophysical applications. Geophysical Research Letters, vol. 25, no. 21, pp. 4035-4038.

[57]    Goodman JW (2007)  Speckle phenomena in optics: theory and applications. Ben Roberts & Company, isbn: 978-0974707792.

[58]    Guida R, Iodice A, Riccio D, Stilla U (2008)  Model-Based Interpretation of High-Resolution SAR Images of Buildings. IEEE Journal of Selected Topics in Applied Earth Observations and Remote Sensing, doi: 10.1109/JSTARS.2008.2001155, vol. 1, no. 2, pp. 107-119.

[59]    Guida R, Iodice A, Riccio D (2010)  Height Retrieval of Isolated Buildings From Single High-Resolution SAR Images. IEEE Transactions on Geoscience and Remote Sensing, doi: 10.1109/TGRS.2010.2041460, vol. 48, no. 7, pp. 2967-2979.

[60]    Hammer H, Schulz K (2011)  SAR-Simulation of Large Urban Scenes Using an Extended Ray Tracing Approach. IEEE Proceedings of Joint Urban Remote Sensing Event, doi: 10.1109/JURSE.2011.5764776, pp. 289-292.

[61]    Hanssen RF (2001)  Radar Interferometry: Data Interpretation and Error Analysis. Kluwer Academic Publishers, Springer Netherlands, isbn: 978-0792369455.

[62]    Harris FJ (1978)  On the Use of Windows for Harmonic Analysis with the Discrete Fourier Transform. Proceedings of the IEEE, doi: 10.1109/PROC.1978.10837, vol. 66, no. 1, pp. 51-83.

[63]    Henderson FM (1982)  An Evaluation of Seasat SAR Imagery for Urban Analysis. Journal of Remote Sensing of Environment, Elsevier Science Publishing Co., doi: 10.1016/0034-4257(82)90019-0, vol. 12, no. 6, pp. 439-461.

[64]    Hill RD, Moate CP, Blacknell D (2008)  Estimating building dimensions from synthetic aperture radar image sequences. IET Radar, Sonar & Navigation, doi: 10.1049/iet-rsn:20070077, vol. 2, no. 3, pp. 189-199.

[65]    Hillman A, Rolland P, Périard R, Luscombe A, Chabot M, Chen C, Martens N (2010)  RADARSAT-2 Continuing System Operations and Performance. IEEE Proceedings of International Geoscience and Remote Sensing Symposium, doi: 10.1109/IGARSS.2010.5649614, pp. 3228-3231.

[66]    Hussin YA (1995)  Effect of polarization and incidence angle on radar return from urban features using L-band aircraft radar data. IEEE Proceedings of International Geoscience and Remote Sensing Symposium, doi: 10.1109/IGARSS.1995.519683, vol. 1, pp. 178-180.

[67]    IEEE Aerospace & Electronic Systems Society (2003) IEEE Standard for Letter Designations for Radar-Frequency Bands. IEEE Std 521TM-2002(R2009) recognized as an American National Standard (ANSI), Revision of IEEE Std 512-1984.

[68]    Infoterra an EADS Astrium company (2008)  Radiometric Calibration of TerraSAR-X Data: Beta Naught and Sigma Naught Coefficient Calculation. TSXX-ITD-TN-0049-radiometric_calculations_I1.00. www.astrium-geo.com/de/825-terrasar-x-technische-informationen.

[69]    Jahangir M, Blacknell D, Moate CP, Hill RD (2007)  Extracting information from shadows in SAR imagery. IEEE Proceedings of the International Conference on Machine Vision, doi: 10.1109/ICMV.2007.4469282, pp. 107-112.

[70]    Just D, Bamler R (1994)  Phase statistics of interferograms with applications to synthetic aperture radar. Journal of Applied Optics, doi: 10.1364/AO.33.004361, vol. 33, no. 20, pp. 4361-4368.

[71]    Kirscht M, Rinke C (1998)  3D-Reconstruction of Buildings and Vegetation from Synthetic Aperture Radar (SAR) Images. Proceedings of International Association for Pattern Recognition, Workshop on Machine Vision Applications, pp. 228-231.

[72]    Klausing H, Holpp W (1999)  Radar mit realer und synthetischer Apertur. Oldenbourg Verlag München, isbn: 978-3486234756.

[73]    Kluth VS, Henning H, Sharp M, Winsand D (1992)  Detecting man-made objects in low resolution SAR using fractal texture discriminators. IEEE Proceedings of International Geoscience and Remote Sensing Symposium, doi: 10.1109/IGARSS.1992.578354, vol. 2, pp. 1105-1107.

[74]  Krieger G, Zink M, Fiedler H, Hajnsek I, Younis M, Huber S, Bachmann M, Gonzalez JH, Schulze D, Boer J, Werner M, Moreira A (2009) The TanDEM-X Mission: Overview and status. IEEE Proceedings of the International Radar Conference, doi: 10.1109/RADAR.2009.4977075, pp. 1-5.

[75]  Kuan DT, Sawchuk AA, Strand TC, Chavel P (1985) Adaptive Noise Smoothing Filter for Images with Signal-Dependent Noise. IEEE Transactions on Pattern Analysis and Machine Intelligence, doi: 10.1109/TPAMI.1985.4767641, vol. 7, no. 2, pp. 165-177.

[76]  Leberl F (1990) Radargrammetric Image Processing. Artech House, Boston, isbn: 978-0890062730.

[77]  Lee JS (1980) Digital Image Enhancement and Noise Filtering by Use of Local Statistics. IEEE Transactions on Pattern Analysis and Machine Intelligence, doi: 10.1109/TPAMI.1980.4766004, vol. 2, no. 2, pp. 165-168.

[78]  Lee JS, Hoppel KW, Mange SA, Miller AR (1994) Intensity and Phase Statistics of Multilook Polarimetric and Interferometric SAR Imagery. IEEE Transactions on Geoscience and Remote Sensing, doi: 10.1109/36.312890, vol. 32, no. 5, pp. 1017-1028.

[79]  Lee JS, Papathanassiou P, Ainsworth TL, Grunes MR, Reigber A (1998) New Technique for Noise Filtering of SAR Interferometric Phase Images. IEEE Transactions on Geoscience and Remote Sensing, doi: 10.1109/36.718849, vol. 36, no. 5, part 1, pp. 1456-1465.

[80]  Lee JS, Papathanassiou P, Hajnsek I, Mette T, Grunes MR, Ainsworth TL, Ferro-Famil L (2005) Applying polarimetric SAR interferometric data for forest classification. IEEE Proceedings of International Geoscience and Remote Sensing Symposium, doi: 10.1109/IGARSS.2005.1526759, vol. 7, pp. 4848-4851.

[81]  Lee JS, Krogager E, Ainsworth TL, Boerner WM (2006) Polarimetric Analysis of Radar Signature of a Manmade Structure. IEEE Geoscience and Remote Sensing Letters, doi: 10.1109/LGRS.2006.879564, vol. 3, no. 4, pp. 555-559.

[82]  Lee JS, Pottier E (2009) Polarimetric Radar Imaging: From Basics to Applications. CRC Press, isbn: 978-1420054972.

[83]  Levine MD, Shaheen SI (1981) A Modular Computer Vision System for Picture Segmentation and Interpretation. IEEE Transactions of Pattern Analysis and Machine Intelligence, doi: 10.1109/TPAMI.1981.4767147, vol. 3, no. 5, pp. 540-556.

[84]  Lewis AJ, Henderson FM (1998) Chapter 3: Radar Fundamentals: The Geoscience Perspective. In: Principle & Applications of IMAGING RADAR, Manual of Remote Sensing, Third Edition, Volume 2, edited by FM Henderson, AJ Lewis, John Wiley & Sons, Inc., isbn: 978-0471330462.

[85]  Li X, Tennant K, Lawrence G (2004) Three-dimensional Mapping with Airborne Ifsar Based Star Technology - Intermap's Experiences. International Archives of the Photogrammetry, Remote Sensing and Spatial Information Sciences, XXth ISPRS Congress, vol XXXV, part 3, pp. 261-266.

[86]  Li Z (2007) Coregistration of image pairs, DEM refinement and evaluation for SAR interferometry. Purdue University (United States, Indiana): Ph.D. Thesis, isbn: 9780549564409.

[87]  Lopes A, Nezry E, Touzi R, Laur H (1993) Structure detection and statistical adaptive speckle filtering in SAR images. International Journal of Remote Sensing, doi: 10.1080/01431169308953999, vol. 14, no. 9, pp. 1735-1758.

[88]  Madsen SN, Zebker HA, (1998) Chapter 6: Imaging Radar Interferometry. In: Principle & Applications of IMAGING RADAR, Manual of Remote Sensing, Third Edition, Volume 2, edited by FM Henderson, AJ Lewis, John Wiley & Sons, Inc., isbn: 978-0471330462.

[89]  Magnard C, Meier E, Ruegg M, Brehm T, Essen H (2007) High Resolution Millimeter Wave SAR Interferometry. IEEE Proceedings of International Geoscience and Remote Sensing Symposium, doi: 10.1109/IGARSS.2007.4423999, pp. 5061-5064.

[90]  Meta A, Trampuz C (2010) MetaSensing compact, high resolution interferometric SAR sensor for commercial and scientific applications. Proceedings of 7th European Radar Conference. pp. 21-24.

[91]  Meyer RH, Roy RJ (2000) Algorithms for Interpreting SAR Imagery of Complex Building Scenes. Proceedings of SPIE Conference on Algorithms for Synthetic Aperture Radar Imagery VII, doi: 10.1117/12.396375, vol. 4053, pp. 642-651.

[92]    Michaelsen E, Arens M, Doktorski L, (2008)  Elements of a gestalt algebra: Steps towards understanding images and scenes. Proceedings of the 1st International Workshop on Image Mining Theory and Applications IMTA 2008, in conjunction with VISIGRAPP 2008, INSTICC Press, isbn: 978-898-8111-25-8, pp. 65-73.

[93]    Moreira A (2006)  Microwaves and Radar Institute, Status Report 2000-2005, Research Results and Projects. Published by German Aerospace Center, A Member of the Helmholtz Society, Microwaves and Radar Institute.

[94]    Moses RL, Ash JN (2008)  Recursive SAR Imaging. Proceedings of SPIE Conference on Algorithms for Synthetic Aperture Radar Imagery XV, doi: 10.1117/12.786307, vol. 6970, pp. 69700P-1- 69700P-12.

[95]    Oriot H, Cantalloube H (2008)  Circular SAR imagery for urban remote sensing. Proceedings of 7th European Conference on Synthetic Aperture Radar, VDE Verlag GmbH, Berlin, isbn: 978-3800730841, vol. 2, pp. 205-208.

[96]    Peichl M, Kempf T, Dill S (2008)  Radar Signature Analysis of Urban Structures. IEEE Proceedings of International Geoscience and Remote Sensing Symposium, doi: 10.1109/IGARSS.2008.4780144, vol. 5, pp. 22-25.

[97]    Petit D, Adragna F (2000)  A new interferogram simulator: 2SIR. Study of coherence losses for tortured reliefs. Proceedings of SAR Workshop: CEOS Committee on Earth Observation Satellites - Working Group on Calibration and Validation, ESA SP-450, isbn: 929-0926414, pp. 591-596.

[98]    Petit D, Adragna F, Durou JD (2000)  The filtering of layover areas in high-resolution IFSAR for the building extraction. Proceedings of SPIE Conference on SAR Image Analysis, Modeling, and Techniques III, doi: 10.1117/12.410663, vol. 4173, pp. 230-240.

[99]    Petit D, Soucille L, Durou JD, Adragna F, Oriot H, Simonetto E (2002)  Spatial phase behaviour in SAR images. Proceedings of SPIE Conference on SAR Image Analysis, Modeling, and Techniques IV, doi: 10.1117/12.453977, vol. 4543, pp. 53-63.

[100]   Quartulli M, Datcu M (2004)  Stochastic geometrical modelling for built-up area understanding from a single SAR intensity image with meter resolution. IEEE Transactions on Geoscience and Remote Sensing, doi: 10.1109/TGRS.2004.833391, vol 42, no 9, pp. 1996-2003.

[101]   Raney RK (1998)  Chapter 2: Radar Fundamentals: Technical Perspective. In: Principle & Applications of IMAGING RADAR, Manual of Remote Sensing, Third Edition, Volume 2, edited by FM Henderson, AJ Lewis, John Wiley & Sons, Inc., isbn: 978-0471330462.

[102]   Reigber A, Moreira A (2000)  First demonstration of airborne SAR tomography using multibaseline L-band data. IEEE Transactions on Geoscience and Remote Sensing, doi: 10.1109/36.868873, vol. 38, no. 5, part 1, pp. 2142-2152.

[103]   Reigber A, Neumann M, Erten E, Jaeger M, Prats P (2007)  Multi-baseline polarimetrically optimised phases and scattering mechanisms for InSAR applications. IEEE Proceedings of International Geoscience and Remote Sensing Symposium, doi: 10.1109/IGARSS.2007.4423382, pp. 2620-2623.

[104]   Roth A, Craubner A, Huegel T (1993)  Standard Geocoded Ellipsoid Corrected Images. In Schreier G. (ed) SAR Geocoding: Data and Systems, Karlsruhe: Wichmann, pp. 159-172.

[105]   Sauer S, Ferro-Famil, Reigber A, Pottier E (2011)  Three-Dimensional Imaging and Scattering Mechanism Estimation Over Urban Scenes Using Dual-Baseline Polarimetric InSAR Observations at L-Band. IEEE Transactions on Geoscience and Remote Sensing, doi: 10.1109/TGRS.2011.2147321, vol. 49, no. 11, pp. 4616-4629.

[106]   Schimpf H, Essen H, Boehmsdorff S, Brehm T (2002)  MEMPHIS – a Fully Polarimetric Experimental Radar. IEEE Proceedings of International Geoscience and Remote Sensing Symposium, doi: 10.1109/IGARSS.2002.1026230, vol. 3, pp. 1714-1716.

[107]   Schmitt M, Stilla U (2011)  Fusion of Airborne Multi-Aspect InSAR Data by Simultaneous Backward Geocoding. IEEE Proceedings of Joint Urban Remote Sensing Event, doi: 10.1109/JURSE.2011.5764717, pp. 53-56.

[108]   Schreier G (1993)  Geometrical Properties of SAR Images. In Schreier G. (ed) SAR Geocoding: Data and Systems, Karlsruhe: Wichmann, pp. 103-134.

[109]   Schulz K, Boldt M, Thiele A (2009)  CoVAmCoh-Analysis: A method to improve the interpretation of high resolution repeat pass SAR images of urban areas. Proceedings of SPIE, Remote Sensing for Environmental Monitoring, GIS Applications, and Geology IX, doi: 10.1117/12.830441, vol. 7478, pp. 747805-1-9.

[110] Schunert A, Balz T, Liu K, Liao MS, Soergel U, Wegner JD (2010) Simulation Assisted High-Resolution PSI Analysis. International Archives of Photogrammetry, Remote Sensing and Spatial Information Sciences, ISPRS Technical Commission VII Symposium, vol. XXXVIII, part 7B, pp. 498-503.

[111] Schwaebisch M, Moreira J (1999) The high resolution airborne interferometric SAR AeS-1. Proceedings of the Fourth International Airborne Remote Sensing Conference and Exhibition, 21st Canadian Symposium on Remote Sensing, pp. 540-547.

[112] Seidel H, Stahl C, Knappe P, Hurst P (2004) Dynamic generation of artificial HRSAR imagery for ATR development and cockpit simulation. Proceedings of SPIE, Automatic Target Recognition XIV, doi: 10.1117/12.541273, vol. 5426, pp. 264-273.

[113] Sekine M, Mao Y (1990) Weibull Radar Clutter. IEE Radar, Sonar, Navigation and Avionics Series 3, Peter Peregrinus Ltd., London, United Kingdom, isbn: 978-0863411915.

[114] Simonetto E, Oriot H, Garello R (2005) Rectangular building extraction from stereoscopic air-borne radar images. IEEE Transactions on Geoscience and Remote Sensing, doi: 10.1109/TGRS.2005.853570, vol. 43, no. 10, pp. 2386-2395.

[115] Soergel U (2003) Iterative Verfahren zur Detektion und Rekonstruktion von Gebäuden in SAR- und InSAR-Daten. Leibniz University of Hannover: Ph.D. Thesis.

[116] Soergel U, Thoenessen U, Stilla U (2003) Visibility analysis of man-made objects in SAR images. IEEE Proceedings of 2nd GRSS/ISPRS Joint Workshop on Remote Sensing and Data Fusion over Urban Areas, doi: 10.1109/DFUA.2003.1219970, pp. 120-124.

[117] Soergel U, Thoenessen U, Brenner A, Stilla U (2006) High resolution SAR data: New opportunities and challenges for the analysis of urban areas. IEE Proceedings on Radar, Sonar & Navigation, vol. 153, no. 3, pp. 294–300.

[118] Soergel U, Michaelsen E, Thiele A, Cadario E, Thoennessen U (2009) Stereo analysis of high-resolution SAR images for building height estimation in cases of orthogonal aspect directions. ISPRS Journal of Photogrammetry and Remote Sensing, vol. 64, no. 5, pp. 490-500.

[119] Stankwitz HC, Dallaire RJ, Fienup JR (1995) Nonlinear Apodization for Sidelobe Control in SAR Imagery. IEEE Transactions on Aerospace and Electronic Systems, doi: 10.1109/7.366309, vol. 31, no. 1, pp. 267-279.

[120] Steger C (1998) An Unbiased Detector of Curvilinear Structures. IEEE Transactions on Pattern Analysis and Machine Intelligence, doi: 10.1109/34.659930, vol. 20, no. 2, pp. 113-125.

[121] Stilla U, Soergel U, Thoennessen U (2003) Potential and limits of InSAR data for building reconstruction in built up-areas. ISPRS Journal of Photogrammetry and Remote Sensing, vol. 58, no. 1/2, pp. 113–123.

[122] Terano T, Asai K, Sugeno M (1987) Fuzzy Systems Theory and Its Applications. English Edition Copyright (1992) by ACADEMIC PRESS, Inc., Harcourt Brace & Company, Publishers, isbn: 978-0126852455.

[123] Thiele A, Cadario E, Schulz K, Thoennessen U, Soergel U (2007) Model Based Building Recognition from Multi-Aspect InSAR Data in Urban Areas. IEEE Proceedings of 4th GRSS/ISPRS Joint Workshop on Remote Sensing and Data Fusion over Urban Areas, doi: 10.1109/URS.2007.371808, pp. 1-6.

[124] Thiele A, Cadario E, Schulz K, Thoennessen U, Soergel U (2007) Building recognition from multi-aspect high resolution InSAR data in urban area. IEEE Transactions on Geoscience and Remote Sensing, doi: 10.1109/TGRS.2007.898440, vol. 45, no. 11, part 1, pp. 3583-3593.

[125] Thiele A, Cadario E, Schulz K, Thoennessen U, Soergel U (2007) InSAR Phase Profiles at Building Locations. International Archives of Photogrammetry, Remote Sensing and Spatial Information Sciences, Workshop on Photogrammetric Image Analysis, vol. XXXVI, part 3/W49A, pp. 203-208.

[126] Thiele A, Cadario E, Schulz K, Soergel U (2010) Analysis of Gable-Roofed Building Signatures in Multiaspect InSAR Data. IEEE Geoscience and Remote Sensing Letters, doi: 10.1109/LGRS.2009.2023476, vol. 7, no. 1, pp. 83-87.

[127] Thiele A, Wegner JD, Soergel U (2010) Building Reconstruction from Multi-Aspect InSAR Data. In: U. Soergel (Ed), Radar Remote Sensing of Urban Areas, Springer, 1st Edition, isbn: 978-9048137500, chapter 8, pp. 187-214.

[128]    Thiele A, Dubois C, Cadario E, Hinz S (2011)  Smart Filtering of Interferometric Phases for Enhancing Building Reconstruction. International Archives of the Photogrammetry, Remote Sensing and Spatial Information Sciences, Workshop on Photogrammetric Image Analysis, vol. XXXVIII, part 3/W22, pp. 161-166.

[129]    Thiele A, Dubois C, Cadario E, Hinz S (2012)  GIS-supported Iterative Filtering Approach for Building Height Estimation from InSAR Data. In: Proceedings of 9th European Conference on Synthetic Aperture Radar, EUSAR 2012, pp. 19-22.

[130]    Tison C, Nicolas JM, Tupin F, Maitre H (2004)  A New Statistical Model for Markovian Classification of Urban Areas in High-Resolution SAR Images. IEEE Transactions on Geoscience and Remote Sensing, doi: 10.1109/TGRS.2004.834630, vol. 42, no. 10, pp. 2046-2057.

[131]    Tison C, Tupin F, Maitre H (2004)  Retrieval of building shapes from shadows in high resolution SAR interferometric images. IEEE Proceedings of International Geoscience and Remote Sensing Symposium, doi: 10.1109/IGARSS.2004.1370681, pp. 1788-1791.

[132]    Tison C, Tupin F, Maitre H (2007)  A fusion scheme for joint retrieval of urban height map classification from high-resolution interferometric SAR images. IEEE Transactions on Geoscience and Remote Sensing, doi: 10.1109/TGRS.2006.887006, vol. 45, no. 2, pp. 496-505.

[133]    Touzi R, Lopes A, Bousquet P (1988)  A Statistical and Geometrical Edge Detector for SAR Images. IEEE Transactions on Geoscience and Remote Sensing, doi: 10.1109/36.7708, vol. 26, no. 6, pp. 764-773.

[134]    Touzi R, Lopes A, Bruniquel J, Vachon PW (1999)  Coherence Estimation for SAR Imagery. IEEE Transactions on Geoscience and Remote Sensing, doi: 10.1109/36.739146, vol. 37, no. 1, part 1, pp. 135-149.

[135]    Tupin F (2003)  Extraction of 3D information using overlay detection on SAR images. IEEE Proceedings of 2nd GRSS/ISPRS Joint Workshop on Remote Sensing and Data Fusion over Urban Areas, doi: 10.1109/DFUA.2003.1219960, pp. 72-76.

[136]    Tupin F, Houshmand B, Datcu M (2002)  Road detection in dense urban areas using SAR imagery and the usefulness of multiple views. IEEE Transactions on Geoscience and Remote Sensing, doi: 10.1109/TGRS.2002.803732, vol. 40, no. 11, pp. 2405-2414.

[137]    Tupin F, Maitre H, Mangin JF, Nicolas JM, Pechersky E (1998)  Detection of Linear Features in SAR Images: Application to Road Network Extraction. IEEE Transactions on Geoscience and Remote Sensing, doi: 10.1109/36.662728, vol. 36, no. 2, pp. 434-453.

[138]    Tupin F (2010)  Fusion of Optical and SAR Images. In: U. Soergel (Ed), Radar Remote Sensing of Urban Areas, Springer, 1st Edition, isbn: 978-9048137500, chapter 6, pp. 133-159.

[139]    Tupin, F (2011)  How Advanced Image Processing Helps For SAR Image Restoration and Analysis. IEEE Geoscience and Remote Sensing Newsletter, Cumulative Issue 158, March 2011, issn: 0274-6338, pp. 10-17.

[140]    Wegner JD, Haensch R, Thiele A, Soergel U (2011)  Building Detection From One Orthophoto and High-Resolution InSAR Data Using Conditional Random Fields. IEEE Journal of Selected Topics in Applied Earth Observations and Remote Sensing, doi: 10.1109/JSTARS.2010.2053521, vol. 4, no. 1, pp. 83-91.

[141]    Wells L, Sorensen K, Doerry A, Remund B (2003)  Developments in sar and ifsar systems and technologies at sandia national laboratories. IEEE Proceedings of International Aerospace Conference, doi: 10.1109/AERO.2003.1235522, vol. 2, pp. 1085-1095.

[142]    Wilkinson AJ (1998)  Synthetic Aperture Radar Interferometry: A Model for the Joint Statistics in Layover Areas. Proceedings of the South African Symposium on Communications and Signal Processing doi: 10.1109/COMSIG.1998.736976, pp. 333-338.

[143]    Wolf E (1986)  Progress in Optics. Volume XXIII, Elsevier Science Publishers B.V., isbn: 0444869824.

[144]    Xu F, Jin YQ (2006)  Imaging simulation of polarimetric SAR for a comprehensive terrain scene using the mapping and projection algorithm. IEEE Transactions on Geoscience and Remote Sensing, doi: 10.1109/TGRS.2006.879544, vol. 44, no. 11, part 2, pp. 3219-3234.

[145]    Xu F, Jin YQ (2007)  Automatic Reconstruction of Building Objects From Multiaspect Meter-Resolution SAR Images. IEEE Transactions on Geoscience and Remote Sensing, doi: 10.1109/TGRS.2007.896614, vol. 45, no. 7, part 2, pp. 2336-2353.

[146]   Yang X (2011)  Urban Remote Sensing: Monitoring, Synthesis and Modeling in the Urban Environment. Editor: Xiaojun Yang, 1. edition, John Wiley & Sons, isbn: 047074958X.

[147]   Zhang F, Shao Y, Zhang X (2010)  Building extraction using dual-aspect high resolution SAR images. Proceedings of 18th International Conference on Geoinformatics, doi: 10.1109/GEOINFORMATICS.2010. 5567994, pp. 1-5.

[148]   Zhang F, Shao Y, Zhang X, Balz T (2011)  Building L-shape Footprint Extraction From High Resolution SAR Image. IEEE Proceedings of Joint Urban Remote Sensing Event, doi: 10.1109/JURSE.2011.5764772, pp. 273-276.

[149]   Zhenghao S, Fung KB (1994)  A comparison of digital speckle filters. IEEE Proceedings of International Geoscience and Remote Sensing Symposium, doi: 10.1109/IGARSS.1994.399671, vol. 4, pp. 2129-2133.

[150]   Zhu XX, Bamler R (2010)  Very High Resolution Spaceborne SAR Tomography in Urban Environment. IEEE Transactions on Geoscience and Remote Sensing, doi: 10.1109/TGRS.2010.2050487, vol. 48, no. 12, pp. 4296-4308.

# Danksagung

> *„Nicht das Beginnen wird belohnt, sondern einzig und allein das Durchhalten."*
>
> (Katharina von Siena)

Dieser Satz ist bezeichnend für den Verlauf meiner Promotionsarbeit, der sich über zwei Arbeitsverhältnisse und einen etwas längeren Zeitraum erstreckte.

Zuallererst möchte ich mich bei meinem Doktorvater Prof. Uwe Sörgel bedanken, der mich über die gesamte Zeit meiner Promotion fachlich kompetent betreute und mich von Anfang an in meinem Promotionsvorhaben bestärkte. Des Weiteren bedanke ich mich bei den drei Mitreferenten Prof. Uwe Stilla, Prof. Stefan Hinz und Prof. Claus Brenner, die ebenfalls zum Gelingen dieser Arbeit beitrugen. Mein besonderer Dank gilt Ulrich Thönnessen und Karsten Schulz, die mir als Abteilungsleiter in meiner wissenschaftlichen Arbeit sehr viel Freiraum ließen.

> *„Zusammenkommen ist ein Beginn, Zusammenbleiben ein Fortschritt, Zusammenarbeiten ein Erfolg."*
>
> (Henry Ford)

Dieses Zitat fasst für mich sehr schön zusammen, was meiner Arbeit zugrunde liegt: ein wunderbarer Kreis an Kollegen mit denen fachliche Diskussionen des Öfteren ein abendfüllendes Programm einnahmen. Herausstellen möchte ich dabei meine langjährigen Kollegen Erich Cadario, Horst Hammer und Markus Even. Hoffentlich lässt sich dies noch über viele Jahre fortführen.

Ein großer Dank geht an Caroline Schweitzer, Clémence Dubois, Erich Cadario, Horst Hammer, Gunnar Ritt, Stefan Hinz und Uwe Sörgel, die das Korrekturlesen meiner Arbeit übernahmen.

Außerdem möchte ich mich für die starke Unterstützung aus meinem großen, über die Jahre gewachsenen Freundeskreis in bzw. aus Karlsruhe bedanken. Zu guter Letzt danke ich meiner Familie und Gunnar für die vielen aufbauenden Worte.

# Curriculum Vitae

| | |
|---|---|
| **Name** | Antje Thiele |
| **Date of birth** | 13th December 1979 |
| **Place of birth** | Freiberg |
| **Nationality** | German |

## Educational background

| | |
|---|---|
| 1998 – 2004 | Dresden University of Technology<br>study of geodesy<br>degree: Diplom (30.06.2004) |
| 1994 – 1998 | Albert-Schweitzer-Gymnasium Erfurt<br>Spezialschulteil mathematisch-naturwissenschaftlicher Richtung<br>degree: Abitur (09.07.1998) |
| 1992 – 1994 | Albert-Schweitzer-Gymnasium Erfurt |
| 1991 – 1992 | Staatliche Regelschule 21 Erfurt |
| 1986 – 1991 | Polytechnische Oberschulen Erfurt, POS 2 und POS 45 |

## Scientific employments

| | |
|---|---|
| since 09.2009 | Karlsruhe Institute of Technology (former: Universität Karlsruhe)<br>Institute of Photogrammetry and Remote Sensing (IPF)<br>position: research associate |
| since 08.2007 | Leibniz Universität Hannover<br>Institute of Photogrammetry and GeoInformation<br>position: external PhD student |
| since 04.2005 | Fraunhofer IOSB (former: FGAN-FOM)<br>department: scene analysis<br>position: research associate |
| 01.2005 | University of Göttingen<br>Institute of Geography<br>position: research associate |
| 08.2003 – 06.2004<br>10.2002 – 04.2003 | Ingenieurbureau Geodelta (NL)<br>position: trainee<br>thesis: Verfahren zur Volumenbestimmung von Eisbergen<br>anhand von Bildsequenzen |